

Early rifting of Gondwana: Conclusions from the crustal structure of the Falkland Plateau

Dissertation

in partial fulfillment of the requirements for the degree of
doctor rerum naturalium (Dr. rer. nat.),
submitted to the Department of Geosciences at the
University of Bremen, Germany, by

Claudia Monika Schimschal

Alfred Wegener Institute
Helmholtz Centre for Polar and Marine Research
Bremerhaven

Assessors:

Prof. Dr. Wilfried Jokat

Prof. Dr. Cornelia Spiegel

Date of submission: 21st March 2018

Date of defence: 8th June 2018

Affirmation

Claudia Monika Schimschal, née Klemt
Mühlenstraße 10D
29221 Celle
Germany

I affirm that

- a) I wrote the present thesis independently and without illicit assistance from third parties,
- b) I used no sources other than those indicated nor aids other than those permissible,
- c) I appropriately referenced any text or content from other sources.

Celle on this 21st March 2018

Claudia Monika Schimschal

Summary

The reconstruction of continents has been a research field for more than 100 years, since Alfred Wegener proposed his theory of continental drift in 1915. The changing configuration of landmasses and oceans influences the evolution of climate and biosphere and is therefore of great scientific importance. In the southern hemisphere, Gondwana, which comprised the present-day continents of Antarctica, South America, Africa and Australia and smaller landmasses like India, New Zealand, Madagascar and the Arabian Peninsula, was the last supercontinent. In the centre of the continent, the Falkland Plateau was located between the South American, African and Antarctic plates.

Today, the Falkland Plateau is a remarkable bathymetric feature in the South Atlantic Ocean offshore southern South America. It stretches for 1500 km eastwards from the Falkland Islands into the Georgia Basin, at depths of between one and three kilometres shallower than its surroundings. The central part of the plateau hosts the Falkland Plateau Basin. A bathymetric high, Maurice Ewing Bank (MEB), is located at the eastern termination of the plateau.

Although the Falkland Plateau is a key element in Gondwana reconstructions, its crustal structure has long remained speculative. Outcrops on the Falkland Islands prove the presence of Precambrian continental crust at the western end of the plateau. At the eastern end, gneisses recovered at DSDP drill site 330 on MEB, were interpreted to show its continental composition. For the crust underneath the Falkland Plateau Basin, a variety of approaches have led to conflicting conclusions on the presence of continental or oceanic crust. The lack of certainty regarding the crustal composition here has both stimulated and permitted a range of contrasting Gondwana reconstructions.

To close this gap, the expedition ANT-XXIX/5 with the research vessel *RV Polarstern* was conducted in 2013. Wide-angle seismic data were acquired using land stations onshore East Falkland and ocean bottom stations along the 1450 km long transect AWI-20130010. Magnetic, bathymetric and sediment echosounder data were recorded along the ship track. Additional airborne magnetic profiles were flown with the ship's helicopter. In this study, I present models of the velocity, density and geology along the transect, derived from ray tracing and amplitude, density and magnetic modelling. By interpreting all of these datasets, I present the first comprehensive crustal model of the Falkland Plateau and the resulting consequences for the earliest rifting of Gondwana within this region.

The crustal model shows the presence of 34 km thick continental crust beneath East Falkland. Across the eastern margin of East Falkland, which can be classified as a volcanic rifted margin, the basement dips steeply into the Falkland Plateau Basin. Seismic velocities and the magnetic anomaly data indicate the presence of a 90 km wide continent-ocean transition zone (COT). Sediments in the Falkland Plateau Basin have

an average thickness of 6.5 km. Underneath lies an oceanic crust of up to 20 km thickness, with high velocities of 7.4 km/s above Moho. Further east, a second COT of 80 km width exists before the basement rises steeply up to MEB. Lower seismic velocities and densities as well as a different velocity structure compared to the crust underneath the Falkland Plateau Basin characterize the MEB as a continental fragment. The continental crust of the central MEB is up to 29 km thick and neither tectonically nor magmatically overprinted. The crust thins towards the east and west. High velocities of more than 7.0 km/s and intracrustal reflections in the western part of MEB indicate the presence of magmatic intrusions. In the Georgia Basin, magnetic isochron M10n indicates the onset of oceanic crust. Here, the crust is of average oceanic crustal thickness at 7.1 km. These results are used as constraints for a refined model of the breakup of Gondwana. The presence of oceanic crust beneath the Falkland Plateau Basin allows to position the Falkland Islands and MEB as a continuous feature off the eastern coast of South Africa. To the south, the Weddell Sea region was located and formed a wide rift area. Radiometric dates from onshore magmatic dykes, the age of sediments above basement east of the Falkland Islands and the ages of crustal stretching and rifting in adjacent regions, indicate that rifting and subsequent seafloor spreading on the Falkland Plateau took place between ~ 178 Ma and ~ 154 Ma. This opening of the Falkland Plateau Basin was accommodated by movement of the Patagonian sub-plate along the Gastre Fault. The exceptionally thick oceanic crust underneath the Falkland Plateau Basin likely results from its development in a back-arc regime over a region of anomalously warm or fertile mantle that was also responsible for the extensive onshore Karoo-Ferrar and Chon Aike volcanic provinces. The emplacement of thick oceanic crust was spatially and temporally limited to the Falkland Plateau Basin and the Jurassic Weddell Rift.

Zusammenfassung

Seit Alfred Wegeners Theorien der Kontinentalverschiebung gibt es unzählige Studien, die sich mit der Rekonstruktion der früheren Kontinente befassen. Die sich ändernde Verteilung von Landflächen und Ozeanen hat weitreichende Folgen für die Entwicklung des Klimas und der Biosphäre. Daher ist die Rekonstruktion früherer Kontinente und die Kinematik der Platten von großem wissenschaftlichen Interesse. Gondwana war der letzte Großkontinent in der südlichen Hemisphäre und umfasste die heutigen Kontinentalmassen der Antarktis, Südamerikas, Afrikas und Australiens sowie kleinere Landmassen wie Indien, Neuseeland, Madagaskar und die Arabische Halbinsel. Im Zentrum Gondwanas lag das Falkland Plateau zwischen der afrikanischen Platte und den südamerikanischen und antarktischen Platten.

Heute ist das Falkland Plateau eine markante bathymetrische Struktur im Südatlantik mit Wassertiefen zwischen 1 und 4 km flacher als in der Umgebung. Es erstreckt sich von den Falklandinseln über 1400 km nach Osten bis hin zum Georgia-Becken. Im zentralen Bereich des Plateaus liegt das Falkland Plateau Becken. Am östlichen Rand befindet sich eine bathymetrische Erhebung, die Maurice Ewing Bank (MEB).

Obwohl das Falkland Plateau ein zentrales Element für die Rekonstruktion Gondwanas ist, war dessen Krustenstruktur bisher spekulativ. Am westlichen Ende des Plateaus ist durch einen Aufschluss auf den Falklandinseln bekannt, dass diese aus prekambrischer kontinentaler Kruste bestehen. Am östlichen Ende des Plateaus wurden Gneise im Bohrklein von DSDP Bohrloch 330 auf der MEB gefunden, woraus auf eine kontinentale Zusammensetzung der MEB geschlossen wurde. Ob es sich bei der Kruste des Falkland Plateau Beckens um gedehnte kontinentale oder ozeanische Kruste handelt ist bisher ungeklärt. Die unbekannte krustale Zusammensetzung führte zu vielen, unterschiedlichen und widersprüchlichen Rekonstruktionen Gondwanas.

Um neue Erkenntnisse über die Struktur des Falkland Plateaus zu erlangen, wurde im Jahr 2013 die Expedition ANT-XXIX/5 mit dem Forschungsschiff *Polarstern* durchgeführt. Weitwinkelseismik wurde mittels Landstationen auf Ostfalkland und Ozeanbodenseismometer Stationen entlang eines 1450 km langen Transekts (AWI-20130010) akquiriert. Außerdem wurden Magnetik-, Bathymetrie- und Sediment-Echolot-Daten aufgezeichnet. Zusätzliche aeromagnetische Daten wurden mit *Polarstern's* Helikopter aufgenommen. Im Zuge dieser Dissertation führte ich eine Geschwindigkeits-, Amplituden-, Dichte- und Magnetikmodellierung durch, um das erste fundierte Krustenmodell des Falkland Plateaus zu erstellen.

Dieses zeigt, dass die kontinentale Kruste unter Ostfalkland 34 km mächtig ist. Nach Osten fällt das Basement steil ab und formt das Falkland Plateau Becken. Der östliche Kontinentalrand der Falklandinseln kann als vulkanisch charakterisiert werden. Die seismischen Geschwindigkeiten und die magnetischen Anomalien deuten auf eine 90 km brei-

te Kontinent-Ozean-Übergangszone hin. Im Falkland Plateau Becken haben die abgelagerten Sedimente eine Mächtigkeit von durchschnittlich 6.5 km. Die darunter liegende Kruste ist ozeanisch und bis zu 20 km mächtig mit hohen seismischen Geschwindigkeiten von 7.4 km/s über der Moho. Nach Osten existiert eine 80 km breite Kontinent-Ozean-Übergangszone. Die MEB ist ein kontinentales Fragment mit einer Krustenmächtigkeit von 29 km im zentralen Bereich, der nicht tektonisch oder magmatisch überprägt ist. Nach Osten und Westen hin ist die Kruste gedehnt. Hohe Geschwindigkeiten über 7.0 km/s und intra-krustale Reflexionen im westlichen Teil deuten auf magmatische Intrusionen hin. Im Georgia-Becken hat die ozeanische Kruste eine Mächtigkeit von 7.1 km, was typisch für ozeanische Kruste ist.

Mit diesen Ergebnissen erstellte ich ein genaueres Aufbruchmodell Gondwanas, in welchem die Unsicherheiten früherer Modelle im Bereich des Falkland Plateaus eliminiert sind. Aufgrund der ozeanischen Kruste unter dem Falkland Plateau Becken, bildeten während des Juras die Falklandinseln und die MEB eine geologische Einheit, die sich östlich von Südafrika befand. Südlich davon lag die heutige Weddell Meer Region und bildete ein großes Rift-Becken. Durch Altersdatierungen des Magmatismus auf den Falklandinseln, der Stratigraphie der Sedimente über dem Basement östlich der Falklandinseln und dem Alter der Dehnungsphasen in Regionen südlich und nördlich des Falkland Plateaus schätzte ich das Alter der ozeanischen Kruste des Falkland Plateau Beckens. Rifting und anschließende Ozeanbildung begannen vor ungefähr ~ 178 Ma und endeten vor etwa ~ 154 Ma. Bedingt durch die Öffnung des Falkland Plateau Beckens, bewegte sich die Patagonische Platte entlang der Gastre Störung Richtung Westen.

Die ungewöhnliche Mächtigkeit des Falkland Plateau Beckens resultiert aus dessen Position während der Krustenbildung in einer Backarc-Region über einer thermischen Mantel Anomalie oder fertilem Mantel, die auch für die ausgedehnten vulkanischen Karoo-Ferrar and Chon Aike Provinzen verantwortlich ist. Die Entstehung dicker ozeanischer Kruste war zeitlich und räumlich begrenzt auf die Bildung der Kruste des Falkland Plateau Beckens und des jurassischen Weddell Rifts.

Content

| | |
|--|-------------|
| Summary | i |
| Zusammenfassung | iii |
| Content | v |
| List of Figures | viii |
| List of Tables | xii |
| Abbreviations | xiii |
| 1. Introduction | 1 |
| 1.1. Geological and geophysical investigations | 1 |
| 1.2. Motivation | 5 |
| 1.3. Research questions of this thesis | 6 |
| 2. Methods, data acquisition and processing | 8 |
| 2.1. Data acquisition on the Falkland Plateau | 8 |
| 2.2. Wide-angle seismic data | 8 |
| 2.2.1. Data acquisition and processing | 9 |
| 2.2.2. Modelling with ray tracing approach | 11 |
| 2.2.3. Amplitude modelling | 13 |
| 2.3. Gravity data | 15 |
| 2.3.1. Density Modelling | 15 |
| 2.4. Magnetic data | 16 |
| 2.4.1. Ship borne magnetic data | 16 |
| 2.4.2. Helicopter borne magnetic data | 17 |
| 2.4.3. Magnetic anomaly modelling | 17 |
| 3. Contributions to scientific journals | 18 |
| 3.1. The crustal structure of the continental margin east of the Falkland Islands | 18 |
| 3.2. The Falkland Plateau in the context of Gondwana breakup | 19 |
| 3.3. The crustal structure of Maurice Ewing Bank from wide-angle seismic data | 20 |
| 4. The crustal structure of the continental margin east of the Falkland Islands | 21 |
| 4.1. Abstract | 21 |
| 4.2. Introduction | 21 |

| | | |
|-----------|--|-----------|
| 4.3. | Geologic setting | 24 |
| 4.3.1. | Seismic Structure of the Falkland Plateau | 26 |
| 4.4. | Data acquisition and data processing | 27 |
| 4.5. | Modelling | 32 |
| 4.5.1. | Seismic refraction data | 32 |
| 4.5.2. | Gravity modelling | 38 |
| 4.5.3. | Error analyses | 38 |
| 4.6. | Results | 41 |
| 4.6.1. | Velocity model | 41 |
| 4.6.2. | Density model | 44 |
| 4.7. | Interpretation | 45 |
| 4.7.1. | Sediments on the shelf and in the Falkland Plateau Basin | 45 |
| 4.7.2. | East Falkland continental margin (km 0 – 180) | 46 |
| 4.7.3. | Continent-ocean transition (km 180 – 270) | 47 |
| 4.7.4. | Falkland Plateau Basin (km 270 – 750) | 47 |
| 4.8. | Discussion | 48 |
| 4.8.1. | Structural classification of the Falkland Islands' eastern margin | 48 |
| 4.8.2. | Is the Falkland area a marginal plateau? | 49 |
| 4.8.3. | Comparison with other continental margins nearby | 49 |
| 4.8.4. | Oceanic crust | 52 |
| 4.9. | Conclusions | 53 |
| 5. | The Falkland Plateau in the context of Gondwana breakup | 54 |
| 5.1. | Abstract | 54 |
| 5.2. | Introduction | 54 |
| 5.3. | The Falkland Plateau's crust | 56 |
| 5.4. | Refined plate kinematic model: Geological/geophysical constraints | 58 |
| 5.4.1. | Early Opening of the Atlantic sector of the Southern Ocean | 60 |
| 5.4.2. | Phases of magmatism and seafloor spreading | 61 |
| 5.4.3. | Remaining Problems | 62 |
| 5.5. | Supplementary information - The Falkland Plateau in the context of Gondwana breakup | 63 |
| 6. | The crustal structure of Maurice Ewing Bank from wide-angle seismic data | 73 |
| 6.1. | Abstract | 73 |
| 6.2. | Introduction | 73 |
| 6.3. | Geologic Setting | 75 |
| 6.3.1. | The Falkland Plateau Basin | 75 |
| 6.3.2. | Maurice Ewing Bank | 75 |
| 6.3.3. | Georgia Basin | 77 |
| 6.4. | Data acquisition and data processing | 77 |
| 6.4.1. | Seismic refraction data | 81 |
| 6.4.2. | Potential field data | 82 |

| | |
|---|------------|
| 6.5. Modelling | 86 |
| 6.5.1. Ray tracing | 86 |
| 6.5.2. Amplitude modelling | 88 |
| 6.5.3. Gravity modelling | 90 |
| 6.6. Results | 91 |
| 6.6.1. Velocity model | 91 |
| 6.6.2. Density model | 100 |
| 6.6.3. Magnetic anomaly data | 102 |
| 6.7. Discussion | 105 |
| 6.7.1. Sediments in the Falkland Plateau Basin | 105 |
| 6.7.2. Crustal fabric of the Falkland Islands and the western MEB . . . | 107 |
| 6.7.3. Eastern MEB continental margin towards the Georgia Basin . . . | 108 |
| 6.7.4. Igneous activity of the Falkland Plateau Basin and processes . . . | 108 |
| 6.7.5. Conclusions | 111 |
| 7. Conclusions | 113 |
| 8. Outlook | 116 |
| References | 118 |
| A. Appendix | 130 |

List of Figures

| | | |
|-------|---|----|
| 1.1. | Topographic and bathymetric map of the Falkland Plateau | 1 |
| 1.2. | Geological map of the Falkland Islands | 2 |
| 1.3. | Map of the Falkland Plateau with seismic and magnetic profiles | 4 |
| 1.4. | The position of the Falkland Plateau in a reconstruction of Gondwana | 5 |
| 2.1. | Schematic plot of the acquisition of wide-angle seismic data. | 8 |
| 2.2. | Example of single G-Gun. | 9 |
| 2.3. | Map with AWI-20130010 and helicopter borne magnetic profiles. | 9 |
| 2.4. | Station 20130015 on East Falkland. | 10 |
| 2.5. | Set-up of an OBS. | 10 |
| 2.6. | Principle design of an OBH. | 11 |
| 2.7. | Data example of OBS 28. | 12 |
| 2.8. | Comparison of ray tracing and FD-modelling. | 14 |
| 2.9. | Fluxgate magnetometer system installed on Polarstern. | 16 |
| 2.10. | Acquisition of helicopter borne magnetic data during ANT-XXIX/5. | 17 |
| 4.1. | Topographic and gravity anomaly map of the Falkland Plateau. | 22 |
| 4.2. | Reconstruction of the breakup of Gondwana. | 24 |
| 4.3. | Geological map of the Falkland Islands with onshore and offshore dykes. | 25 |
| 4.4. | Seismic reflection line 139. | 26 |
| 4.5. | Data example for land station 15. | 28 |
| 4.6. | Data example for OBS 21. | 29 |
| 4.7. | Data example for OBS 40. | 30 |
| 4.8. | Data example for OBS 48. | 31 |
| 4.9. | Data example for the sediment phases (OBS 48). | 33 |
| 4.10. | Results of the FD-modelling for OBS 40. | 35 |
| 4.11. | Results of the FD-modelling for OBS 48. | 36 |
| 4.12. | Seismogram of OBS 48 with picks. | 37 |
| 4.13. | Ray coverages for the reflected and refracted phases of the western transect. | 40 |
| 4.14. | P-wave velocity model of the western transect. | 41 |
| 4.15. | Seismic reflection line 139 combined with the P-wave velocity model. | 42 |
| 4.16. | Free-air gravity anomaly and density model of the western transect. | 44 |
| 4.17. | Velocity-depth functions. | 46 |
| 4.18. | Geological interpretation of the western transect. | 48 |
| 4.19. | P-wave velocity model of the FRSC. | 51 |
| 5.1. | Bathymetric and free-air gravity anomaly map of the Falkland Plateau. | 55 |

| | |
|--|-----|
| 5.2. Magnetic anomaly data, P-wave velocity model and geological interpretation of profile AWI-20130010. | 57 |
| 5.3. Reconstruction of Gondwana. | 59 |
| 5.4. Data example for OBS 37. | 64 |
| 5.5. Data example for OBS 66. | 65 |
| 5.6. All stations with picked arrivals and modelled arrivals. | 66 |
| 5.7. Ray coverage of the entire model. | 70 |
| | |
| 6.1. Bathymetric and free-air gravity anomaly map of the Falkland Plateau and the Georgia Basin. | 74 |
| 6.2. Seismic reflection line 139. | 76 |
| 6.3. Data example for OBS 66. | 78 |
| 6.4. Data example for OBS 71. | 79 |
| 6.5. Data example for OBS 80. | 80 |
| 6.6. Data example for OBS 92. | 81 |
| 6.7. Picked and modelled arrivals of the eastern transect. | 83 |
| 6.8. Ray coverage of the eastern transect. | 86 |
| 6.9. Results of the FD-modelling for OBS 66. | 89 |
| 6.10. P-wave velocity model of AWI-20130010. | 91 |
| 6.11. Magnetic anomaly data and velocity model of the Falkland Plateau Basin. | 93 |
| 6.12. Seismic reflection line 139 combined with the P-wave velocity model. | 94 |
| 6.13. Magnetic anomaly data and velocity model of Maurice Ewing Bank. | 95 |
| 6.14. Sediments in the Georgia Basin. | 96 |
| 6.15. Velocity-depth functions from the COTs, Maurice Ewing Bank and the Georgia Basin. | 97 |
| 6.16. Magnetic anomaly data and velocity model of the Georgia Basin. | 99 |
| 6.17. Free-air gravity anomaly, magnetic anomaly and density model of AWI-20130010. | 101 |
| 6.18. Effect of the additional density body. | 102 |
| 6.19. Free-air gravity anomaly map with the magnetic anomaly data. | 102 |
| 6.20. Magnetic anomaly data and spreading model for the Georgia Basin. | 103 |
| 6.21. Geological interpretation of profile AWI-20130010. | 104 |
| 6.22. Theoretical igneous crustal thickness versus velocity of igneous crust. | 110 |
| | |
| A1. Seismic section of land station 12. | 131 |
| A2. Seismic section of land station 14. | 132 |
| A3. Seismic section of land station 15. | 133 |
| A4. Seismic section of land station 16. | 134 |
| A5. Seismic section of land station 17. | 135 |
| A6. Seismic section of station 18. | 136 |
| A7. Seismic section of station 19. | 137 |
| A8. Seismic section of station 21. | 138 |
| A9. Seismic section of station 22. | 139 |
| A10. Seismic section of station 23. | 140 |

| | |
|---|-----|
| A11. Seismic section of station 24. | 141 |
| A12. Seismic section of station 25. | 142 |
| A13. Seismic section of station 26. | 143 |
| A14. Seismic section of station 28. | 144 |
| A15. Seismic section of station 29. | 145 |
| A16. Seismic section of station 32. | 146 |
| A17. Seismic section of station 33. | 147 |
| A18. Seismic section of station 35. | 148 |
| A19. Seismic section of station 36. | 149 |
| A20. Seismic section of station 37. | 150 |
| A21. Seismic section of station 39. | 151 |
| A22. Seismic section of station 40. | 152 |
| A23. Seismic section of station 41. | 153 |
| A24. Seismic section of station 42. | 154 |
| A25. Seismic section of station 43. | 155 |
| A26. Seismic section of station 44. | 156 |
| A27. Seismic section of station 46. | 157 |
| A28. Seismic section of station 47. | 158 |
| A29. Seismic section of station 48. | 159 |
| A30. Seismic section of station 49. | 160 |
| A31. Seismic section of station 50. | 161 |
| A32. Seismic section of station 52. | 162 |
| A33. Seismic section of station 53. | 163 |
| A34. Seismic section of station 54. | 164 |
| A35. Seismic section of station 55. | 165 |
| A36. Seismic section of station 56. | 166 |
| A37. Seismic section of station 57. | 167 |
| A38. Seismic section of station 58. | 168 |
| A39. Seismic section of station 59. | 169 |
| A40. Seismic section of station 60. | 170 |
| A41. Seismic section of station 61. | 171 |
| A42. Seismic section of station 62. | 172 |
| A43. Seismic section of station 64. | 173 |
| A44. Seismic section of station 65. | 174 |
| A45. Seismic section of station 66. | 175 |
| A46. Seismic section of station 68. | 176 |
| A47. Seismic section of station 69. | 177 |
| A48. Seismic section of station 70. | 178 |
| A49. Seismic section of station 71. | 179 |
| A50. Seismic section of station 72. | 180 |
| A51. Seismic section of station 73. | 181 |
| A52. Seismic section of station 74. | 182 |
| A53. Seismic section of station 75. | 183 |
| A54. Seismic section of station 76. | 184 |

| | |
|---|-----|
| A55. Seismic section of station 77. | 185 |
| A56. Seismic section of station 78. | 186 |
| A57. Seismic section of station 79. | 187 |
| A58. Seismic section of station 80. | 188 |
| A59. Seismic section of station 81. | 189 |
| A60. Seismic section of station 82. | 190 |
| A61. Seismic section of station 83. | 191 |
| A62. Seismic section of station 84. | 192 |
| A63. Seismic section of station 86. | 193 |
| A64. Seismic section of station 87. | 194 |
| A65. Seismic section of station 88. | 195 |
| A66. Seismic section of station 89. | 196 |
| A67. Seismic section of station 90. | 197 |
| A68. Seismic section of station 91. | 198 |
| A69. Seismic section of station 92. | 199 |
| A70. Seismic section of station 93. | 200 |
| A71. Seismic section of station 94. | 201 |
| A72. Seismic section of station 95. | 202 |

List of Tables

| | |
|---|-----|
| 2.1. Position, configuration and data quality of the land stations. | 10 |
| 4.1. Statistics of the picked phases of the western transect. | 39 |
| 4.2. Layer type, velocity and density of the western transect. | 43 |
| 5.1. Summarized statistics of the picked phases for the entire model. | 69 |
| 5.2. Finite rotations for the breakup of Gondwana. | 71 |
| 6.1. Statistics of the picked phases of the eastern transect. | 87 |
| 6.2. Layer type, velocity and density for the entire model. | 92 |
| 6.3. Unconformities with geological units, ages and velocities. | 106 |

Abbreviations

| | |
|--------------|--|
| AFFZ | Agulhas Falkland Fracture Zone |
| AGC | Automatic Gain Control |
| AP | Antarctic Peninsula |
| Ar | Argon |
| AWI | Alfred Wegener Institute for Polar and Marine Research |
| COL | Colorado sub-plate |
| COT | Continent-ocean transition zone |
| DSDP | Deep Sea Drilling Project |
| E-ANT | East Antarctica |
| FB | Falkland Plateau Basin |
| FD | Finite differences |
| FI | Falkland/Malvinas block |
| FR | Filchner-Ronne-Shelf |
| GEBCO | General Bathymetric Chart of the Oceans |
| IGRF | International Geomagnetic Reference Field |
| IODP | International Ocean Discovery Program |
| K | Potassium |
| LIP | Large igneous province |
| Ma | Million years (before present) |
| MA | Madagascar |
| MB | Malvinas Basin |
| MEB | Maurice Ewing Bank |
| Moho | Mohorovičić discontinuity |
| MozB | Mozambique Basin |
| MozR | Mozambique Ridge |
| Myrs | Millions of years |
| NAR | Northern Astrid Ridge |
| NF | North Falkland Basin |
| OBH | Ocean bottom hydrophone |
| OBS | Ocean bottom seismometer |
| OuB | Outeniqua Basin |
| PAR | Parana sub-plate |
| PAT | Patagonia subplate |
| RMS | Root mean square |
| SAM | northern South American sub-plate |
| SAL | Salado sub-plate |
| SAR | Southern Astrid Ridge |

| | |
|--------------|------------------------------------|
| SDR | Seaward dipping reflector sequence |
| TWT | Two-way travel time |
| W-ANT | West Antarctica |
| WRift | Weddell Rift |

1. Introduction

1.1. Geological and geophysical investigations

The Falkland Islands are located in the South Atlantic Ocean 500 km off the Argentine coast (Figure 1.1). They are composed of two main islands, East and West Falkland. The Falkland Islands are surrounded by four basins: the Falkland Plateau Basin to the east, the South Falkland Basin to the south, the Malvinas Basin to the west and the North Falkland Basin to the north. The Falkland Plateau stretches eastwards from the Falkland Islands for more than 1500 km into the Georgia Basin. At its eastern termination, the Maurice Ewing Bank (MEB), a bathymetric high, is located.

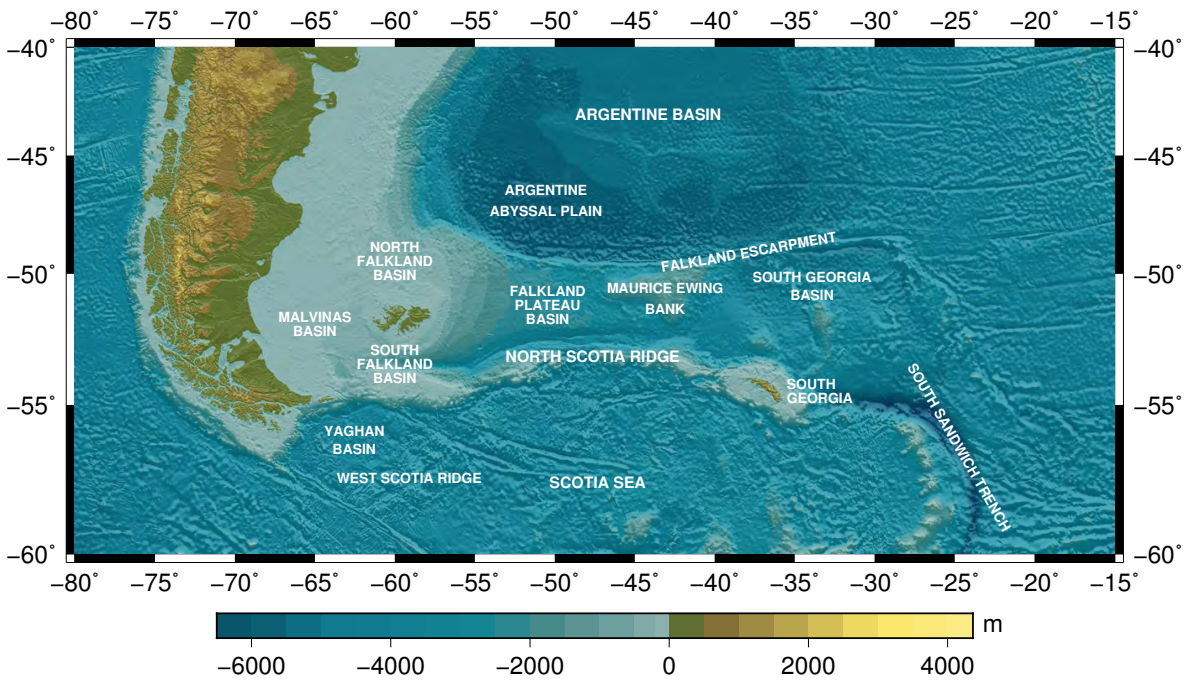


Figure 1.1.: Topographic and bathymetric map of the Falkland Islands and the Falkland Plateau (GEBCO, 2014).

Onshore investigations on the Falkland Islands

The investigation of the Falkland Islands' geology had its beginning with two visits of Charles Darwin in 1833 and 1834. He described a folded and cleaved succession of quartzites and sandstones and discovered already the presence of dolerite dykes (Darwin, 1846). Nevertheless Darwin was hardly impressed by the islands and noted '... excepting some little geology nothing could be less interesting' (Stone, 2008).

In 1911, Halle already recorded the granite-gneiss complex (Cape Meredith Complex, which represents the basement) and identified a glacigenic unit (Fitzroy Tillite Formation), which he correlated correctly with Upper Carboniferous to Lower Permian Dwyka tillites of South Africa. This finding was used by Alfred Wegener in his book *‘Die Entstehung der Kontinente und Ozeane’* as evidence for his theory of continental drift. In 1952, the South African geologist Adie proposed a position of the Falkland Islands southeast of South Africa. For structural continuity of the South African geological units with the Falkland Islands’ ones he suggested a 180° rotation of the Falkland Islands’ block. Later additional paleomagnetic (Mitchell et al., 1986, Stone et al., 2009, Taylor and Shaw, 1982), stratigraphic (Marshall, 1994) and structural (Curtis and Hyam, 1998) data seemed to confirm this assumption and drives an ongoing controversy (Stone, 2016). Nevertheless no evidence for rotation can be observed in the marine seismic data. Instead these data suggest that the North Falkland Basin, the Malvinas Basin and the Falkland Plateau Basin were exposed to initial east-west extension only (Richards et al., 1996).

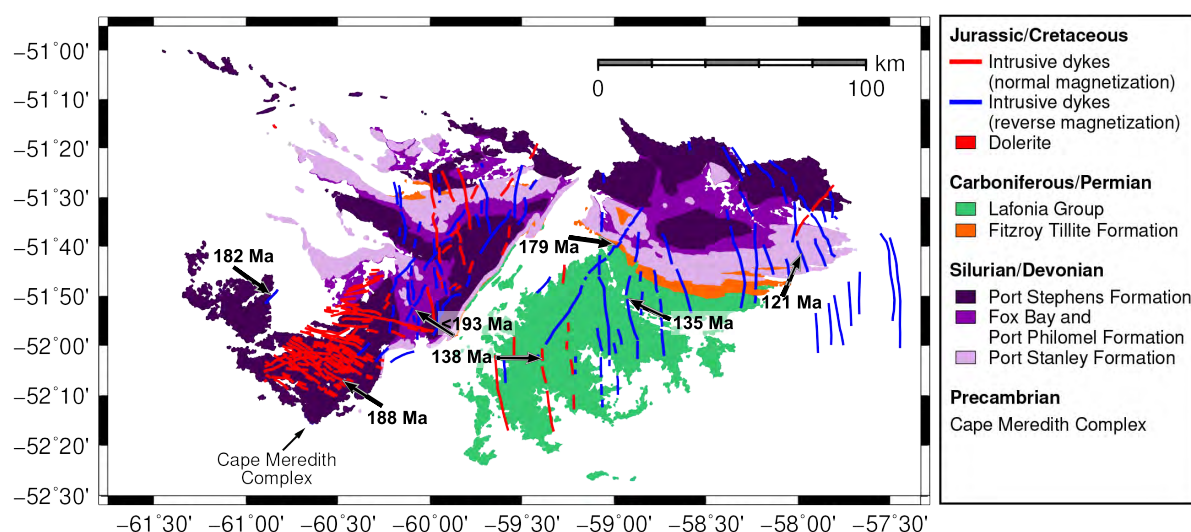


Figure 1.2.: Geological map of the Falkland Islands with onshore dykes (Stone et al., 2008) and age samples (Hole et al., 2015; Mussett and Taylor, 1994; Richards et al., 2013; Stone et al., 2008) and offshore dykes (Barker, 1999). Geological units are provided by the Falkland Islands’ Government.

Mapping of the Falkland Islands geologic units was first conducted by Baker (1922). Later Greenway (1972) used a photogeological interpretation to refine the geologic map. The first field-based geological survey was conducted in the 1990s and resulted in a comprehensive report and map (Figure 1.2) of the onshore geological units (Aldiss and Edwards, 1999). A description of the units is provided in section 4.3.

In 2004, an aeromagnetic survey was flown and resulted in the identification of three different dyke swarms, that intruded into the basement and sediments (Stone et al., 2008). I use these dykes as an age constraint for my breakup model (chapter 5), so I will briefly describe the dykes here.

The oldest dykes ($^{40}\text{Ar}/^{39}\text{Ar}$ age of 188 ± 2 Ma, Mussett and Taylor, 1994) intruded in

the south of West Falkland. The swarm trends east-west and is normally magnetized. A second swarm of Jurassic age trends northeast-southwest and has, in general, reverse magnetization but contain also normally magnetized segments. $^{40}\text{Ar}/^{39}\text{Ar}$ age dating revealed an age of 178.6 ± 4.9 Ma (Stone et al., 2008) and 182.3 ± 1.5 Ma (Hole et al., 2015) and K-Ar dating ages of 176 ± 7 Ma and 162 ± 6 Ma (Thistlewood et al., 1997). Both of the Jurassic dyke swarms are considered to be linked to Karoo-Ferrar magmatism, which is associated with the initial breakup of Gondwana. Furthermore Mitchell et al. (1986) described the geochemistry of the Jurassic dykes on the Falkland Islands as marking a transition between the African (Karoo) and Antarctic (Ferrar) provinces of breakup-related magmatism: While the composition of the east-west dykes is comparable to Karoo-type dolerites, the northeast-southwest trending swarm shows more affinities to Ferrar-type dolerites. A third dyke swarm, of Cretaceous age, trends north-south. $^{40}\text{Ar}/^{39}\text{Ar}$ dating of one East Falkland dyke of this group revealed an age of 121.3 ± 1.2 Ma (Stone et al., 2008). The dyke is reverse magnetized despite the age of 121 Ma lying within the normal polarity Cretaceous Quiet Zone. Richards et al. (2013) report further $^{40}\text{Ar}/^{39}\text{Ar}$ age dates of 133 ± 4 Ma, 137 ± 4 Ma (reverse polarization) and 138 ± 4 Ma (normal polarization). Consequently the intrusion must have lasted long enough to span a magnetic reversal.

Offshore investigations on the Falkland Plateau

Offshore, the first seismic refraction data were gathered on the Falkland Plateau in the late 1950s and the plateau was interpreted to be a southward-tilted continental block covered by thick sediments (Ewing et al., 1971). In the 1970s, multichannel seismic reflection profiles and sonobuoy wide-angle measurements (lines 139 to 145, Figure 1.3) were gathered (Ludwig, 1983; Ludwig et al., 1978; Ludwig and Rabinowitz, 1980) and provide insights into the sediment structure and the depth of the basement. The data show that east of the Falkland Islands the basement dips steeply and forms the Falkland Plateau Basin. The basin is filled with up to 8 km thick sediments. The MEB is a basement high, on which the sediment thickness decreases to a minimum of 250 m. Based on a few high-speed refracted arrivals in the sonobuoy data, the crustal thickness beneath the Falkland Plateau Basin was estimated to be 6 km and interpreted to be either stretched continental crust (Ludwig and Rabinowitz, 1980) or oceanic crust (Lorenzo and Mutter, 1988).

In 1974, the MEB was the target area of the Deep Sea Drilling Project (DSDP). During leg 36, three boreholes were drilled on the basement high (327, 329, 330, Figure 1.3) and one in the Georgia Basin (328, Figure 1.3). At site 330 gneisses were drilled in 547 m depth, which is interpreted as strong evidence for the continental origin of the MEB (Barker and Dalziel, 1977). The gneisses are similar in lithology and composition to the Cape Meredith Complex onshore the Falkland Islands, but are significantly younger (535 ± 66 Ma compared to 1000 – 1100 Ma). Reasons for the age difference could be a hydrothermal event or metamorphic re-crystallization (Beckinsale et al., 1977).

In 1980, during DSDP leg 71, two wells (511, 512) were drilled on the MEB and penetrated sediments from Late Jurassic to Quaternary age (Ludwig and Krasheninnikov, 1983).

Based on marine potential field data, Barker (1999) interpreted strongly lineated magnetic anomalies and a coincident linear gravity high to show the presence of a volcanic rifted margin southeast of the Falkland Islands. Another potential field study was conducted by Kimbell and Richards (2008). These authors used satellite free-air gravity anomalies to derive a three-dimensional isostatically-compensated density model for the lithosphere. Their model implies that the crustal thickness beneath the Falkland Plateau Basin is twice as thick (14 km) as that estimated from seismic data.

Since the 1980s, the Falkland Plateau and the North Falkland Basin were in the focus of the oil and gas industry. The data mainly remained proprietary and were not published. Nevertheless, Richards et al. (2013) report important results from commercial drilling and seismic reflection surveys. In well 61/5-1 southeast of the Falkland Islands (Figure 1.3) dolerites were encountered in 2416 m depth. The dolerites were not age dated, but their composition resembles that of the east-west stretching dyke swarm onshore the Falkland Islands. The dolerites most likely are intruded into the basement and do not represent it as the seismic character changes in the vicinity of the well. The sediments deposited overlying the dolerites are dated to be Tithonian (152 – 141 Ma).

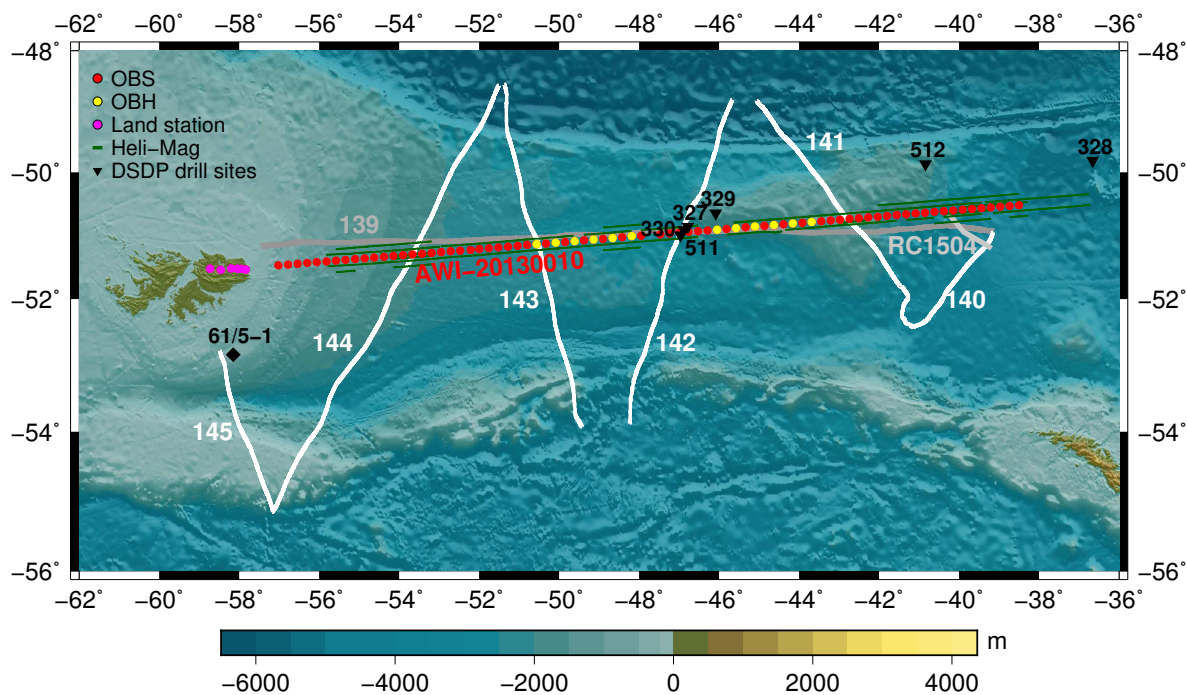


Figure 1.3.: Topographic and bathymetric map of the Falkland Islands and the Falkland Plateau (GEBCO, 2014) with seismic reflection profiles (white and grey lines), DSDP drill sites, seismic refraction profile AWI-20130010 and the magnetic profiles acquired with *Polarstern*'s helicopter. The location of well 61/5-1 is estimated from Richards et al. (2013) (their Figure 5).

The existing seismic and potential field data could not resolve the nature of the crust beneath the Falkland Plateau Basin. To close this gap, the 1450 km long wide-angle

seismic transect (AWI-20130010) was acquired during the expedition ANT-XXIX/5 with *RV Polarstern* in 2013 (Jokat, 2013). Additional magnetic profiles were flown with the ship's helicopter to retrieve further constraints about the magnetic signature of the plateau.

1.2. Motivation

Plate tectonics provide the explanation for almost all major surface features on Earth and is the unifying concept for most geologic processes. The configuration of land masses has global consequences on the climate, biosphere and on the local morphology and georisks. The understanding of the plate tectonic movements in the past and the processes that led to continental breakup are crucial to predict future plate motion. Therefore, the reconstruction of ancient continents is of great scientific importance.

The investigation of plate tectonics began with the theories of Alfred Wegener, who proposed that all land masses were united in one continent before it broke into several apart drifting fragments (Wegener, 1922). From the current point of view, Wegener's 'Ur-Kontinent' is Pangaea, which was the last supercontinent that included all land masses. Pangaea broke up into Laurasia, the continental masses of the northern hemisphere, and Gondwana in the southern hemisphere.

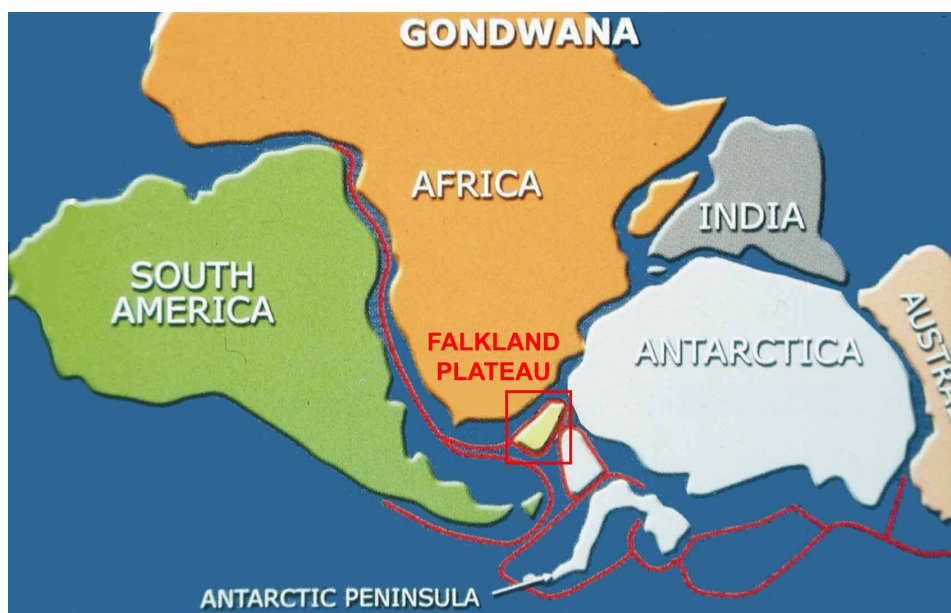


Figure 1.4.: The position of the Falkland Plateau in a reconstruction of Gondwana (modified after Falkland Islands Government, www.fig.gov.fk/minerals/index.php/geology/onshore-geology).

Numerous differing plate kinematic reconstructions exist for the breakup of Gondwana. The accuracy of reconstructions strongly depends on the knowledge of the present day

composition of the crust and margins, and on the validity of available age constraints, e.g. dated seafloor anomalies, for plate motions.

In the centre of Gondwana, between the South American, African and Antarctic plates, the Falkland Plateau was located during the Jurassic (Figure 1.4). Its unknown crustal composition stimulated a wide range of contrasting reconstructions, in which the plateau was either regarded as a rigid part of the South American continent (Eagles and Vaughan, 2009), stretched continental crust was supposed (Jokat et al., 2003a; König and Jokat, 2006; Macdonald et al., 2003; Torsvik et al., 2010) or the Falkland Islands and MEB were regarded as one unit implying oceanic crust between the blocks (Storey and Kyle, 1997). Other studies included, in addition to MEB and the Falkland Islands block, the independent motions of various small plates and continental blocks in the Weddell Sea region south of the Falkland Plateau (Dalziel et al., 2013; Martin, 2007).

1.3. Research questions of this thesis

This thesis aims to provide a sound model of the crustal fabric of the Falkland Plateau and to provide an improved Gondwana reconstruction, which diminishes the uncertainties in the Falkland Plateau's region and that incorporates the currently available data. Thus, the main research questions of this dissertation focus on the crustal fabric of the Falkland Plateau and on the reconstruction of Gondwana.

The crustal structure of the Falkland Plateau

Existing geophysical data cannot resolve the crustal structure of the Falkland Plateau. The central research questions considering the Falkland Plateau and the Georgia Basin are:

- What is the crustal thickness and composition of the entire Falkland Plateau?
- How far does the Falkland Islands' continental basement extend?
- If there is oceanic crust beneath the Falkland Plateau Basin, what is the structure of the continental margin and the COT?
- Is there evidence for a high lower crustal velocity body underneath the plateau?
- Is the MEB a volcanic structure or extended continental crust?
- How does the transition from the MEB to the oceanic Georgia Basin look like?
- What kind of β factor (stretching) can be calculated to constrain the maximum pre-rift extension of the plateau?
- Which age model is supported by the new magnetic investigations for the Georgia Basin?

Implications for the breakup of Gondwana

Knowledge of the Falkland Plateau's crustal fabric and magnetic signature will provide new constraints for the breakup of Gondwana:

- What was the initial fit of Gondwana in the Falkland Plateau's area?
- Which age constraints can be deduced for the breakup of Gondwana?
- Are there indications for the processes that led to continental desintegration?

New geophysical data were acquired during expedition ANT-XXIX/5 in order to answer these research questions. The experiment and the methods are introduced in chapter 2. The results are provided in chapters 4, 5 and 6, formatted for publishing in scientific journals. The conclusions and an outlook are presented in chapters 7 and 8.

2. Methods, data acquisition and processing

2.1. Data acquisition on the Falkland Plateau

The expedition ANT-XXIX/5 with *RV Polarstern* was conducted by the Alfred Wegener Institute for Polar and Marine Research (AWI) from April 18th until May 29th 2013. The cruise started in Stanley/Falkland Islands and ended in Saldanha/South Africa. On the Falkland Plateau, seismic refraction measurements were acquired along a 1450 km long west-east oriented profile (AWI-20130010). Parallel to the wide-angle seismic experiment, magnetic, bathymetric and sediment echosounder data were acquired. Additional magnetic profiles were flown with the ship's helicopter. Because of time and weather constraints it was not possible to acquire seismic reflection data (Jokat, 2013).

2.2. Wide-angle seismic data

Seismic refraction measurements yield information about the subsurface velocity structure. A source emits seismic waves that propagate through the Earth's interior.

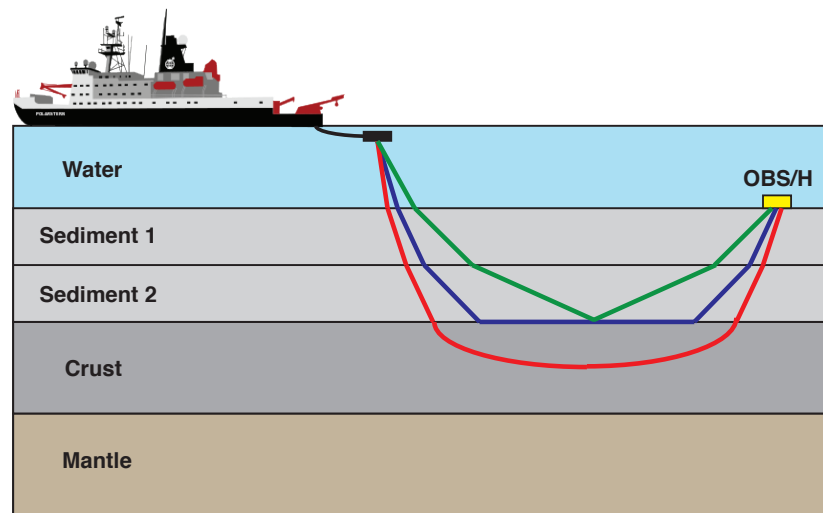


Figure 2.1.: Schematic plot of the acquisition of wide-angle seismic data. The travel path of a refracted/diving (red), reflected (green) and a head wave (blue) are depicted.

Depending on the impedance contrast and the angle of incidence, the waves are reflected, refracted, diffracted and/or converted. A wave is reflected at its angle of incidence at a boundary between two layers with a different seismic velocity/density (ray path plotted in green, Figure 2.1). A refracted wave develops when a wave strikes a medium boundary at a critical angle of incidence. These waves (head waves) travel along the interface of the two velocity layers and permanently emit energy, resulting in a wave front that propagates back to the surface at the angle of incidence (blue, Figure 2.1). When a constant, vertical velocity gradient exists throughout a layer, diving waves are generated, which turn in the layer (red, Figure 2.1). The travel times of waves are recorded at the surface and can be used to calculate the velocity structure of the underground.

2.2.1. Data acquisition and processing



Figure 2.2.: Example of single G-Gun.

As seismic source for the acquisition of profile AWI-20130010, 8 G-Guns (Figure 2.2) with a total volume of 681 (4160 in³) were towed behind the ship at a depth of 10 m. Seismic energy was generated every 60 s at a ship's speed of 5 kn, which yielded in a shot distance of 150 m. In total, air gun operation was conducted along 1300 km (Figure 2.3). 5028 shots were generated on the eastern transect and 3864 on the western part. Seismic shooting was not permitted in a water depth shallower than 350 m. Thus, air gun operation had to be

stopped 74 km east of East Falkland (close to OBS 19).

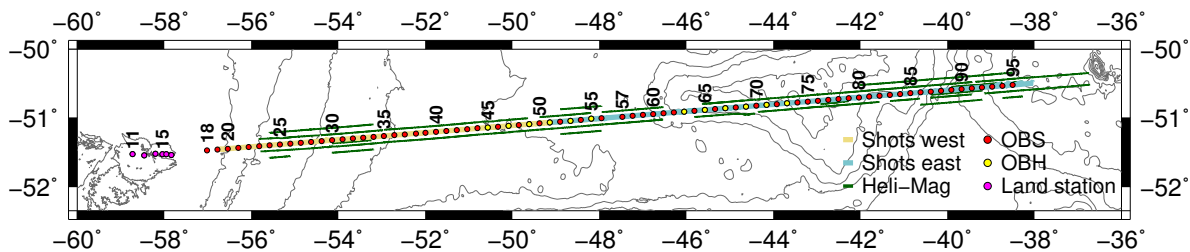


Figure 2.3.: Map with AWI-20130010 and helicopter borne magnetic profiles.

To record the seismic waves, 6 RefTek land stations (Figure 2.4) were installed on East Falkland at an average spacing of 12 km. The stations 2013011, 20130012 and 20130014 were deployed by car, while stations 2013015, 20130016 and 20130017 were deployed by helicopter. Recovery of all land stations was performed by helicopter. The stations were equipped with a varying number of 4.5 Hz geophone chains (Table 2.1) and recorded continuously with a sample rate of 100 Hz. The gain was set to 32. The closest distance of any of the land stations to the westernmost shot was 75 km.

The land station data were converted to SEGY-format using PASSCAL routines (www.passcal.nmt.edu) and own codes written in MATLAB. The seismic sections were bandpass filtered with corner frequencies of 4 and 15 Hz and an automatic gain control (AGC) with a time window of 1 s was applied. The data quality varies strongly (Table 2.1). The record sections of land stations number 20130012 to 20130017 are provided in the appendix (Figures A1 to A5).

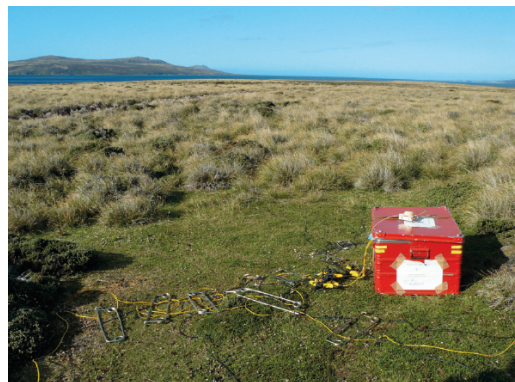


Figure 2.4.: Station 20130015 on East Falkland (Jokat, 2013).

Table 2.1.: Position, configuration and data quality of the land stations. The offset refers to the offset at which phases could be identified and picked reliably.

| Station | Longitude | Latitude | Channels x Chains | Location | Offset [km] |
|----------|-------------|-------------|-------------------|------------|-------------|
| 20130011 | 58°43.744 W | 51°31.728 S | 3 x 3 | grass | - |
| 20130012 | 58°27.706 W | 51°32.770 S | 2 x 3 | hill slope | 120-250 |
| 20130014 | 58°12.202 W | 51°31.426 S | 2 x 2 | grass | 100-230 |
| 20130015 | 58°02.573 W | 51°31.769 S | 3 x 3 | grass | 90-220 |
| 20130016 | 57°57.241 W | 51°31.776 S | 3 x 4 | hill slope | 115-130 |
| 20130017 | 57°50.280 W | 51°32.507 S | 2 x 4 plus 1 x 3 | hill slope | 100-145 |

Offshore, 39 ocean bottom stations, all provided by GEOMAR, were used with an average spacing between the receivers of 16 km. The stations were deployed twice along an eastern and a western profile, resulting in 78 recording locations (Figure 2.3). The western (offshore) profile starts at station 18 and terminates at 56, the eastern one starts 33 km east at station 57 and terminates at station 95.

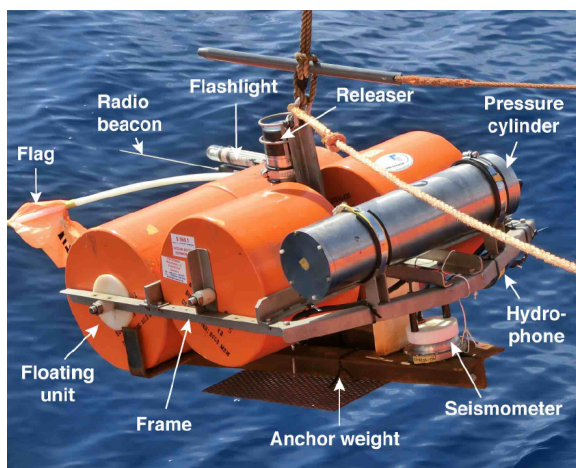


Figure 2.5.: Set-up of an OBS (Mueller, 2017).

33 ocean bottom seismometers (OBS) of different types were used: 4 LOBSTER (longterm Ocean Bottom Seismometers for Tsunami and Earthquake Research), 9 cube-designed OBS and 20 2002-designed OBS. An OBS consists of a frame with 2 or 4 flotation units, a 4.5 Hz 3-component seismometer, a hydrophone, an anchor weight that is fixed via an acoustic release unit, a flash light, a radio beacon, a swimming line with a small flotation ball and a titanium pressure cylinder, which contains the data logger and the power supply (Figure 2.5).

6 ocean bottom hydrophones (OBH) were

deployed during ANT-XXIX/5. An OBH consists of a steel tube with a buoyancy body on the top. A flash light, radio beacon and flag are fixed directly to the floatation body (Figure 2.6). Below the buoyant body, the titanium pressure cylinder, the acoustic release unit, at which the anchor is fixed, and the hydrophone are attached. For all systems, the sampling rate was set to 200 Hz.

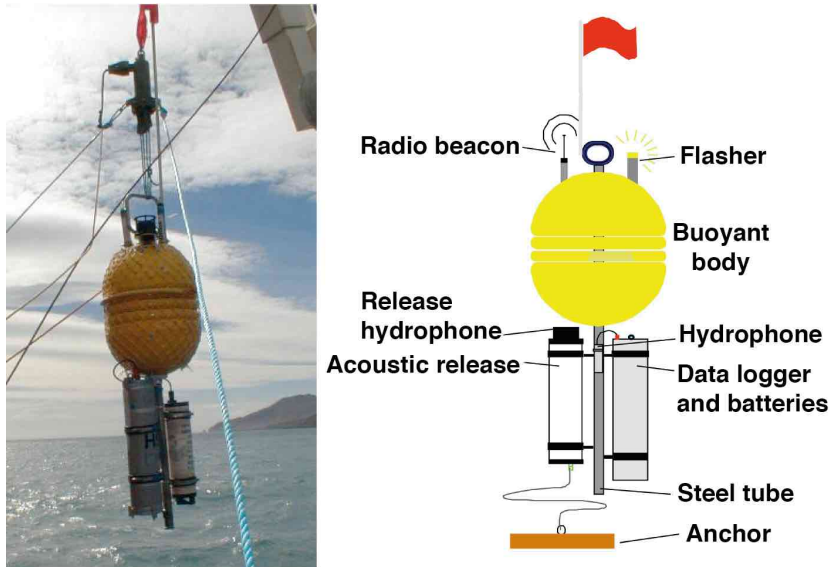


Figure 2.6.: Principle design of an OBH (modified after Flueh and Bialas, 1996).

All OBS/OBH could be recovered. However, no data could be obtained from eight stations on the western transect and from three on the eastern transect. After recovery, the internal clock of the instruments was synchronized with the GPS signal and the data were downloaded afterwards for processing. SEG-Y-files were created and contained the recorded seismic data, which was cut into traces starting with zero at the time of signal release. The offsets to the shot positions were written into the trace header of the SEG-Y-files. The positions of the OBS/OBH were relocated in line using direct arrivals for estimating the amount of drift during the stations subsidence. An AGC with a time window of 1 s and a deconvolution filter were applied and the data were bandpass filtered with corner frequencies of 4 and 20 Hz. For most stations, the hydrophone channel has the best data quality. All seismic sections are displayed in the appendix in Figures A6 to A72 with a reduction velocity of 8 km/s.

2.2.2. Modelling with ray tracing approach

The identification and picking of phases was performed with the ZP software by B.C. Zelt (<http://www.soest.hawaii.edu/users/bzelt/zp/zp.html>). On the basis of travel times, curvature and appearance, the arrivals were allocated to certain reflected and refracted phases, which correspond to different velocity layers. Reflected phases have a hyperbolic shape in the seismic section. If not influenced by topography, refracted

phases appear to be straight lines or slightly bend in the presence of a vertical velocity gradient within a layer (Figure 2.7).

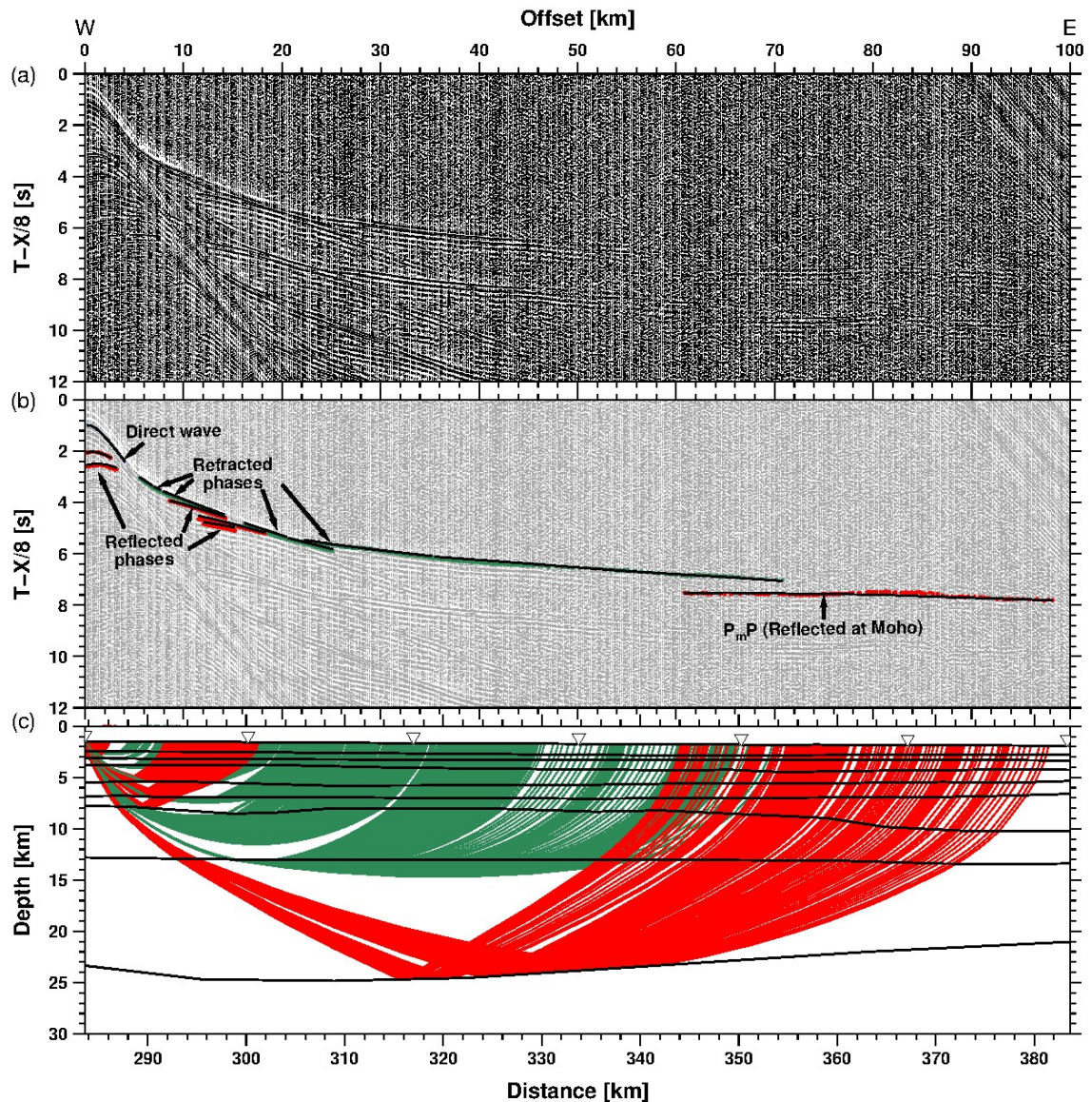


Figure 2.7.: Data example for OBS 28. (a) Seismic section filtered with a 4-15 Hz bandpass filter and displayed with a reduction velocity of 8 km/s. (b) Picked phases with error bars. The modelled arrivals are plotted as black lines. (c) Ray path for picks shown in (b).

The velocity of layers can be directly derived from refracted phases. The reflected phases are mainly used to determine the depth of layer boundaries. In addition their move out hyperbolae can be analyzed to calculate the average velocity (root mean square velocity) of all layers above the reflector. This is less accurate than the velocity determination

from refracted phases and were used when refracted phases are absent (e.g. in the upper sediment layers). Furthermore I controlled if the average velocity of the model above a reflector fits to its root mean square velocity in the seismic section. Because seismic S-waves are sparse or absent in the data, only P-waves are picked and used to calculate the (P-wave) velocity model.

Forward modelling was performed with *RAYINV*R (Zelt and Smith, 1992) together with the *P*Ray graphical user interface (Fromm, 2016), where modelling bases on ray tracing. The high-frequency approximation of the wave equation allows to consider the propagation of seismic waves as rays. More detailed information on the modelling approach is provided in section 4.5.1. The method usually provides sound results, but has limitations in regions with strong layer topography. At an edge in the velocity model, where the topographic change is not significantly greater than the wavelength of the propagating wave, the ray tracing method fails to calculate rays and the corresponding travel time curve ends abruptly (Figure 2.8). Furthermore, diffractions are not reproduced by *RAYINV*R. The amplitude information of the seismic waves is mainly neglected in ray tracing, although it provides additional constraints especially for layers with limited ray coverage.

2.2.3. Amplitude modelling

To overcome these limitations and further constrain the velocity model, especially in parts with limited ray coverage, an additional amplitude modelling is performed using the *SOFI2D* (Seismic mOdelling with FInite Differences, Bohlen, 2002) software. The code computes the 2-dimensional propagation of P- and SV-waves through a viscoelastic medium and generates corresponding synthetic seismograms. For calculation, the model is discretized and differential operators approximate the partial spatial derivatives of the wave equation (Bohlen et al., 2015). The advantage in comparison to ray tracing is that also converted and diffracted waves are calculated and that the FD-method provides enhanced results for regions with topography. Propagating waves can be calculated at edges, where the ray tracing method fails. Figure 2.8 illustrates this, showing a simple model with an edge (Figure 2.8a, modified after Schmidt-Aursch, 2003) and the rays that are reflected at the Moho (P_mP) of OBS 29 (Figure 2.8b). For both models the travel time curve calculated with ray tracing ends abruptly (blue in Figure 2.8c and 2.8d), although the P_mP can be observed also for offsets between km 120 and 150 in the seismogram of OBS 29 (picks in red, Figure 2.8d). In contrast to the ray tracing method, the wavefield calculated with the FD-method illuminates the edge. The resulting travel time curves for the model with an edge are shown in Figure 2.8g. Here, also later arrivals are visible, which are caused by diffractions at km 10 and 20, where the topography of the layer changes. In the synthetic seismogram of OBS 29 (Figure 2.8h), calculated with the FD-method, the P_mP and also the P_n (refracted phase of the mantle) are visible. The P_n has smaller amplitudes than the P_mP and, because of noise, cannot be observed in the real seismogram. This, together with the computation of later arrivals and converted phases, facilitates phase identification. An example for an improved phase identification with the synthetic seismogram is provided in section 6.5.2.

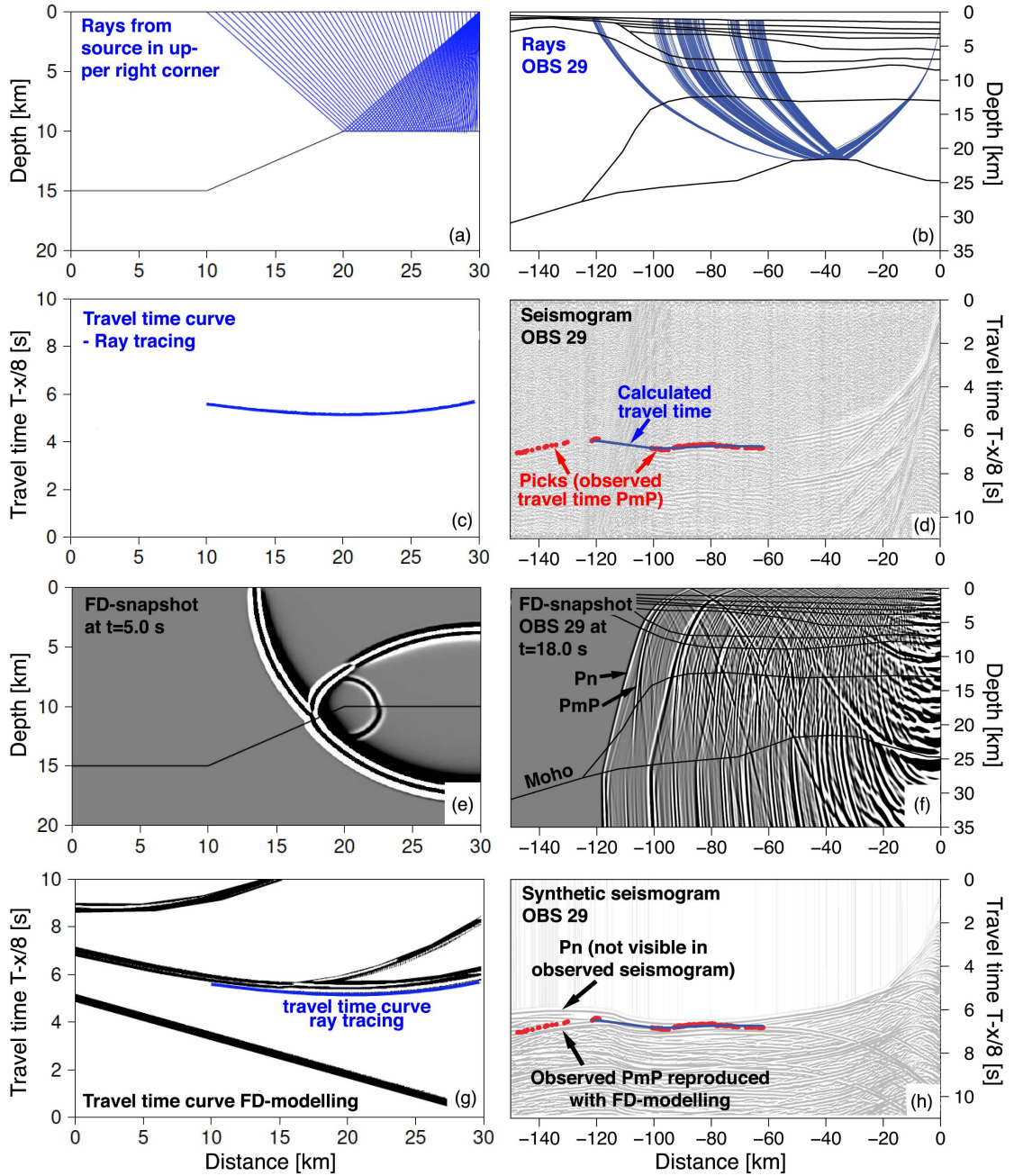


Figure 2.8.: Comparison of ray tracing and FD-modelling. Panels on the left side modified after Schmidt-Aursch (2003). (a) Calculated rays in a simple model with an edge. (b) Calculated rays of the P_mP of OBS 29. (c) Travel time curve for rays in a. (d) Seismogram of OBS 29 with P_mP picks and their calculated travel time. (e) Snapshot of the propagation of wavefields with the FD-method of the model in a. (f) Snapshot of the propagation of wavefields with the FD-method for the model in b. (g) Travel time curves calculated with the FD-method. (h) Synthetic seismogram of OBS 29 calculated with the FD-method.

With *SOFI2D* synthetic seismograms were calculated for different velocity models of the lower crust. These seismograms served already as a quality control for the velocity model. The comparison with the observed data allowed to check if all modelled phases are visible in the synthetic seismogram and that no phases appear, which are absent in the observed seismogram. Furthermore, the move out of the P_mP , of the real and synthetic seismograms are compared. In addition, the amplitudes of the P_mP and the lower crustal reflected phase (P_n) are picked in the synthetic seismograms and exported. Their trend can be compared to the recorded data. At a certain offset, the P_mP and P_n superpose. Because of constructive interference, the amplitudes sum up and a maximum is visible in the amplitude trend. More details on the application of the method in this study is provided in sections 4.5.1 and 6.5.2.

2.3. Gravity data

2.3.1. Density Modelling

To verify that the derived crustal structure is consistent with the free-air gravity anomaly from satellite data (Sandwell et al., 2014), density modelling was conducted with the *IGMAS+* software package (Götze, 1978; Schmidt and Götze, 1998). The program calculates the gravimetric effect of a series of 2D cross sections, which are connected by triangulation. The gravitational response is calculated for the resulting polyhedrons. The general problem of potential field data is that numerous solutions exist to explain an anomaly. Therefore, the seismic layer geometry and velocity information are used for the initial density model to limit the number of possible solutions. The sediment velocities are calculated into densities with the empirical velocity-density relationship of Gardner et al. (1985) and the crustal velocities are converted with the relationship of Christensen and Mooney (1995). I divided seismic layers into several polygons to account for lateral density changes. During the modelling process, the basic geometry was left unchanged as far as possible. I changed the densities iteratively until the calculated free-air gravity anomaly fitted to the observed anomaly within a 5 mGal uncertainty range. Larger uncertainties exist in areas with lateral density changes offset to the profile and at the transition between different crustal types.

2.4. Magnetic data

Magnetic surveying was conducted using the magnetometer onboard *Polarstern* and the helicopter borne system.

2.4.1. Ship borne magnetic data

The two ship's three-component fluxgate magnetometers (Figure 2.9) recorded continuous magnetic data throughout the entire cruise. The systems are mounted at the port and starboard side at the crow's nest onboard *RV Polarstern*. The measured raw data have to be corrected for the ship's interfering field, which is described by a set of compensation coefficients. For their determination, precise knowledge of the ship's attitude and position is crucial. This is achieved onboard *Polarstern* with an Anschuetz Marine Inertial Navigation System (MINS), which permanently records the ship's attitude and position. This data can be used to correct the measured data for the ship's magnetic field and transfer the vector of the compensated magnetic field in a geodetic coordinate system. Further details on the compensation of the ship's interfering field can be retrieved from König (2005). In order to determine the compensation coefficients, seven calibration circles were sailed during ANT-XXIX/5. In addition to the compensation of the ship's field, the data were corrected of the IGRF (International Geomagnetic Reference Field) and de-spiked. Furthermore, the ship's magnetic data is tied to the helicopter borne magnetic anomaly.



Figure 2.9.: Fluxgate magnetometer system installed on *Polarstern* (Jokat, 2013).

2.4.2. Helicopter borne magnetic data



Figure 2.10.: Acquisition of helicopter borne magnetic data during ANT-XXIX/5.

Helicopter borne magnetic data were acquired with a high precision Scintrex CS3 Cesium vapor magnetometer, which was towed in an amagnetic bird 30 m underneath *Polarstern's* helicopter (Figure 2.10). It is part of the airborne geophysical information system (AGIS), which consists also of a magnetometer processor and a computer for data display, acquisition control and navigation. The exact location was provided by a Hemisphere Crescent R100 GPS receiver. The helicopter flew at an altitude of 100 m and at a nominal cruise speed of 80 kn. Flights were planned with the Pico software *PEIConvert* using straight lines in UTM projection. The obtained magnetic data were corrected for the IGRF.

2.4.3. Magnetic anomaly modelling

In the Georgia Basin, previous studies identified magnetic isochrons east of the MEB (Labrecque and Hayes, 1979; Martin et al., 1982). To verify their identification, forward modelling of marine magnetic anomalies was conducted using the MATLAB-based program MODMAG (Mendel et al., 2005). The program provides various parameters that can be changed until the synthetic magnetic anomaly fits to the observed one. The profile (coordinates, depth to basement) and the magnetic field components (declination and inclination at the time of observation) are imported. The source layer characteristics (e.g. the magnetization) can be set and were estimated on literature values. The synthetic anomalies are calculated with the timescale of Gradstein et al. (2004). The spreading rates during corresponding time periods can be adapted until the synthetic marine magnetic anomaly fits to the observed one. The results of the magnetic modelling are provided in section 6.6.3.

3. Contributions to scientific journals

Within the context of this dissertation, I prepared three scientific articles, which present the data and my main findings. The first paper comprises a detailed analysis of the continental margin east of the Falkland Islands. The second article is a short summary of the entire transect and its implications for the breakup of Gondwana. The third paper provides a more detailed presentation of the eastern transect and focuses on the crustal structure of the MEB. The publication strategy did not allow to submit the third, long data paper before the second, summarizing paper is published. Therefore, the third paper is not submitted yet.

This chapter summarizes the titles, the main topics, the author's and co-author's contributions and the status of the manuscripts. The articles are presented in chapters 4, 5 and 6.

3.1. The crustal structure of the continental margin east of the Falkland Islands

Authors: Claudia Monika Schimschal^a, Wilfried Jokat^{a,b}

Affiliations: ^a Alfred Wegener Institute Helmholtz Centre for Polar and Marine Research, Bremerhaven, Germany

^b University of Bremen, Bremen, Germany

Journal: Tectonophysics

Status: Published on 31st January 2018

DOI: 10.1016/j.tecto.2017.11.034

We present the velocity and density model of the western transect of profile AWI-20130010. The crustal model shows the extent of the Falkland Islands' continental crust, the COT and the oceanic crust of the Falkland Plateau Basin. The structure of the margin is compared to the adjacent margins north (offshore Argentina) and south (Weddell Rift) of the Falkland Plateau. By comparison with regions, where the crustal composition is known, the crust beneath the Falkland Plateau Basin is characterized as thick oceanic crust. We speculate if the exceptional igneous crustal thickness is caused by a mantle thermal anomaly, which also influenced the crustal formation of the Weddell

Rift.

I processed the wide-angle seismic data, calculated the velocity model using ray tracing techniques and amplitude modelling, determined the density model and prepared the manuscript and all figures. Wilfried Jokat was chief scientist of the expedition ANT-XXIX-5 and supervised my work. He and Graeme Eagles (AWI) revised this manuscript.

3.2. The Falkland Plateau in the context of Gondwana breakup

Authors: Claudia Monika Schimschal^a, Wilfried Jokat^{a,b}

Affiliations: ^a Alfred Wegener Institute Helmholtz Centre for Polar and Marine Research, Bremerhaven, Germany

^b University of Bremen, Bremen, Germany

Journal: Gondwana Research

Status: Submitted on 15th March 2018

This article provides an overview on the entire transect along the Falkland Plateau. The seismic velocity structure shows that the Falkland Plateau Basin is composed of thick oceanic crust and Maurice Ewing Bank is a continental fragment. These results are incorporated in a new breakup model for Gondwana. The exceptional thick oceanic crust beneath the Falkland Plateau Basin is explained with its development in a back-arc regime in a region with enhanced melt supply.

I calculated the velocity model of the entire transect and set up the reconstruction with GPlates. Therefore, I used rotation poles from literature and included my own findings. I wrote the manuscript and prepared all figures. My work was supervised by Wilfried Jokat, who also revised the manuscript. In addition, the article was revised by Graeme Eagles.

3.3. The crustal structure of Maurice Ewing Bank from wide-angle seismic data

Authors: Claudia Monika Schimschal^a, Wilfried Jokat^{a,b}

Affiliations: ^a Alfred Wegener Institute Helmholtz Centre for Polar and Marine Research, Bremerhaven, Germany

^b University of Bremen, Bremen, Germany

Status: To be submitted to Tectonophysics

In this article, we present the data and results for the eastern transect. The velocity and density model show that Maurice Ewing Bank is composed of continental crust, which is in parts stretched and magmatically intruded. The crustal structure is compared to the one beneath East Falkland. The Georgia Basin is underlain by oceanic crust of average crustal thickness. Magnetic anomaly modelling confirms the onset of oceanic crust formation at M10n time. For the crust beneath the Falkland Plateau Basin, the analysis of the bulk crustal velocity shows, that crustal formation was influenced by active upwelling of the mantle, which I attribute to the plateau's position in a back-arc environment during crustal development.

I conducted the velocity, amplitude and density modelling and for the Georgia Basin an additional magnetic modelling. I prepared the manuscript and all figures. Graeme Eagles supported the processing of the ship's magnetic data. Wilfried Jokat supervised my work and revised the manuscript.

4. The crustal structure of the continental margin east of the Falkland Islands

Claudia Monika Schimschal^a, Wilfried Jokat^{a,b}

^a Alfred Wegener Institute Helmholtz Centre for Polar and Marine Research

^b University of Bremen

4.1. Abstract

The 1500 km long Falkland Plateau is the most prominent morphological structure in the southern South Atlantic Ocean, which crustal composition and development is mainly unknown. At the westernmost boundary of the plateau, the Falkland Islands' Precambrian geology provides the only insight into basement structure and age. The question of whether continental basement of a similar age and origin underlies the Falkland Plateau further east is strongly disputed. We present new high quality constraints on the crustal fabric of the plateau east of the Falkland Islands, based on wide-angle seismic and potential field data acquired in 2013. The P-wave velocity model, supported by amplitude and density modelling, shows that the Falkland Plateau Basin is filled with 8 km of sediments. Continental crust of 34 km thickness underlies the Falkland Islands. The eastern continental margin of the Falkland Islands can be classified as a volcanic rifted margin. The Falkland Plateau Basin is floored by up to 20 km thick oceanic crust. The exceptional thick igneous crust and its high lower crustal velocities (up to 7.4 km/s) indicate the influence of a regional thermal mantle anomaly during its formation, which provided extra melt material. The wide-angle model revises published crustal models, which predicted thin oceanic or thick extended continental crust below the Falkland Plateau Basin. Our results provide a sound basis for future tectonic interpretations of the area.

4.2. Introduction

The Falkland Islands are situated in the South Atlantic Ocean 500 km east of Patagonia/South America and are composed of two main islands, East and West Falkland. Eastwards of the Falkland Islands, the Falkland Plateau stretches for more than 1500 km

into the Georgia Basin. The central part of the plateau, between the Falkland Islands in the west and Maurice Ewing Bank in the east, hosts the Falkland Plateau Basin (Figure 4.1). Here, the average water depth is 2600 m, while the seafloor shallows to 1500 m on the Maurice Ewing Bank. In the north, the plateau bounds the Argentine Basin across the east-west trending Falkland Escarpment (Figure 4.1). This escarpment is a sheared continental margin segment, which formed during opening of the South Atlantic. In the south the plateau deepens to form the Falkland Trough (52.5° S), the result of flexural loading by Neogene convergent tectonics along the North Scotia Ridge (Bry et al., 2004). During the Jurassic (about 170 Ma ago) the Falkland Islands were part of the supercontinent Gondwana (Figure 4.2) and the Falkland Islands were located off southern Africa (e.g. Dalziel and Lawver, 2001; Ghidella et al., 2007; Jokat et al., 2003b; König and Jokat, 2006; Torsvik et al., 2010).

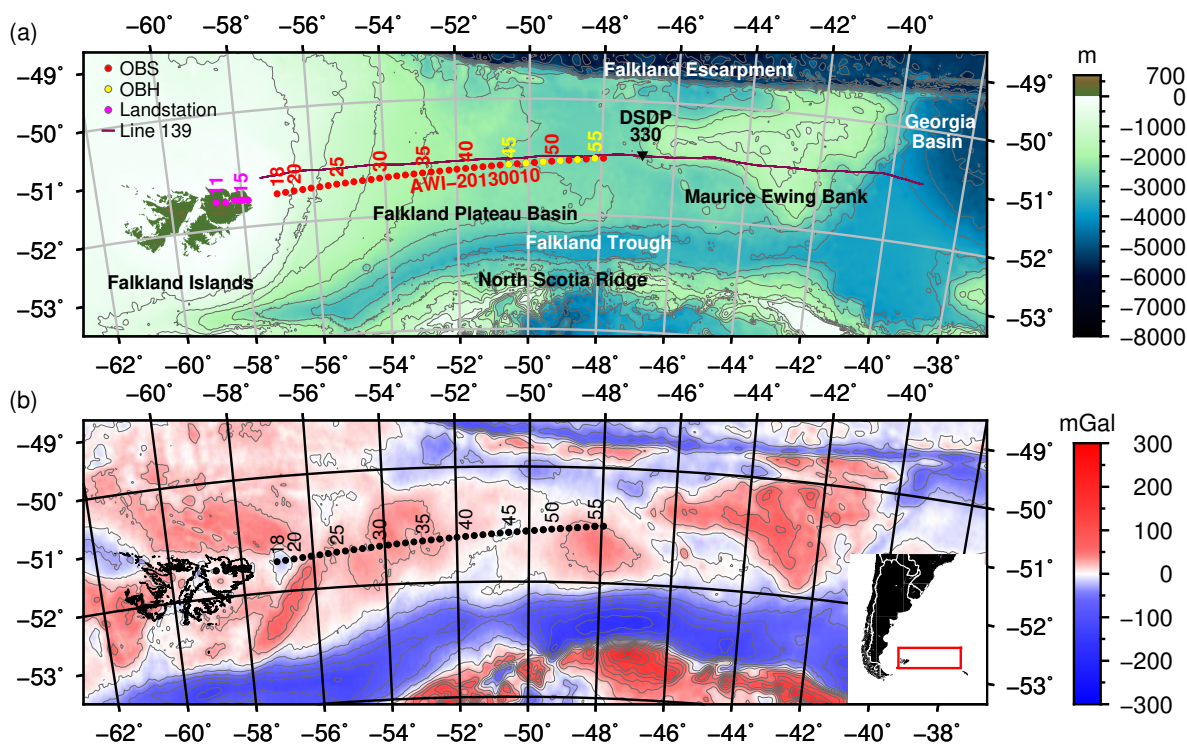


Figure 4.1.: (a) Topographic and bathymetric map of the Falkland Islands and the Falkland Plateau (GEBCO, 2014) with OBS, OBH and land station positions. In addition the seismic reflection line 139 (Ludwig et al., 1978) and the DSDP drill site 330 are depicted. (b) Free-air gravity anomaly map of the Falkland Islands and the Falkland Plateau (Sandwell et al., 2014).

Knowledge of the plateau’s crustal fabric is essential for any sound reconstruction of its development and role in the initial fragmentation of Gondwana. Strongly contrasting paleogeographical scenarios are possible depending on whether oceanic or stretched continental crust is assumed to underlie the plateau. While the surface geology of the Falkland Islands is reasonably well mapped, little is known about the deeper crustal

fabric. Further east, beneath the Falkland Plateau Basin, the nature of the crust and thus its classification is not clear at all on the basis of existing seismic reflection and potential field data.

At the eastern margin of the Falkland Islands platform, Barker (1999) interpreted linear coincident magnetic and gravimetric anomalies to be caused by seaward dipping basalt flows. He speculated that the northeast-southwest striking margin is a volcanic rifted margin. In general, rifted margins can be classified as volcanic and non-volcanic depending on the quantity of igneous features related to the breakup process. In this context, volcanic and non-volcanic represent end-members and margins exist, which neither show clear indications of volcanic margins nor of non-volcanic margins (e.g. the margin west of Melville Bay (Greenland), Altenbernd et al. (2015)). In interpreted seismic profiles, volcanic rifted margins are characterized by extrusive features like volcanoes, vents, and seaward dipping basalt sequences (Hinz, 1981; Hinz et al., 1987), intrusive complexes of batholiths, sills and dykes (Eldholm et al., 1995) and the presence of a thick gabbro layer in the lower crust (Kelemen and Holbrook, 1995; White and McKenzie, 1989). The continent-ocean transition zone (COT) at non-volcanic margins, in contrast, is characterized by highly stretched continental crust with rotated fault blocks, regional low-angle or horizontal detachment surfaces, and no or only minor volcanic features (White et al., 1992).

Independent from its margin type the Falkland Plateau was also interpreted as a marginal plateau (Mercier de Lépinay et al., 2016) though its crustal nature was unknown. Marginal plateaus are bathymetric features, which are bounded to at least one side to a transform margin. They are characterized by a flat but deep surface inside the continental slope. Marginal plateaus are often associated with crustal thinning prior to transform faulting. According to Mercier de Lépinay et al. (2016) all marginal plateaus share a multi-stage evolution, with at least one period of rifting prior to transform formation. Most marginal plateaus are located at an intersection of two oceanic domains with different ages (Mercier de Lépinay et al., 2016). For the Falkland Plateau a transform fault bounds the plateau to the north. Rifting occurred east of the Maurice Ewing Bank, which resulted in a westward movement of the Falkland Plateau. However, without deep seismic sounding data such an interpretation remains vague.

The few scientific seismic reflection and sonobuoy refraction measurements on the Falkland Plateau conducted in the 1970s (Ludwig, 1983; Ludwig et al., 1978; Ludwig and Rabinowitz, 1980) are not sufficient to support any of such classifications. Those authors concluded on the presence of oceanic crust with a Moho at 12 km depth beneath the Falkland Plateau Basin. By incorporating all existing geophysical data, Kimbell and Richards (2008) calculated a 3D isostatically compensated density model for the crustal structure of the Falkland Plateau. Their model shows a crust twice as thick as that calculated from the existing seismic sonobuoy data, but equivocates on the density structure, leaving interpretations as either igneous or stretched continental crust possible.

To provide sound constraints on its crustal fabric, we completed a deep seismic refraction experiment across the eastern margin of the Falkland Islands in 2013 (Figure 4.1), using ocean bottom stations and RefTek land stations as recording instruments and air-

guns as seismic source. The resulting crustal seismic velocity model comprises entirely new constraints on the formation and history of the plateau. This study presents the experiment, its results, and their interpretation.

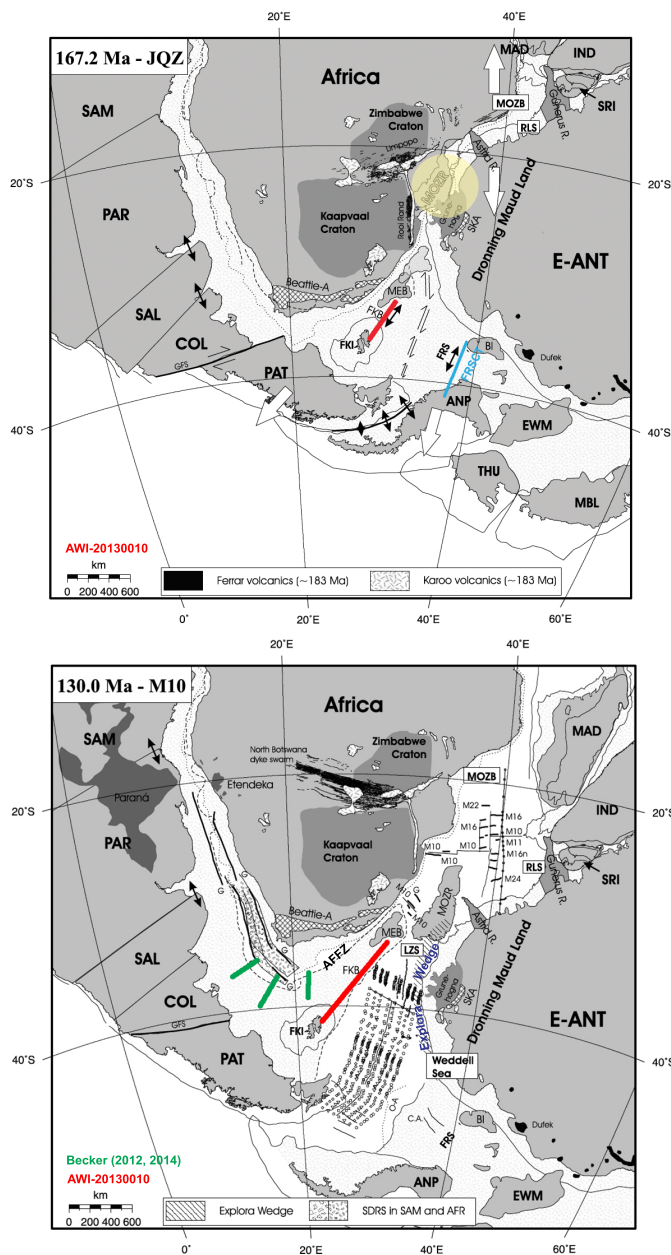


Figure 4.2: Reconstruction for the breakup of Gondwana (König and Jokat, 2006) with the profiles AWI-20130010 (red), the FRSC (blue) and the profiles presented by Becker et al. (2012, 2014) in green. In the 167.2 Ma plot the estimated position of the Bouvet Hotspot (Storey, 1995) is depicted in yellow. Abbreviations are: AFFZ: Agulhas Falkland Fracture Zone; ANP: Antarctic Peninsula; Beattie-A: Beattie Anomaly; C.A.: central anomalies; COL: Colorado; E-ANT: East Antarctica; EWM: Ellsworth Whitmore Mountains; FKB: Falkland Plateau Basin; FKI: Falkland Islands; FRS: Filchner-Ronne Shelf; GFS: Gastre Fault System; IND: India; JQZ: Jurassic Quiet Zone; LZS: Lazarev Sea; MAD: Madagascar; MBL: Marie Byrd Land; MEB: Maurice Ewing Bank; MOZB: Mozambique Basin; MOZR: Mozambique Ridge; O-A: Orion Anomaly; PAR: Parana; PAT: Patagonia; RLS: Riiser-Larsen Sea; SAL: Salado; SAM: South America (northern part); SKA: Sverdrupfjella Kirwanveggen Anomaly; SRI: Sri Lanka; THU: Thurston Island.

4.3. Geologic setting

The Falkland archipelago is composed of two main islands, East and West Falkland, and hundreds of smaller islands and rocks. A detailed and comprehensive description

of the geological units (Figure 4.3) is provided by Aldiss and Edwards (1999) and is summarized here.

On the southernmost point of West Falkland, Mesoproterozoic crystalline basement crops out as the Cape Meredith Complex. It is mainly composed of gneisses and granitoids. Radiometric age dating revealed ages between 1.1 and 1 billion years (Jacobs et al., 1999).

The siliciclastic West Falkland Group overlying these basement rocks is a succession of three formations containing mainly quartzites, sandstones and mudstones of Silurian-Devonian to Carboniferous age. The West Falkland Group covers most of West Falkland and the northern part of East Falkland.

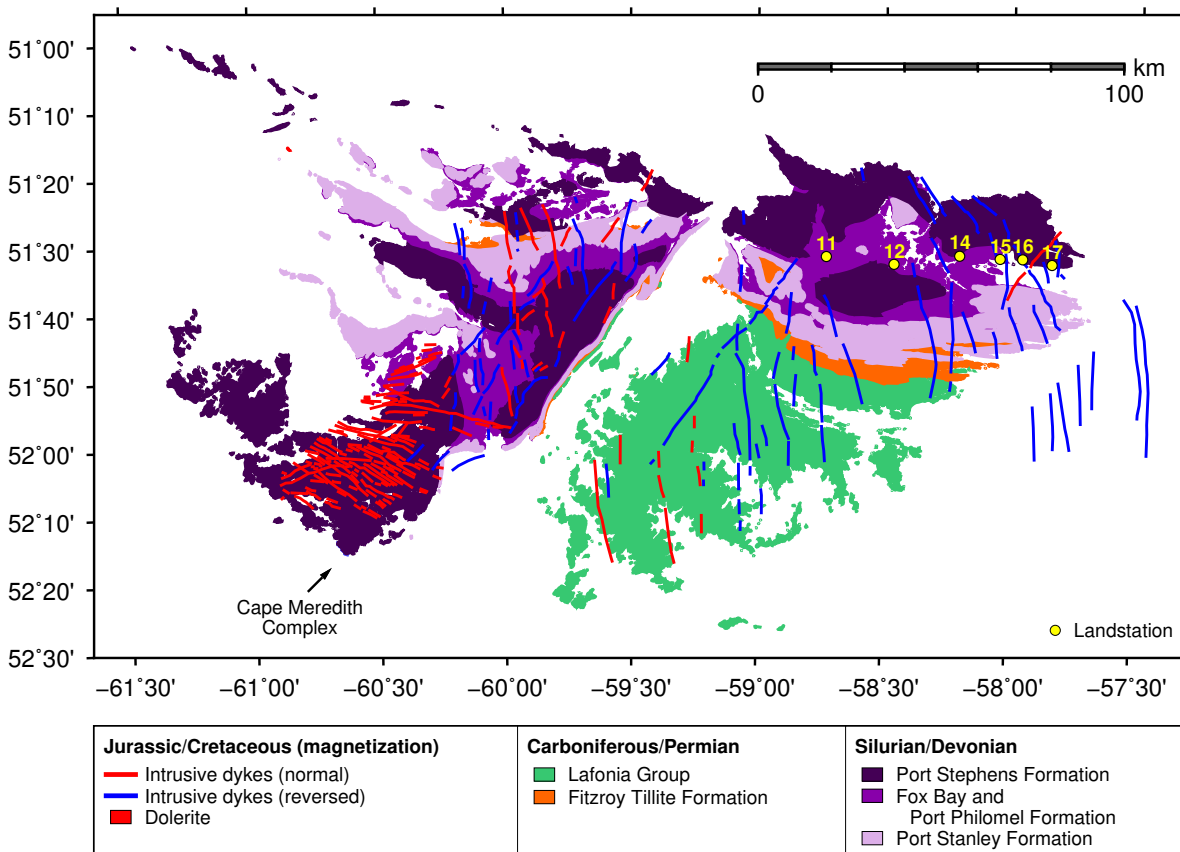


Figure 4.3.: Geological Map of the Falkland Islands with onshore dykes (Stone et al., 2008) and offshore dykes (Barker, 1999). Geological units are provided by the Falkland Islands' Government.

The peninsula at the southern part of East Falkland is called Lafonia and is composed of the eponymous geological unit (Figure 4.3; Falkland Islands' Government). The Carboniferous to Permian Lafonia Group can be divided into lower and upper portions. The lower portion consists of sandstones and mudstones, while the upper portion is a clastic sequence.

The Fitzroy Tillite Formation was deposited from floating ice sheets and is composed of

mud, sand, erratic pebbles and boulders. Over 400 dolerite dykes are intruded into these rocks. Stone et al. (2008) divided the dykes into three swarms: The oldest ($^{40}\text{Ar}/^{39}\text{Ar}$ age: 188 ± 2 Ma, Mussett and Taylor (1994)) intruded in the south of West Falkland, is east-west trending and normally magnetized. A second swarm of Jurassic age ($^{40}\text{Ar}/^{39}\text{Ar}$ age: 178.6 ± 4.9 Ma, Stone et al. (2008); K-Ar ages: 176 ± 7 Ma and 162 ± 6 Ma, Thistlewood et al. (1997)) trends northeast-southwest and the dykes have, in general, reverse magnetization but contain also normally magnetized segments. Both of the Jurassic dyke swarms are considered to be linked to Karoo-Ferrar magmatism and Mitchell et al. (1986) describe their geochemistry as a transition between the African (Karoo) and Antarctic (Ferrar) provinces. A third dyke swarm, of Cretaceous age ($^{40}\text{Ar}/^{39}\text{Ar}$ ages: 121.3 ± 1.2 Ma, Stone et al. (2008); 133 ± 4 Ma and 137 ± 4 Ma, Richards et al. (2013)), trends north-south. The intrusion must have lasted long enough to span a magnetic reversal as Cretaceous dykes of normal and reverse polarization exist (Richards et al., 2013; Stone et al., 2009).

4.3.1. Seismic Structure of the Falkland Plateau

Platt and Philip (1995) used industry seismic data to set up a stratigraphy for the region southeast of the Falkland Islands, which will be briefly repeated here. Close to the coast, the sedimentary deposits lie unconformably on faulted acoustic basement, which is of probable Paleozoic or Mesozoic age. In the east, sediment layers pinch out onto a platform surrounding the islands. Oblique faults and complex fault terraces compose the margin of this platform (Platt and Philip, 1995). Towards the Falkland Plateau, the basement dips steeply eastwards beneath increasingly thick sediments (Ludwig et al., 1978; Platt and Philip, 1995).

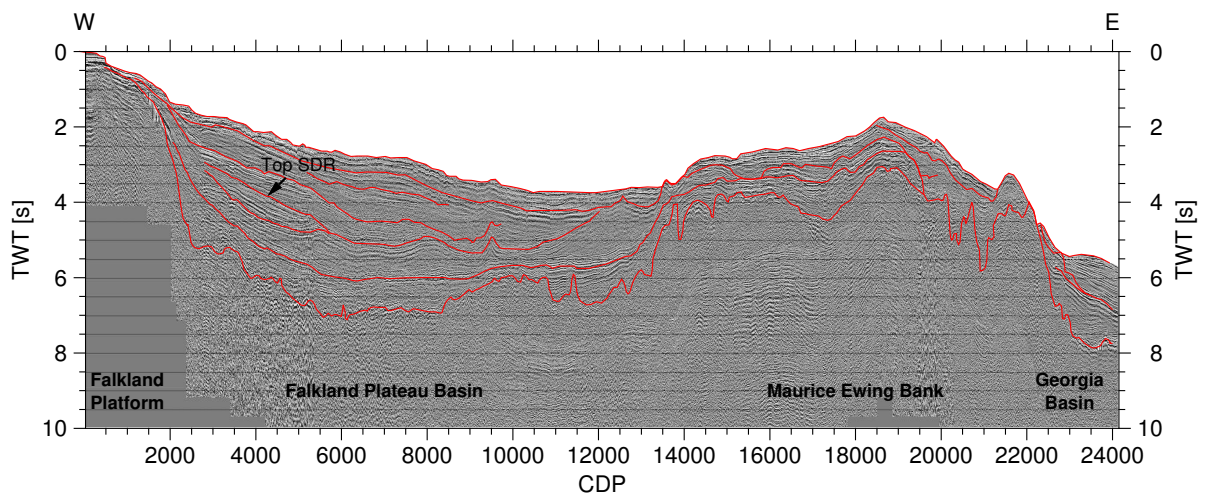


Figure 4.4.: Seismic reflection line 139 (Ludwig et al., 1978) with the top of the seaward-dipping reflector sequences (SDR, Barker, 1999) and basement and major unconformities (red lines, Lorenzo and Mutter, 1988).

In the Falkland Plateau Basin, the extensive Mesozoic to Tertiary sedimentary succession

is organised into onlapping sequences that probably represent prograding submarine fan and wedge deposits. The succession thickens with increasing water depth. High amplitude events are interpreted to show intra-sedimentary volcanic rocks and intrusive sills (Platt and Philip, 1995). In general, the sediments form widespread southwards-dipping units, of which the uppermost are truncated up-dip by an erosional surface (Figure 4.4, Ludwig et al., 1978). The northern edge of the plateau is formed by the Falkland Escarpment, a basement ridge that was locally formed by a collapse of platform sediments along faults (Ludwig, 1983). In the south, oblique convergence of the North Scotia Ridge towards the plateau caused disruption of the depositional sequences (Ludwig and Rabinowitz, 1982).

Indications for magmatism are found in several 30 km wide, isolated, cone-shaped bodies southwest of Maurice Ewing Bank, that are interpreted to be volcanic edifices, and in dipping reflectors below the Falkland Plateau Basin's basement characteristic of sub-aerial lava flows (Lorenzo and Mutter, 1988). In the commercial well 61/5-1 southeast of the Falkland Islands dolerite was drilled in 2416 m depth, but it is not clear if it is representative for the basement (Richards et al., 2013). Richards et al. (2013) concluded that the intrusion of Early Cretaceous dykes on the island was contemporaneous with the extrusion of lavas and intrusion of sills in the Falkland Plateau Basin, and linked this extensive magmatism to thermally-driven regional uplift during the initial opening of the South Atlantic.

Information about the basement fabric beneath the Falkland Plateau Basin is limited to seismic investigations by Ludwig et al. (1978); Ludwig (1983); Ludwig and Rabinowitz (1980) and the potential field studies by Barker (1999) and Kimbell and Richards (2008). The sediments and basement of Maurice Ewing Bank were drilled at DSDP drill site 330 up to a depth of 550 m. The cuttings contained gneisses, which are similar in lithology and composition to gneisses of the Cape Meredith Complex (Barker, 1977). The radiometric age of 535 ± 66 Ma, however, is significantly younger than those for the Cape Meredith Complex (1,000–1,100 Ma). Assuming the drilled gneisses formed at the same time as the Cape Meredith Complex, the difference in age might be related to either a hydrothermal event or to metamorphic re-crystallization (Beckinsale et al., 1977).

4.4. Data acquisition and data processing

To obtain a crustal model for the eastern margin of the Falkland Islands, the Alfred Wegener Institute for Polar and Marine Research (AWI) conducted the expedition ANT-XXIX/5 with the research vessel *Polarstern* from April 18th 2013 until May 29th 2013 (Jokat, 2013). Seismic refraction measurements were conducted along a 750 km long west-east oriented profile (AWI-20130010, Figure 4.1). Because of time and weather constraints it was not possible to acquire additional seismic reflection data to better constrain the sediment structure along the deep seismic transect. The seismic source was an array of eight G-Guns with a total volume of 68 l (4160 in³). In total, 3864 shots were generated along a 615 km transect. The shot interval was 60 s, resulting in an average spacing of 150 m. On East Falkland, six land stations were installed. The RefTek data

loggers were deployed at an average spacing of 12 km. The loggers were equipped with 4.5 Hz geophone chains and recorded the data at a sampling rate of 100 Hz. The closest distance of any of the land stations to the start of the marine profile was 75 km. After conversion to SEG-Y-format, the land station data were bandpass filtered with corner frequencies of 4 and 15 Hz. An automatic gain control (AGC) with a time window of 1 s was applied. The data quality from the land stations varies strongly, with stations 12, 14 and 15 providing the best quality with phases still visible at 240 km distance. Stations 11, 16 and 17 yielded hardly any usable data. Figure 4.5 shows the record section from land station 15.

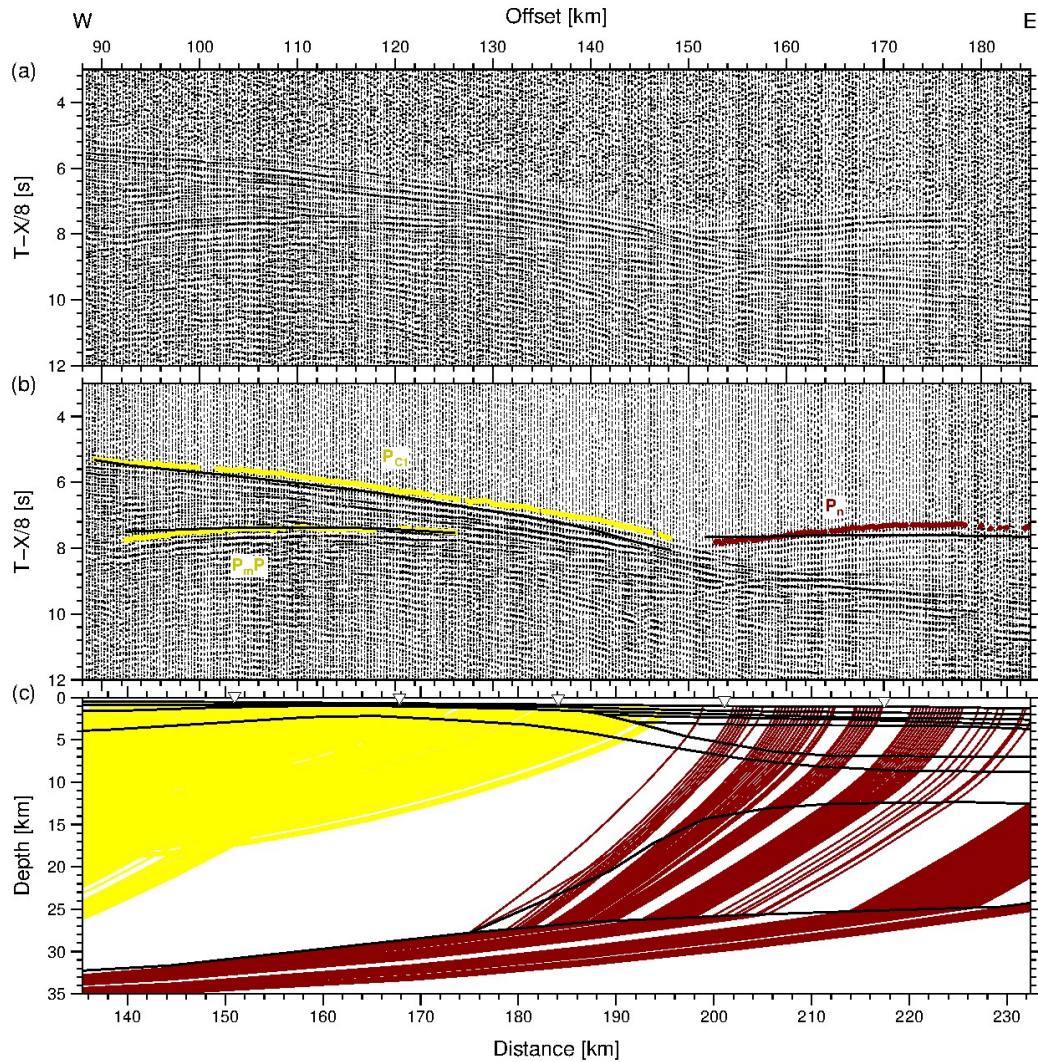


Figure 4.5.: Data example for land station 15. (a) Seismic section filtered with a 4-15 Hz bandpass filter and displayed with a reduction velocity of 8 km/s. (b) The same section without AGC. Picked phases with error bars and corresponding phase names. The modelled first arrivals are plotted as black lines. (c) Ray path for picks shown in (b). Station positions are marked as triangles.

Offshore, 39 ocean bottom receivers, provided by GEOMAR, were deployed with a spacing of ~ 16 km. Two different types of ocean bottom instruments were used: 33 ocean bottom seismometers (OBS) and 6 ocean bottom hydrophones (OBH). Both instrument types were equipped with a hydrophone and the OBS recorded the data with an additional three component seismometer. The sampling rate was 200 Hz.

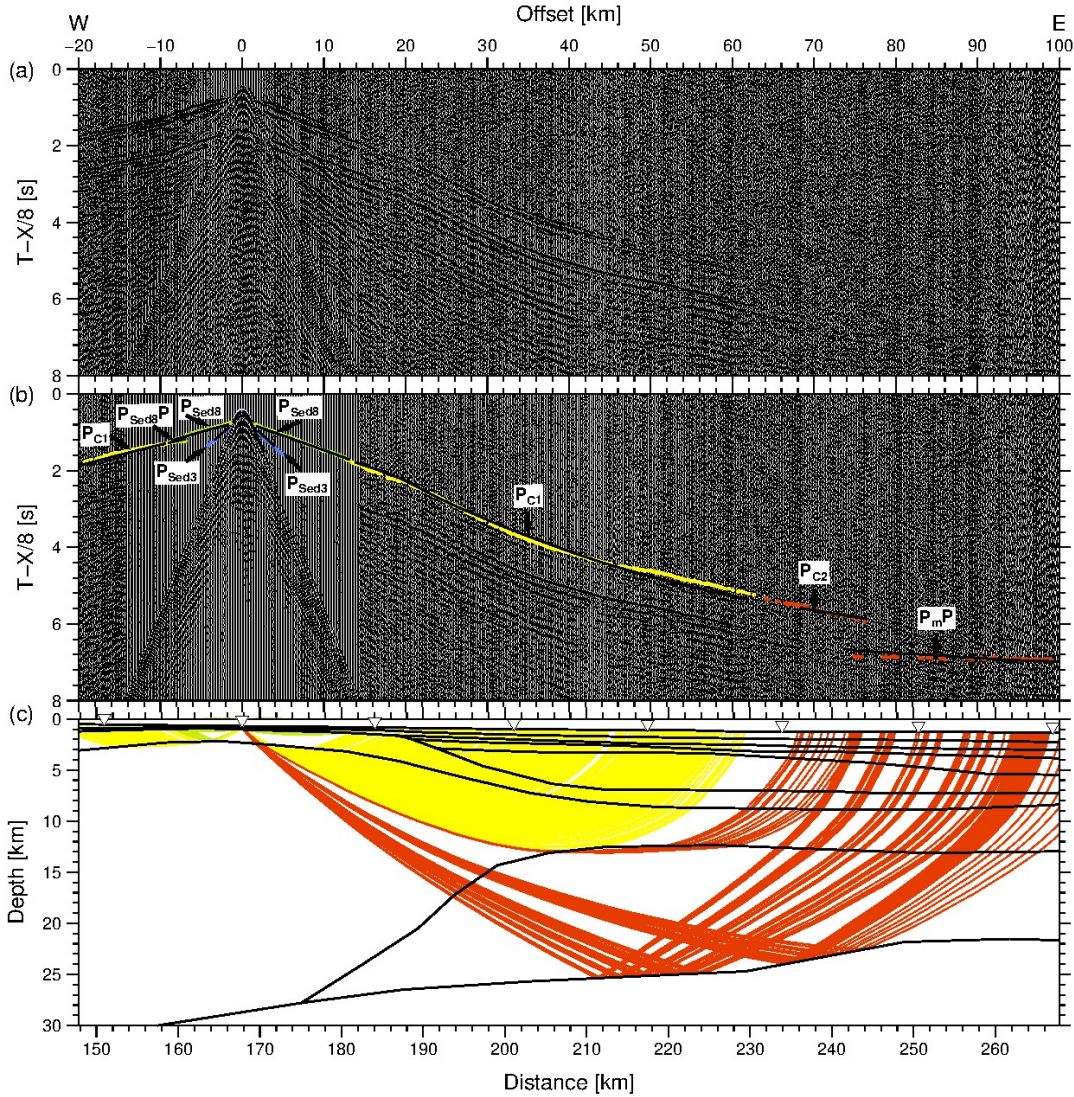


Figure 4.6.: Data example for OBS 21. (a) Seismic section filtered with a 4-15 Hz bandpass filter and displayed with a reduction velocity of 8 km/s. (b) The same section without AGC. Picked phases with error bars and corresponding phase names. The modelled first arrivals are plotted as black lines. (c) Ray path for picks shown in (b). Station positions are marked as triangles.

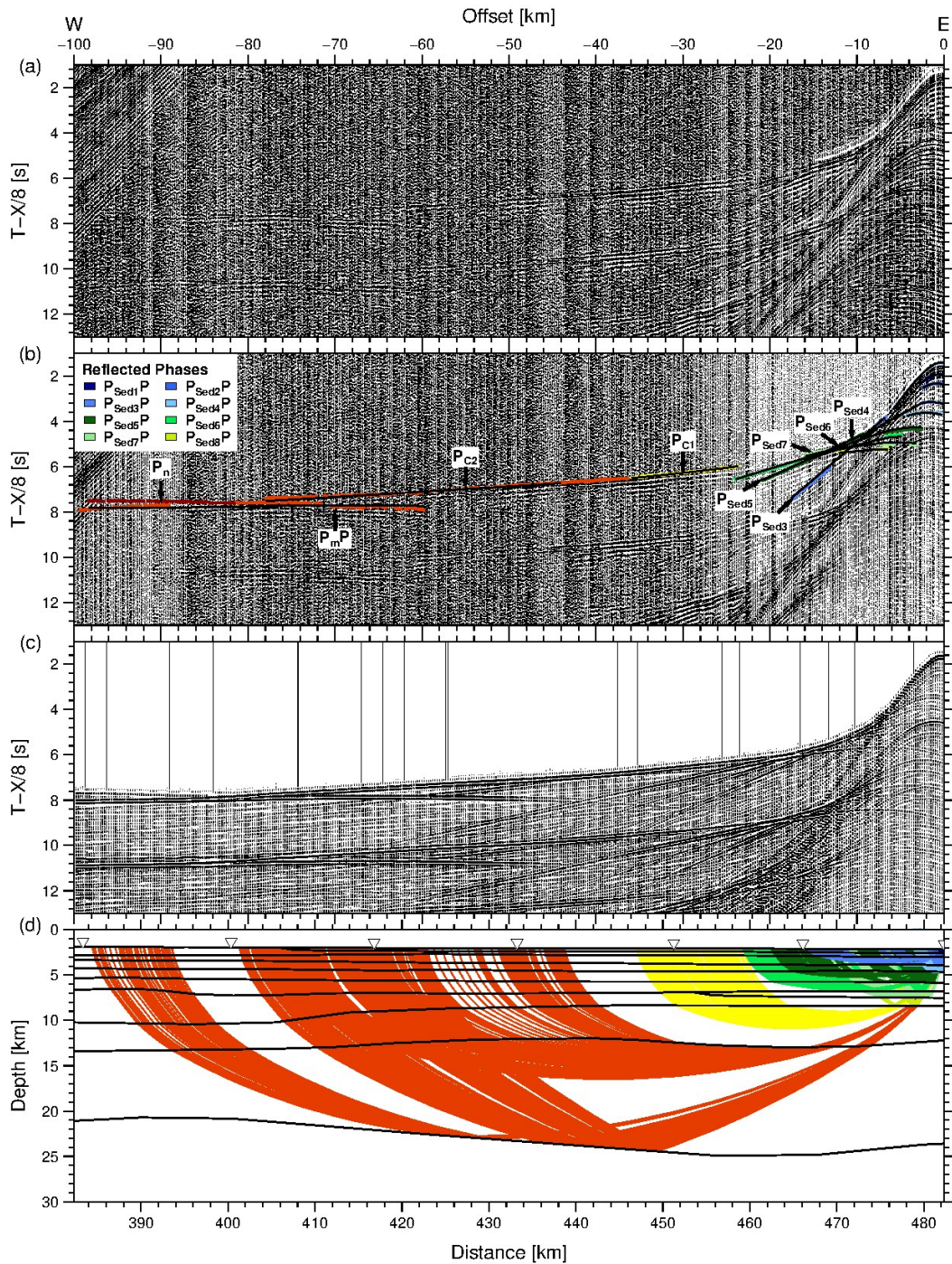


Figure 4.7.: Data example for OBS 40. (a) Seismic section filtered with a 4-15 Hz bandpass filter and displayed with a reduction velocity of 8 km/s. (b) The same section without AGC. Picked phases with error bars and corresponding phase names. The names of the reflected sediment phases are given in the left corner. The modelled first arrivals are plotted as black lines. (c) Synthetic seismogram for OBS 40 calculated with the final P-wave velocity model. (d) Ray path for picks shown in (b). Station positions are marked as triangles.

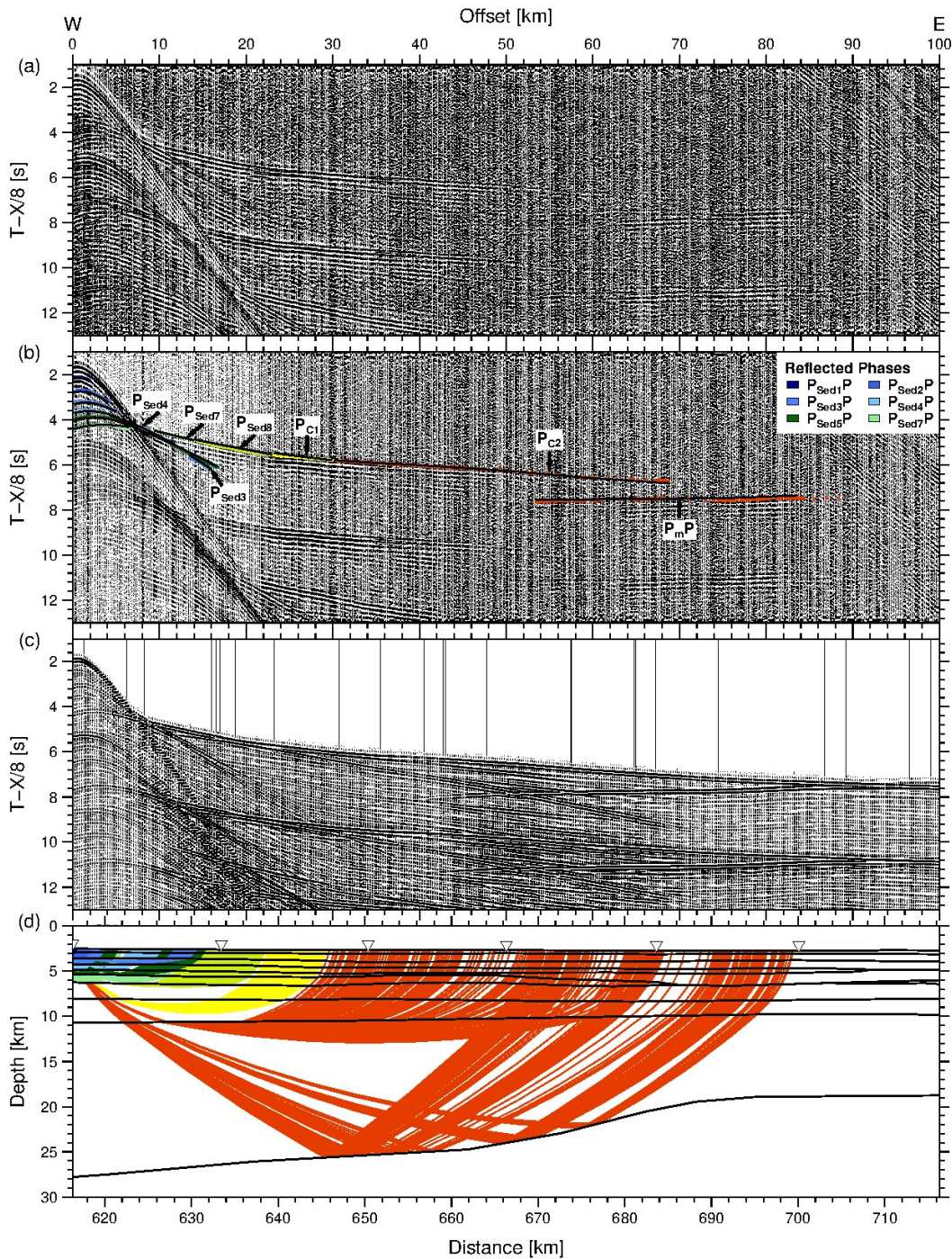


Figure 4.8.: Data example for OBS 48. (a) Seismic section filtered with a 4-15 Hz bandpass filter and displayed with a reduction velocity of 8 km/s. (b) The same section without AGC. Picked phases with error bars and corresponding phase names. The names of the reflected sediment phases are given in the right corner. The modelled first arrivals are plotted as black lines. (c) Synthetic seismogram for OBS 48 calculated with the final P-wave velocity model. (d) Ray path for picks shown in (b). Station positions are marked as triangles.

All receivers were recovered, but eight stations returned no data due to malfunctions. The data were converted to SEG-Y-format and corrected for the clock drift. Afterwards, the instruments were relocated along the line by adjusting their positions until the shapes of the direct water waves became symmetrical. A bandpass filter with corner frequencies of 4 and 20 Hz and an AGC with a time window of 1 s were applied. An additional deconvolution filter was applied in instances with strong ringing to enhance the signal to noise ratio for the secondary arrivals. In general, the data quality is good, with the hydrophone channel providing the best data quality. For most of the stations, phases can be identified up to 100 km offset, beyond which ‘wrap-around’ noise occurs. For the stations with the best data quality, phases can be identified to an offset of 150 km. Examples of the recorded data for OBS 21, 40 and 48 are shown in Figures 4.6, 4.7 and 4.8.

4.5. Modelling

4.5.1. Seismic refraction data

Forward modelling using ray tracing

The 2D crustal velocity model was obtained by forward modelling using ray tracing techniques. Picking of P-wave arrivals of refracted and reflected phases was performed using the ZP software (<http://www.soest.hawaii.edu/users/bzelt/zp/zp.html>). Examples of phases picked in the resulting receiver gather of land station 15 and OBS 21, 40 and 48 are given in Figures 4.5b, 4.6b, 4.7b and 4.8b. For all stations the seismic sections and picks are provided in the supplementary material (in the appendix). The picked phases were assigned to layers with the nomenclature of Table 4.1. The velocities for the upper layers *Sed1* and *Sed2* were calculated by analysing the moveout hyperbolae of reflected phases in the OBS data. An example is shown in Figure 4.9, displaying the seismogram (a), the picked phases (b) and the ray coverage (c) of station 48.

Note that although more reflected phases are visible in the data, we found that using them to add more layers did not enhance the velocity-depth model. Except for the upper two layers, only reflected phases, which have clear refracted phases, are used. In total, eight sedimentary velocity layers can be distinguished and their refracted phases correspond with P_{Sed1} to P_{Sed8} and $P_{Sed1}P$ to $P_{Sed8}P$ for reflected phases, respectively. The crust is divided into an upper layer *C1* and a lower layer *C2*. Moho reflections ($P_M P$) are clearly visible and the upper mantle refraction (P_N) can be observed in several seismograms.

Forward modelling was realized using *RAYINV*R (Zelt and Smith, 1992) together with the *P*Ray graphical user interface (Fromm, 2016). For modelling, all station locations were projected onto a straight line between the first land station and the last OBS. Forward modelling was performed layer-wise from top to bottom. Constraints for modelling the sediment layers and the crustal basement were provided from existing reflection data (line 139, Figure 4.4) along a profile that lies offset and sub-parallel to the wide-angle line at distances of between 35 and 6 km (Ludwig et al., 1978, Figure 4.1).

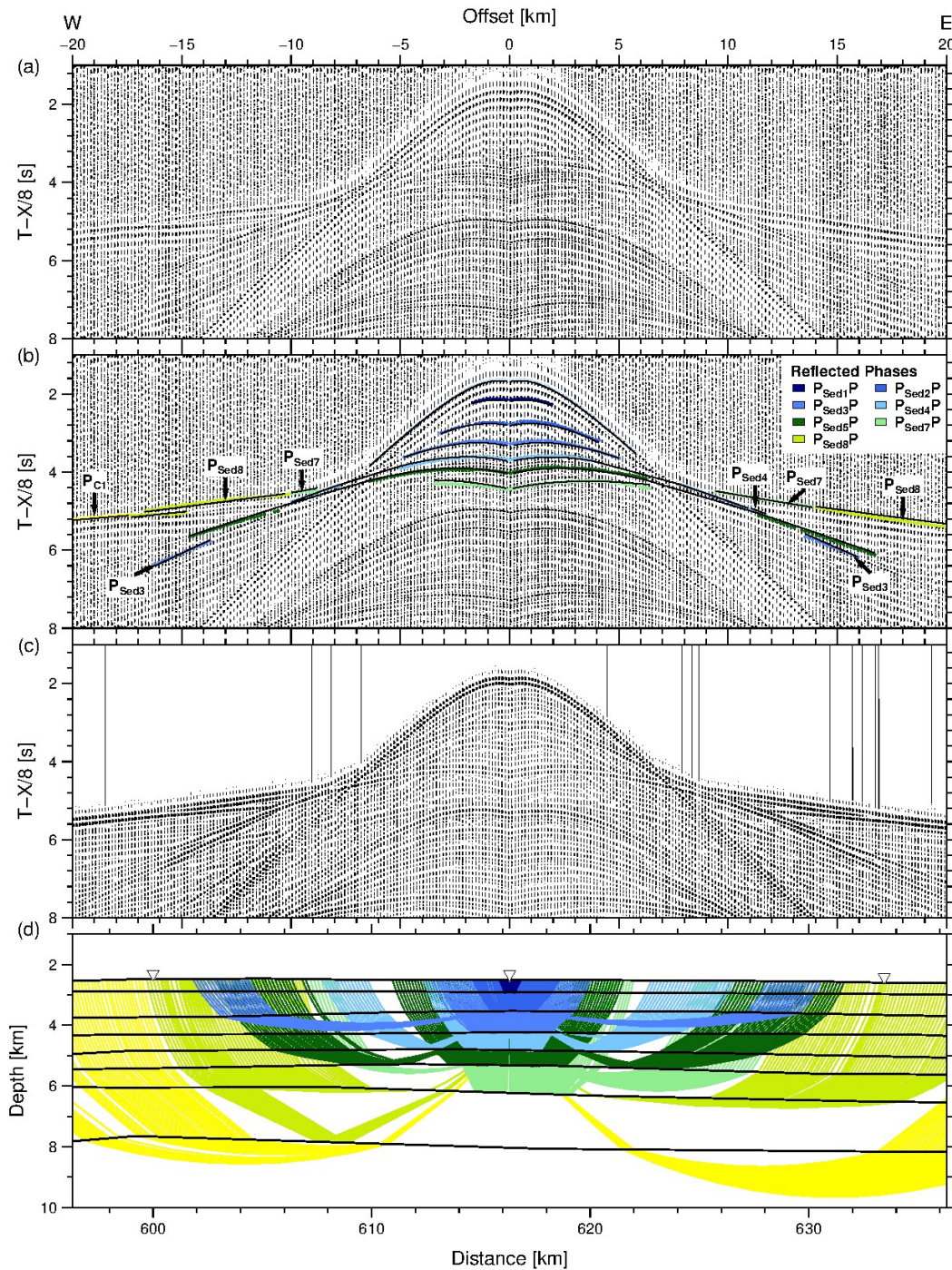


Figure 4.9.: Data example for the sediment phases (OBS 48). (a) Seismic section filtered with a 4-20 Hz bandpass filter and displayed with a reduction velocity of 8 km/s. (b) The same section without AGC. Picked phases with error bars and corresponding phase names. The names of the reflected sediment phases are given in the right corner. The modelled first arrivals are plotted as black lines. (c) Synthetic seismogram for OBS 48 calculated with the final P-wave velocity model. (d) Ray path for picks shown in (b). Station positions are marked as triangles.

Depth and velocity uncertainties were estimated according to Schlindwein and Jokat (1999). Velocity and boundary knots were perturbed until the calculated travel times were outside the range of assigned uncertainties of the observed data. The perturbations were applied layer-wise and separately for velocities and depths. Uncertainties for sediment layers in the Falkland Plateau Basin range from ± 100 m for the two uppermost layers to ± 300 m for sediment layers in greater depth and the basement. The boundary between the upper and lower crust is expressed only as a change of gradient, so varying its depth would only change the velocities of the layers, which are investigated in the next step. For the Moho underneath the plateau, the depth uncertainty is estimated to be less than ± 2.5 km. Uncertainties for sediment layer velocities depend on whether the layer is constrained only by reflected phases or also by refractions. Consequently, velocity uncertainties for the upper two layers are comparably large (± 0.3 km/s) and decrease for the deeper sediment layers *Sed3* and *Sed4* to ± 0.2 km/s. Uncertainties for the lowermost sediment layers and the upper crust are within ± 0.3 km/s. The uncertainty for the velocity at the upper layer boundary of the lower crust is estimated to be ± 0.3 km/s. Below ~ 18 km depth, the lower crust is not covered by refracted phases. Here, the velocity is constrained by the moveout velocity of P_mP and constrained by amplitude modelling. A constant gradient is assumed for the entire layer.

Amplitude modelling

Velocity modelling by ray tracing usually yields reasonable results, but has limitations in areas with limited ray coverage by diving waves (e.g. in the lower crust). To overcome these difficulties and further constrain the ray tracing model, forward amplitude modelling was conducted using the *SOFI2D* (Seismic mOdelling with FInite Differences, Bohlen, 2002) software. *SOFI2D* is a parallel modelling code, based on finite differences (FD), which solves the wave equation in the time domain. P- and SV-wave propagation are modelled for the viscoelastic case by using the ray tracing depth model as input. The way, the method has been applied, is described also in greater detail by Mueller et al. (2016).

P-wave velocities in the model had to be converted into S-wave velocities for *SOFI2D*. In the absence of clear S-wave arrival, this is achieved by a simple division by $\sqrt{3}$ (except in water). Densities for *SOFI2D*'s boundary impedance calculations were determined from the P-wave velocity model using Barton's rule (Barton, 1986). In addition, the intrinsic attenuations for P- and S-waves necessary for the viscoelastic model calculations are determined according to Brocher (2008).

For calculating wave propagation, the model was discretized with a 25 m cell spacing in both dimensions and the wave field was modelled at 1 ms time steps for 30 s, which ensured the stability of the FD code. A Ricker wavelet with a centre frequency of 5 Hz was used as source signal. This is slightly lower than the main frequency of the filtered real data, but was used to avoid numerical dispersion effects and to optimize the computing time.

To avoid artificial phases from the model boundaries, a free surface for the top edge of the model was introduced and the model was continued beyond the side and bottom

boundaries using a convolutional perfectly matched layer with a damping zone of 250 m width. A 4th order finite difference operator was used.

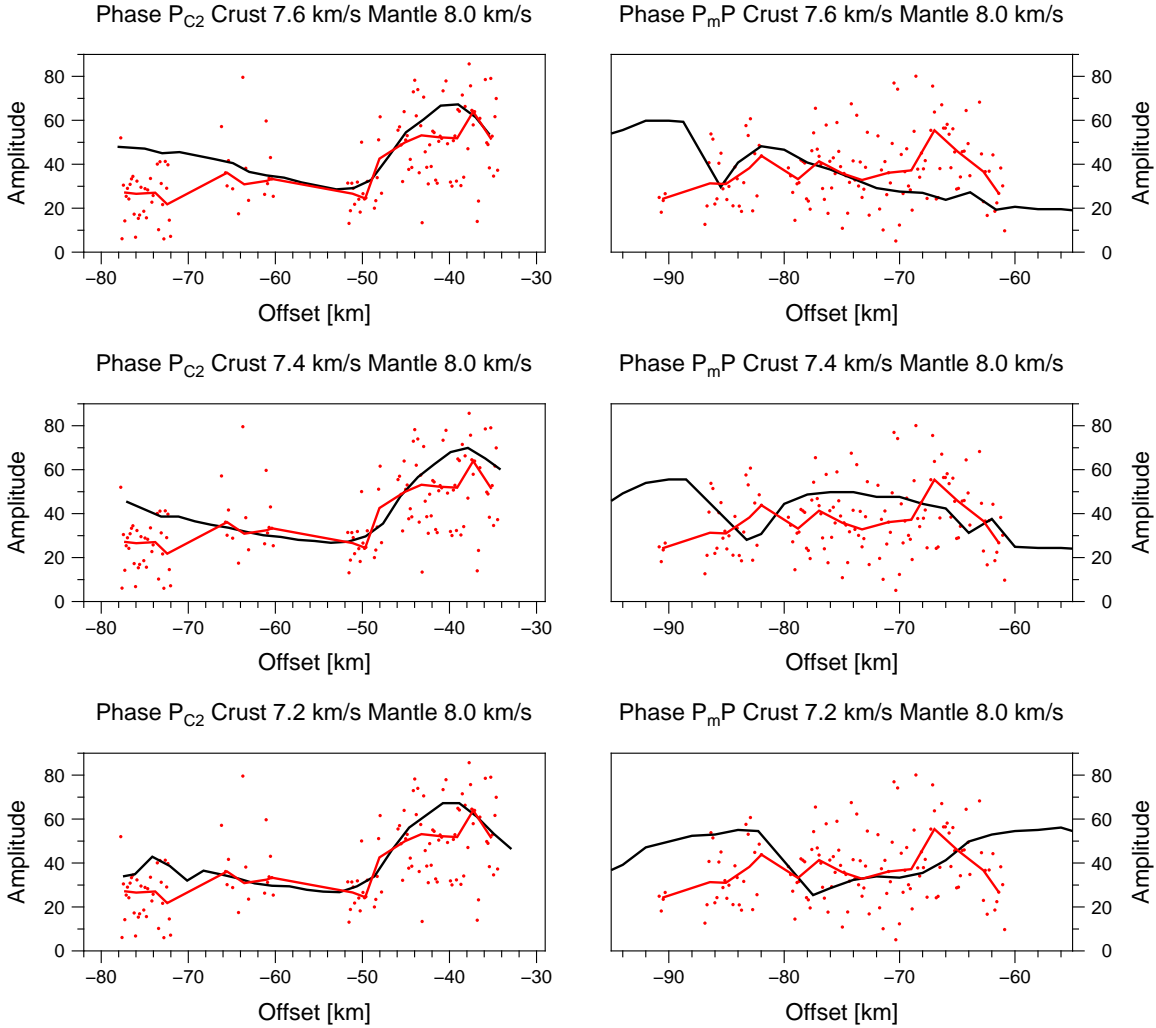


Figure 4.10.: Results of the FD-modelling for OBS 40 for three different velocity models. The left side shows the amplitude trend for the lower crustal phase P_{C2} and the right side for the mantle reflection P_{mP} . The red line represents the 2 km median for the real amplitudes (red dots). The black line shows the trend of the synthetic amplitudes.

The resulting synthetic seismograms are scaled and normalized to their maximum amplitude, so that they can be compared with the observed ones. This allows the possibility for quality control by checking that all picked phases are present in the synthetic seismogram, that no modelled phases appear that are not observed in the data, and that the moveouts of the observed and calculated P_{mP} phases resemble each other closely. Furthermore, the amplitude variations in the synthetic seismograms are compared to the original data. The main focus in this step is the lower crustal velocity, which is

not covered by refracted phases. By varying the crustal velocity gradient, the synthetic amplitudes of P_{C2} and P_{mP} vary, allowing different velocity models for the lower crust to be tested and the corresponding amplitude trends compared.

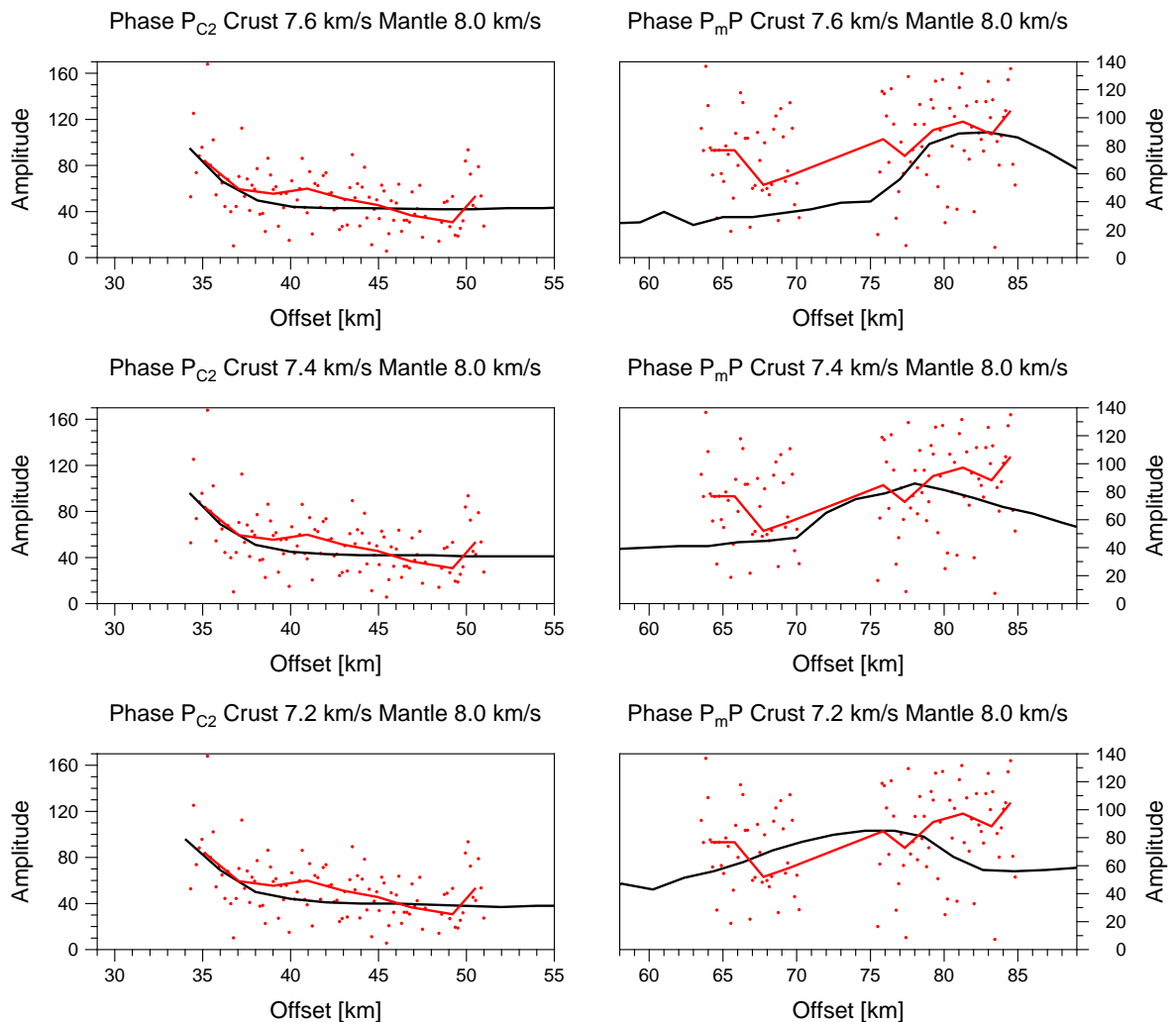


Figure 4.11.: Results of the FD-modelling for OBS 48 for three different velocity models. The left side shows the amplitude trend for the lower crustal phase P_{C2} and the right side for the mantle reflection P_{mP} . The red line represents the 2 km median for the real amplitudes (red dots). The black line shows the trend of the synthetic amplitudes.

Figures 4.7c and 4.8c show the synthetic seismograms for the final model of OBS 40 and 48. Synthetic seismograms are calculated for models in which all velocities and depths were kept constant except for the lower crustal velocity and Moho depth. Velocities of 7.2 km/s, 7.4 km/s and 7.6 km/s were tested directly above the Moho, whose depth in turn was adjusted such that the tested model explained the arrivals. For two specific phases, the corresponding amplitude maxima were picked within a 25 ms window in the synthetic data and a 40 ms window in the observed data. The difference in window

lengths is reasonable because the signal of the synthetic data is only an approximation to the observed one, owing to differences in the source of the signal (5 Hz Ricker-wavelet compared to the real signal of used airguns). Figures 4.10 and 4.11 display the amplitudes versus offsets for the lower crustal P_{C2} and P_{mP} .

For OBS 40 in Figure 4.10, it is visible that the real amplitudes scatter strongly. Nevertheless a clear trend can be seen in the curves of all three velocity models for P_{C2} between profile km -50 and -30. Since the main focus of this modelling is the velocity structure of the lower crust it is sufficient to take only offsets from -50 km into account. Here, the problem is that the real amplitudes show strong scattering, because of natural noise influence, while the synthetic amplitudes are noise-free. The real P_{mP} amplitudes are also affected by excessive scatter, making comparison with the synthetic seismograms difficult. The situation is similar for OBS 48 (Figure 4.11). The synthetic and real amplitude curves show similar trends for P_{C2} at proximal offsets. There are no meaningful differences in the medians of the different models for the furthest offset at which P_{C2} could be picked reliably. For P_{mP} , again, amplitudes in the real data vary too much to see a clear trend. Unfortunately these problems, of strong scattering in real amplitudes for the P_{mP} and low P_{C2} at long offsets, are observed at all stations, making it impossible to use the amplitude trends to verify the models.

Despite this, synthetic seismograms generated with the final velocity model agree well with the observed seismograms. Figure 4.12 illustrates this using results from OBS 48 and for all three modelled lower crustal velocities. The different lower crustal velocities in P_{C2} can only be observed at far offsets, where no real picks exist. Hence, P_{mP} move-out must be used to constrain the velocity above the Moho, with the best reproduction of the observed moveout at most stations obtained using the lower crustal velocity of 7.4 km/s.

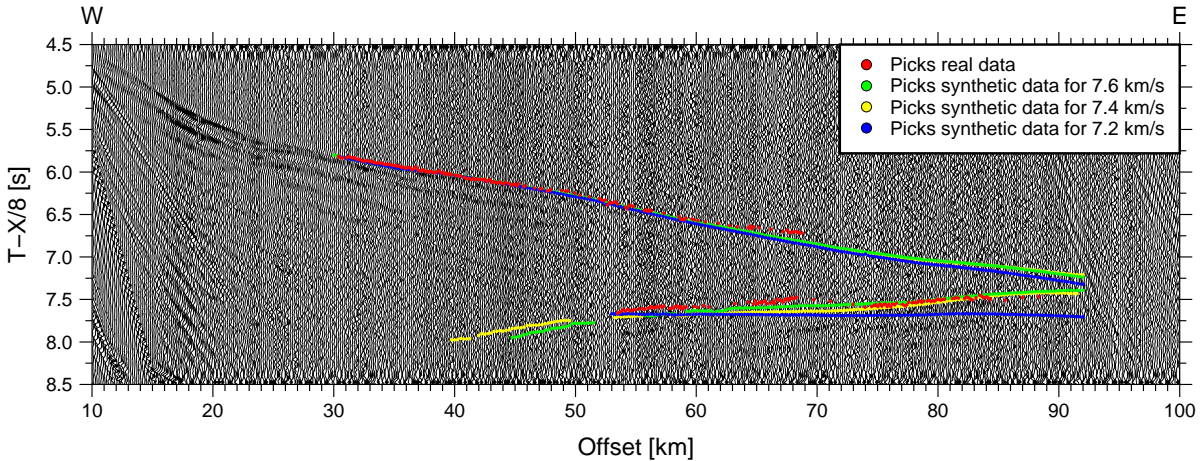


Figure 4.12.: Seismogram of OBS 48 with real picks (red) and the picks from the three different synthetic seismograms, which were also used for the amplitude trend in Figure 4.11.

4.5.2. Gravity modelling

2.5D density modelling was performed to ensure that the model obtained from ray tracing is consistent with the observed free-air gravity anomaly from the Sandwell et al. (2014) grid. Modelling was completed using the *IGMAS+* software package (Götze, 1978; Schmidt and Götze, 1998). *IGMAS+* calculates the gravimetric effect of a series of parallel vertical cross sections, which got connected by triangulation. For the resulting polyhedrons the gravitational response is computed.

The geometry and the layer boundaries were constrained by the velocity model. To avoid edge effects, the modelled bodies at the eastern and western boundaries were laterally prolonged for 100 km. 10 km north and south to the profile, slices with the same density configuration than our profile were used for modelling in *IGMAS+*.

In the Falkland Plateau Basin, sediment densities were estimated using the relationship of Gardner et al. (1985). Initial crustal densities were based on Christensen and Mooney (1995). Brocher (2008) provides an overview of the applied velocity – density relationships. Layers were subdivided depending on lateral velocity changes. During the modelling process, densities were iteratively adapted until the calculated free-air gravity anomaly fitted to the observed one within a 5 mGal uncertainty range. The densities of the final model are shown in Table 4.2.

4.5.3. Error analyses

The root mean square (RMS) travel time residuals depend on the misfit between calculated and observed arrival times. Together with the normalized χ^2 , these values are estimates of the velocity model's resolution. The normalized χ^2 is defined as the RMS misfit normalized to the picking uncertainty. The uncertainty for each pick depends on the corresponding signal to noise ratio and is calculated by *ZP*. The software compares the ratio of energy within a time window of 200 ms after and before the pick. Depending on the energy uncertainty values between 20 ms and 125 ms are assigned. For each phase the assigned average pick uncertainty, the RMS misfit and the normalized χ^2 are shown in Table 4.1. For the final model, based on 32922 data points, the overall RMS travel time residual is 86 ms and the normalized χ^2 is 1.303, which is close to the optimal value of one.

The RMS travel time residuals in the sediment layers range between 29 ms and 66 ms and χ^2 estimates vary between 0.211 and 0.863. The upper and lower crustal refractions have χ^2 values of 2.107 and 1.165 and RMS misfits of 99 ms and 90 ms. For P_{mP} , χ^2 is 1.304 and RMS 100 ms. The P_n is recorded by three stations underneath the Falkland Plateau Basin. Here, the χ^2 is 0.139 and the RMS misfit 35 ms. Large overall RMS misfits of 241 ms result from the P_n , that is recorded by the land stations. Here, high RMS values result from the complex topography of the Moho at the transition towards the Falkland Plateau Basin.

The ray coverage for the entire profile is shown in Figure 4.13. As mentioned before, only reflected phases are observed for the upper two layers. The deeper sediment layer velocities are defined by both reflected and refracted phases. For sediment layers *Sed4*,

Sed6 and *Sed8*, the penetration of refracted rays is comparably small. Here, reflections at the lower layer boundaries and patterns of body geometry observed on the nearby seismic reflection profile (Ludwig et al., 1978) provide further constraints. The upper crustal layer *C1* is very well covered by refracted rays (P_{C1}). Below this, refracted rays penetrate only into the upper half of the deeper crustal body *C2*. The topography of the Moho is well constrained by reflected phases (P_mP); as we have seen this is the reason why P_mP moveout was suitable for calculating the interval velocity in the lower crustal portion. A constant velocity gradient is assumed for *C2* because it has no internal reflections.

Table 4.1.: Statistics of the picked phases. The columns contain the nomenclature of the picked phases, the number of observations of each phase (No of picks), the assigned average pick uncertainty (t_{unc}), the root mean square of the travel time residual (t_{rms}) and the normalized χ^2 .

| Layer | Phase | No of Picks | t_{unc} [ms] | t_{rms} [ms] | χ^2 |
|-----------------------------------|--------------|-------------|----------------|----------------|----------|
| Waterwave | $P_{Water}P$ | 1814 | 46 | 59 | 2.209 |
| Reflection at base of <i>Sed1</i> | $P_{Sed1}P$ | 437 | 125 | 64 | 0.266 |
| Reflection at base of <i>Sed2</i> | $P_{Sed2}P$ | 661 | 122 | 58 | 0.279 |
| Refraction in <i>Sed3</i> | P_{Sed3} | 698 | 82 | 60 | 0.839 |
| Reflection at base of <i>Sed3</i> | $P_{Sed3}P$ | 1271 | 115 | 63 | 0.812 |
| Refraction in <i>Sed4</i> | P_{Sed4} | 503 | 75 | 48 | 0.602 |
| Reflection at base of <i>Sed4</i> | $P_{Sed4}P$ | 1104 | 113 | 39 | 0.211 |
| Refraction in <i>Sed5</i> | P_{Sed5} | 1085 | 74 | 44 | 0.537 |
| Reflection at base of <i>Sed5</i> | $P_{Sed5}P$ | 1427 | 104 | 62 | 0.596 |
| Refraction in <i>Sed6</i> | P_{Sed6} | 990 | 64 | 43 | 0.844 |
| Reflection at base of <i>Sed6</i> | $P_{Sed6}P$ | 1151 | 108 | 63 | 0.655 |
| Refraction in <i>Sed7</i> | P_{Sed7} | 393 | 62 | 29 | 0.571 |
| Reflection at base of <i>Sed7</i> | $P_{Sed7}P$ | 386 | 115 | 53 | 0.357 |
| Refraction in <i>Sed8</i> | P_{Sed8} | 1828 | 74 | 52 | 0.863 |
| Reflection at base of <i>Sed8</i> | $P_{Sed8}P$ | 731 | 100 | 66 | 0.528 |
| Refraction in <i>C1</i> | P_{C1} | 5074 | 89 | 99 | 2.107 |
| Reflection at base of <i>C1</i> | $P_{C1}P$ | 243 | 110 | 134 | 1.771 |
| Refraction in <i>C2</i> | P_{C2} | 6921 | 106 | 90 | 1.165 |
| Reflection at the Moho | P_mP | 5450 | 111 | 100 | 1.304 |
| Refraction in mantle | P_n | 755 | 97 | 241 | 8.138 |
| All layers | all | 32922 | 96 | 86 | 1.303 |

In general, the misfit between the calculated and observed free-air gravity anomalies is smaller than 5 mGal. The RMS misfit is 4.6 mGal and the standard deviation is 2.9 mGal. The maximum misfit of around 10 mGal is found near the transition between the Falkland Plateau Basin and the Falkland Islands (circa at profile km 130). A smaller misfit occurs eastwards of profile km 650, where the calculated anomaly is smaller than the observed one. We have not attempted to adjust the model east of 650 km under the

assumption that the misfit is related to the presence of a strong negative anomaly out of plane to the south (compare Figure 4.1b).

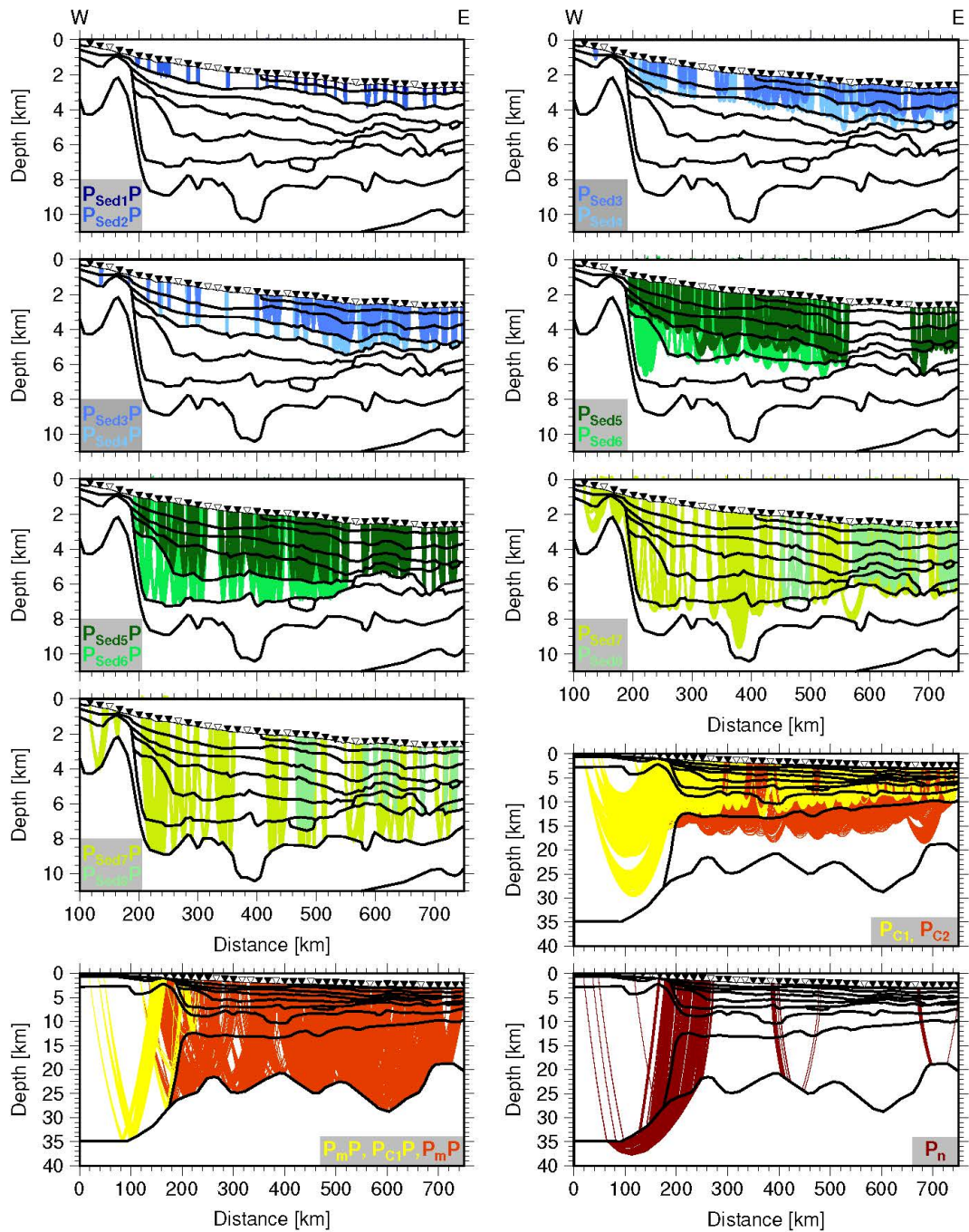


Figure 4.13.: Ray coverages for the reflected phases (left side) and the refracted phases (right side). Station positions are marked as triangles (white filling indicate stations without data output). Black lines mark velocity layer boundaries.

4.6. Results

4.6.1. Velocity model

The final velocity model for the Falkland Islands and the western Falkland Plateau Basin is displayed in Figure 4.14. Beneath its sediment layers, the seismic model shows velocity and thickness variations that allow the interpretation of the crust into three divisions: continental crust of the East Falkland Island and shelf area, a continent-ocean transition zone and igneous crust beneath the Falkland Plateau Basin.

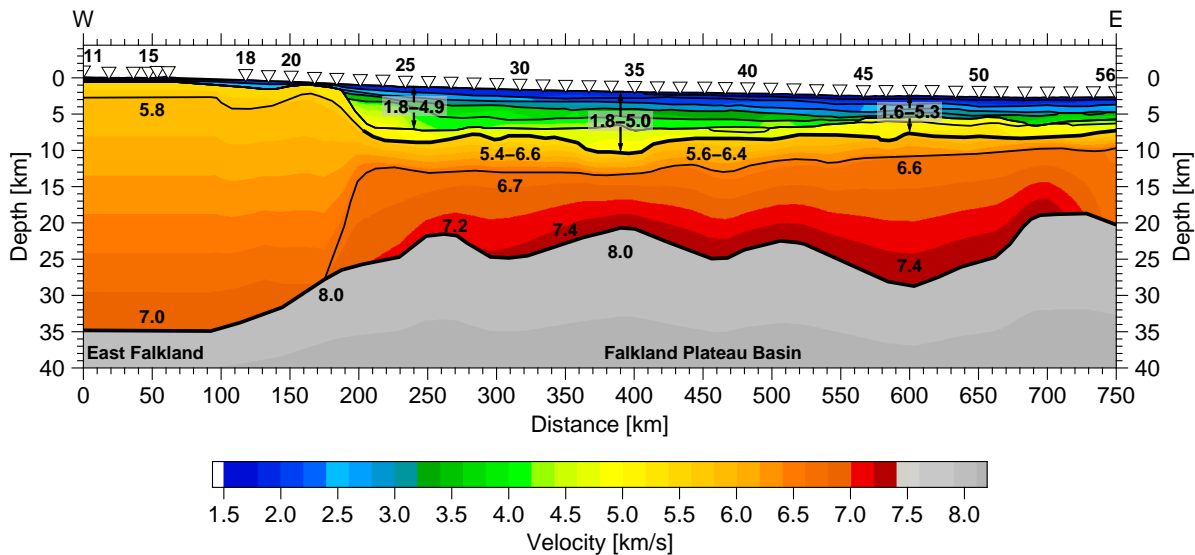


Figure 4.14.: P-wave velocity model of AWI-20130010. The numbers indicate P-wave velocities in km/s. Station positions are plotted as triangles. Black lines mark the layer boundaries between velocity layers. Thick black lines indicate the basement and the Moho.

Sediments on the shelf and in the Falkland Plateau Basin

The velocity-depth structure of the sediments is an important component of the model, but in this study we will only provide a more general description. More detailed information of the sediment velocities and their interpretation will be given in another publication.

On the shelf, the maximum sediment thickness is 1 km. Two sediment layers can be identified. The upper layer is modelled with a velocity of 2.0 km/s and a maximum thickness of 0.4 km. The velocity value is estimated because the layer is not covered by refracted or reflected phases. The lower unit is at maximum 0.6 km thick and is modelled with a vertical velocity gradient from 2.4 km/s to 2.6 km/s. Between OBS 20 and 21 (km 150 – 190) the basement shallows to 1 km depth and forms a platform. Both sediment layers thin onto the platform.

In the Falkland Plateau Basin, eight sediment layers are introduced in our seismic velocity model and their nomenclature is given in Figure 4.15b. The average sediment thick-

ness in the basin is about 6.5 km with a maximum thickness of 8.5 km (km 370 – 405). Sediment velocities range from 1.6 km/s in the uppermost layer (*Sed1*) to 5.0 km/s above basement (*Sed8*). An exception is the part between km 560 and 685. Here, velocities of the lower two layers (*Sed7*, *Sed8*) are higher than elsewhere in the same depth reaching a maximum of 5.3 km/s. The velocities for each layer are provided in Table 4.2.

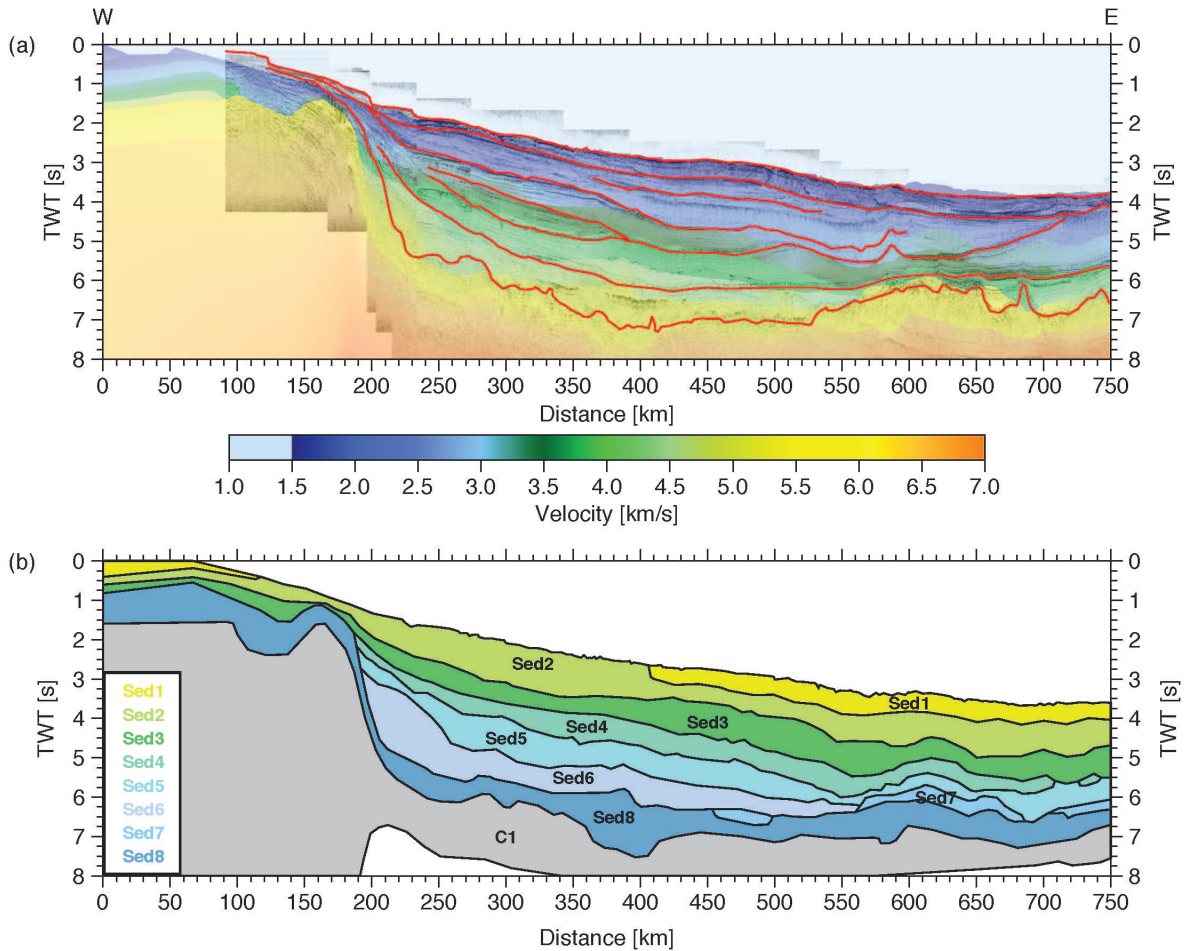


Figure 4.15.: (a) Seismic reflection line 139 (Ludwig et al., 1978) with basement and major unconformities (red lines, Lorenzo and Mutter, 1988) combined with the P-wave velocity model in two-way travel time (TWT). (b) Nomenclature of the sediment layers above the crustal layers *C1* in TWT.

East Falkland continental margin (km 0 – 180)

Basement lies 0.6 km beneath the East Falkland shelf and deepens eastwards to 1.5 km below OBS 19. An intra-crustal reflection is visible beneath East Falkland at depths varying between 2 and 4 km, marking the lower boundary of the upper crustal layer. The velocity of this 1.3 to 2.8 km thick layer ranges from 5.5 to 5.8 km/s. The underlying layer of up to 32 km thickness forms the main part of the crust, and is devoid of internal reflections. It has a comparably low velocity gradient (0.04 s^{-1}) from 5.8 km/s at its

top to 7.0 km/s at the Moho. The Moho lies at 35 km depth beneath East Falkland. Seawards, it shallows to 27 km (km 180).

Table 4.2.: Layer type and the according velocity and density range.

| Layer | Type | Location | P-wave velocity [km/s] | Density range [g/cm ³] |
|--------|-----------------|--------------------|---------------------------|---------------------------------------|
| Sed1 | Sediment | Island and shelf | 1.6–1.8 | 1.95 |
| | Sediment | Basin | 1.6–1.6 | 1.95 |
| Sed2 | Sediment | Island and shelf | 1.8–2.1 | 2.05 |
| | Sediment | Basin | 1.7–2.1 | 2.05 |
| Sed3 | Sediment | Island and shelf | 2.2–2.6 | 2.20 |
| | Sediment | Basin | 2.1–2.9 | 2.20 |
| Sed4 | Sediment | Basin | 2.6–3.3 | 2.30 |
| Sed5 | Sediment | Basin | 3.4–3.9 | 2.20–2.54 |
| Sed6 | Sediment | Basin (km 200–260) | 4.1–4.9 | 2.45 |
| | Sediment | Basin (km 260–750) | 4.0–4.3 | 2.48 |
| Sed7 | Sediment | Basin | 4.5–4.6 | 2.55 |
| | Magm. intrusion | Basin (km 560–680) | 4.5–5.0 | 2.65 |
| Sed8 | Cont. crust | Island and shelf | 5.5–5.7 | 2.58–2.65 |
| | Sediment | Basin | 4.6–5.0 | 2.70 |
| C1 | Cont. crust | Island and shelf | 5.8–7.0 | 2.60 |
| | Trans. crust | km 180–270 | 5.3–6.6 | 2.75–2.80 |
| | Oceanic crust | km 270–750 | 5.4–6.6 | 2.93 |
| C2 | Trans. crust | km 180–270 | 6.6–7.2 | 2.85–2.90 |
| | Oceanic crust | km 270–750 | 6.6–7.4 | 3.05 |
| Mantle | Mantle | Entire profile | 8.0–8.2 | 3.40 |

Continent-ocean transition (km 180 – 270)

The shelf break off East Falkland is situated between km 187 and 211. Basement ($V_p > 5.3$ km/s) deepens in this area from 1.7 km to 8.1 km, with an average dip of about 11° .

From km 180 eastwards, the crust-mantle boundary gradually shallows, and the velocity structure changes from one thick layer to a two-layered velocity structure. Within the COT, the the upper crustal layer *C1* is ~ 4 km thick and shows a vertical velocity gradient of 0.2 s^{-1} for velocities ranging from 5.7 km/s to 6.5 km/s. The lower crustal layer *C2* is 15.6 km thick and its velocities range from 6.6 km/s at its top to 7.0 km/s at its base near km 200, and 7.2 km/s at its base near km 270. Here, layer *C2* is just 8.6 km thick. At km 270, the total crustal thickness is 13 km. In the COT, intra-crustal reflections can be observed at the layer boundary between *C1* and *C2*. The Moho rises from 27 km depth at km 180 to 22 km at km 270.

Falkland Plateau Basin (km 270 – 750)

The basement of the Falkland Plateau Basin lies at about 8 km depth. Between km 360 and 410 the basement topography reaches a maximum depth of 10.4 km in a 50 km wide depression. The crystalline crust consists of two layers defined by contrasting velocity gradients rather than any sharp or reflective velocity contrast, typical for oceanic crust. The upper crustal layer *C1* (oceanic layer 2) varies in thickness between 1.3 km and 4.2 km and its velocity gradient is relatively steep between upper velocities of 5.6 km/s and lower velocities of 6.5 km/s. In the lower crust, *C2*, the gradient is lower and starts with velocities around 6.6 km/s. The velocity at the base of *C2* above the Moho varies, increasing from 7.2 km/s in the west (km 270) to 7.4 km/s east of km 300. *C2* (oceanic layer 3) is between 7 km and 17 km thick. The total crustal thickness ranges between 11 km (km 700) and 20 km (km 600). The Moho lies at a minimum depth of 19 km near the eastern end of the profile and a maximum depth of almost 29 km at km 600. The mantle velocity is modelled with 8.0 km/s.

4.6.2. Density model

Figure 4.16 shows the final 2D density model in (b) and its corresponding calculated free-air gravity anomaly along with the observed free-air gravity anomaly from the Sandwell et al. (2014) grid in (a).

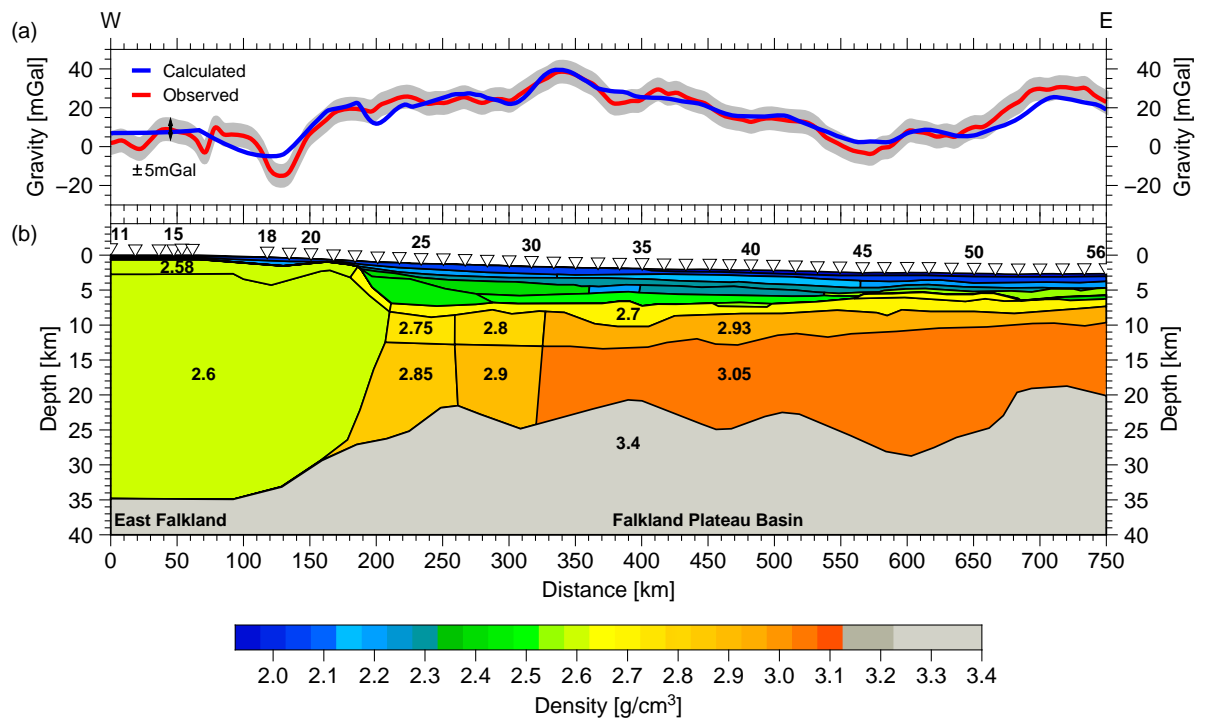


Figure 4.16.: (a) Observed free-air gravity anomaly from the Sandwell et al. (2014) grid and free-air gravity anomaly calculated with *IGMAS+*. (b) Density model along AWI-20130010. The numbers indicate the density of bodies in g/cm³.

The free-air gravity anomaly varies between -15 mGal at the transition between East Falkland and the Falkland Plateau Basin and 38 mGal around km 350. In general, the free-air gravity anomaly has lower values above the Falkland Islands and increases towards the Falkland Plateau Basin.

During the modelling process, nearly all of the layer boundaries from the velocity model were kept constant. Layer densities were adjusted and some layers subdivided vertically to reproduce the density equivalents to velocity gradients within them. The seismic-derived layers were used for density modelling. Around km 180 between 13 and 27 km depth, the boundary between *C1* and *C2* forms the limit between the continental crust of East Falkland and the transitional crust further eastwards. Here, the boundary is not constrained by reflected phases and was estimated by gravity modelling.

Sediment densities in the Falkland Plateau Basin range from 1.95 g/cm³ in the uppermost layer to 2.7 g/cm³ in the layer immediately overlying the basement. The crust below East Falkland has a mean density of 2.6 g/cm³. The Falkland Plateau Basin is underlain by much denser crust. The transition between the two crustal domains is modelled with two additional bodies between km 180 and 330. The free-air gravity anomaly rises from -15 mGal (km 130) to 25 mGal (km 216, Figure 4.16a), which is reflected in the density model by a density contrast of 2.6 g/cm³ to 2.75 g/cm³ in the upper crustal layer and 2.85 g/cm³ in the lower crustal layer (Figure 4.16b).

At km 270, the crustal density in the model changes from 2.75 g/cm³ to 2.8 g/cm³ in the upper layer and 2.85 g/cm³ to 2.9 g/cm³ in the lower one. From km 330 eastwards, the density in the upper crustal layer (*C1*) is 2.93 g/cm³ and in the lower crustal layer (*C2*) it is 3.05 g/cm³. Modelling resulted in a comparably high density of 3.4 g/cm³ for the mantle.

4.7. Interpretation

4.7.1. Sediments on the shelf and in the Falkland Plateau Basin

To compare the velocity model with the nearby seismic reflection line 139 (Ludwig et al., 1978), the depths in the velocity model is converted into two-way traveltime (TWT) and plotted together with the seismic reflection data. Towards the islands, the increasing separation (35 km) of the two profiles is evident from bathymetric differences. In the Falkland Plateau Basin, most of the modelled velocity discontinuities correlate well with distinct, mostly flat-lying reflectors. Larger differences between the two profiles occur, however, between km 560 and 685. Here, the seismic reflection data image what appears to be very rough basement at about 6 s TWT. In contrast, the wide-angle velocity model shows a clear velocity jump, consistent with the presence of acoustic basement, at greater delays of about 8 s TWT. The intervening fast velocities of 4.5 to 5.3 km/s together with high densities of 2.65 g/cm³ indicate the presence of volcanic intrusions into the oldest sediment unit. In general, the high density of 2.7 g/cm³ in the layer immediately overlying the basement can be interpreted to represent sediments, which are highly compacted or in the early stages of burial metamorphosis.

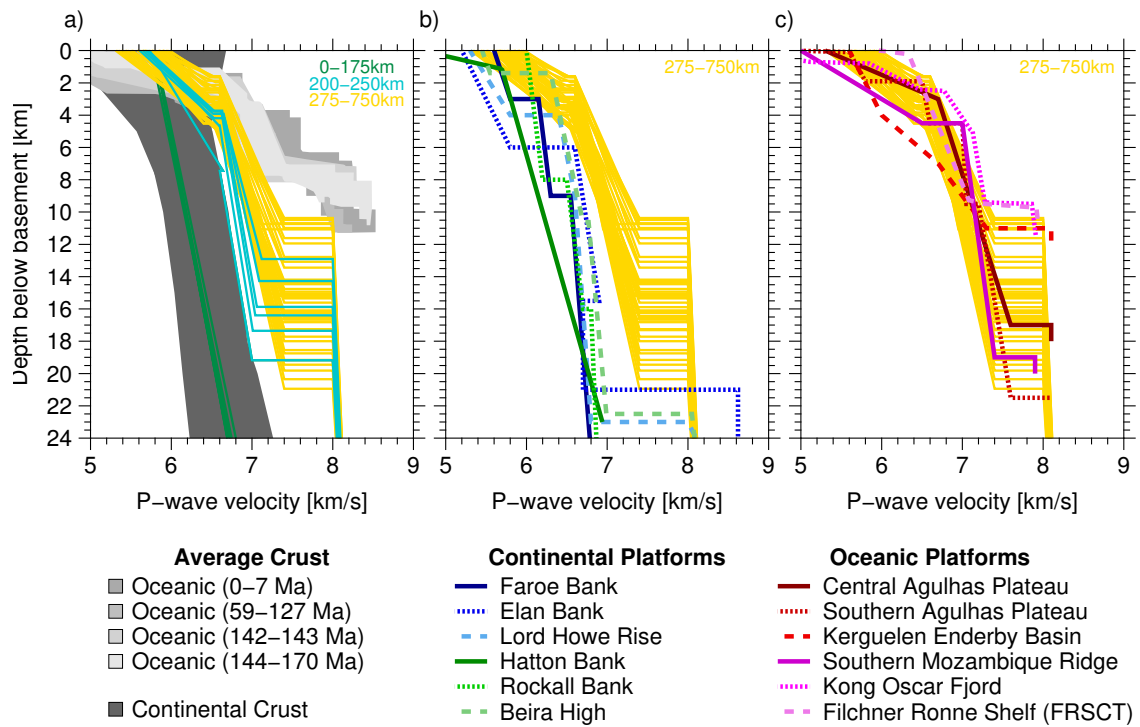


Figure 4.17.: Velocity-depth functions for the crust along AWI-20130010 compared with (a) normal oceanic (White et al., 1992) and continental crust (Christensen and Mooney, 1995), (b) continental crust of the Faroe Bank (Funck et al., 2008), Elan Bank (Borissova et al., 2003), Lord Howe Rise (Klingelhoefer et al., 2007), Hatton Bank (White and Smith, 2009), Rockall Bank (Vogt et al., 1998) and Beira High (Mueller et al., 2016) and (c) Large Igneous Provinces/thickened oceanic crust of the Central Agulhas Plateau (Parsieglä et al., 2008), Southern Agulhas Plateau (Gohl and Uenzelmann-Neben, 2001), Kerguelen Enderby Basin (Charvis and Operto, 1999), Southern Mozambique Ridge (Gohl et al., 2011), Kong Oscar Fjord (Hermann and Jokat, 2016) and Filchner Ronne Shelf (FRSCT) (Jokat and Herter, 2016).

4.7.2. East Falkland continental margin (km 0 – 180)

In Figure 4.17, 1D crustal velocity profiles extracted every 10 km from our deep seismic line are plotted together with velocity functions from other settings and regions. Figure 4.17a shows that the velocity distribution beneath East Falkland is typical for continental crust. The mean density of 2.6 g/cm^3 is comparably low. On West Falkland, density measurements for the Gneisses of the Cape Meredith Complex yielded in a similar density with 2.56 g/cm^3 (Martin et al., 1982). A low density is also observed for Precambrian crust elsewhere (e.g. 2.67 g/cm^3 for the Namaqua-Natal Belt/South Africa, De Beer and Meyer (1984)).

4.7.3. Continent-ocean transition (km 180 – 270)

The COT begins at km 180. The crust here is thinner than beneath East Falkland, and its velocity structure changes from one thick layer of clearly continental composition to a two-layered velocity structure. Reflections at the base of *C1* (Figure 4.13) and lower velocities and densities compared to the igneous section further eastwards show that the crustal composition can be interpreted as transitional. While the beginning of the COT is related to a major change from a thick layer to two crustal layers, the seaward onset of oceanic crust remains poorly defined, since clear seafloor spreading anomalies could not be identified in the available data. The lower crustal velocity increases to more than 7.2 km/s from km 270 eastwards. Here, no reflections exist between upper and lower crustal layer. At km 270, the crustal density changes from 2.75 g/cm³ to 2.8 g/cm³ in the upper layer and 2.85 g/cm³ to 2.9 g/cm³ in the lower one. Thus, we tentatively interpreted the appearance of oldest oceanic crust near km 270 with a total COT width of 90 km.

4.7.4. Falkland Plateau Basin (km 270 – 750)

To make a decision if the Falkland Plateau is underlain by stretched continental or thick oceanic crust east of km 270, we compare velocity-depth distributions along the profile with those of known regions consisting of continental and oceanic crust elsewhere in the world. Figure 4.17a shows that the crustal thickness of 11 to 20 km beneath the Falkland Plateau Basin is significantly thicker than average oceanic crust (~ 7.1 km, White et al., 1992) and faster than average continental crust. Figure 4.17b displays 1D velocity profiles from continental fragments and Figure 4.17c from regions of unusually thick igneous crust.

The comparisons show that, in general, continental platforms exhibit slower crustal velocities (not exceeding 7.0 km/s) than those encountered beneath the Falkland Plateau Basin. Their velocity gradients are also lower ($0.01 - 0.07 \text{ s}^{-1}$) than observed ($0.05 \text{ s}^{-1} - 0.2 \text{ s}^{-1}$). Oceanic platforms consist of massive emplacements of extrusive and intrusive rocks. In contrast to continental crust, they exhibit faster velocities and higher velocity gradients and often reveal a velocity distribution similar to that in oceanic crust. It is evident that the crustal thickness and velocity distribution beneath the Falkland Plateau Basin more closely resemble those of oceanic platforms. Thus, we interpret the crust of the investigated Falkland Plateau Basin to be igneous and that it represents thickened oceanic crust.

Although the crust beneath the Falkland Plateau Basin is significantly thicker (11 – 20 km) than standard oceanic crust, it exhibits a similar velocity distribution. Our profile reveals the basin to be underlain by a 1.3 km to 4.2 km thick oceanic layer 2 with a steep velocity gradient ($\sim 0.2 \text{ s}^{-1}$) and a 7 to 17 km thick oceanic layer 3 with a more modest gradient (between 0.05 s^{-1} and 0.1 s^{-1}). In average oceanic crust layer 3 forms two-thirds of the crustal thickness. As the thicknesses of both crustal layers vary strongly underneath the Falkland Plateau Basin, their relative proportions vary. The deeper layer accounts for 60% of the Falkland Plateau's crustal thickness between km

250 and 500, and up to 85% of it at km 600.

The high densities beneath the Falkland Plateau Basin are another indication that it consists of oceanic crust. The mean crustal density of $\sim 3.02 \text{ g/cm}^3$ is greater than the global average for oceanic crust ($2.89 \pm 0.04 \text{ g/cm}^3$ according to Carlson and Raskin (1984)), as already indicated by the faster than normal crustal velocities.

The geologic section that results from the interpretation of the velocity and density model is displayed in Figure 4.18.

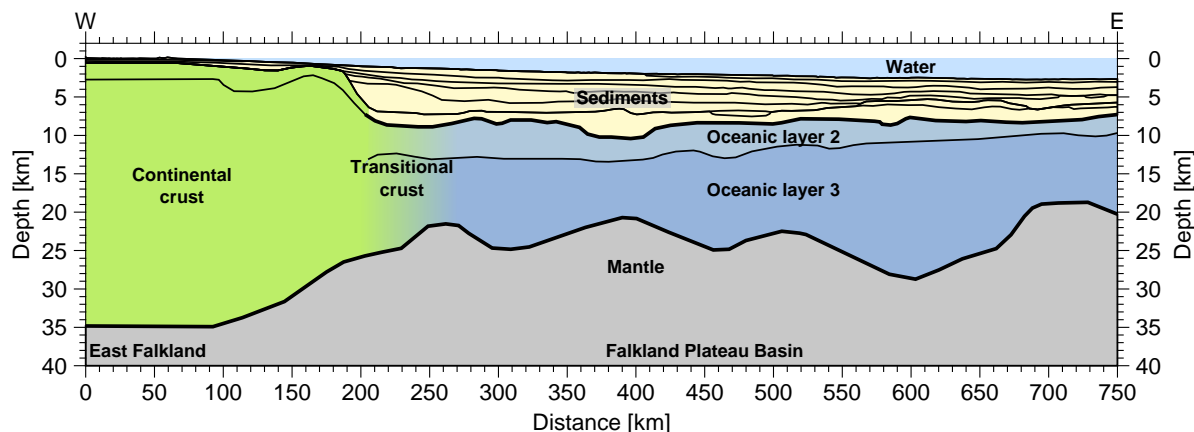


Figure 4.18.: Geological interpretation of the western transect.

4.8. Discussion

4.8.1. Structural classification of the Falkland Islands' eastern margin

To classify the eastern margin of the Falkland Islands into volcanic or non-volcanic, the presence of igneous features like seaward dipping reflectors sequences, intrusive complexes and high velocity lower crustal bodies has to be considered. Seaward dipping reflectors from the basalt package are visible in the nearby seismic reflection data of Ludwig et al. (1978) (Figure 4.4), stretching eastward from the shelf break (Barker, 1999), but cannot be spatially resolved in our wide-angle data. Barker (1999) estimated the tops of the flows to lie in $\sim 7 \text{ km}$ depth showing a velocity increase from 4.1 km/s to more than 4.3 km/s . Despite the large uncertainties in those data, our model shows corroborative velocities of around 4.4 km/s at the same depth. New high resolution seismic reflection data would be necessary to confirm the presence of such volcanic sequences. In addition to seaward dipping basalt flows, distinct high velocity ($> 7 \text{ km/s}$) lower crustal bodies in the COT are characteristic of volcanic margins. Velocities beneath the East Falkland COT do exceed 7.0 km/s , but are not confined to a distinct body within it. This might be related to the resolution of the method. Despite this, the evidence for breakup-related excess volcanism at the rifted margin of East Falkland is clearly

in favour of its classification as a volcanic extended margin. The thick oceanic crust together with the dykes onshore (Stone et al., 2009) and sills and intrusive complexes in the sediments offshore (Richards et al., 2013) provides indications that the plateau developed in an environment with an enhanced magma supply.

Seismic data at the Faroe and Hatton Bank reveal a COT that is intruded with sills and dykes, with velocity-depth functions that are intermediate between those for continental and oceanic crust (White et al., 2008). They concluded that the COT there formed as excess melt extensively intruded into the pre-existing stretched continental lithosphere. The COT at the Namibian margin (Bauer et al., 2000), in contrast, shows significantly higher crustal velocities (almost entirely exceeding 7.1 km/s) that they interpret in terms of an igneous crust within the COT. Our profile reveals a comparable situation to that at the Faroe-Hatton Bank margin, with crustal seismic velocities in the COT somewhere intermediate between those for continental and oceanic crust. We thus interpret the East Falkland COT to consist of extended, strongly intruded continental crust.

4.8.2. Is the Falkland area a marginal plateau?

Mercier de Lépinay et al. (2016) characterized the Falkland Plateau as a marginal plateau. If we compare the velocity structure of the Falkland Plateau with the Demara Plateau, which is also characterized as a marginal plateau, we observe some similarities. The crust of the Demara Plateau thins gradually oceanward from 34 km thickness to 22 km over 165 km and then more rapidly to 10.6 km over 67 km. While the gradual thinning is linked to a transform fault offset to the profile, the rapid thinning is linked to the transform fault (Greenroyd et al., 2008). The crustal thickness of 34 km is comparable to what we observe beneath East Falkland. Here, it thins over 125 km to 17 km thickness (between km 90 and 215). Although we have to say, that the profile, that covers the Demara Plateau, cuts the transform margin of the plateau and not the rifted margin, which is the case in our profile. The velocity distribution is similar to what we observe for East Falkland with a thick velocity layer and a maximum velocity of 7.0 km/s. Mercier de Lépinay et al. (2016) characterized the entire Falkland Plateau as a marginal plateau. This is based on studies of Ben-Avraham et al. (1993) and Lorenzo and Wessel (1997), who report that continental crust is present south of the Falkland Escarpment. As the central part of the Falkland Plateau Basin is composed of oceanic crust, we disagree to characterize the entire plateau as a marginal plateau.

4.8.3. Comparison with other continental margins nearby

Margins north of the Falkland Plateau

Becker et al. (2014, 2012) (green profiles in Figure 4.2) investigated the crustal structure of the COT along the north-south trending rifted margin offshore Argentina and the east-west trending transform margin of the Falkland-Agulhas Fracture Zone, which delimitates the Falkland Plateau in the north to the Argentine Basin. The transform margin segment does not exhibit magmatic features. Unusually thin oceanic crust (3 – 4 km) forms the oceanic Argentine Basin north of the Falkland Escarpment (Figure 4.1),

which indicates reduced magma supply. The rifted margin offshore Argentina was characterized as magma poor in the southern part as there are no indications for seaward dipping reflectors, although seismic refraction data revealed small high velocity lower crustal bodies (Becker et al., 2014, 2012).

The thin oceanic crust and amagmatic margin north of the Agulhas Falkland Fracture Zone contrasts with the thick oceanic crust of the Falkland Plateau Basin and its seaward dipping reflectors. This discrepancy shows that the oceanic crust north of the Falkland Plateau and the one underneath the Falkland Plateau Basin likely have developed in different environments and at different ages.

Southern margin of the Falkland Plateau

The southern conjugate margin of the Falkland Plateau is nowadays situated in the Weddell Sea (Figure 4.2), which was characterized by extensive Jurassic rifting and subsequent massive subaerial volcanism. The initial extension was oriented southwest-northeast likely as a reaction of subduction processes along the Pacific margin of Gondwana. Seafloor spreading started by 147 Ma perpendicular to the initial rifting direction (König and Jokat, 2006). From kinematic models (König and Jokat, 2006), it is obvious that both margins developed in a tectonically complex area and that the Weddell Rift and the Falkland Plateau Basin were probably affected by the same rifting event as a likely spreading ridge of the Falkland Plateau Basin is in the prolongation of the Weddell Sea rift (Figure 4.2, 167.2 Ma panel). Martin (2007) proposed that the entire area from the present-day Falkland Plateau to the southernmost parts of the Weddell Sea (Figure 4.2, EWM terrane) developed within a huge Paleozoic/Mesozoic rift system. We like to discuss if the new and existing geophysical data support his model or not.

Starting with the Weddell Sea a published velocity model (Jokat and Herter, 2016) for a southeast-northwest profile parallel to the Filchner-Ronne Ice Shelf between the Antarctic Peninsula and East Antarctica is shown in Figure 4.19. Velocity functions and generally flat magnetic anomalies indicate the presence of a 160 km wide corridor of oceanic or predominantly igneous crust.

The Antarctic Peninsula, at the western margin of this corridor, has a different velocity structure than the East Falkland rifted margin. The peninsula consists of two velocity layers with a strong velocity discontinuity from 6.0 km/s to 6.4 km/s in between, while our data set suggests that the East Falkland crust can be modelled as one thick layer only. The upper crustal velocity is significantly faster (6.6 km/s) beneath the Antarctic Peninsula than beneath East Falkland (5.5 km/s).

There are also strong contrasts between the margins east of the Antarctic Peninsula and east of the Falkland Islands. The crust of the Antarctic Peninsula thins gradually towards the southeast from 38 km thickness to 19 km thickness over 260 km, while the crust of East Falkland thins more rapidly from 34 km to 17 km over 125 km. Especially the depth of the basement increases from 1.6 km to 8 km and forms a steep slope east of East Falkland, which is not observed at the margin east of the Antarctic Peninsula. A high velocity body (Figure 4.19, up to 7.3 km/s) and maximum thickness of 7 km is evident close to the Antarctic Peninsula. We cannot observe such a distinct high velocity

lower crustal body in our data, but observe high lower crustal velocities throughout the entire Falkland Plateau Basin.

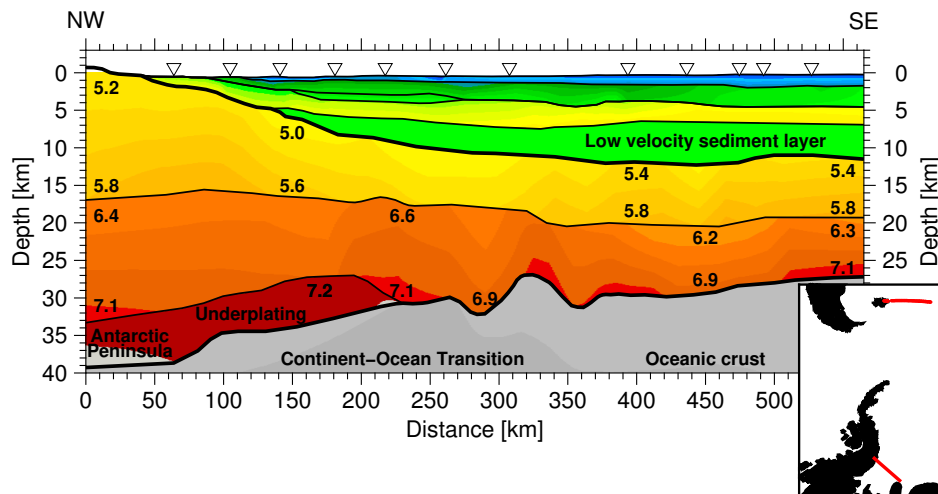


Figure 4.19.: P-wave velocity model of the FRSC (Jokat and Herter, 2016) plotted with the same color scale and in the same scale as the velocity model for AWI-20130010 (Figure 4.14). The numbers indicate crustal P-wave velocities in km/s.

While Barker (1999) reported seaward dipping basalt flows southeast of East Falkland, none are reported for the eastern side of the Antarctic Peninsula due to the absence of deep penetrating seismic reflection data and missing strong magnetic anomalies. Only at the East Antarctic margin of Jokat and Herter's corridor, the Explora Wedge (Figure 4.2, plot for 130 Ma) is likely to be related to seaward dipping basalt sequences (Hunter et al., 1996).

In Figure 4.17c, a velocity-depth function from the igneous part of the FRSC is plotted. In comparison with the crustal thickness beneath the Falkland Plateau Basin, the oceanic crust parallel to the Filchner-Ronne Ice Shelf is slightly thinner (9 km compared to a minimum of 11 km). Maximum velocities are higher underneath the Falkland Plateau Basin (7.4 km/s compared to 7.1 km/s) with a similar velocity gradient in the lower crust. Intra-crustal reflections are visible in the FRSC data.

The clear differences in crustal structure of the rifted margins along the FRSC and Falkland Islands indicate that both regions underwent a different rift history, e.g. the COT of the Antarctic Peninsula is by far wider than off East Falkland. On the other hand, the crustal thickness of the oceanic crust along both lines are very similar indicating that both spreading systems might have received extra melt material from a deep seated thermal anomaly resulting in thick oceanic crust. This is in good agreement with the geochemistry and age of the Jurassic dykes onshore the Falkland Islands (Mitchell et al., 1986). In any case our results do not contradict the model of Martin (2007). There are clear evidences from the two seismic transects that the entire area underwent strong extension.

4.8.4. Oceanic crust

The oceanic crust beneath the Falkland Plateau Basin is twice as thick as normal oceanic crust and the unusual crustal thickness needs to be explained. We favour a model that a deep seated thermal anomaly added additional material to the spreading system creating the observed thick oceanic crust independent from the spreading rates. A good example for such an influence is observed off the Kong Oscar Fjord, East Greenland. The existing deep seismic line has a similar velocity-depth distribution to the Falkland Plateau's with thicker (9 km) than average oceanic crust (Figure 4.17c, Hermann and Jokat (2016)). Velocities of more than 7.0 km/s with a thickness of 5 km are present in the lower crust (compared to up to 9 km beneath the Falkland Plateau Basin). Maximum velocities are high with 7.5 km/s (7.4 km/s Falkland). Density modelling resulted in the same densities for layer 2 (2.93 g/cm³) and layer 3 (3.05 g/cm³) in both locations. The surprising context for these findings along the Kong Oscar Fjord profile is that the basin formed at the ultra slow spreading Kolbeinsey Ridge (Mosar et al., 2002). Ultra-slow spreading would usually be expected to lead to the development of thin oceanic crust (e.g. 1.4 – 3.5 km at the Gakkel Ridge, Ehlers and Jokat, 2009; Hermann and Jokat, 2013; Jokat et al., 2003a; Jokat and Schmidt-Aursch, 2007) owing to the suppression of adiabatic decompression in the narrow and slowly-growing space between the diverging plates. The development of a thick oceanic crust with high lower crustal velocities in the Kolbeinsey Basin can be attributed to the influence of the Icelandic mantle thermal anomaly (Mjelde et al., 2008), which might have added material for extra 5 – 7 km of oceanic crust.

For the Falkland Plateau Basin the spreading velocity is unknown. There is little doubt that its oceanic crust received also additional melt supply during its formation. Thus, if a standard original crustal thickness of 7 km is assumed at maximum 13 km of extra oceanic crust was added due to the presence of the thermal anomaly.

The margin and basin evolved during Jurassic/Cretaceous times in a broad region affected by anomalous hot mantle that promoted regional excess melt production and the formation of continental (Karoo, Ferrar), oceanic (Mozambique Ridge, Agulhas Plateau, NE Georgia Rise, Maud Rise) and marginal (Explora margin, Astrid Ridge) volcanic-intrusive complexes. During seafloor spreading of the Falkland Plateau Basin the presence of this hotspot provided similar to the present day Iceland hotspot in the North Atlantic additional melt to produce the up to 20 km thick oceanic crust. Like in other regions, this is characterized by a thick oceanic layer 3 (up to 17 km) and lower crustal velocities higher than 7.0 km/s. In this context, the high density of the mantle might indicate an enrichment of pyroxenite in the mantle material. As shown by Shorttle et al. (2014) a higher proportion of pyroxenite compared to lherzolite and harzburgite results in a higher density.

4.9. Conclusions

We present a deep crustal profile from the Falkland Islands into the western Falkland Plateau. The data indicate that thick oceanic crust is present below the Falkland Plateau Basin bounded in the west by a volcanic rifted margin. Close to the eastern Falkland Island margin the continental crust is 34 km thick and has velocities ranging from 5.5 km/s to 7.0 km/s. The COT has a width of 90 km. The sediments in the Falkland Plateau Basin have an average total thickness of 6.5 km with velocities ranging from 1.7 km/s in the uppermost layer to ~ 4.7 km/s above basement. The Falkland Plateau Basin is floored, in contrast to previous models, by thick oceanic crust. Its crustal thickness ranges between 11 and 20 km, with maximum lower crustal velocities of up to 7.4 km/s for oceanic layer 3. The Moho depth varies between 19 km and 29 km. We speculate that the thick Jurassic oceanic crust and the high lower crustal velocities are consequences of a regional thermal mantle anomaly, which influenced the spreading system by providing excessive melt material. Finally, these results are important constraints for any future kinematic and geodynamic models for the early dispersal of Gondwana. Furthermore, it provides compelling geophysical evidences for the existence of one or more massive deep seated thermal mantle anomalies as proposed from onshore geology controlling the rift magmatism.

Acknowledgements

We thank Captain Stefan Schwarze and his crew of *RV Polarstern* for their excellent support during expedition ANT-XXIX/5 with its difficult weather conditions. We gratefully acknowledge Graeme Eagles for his effort to enhance the manuscript. Christian Olaf Mueller is thanked for his support during data processing. We also thank Frauke Klingelhofer and one anonymous reviewer for their helpful comments that improved this article.

5. The Falkland Plateau in the context of Gondwana breakup

Claudia Monika Schimschal^a, Wilfried Jokat^{a,b}

^a Alfred Wegener Institute Helmholtz Centre for Polar and Marine Research

^b University of Bremen

5.1. Abstract

During the Jurassic, the Falkland Plateau was part of Gondwana and occupied a position between the African and Antarctic plates. Several contrasting models exist for the breakup of Gondwana that depend on assumptions about the currently unknown crustal structure of the Falkland Plateau. Here, we present the results of recently acquired wide-angle seismic data along the entire plateau that provide sound constraints on its role in geodynamic reconstructions. In contrast to published crustal models, the new data show that the Falkland Plateau Basin consists of up to 20 km thick oceanic crust, which is bounded to the east by a continental fragment, the Maurice Ewing Bank. In a refined geodynamic model, rifting started between the Falkland Islands and the Maurice Ewing Bank at ~ 178 Ma and ceased at around ~ 154 Ma. Accepting a close relationship between the Falkland Islands and the Cape Province geology we still have to introduce a substantial movement of the Patagonian sub-plate eastwards along the Gastre Fault. The plateau's exceptionally thick oceanic crust likely results from its position in an extensional back-arc-regime situated over a mantle thermal anomaly that was also responsible for the extensive onshore Karoo-Ferrar and Chon Aike volcanic provinces.

5.2. Introduction

Until now, plate kinematic reconstructions of Gondwana breakup had to assume the nature and evolution of the Falkland Plateau, a 1500 km long plateau in the southern Atlantic Ocean (Figure 5.1), on the basis of inconclusive constraints. The plateau hosts the Falkland Islands in the west and terminates in the east at a bathymetric high, Maurice Ewing Bank (MEB). In between, the Falkland Plateau Basin is located in an overall area of a complex geology and sparse geophysical data, which have numerous contrasting interpretations. Prior to breakup, the Falkland Islands were situated in the

present-day Weddell Sea region off East Antarctica, a geologically complicated area. Its early geological evolution is still not solved, because of its remoteness. However, the current geophysical data base indicates that a large extensional area existed in the Weddell Sea region (Martin, 2007) prior to the initial formation of Late Jurassic oceanic crust (Jokat and Herter, 2016; König and Jokat, 2006).

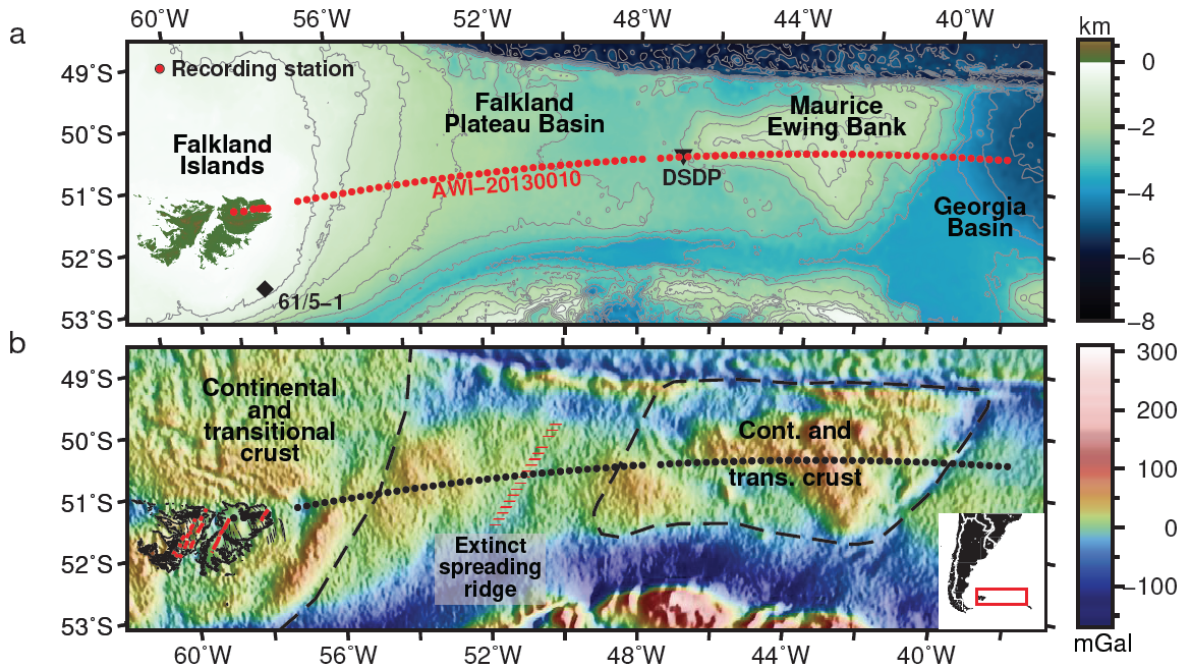


Figure 5.1.: (a) Bathymetric and topographic map of the Falkland Plateau with station locations and DSDP drill site 330 (DSDP). Location of well 61/5-1 is estimated from Richards et al. (2013). (b) Free-air gravity anomaly map (Sandwell et al., 2014). The SW-NE dyke swarm (Stone et al., 2008) is plotted in red.

One anchor point of all models for the early plate movements between South America/South Africa and the Weddell Sea region is the well-mapped Precambrian basement of the Falkland Islands. It clearly indicates that at least the westernmost part of the Falkland Plateau consists of continental crust, and that its basement is similar to that known from the Cape Region of southern Africa and Dronning Maud Land, Antarctica. Such information is not available for the remainder of the plateau. On MEB, Precambrian continental basement was only sampled at a single DSDP drill site (330, Barker and Dalziel, 1977). Despite this important finding it remained unclear if this rock sample is typical for the fabric of the entire MEB. For the Falkland Plateau Basin, seismic reflection and sonobuoy refraction measurements have been interpreted to show the presence of either oceanic crust (Ludwig and Rabinowitz, 1980) or stretched continental crust (Lorenzo and Mutter, 1988) with a Moho at 12 km depth. Recent 3D density modelling of the Falkland Plateau yielded a crustal thickness that is twice as thick as calculated from the sonobuoy data, but could not provide constraints for the crustal composition (Kimbell and Richards, 2008).

In plate reconstructions, the Falkland Plateau has variously been regarded as a rigid part of the South American plate with its present-day extent during the Jurassic (Eagles and Vaughan, 2009), as being composed of stretched continental crust with a smaller extent of the Falkland Plateau Basin during the Jurassic (Jokat et al., 2003a; König and Jokat, 2006; Torsvik et al., 2010) or as the product of independent motions between various small plates and continental blocks during Gondwana breakup implying the presence of oceanic crust beneath the Falkland Plateau Basin (Storey and Kyle, 1997).

The western transect of the crustal model presented here is published and provides compelling evidence for the existence of a rifted continental margin off the eastern Falkland Islands and the presence of thick oceanic crust beneath the western Falkland Plateau (Schimschal and Jokat, 2018).

Here, we present the results of the entire 1450 km long wide-angle seismic profile running from East Falkland to the Georgia Basin (Figure 5.1; AWI-20130010; supplementary material), as well as new ship borne magnetic data. Ocean Bottom Stations were deployed at 78 locations along the transect, which was prolonged onshore with 6 land stations on East Falkland (Jokat, 2013). On the basis of our results, we propose a refined model for the initial fit of Gondwana and the Mesozoic plate kinematic for this complex area.

5.3. The Falkland Plateau's crust

Figure 5.2b shows the velocity model and Figure 5.2c our interpretation of the data along the entire plateau. The crustal thickness below the island starts to thin eastwards of km 90 from a Moho depth of 35 to 22 km (Figure 5.2b, km 260). Here, the continent-ocean transition zone (COT) is 90 km wide (km 180 – 270; Schimschal and Jokat, 2018). The onset of oceanic crust at km 270 is situated at the outer edge of a gravity high, part of a large anomaly complex that encircles the Falklands. Oceanic crust of up to 20 km thickness (Schimschal and Jokat, 2018) is modelled beneath the Falkland Plateau Basin over a width of 450 km (Figure 5.2b; km 270 – 720). Eastwards of km 720, at the western end of MEB, the crust thickens with crustal velocities significantly slower than in the oceanic part of the Falkland Plateau Basin. Thus, between km 720 and 800, we suggest the presence of a COT that is at least 80 km wide. Below MEB, seismic velocities further decrease to typical values and gradients for continental crust above a variable Moho topography. The crust beneath the central part of MEB (km 1020 – 1150) is up to 29 km thick. MEB is bounded in the east and west by stretched continental crust. Between km 900 and 990, almost in the middle of MEB, lower crustal velocities exceed 7.0 km/s, perhaps due to the presence of lower crustal intrusions. Towards the Georgia Basin, the MEB crust thins to a minimum of 11 km in a COT (km 1220). The precise extent of this transition is not determinable due to the absence of high quality seismic reflection data to map the faults that indicate the onset of extension. In the very east of the transect, 7.1 km thick oceanic crust is modelled in the Georgia Basin.

A consequence of our crustal model is that an extinct spreading ridge is likely to exist somewhere along the transect. However the wide-angle seismic data do not provide good constraints on its location. The new magnetic data (Figure 5.2a) show no clear

pattern of magnetic reversal anomalies. To compare the anomalies of the Falkland and MEB margin, we mirrored the magnetic data between km 540 and 760 (Figure 5.2a, red line) to identify similarities with those of the Falkland Islands rifted margin (Figure 5.2a, black line). On a first view the anomalies show no good correlation between both margins (Figure 5.2a, red/black line). In a next step we stretched the data to investigate whether the anomalies might depict asymmetrical seafloor spreading. The closest fit to symmetry was achieved with a factor of 1.5 (blue/black line), implying that the spreading was highly asymmetric. Based on this, we suggest that the extinct spreading axis is located around km 540. In the free-air gravity anomaly map (Figure 5.1), the area of the proposed extinct spreading ridge is marked by a southwest-northeast trending linear gravity anomaly (extinct spreading ridge in Figure 5.1) of 20 mGal that crosses the profile between km 535 and 550. Finally, since the magnetic data show no distinct seafloor spreading anomalies, we cannot calculate any reliable spreading velocities at which the Falkland Plateau Basin formed. In contrast, clear spreading M-anomalies are visible in the Georgia Basin confirming older interpretations (Martin et al., 1982).

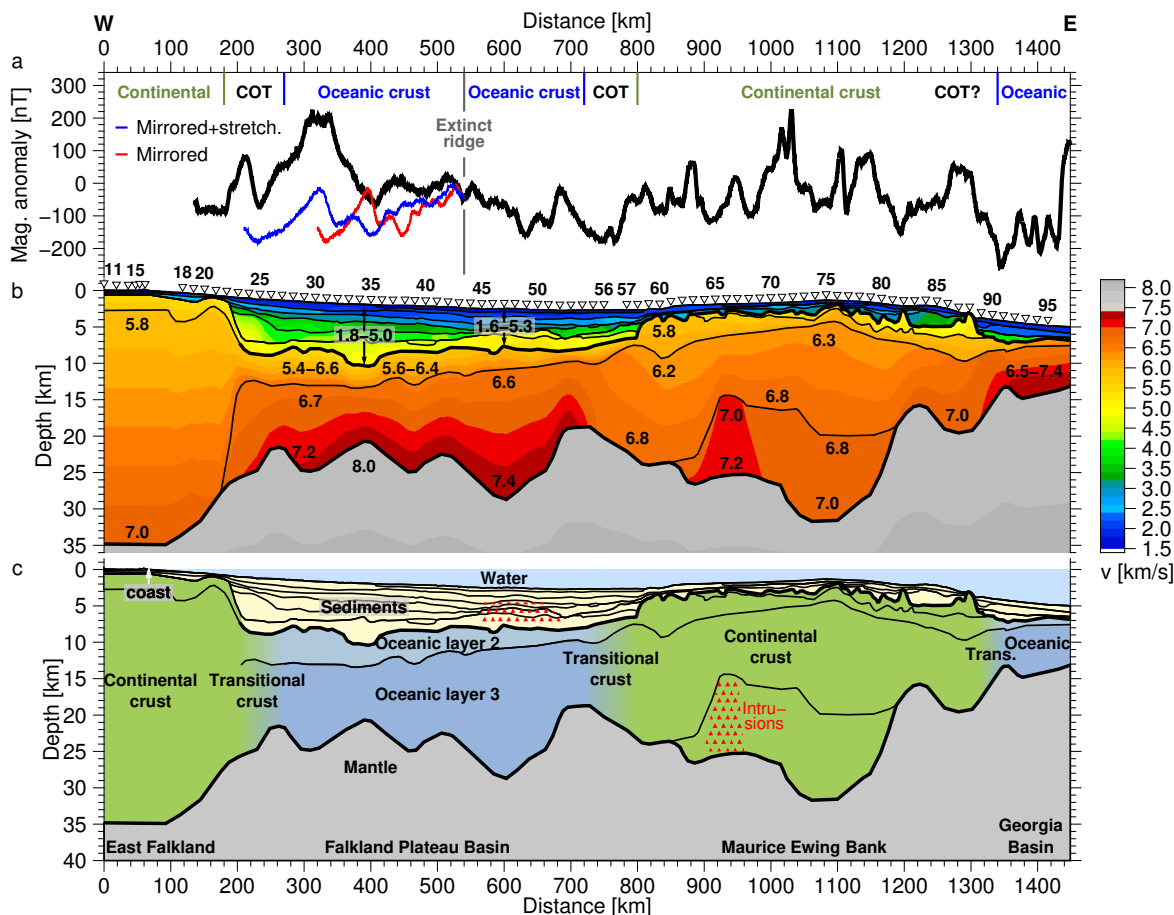


Figure 5.2.: (a) Observed magnetic anomaly (black line). The magnetic anomaly from km 540 – 760 is mirrored (red) and mirrored and stretched with a factor of 1.5 (blue). (b) P-wave velocity model and (c) geological interpretation of profile AWI-20130010.

5.4. Refined plate kinematic model: Geological/geophysical constraints

The surprising result of our study is that the Falkland Plateau was at least 450 km shorter during the Jurassic, before the formation of the Falkland Plateau Basin by seafloor spreading. Consequently the Falkland Islands and MEB likely formed one geological unit. With a tight fit of MEB between the African and East Antarctic continents and the much-reduced Jurassic extent of Falkland Plateau, we have to introduce 465 km of dextral transcurrent movement of the Patagonian sub-plate along the Gastre Fault (182 Ma plot, Figure 5.3) to avoid overlap of the South American sub-plates that lie to the north of the fault with the African plate. However, the existence of the Gastre Fault and the corresponding displacement of sub-plates is disputable and will be further discussed later in the text.

For the initial fit, we positioned the Falkland/Malvinas block closer to the Patagonian sub-plate, taking into account two Cretaceous crustal extensional phases (145 – 139 Ma and 130 – 110 Ma) that have been identified from seismic data in the Malvinas Basin (MB in 141 Ma plot, Figure 5.3, Baristead et al., 2013; Tassone et al., 2008).

South of the Falkland Plateau, a tight fit of the Falkland/Malvinas block and MEB with the Antarctic plates is achieved, when applying the most recent regional rotation poles of Mueller (2017). The East and West Antarctic plates move apart according to the constraints supplied from a Jurassic failed rift floored by 160 km of oceanic crust below the Filchner-Ronne-Shelf (oceanic crust of the Weddell Rift (WRift) red in Figure 5.3, Jokat and Herter, 2016). Even within this context closure of the Falkland Plateau Basin by movement of the Patagonian sub-plate along the Gastre Fault must be accompanied by a further rotation of the Antarctic Peninsula relative to West Antarctica to avoid overlaps, owing to later stretching in the Weddell rift basin (Hübscher et al., 1996; Jokat and Herter, 2016).

The timing of the onset of rifting and the age of the thick oceanic crust in the Falkland Plateau Basin are not well constrained. Evidence for Jurassic magmatism is found onshore the Falkland Islands, where two different dyke swarms intruded into the Proterozoic basement. The oldest dyke swarm trends in an east-west direction and is of Early Jurassic age (188 ± 2 Ma, Mussett and Taylor, 1994). A northeast-southwest trending dyke swarm has slightly younger ages between 162 ± 6 Ma (Thistlewood et al., 1997) and 178.6 ± 4.9 Ma (Stone et al., 2008). The northeast-southwest strike direction ($N35^\circ E$) of the Falkland Plateau spreading ridge (red, Figure 5.1b) is identical with that of the younger 178 – 162 Ma-dyke swarm (red, Figure 5.1b) on the islands, suggesting both might have developed in the same stress regime. Thus, in our model we assume that the first oceanic crust at the Falkland Plateau was emplaced contemporaneously with or shortly after the intrusion of the northeast-southwest trending Jurassic dyke swarm. Additional age constraints come from dated sediments in the commercial well 61/5-1 (Figure 5.1) southeast of the Falkland Islands (Richards et al., 2013). Here, dolerites were drilled at 2476 m depth in or close to the basement, but were not age dated. The sediments deposited overlying the dolerites are dated to be Tithonian (152 – 141 Ma).

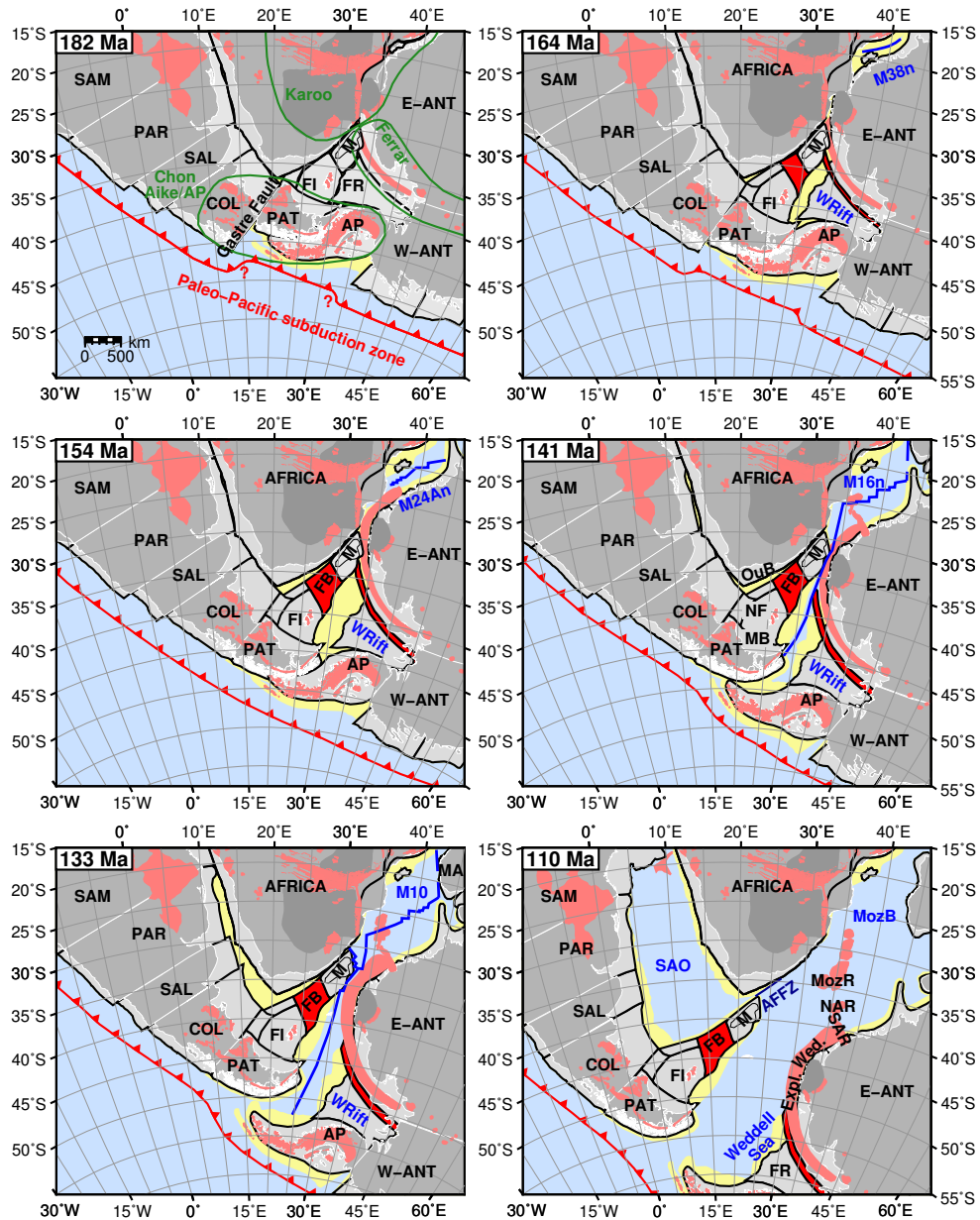


Figure 5.3.: Reconstruction of Gondwana using GPlates with Africa fixed in its present day position. Plate boundaries (black lines), coastlines (white lines), stretched continental and transitional crust (yellow), oceanic crust (blue), magmatic features (light red) and the outline of volcanic provinces (green, after Storey and Kyle, 1997) are depicted. The extent of the Falkland Plateau Basin and the thick oceanic crust of the Weddell Rift are plotted in red. Abbreviations are: AFFZ: Agulhas Falkland Fracture Zone, AP: Antarctic Peninsula, COL: Colorado sub-plate, E-ANT: East Antarctica, Expl. Wedge: Explora Wedge, FI: Falkland/Malvinas block, FB: Falkland Plateau Basin, FR: Filchner-Ronne-Shelf, MA: Madagascar, MB: Malvinas Basin, M: Maurice Ewing Bank, MozB: Mozambique Basin, MozR: Mozambique Ridge, NAR: Northern Astrid Ridge, NF: North Falkland Basin, OuB: Outeniqua Basin, PAR: Parana sub-plate, PAT: Patagonia sub-plate, SAM: northern South American sub-plate, SAL: Salado sub-plate, SAR: Southern Astrid Ridge, W-ANT: West Antarctica, WRift: Weddell Rift.

We think that it is unlikely that any seafloor spreading occurred after the deposition of these sediments, thus, rifting and subsequent seafloor spreading must have ended before 152 Ma.

The spreading velocities can only be guessed at by comparison to other areas. Approximately 270 km of oceanic crust lies west of the proposed extinct spreading ridge. We assume a slow-to-intermediate spreading half rate of 20.0–23.5 km/Myr, as observed for the Mesozoic magnetic anomalies in the Mozambique Basin (MozB in 110 Ma plot, Figure 5.3, König and Jokat, 2010). This suggests the basin formed during 13.5 – 11.5 Myrs of spreading. Consequently, in the same time span the 180 km of oceanic crust east of the spreading ridge formed at a half rate of ~ 13.3 to ~ 15.7 km/Myr. Also analogous to the initial rifting of the Mozambique Basin (Mueller, 2017), we propose a 12 Myrs-long rifting phase that started at 178 Ma. The subsequent 12 Myrs-long phase of oceanic accretion might have lasted from 166 to 154 Ma. Our model thus suggests that strike-slip movement along the Gastre Fault ceased at ~ 154 Ma, when the Falkland spreading centre became extinct.

Rifting and subsequent seafloor spreading between 178 Ma and 154 Ma is comparable to the timing of crustal stretching and growth in the regions adjacent to the Jurassic Falkland Plateau (Figure 5.3). In the Outeniqua Basin (OuB in 141 Ma plot, Figure 5.3), north of the Falkland Plateau, Parsiegla et al. (2009) report that north-south oriented stretching occurred between 169 and 155 Ma. For the North Falkland Basin (NF in 141 Ma plot, Figure 5.3), Lohr and Underhill (2015) report rifting between ~ 160 and ~ 146 Ma.

5.4.1. Early Opening of the Atlantic sector of the Southern Ocean

South of the Falkland Plateau in the Weddell Sea region, Jokat and Herter (2016) report an age of 160 Ma to be the most likely age for the oceanic crust of the Weddell Rift (red in Figure 5.3). The similar thicker-than-average oceanic crustal thickness suggests that the Weddell Rift and the Falkland Plateau Basin developed in comparable environments characterized by additional melt supply. In the Weddell Sea region, opening of the Falkland Plateau Basin and the southward motion of Antarctica led to dextral-transensional shearing between the continental blocks of the Falkland Plateau and the continental crust of the Filchner-Ronne Shelf (FR in 182 Ma plot, Figure 5.3). Our kinematic model shows that the Antarctic Peninsula rotated from its pre-rift position to its present-day position relative to West Antarctica at earliest from 157 Ma onwards. An earlier rotation is unlikely because the space is occupied by the Patagonian sub-plate. The ongoing southward motion of Antarctica relative to Africa caused the detachment of the Falkland Plateau from Antarctica. By 147 Ma (M20), oceanic crust was being emplaced between South America and Antarctica in the southern Weddell Sea (König and Jokat, 2006). In contrast to the crust beneath the Falkland Plateau Basin and the crust of the Jurassic Weddell Rift, the Cretaceous oceanic crust of the Weddell Sea is of average thickness (Jokat et al., 2004).

Rifting between South America and Africa started by 138 Ma Pérez-Díaz and Eagles (2014). In the Georgia Basin, east of MEB, the first oceanic crust was emplaced at M10n

times (133.88 – 133.58 Ma) (Martin et al., 1982). The opening of the South Atlantic resulted in movement of the Falkland Plateau along the Agulhas Falkland Fracture Zone (AFFZ in 182 Ma plot, Figure 5.3), leading to oblique stretching in the Outeniqua Basin (Parsiegla et al., 2009) and orthogonal stretching in the North Falkland Basin (Lohr and Underhill, 2015) by \sim 136 Ma. The spreading anomalies east of MEB and north of the Agulhas Falkland Fracture Zone result in minor motions of the Falkland Plateau and crustal extension in the Malvinas Basin (Baristead et al., 2013) between 130 and 110 Ma.

5.4.2. Phases of magmatism and seafloor spreading

The geochemistry of the onshore dykes provides important constraints on the environment in which exceptionally thick oceanic crust of the Falkland Plateau developed. Late stage rifting is well documented over a wide area of Patagonia and the Antarctic Peninsula by silicic basalts of the Chon Aike province and in Africa and Antarctica by the preceding Ferrar and Karoo volcanic provinces, which have a more variable geochemistry of basaltic, rhyolitic, silicic and gabbroic character. Their ages cluster between 184 and 174 Ma (Jourdan et al., 2007). The Falkland Islands were located in between these large volcanic provinces (regions outlined by green lines, 182 Ma plot in Figure 5.3). The islands' onshore dykes show a geochemistry that can be classified as transitional between the African Karoo and the Antarctic Ferrar basalts (Hole et al., 2015; Mitchell et al., 1986). The emplacement of these large volcanic provinces shows that a region, which extended all the way from the paleo-Pacific margin to the centre of Gondwana, was influenced by enhanced melt supply.

The position of the Falkland Plateau and Weddell Rift between these provinces of enhanced melt supply during crustal formation certainly added extra melt. In addition, the Falkland Plateau and the Weddell Rift were situated in a back-arc regime of the paleo-Pacific subduction zone (red in Figure 5.3, Martin, 2007). The extensional back-arc regime generated enough space for the formation of oceanic crust.

The cause for enhanced melt supply of the large volcanic regions (Chon Aike, Karoo-Ferrar, Falkland Islands dykes) could be either a vast thermal anomaly, which influenced the entire region, or a limited mantle thermal anomaly and lithospheric melt migration. We favour the latter. Our estimates provide an age range for the 20 km thick Falkland Plateau oceanic crust of 166 to 154 Ma. For the up to 20 km thick southern Weddell Sea oceanic crust a range of 160 to 147 Ma is proposed (Jokat and Herter, 2016). Exceptionally thick oceanic crust is neither observed in basins of similar age in the Mozambique Basin (Mueller and Jokat, 2017) nor in the central Weddell Sea (König and Jokat, 2006), favouring our assumption of a limited-sized mantle thermal anomaly. The beginning of the opening of the Mozambique Basin (Mueller and Jokat, 2017) was most likely contemporaneous with the opening of the Falkland Plateau. In the central Weddell Sea, the extensional regime changed at 147 Ma from approximately E-W to N-S directed. In the later phase, well constrained by seafloor spreading anomalies (König and Jokat, 2006), normal thickness (\sim 7 km) oceanic crust was emplaced (Jokat et al., 2004). At this time, South America together with the Falkland Plateau became detached from East

Antarctica. From the few geophysical data available, there is no evidence that excess melt contributed to regional thickening of oceanic crust after this period.

Thus, the exceptionally thick oceanic crust of the Falkland Plateau and Weddell Rift likely results from their position in a back-arc regime over a region with enhanced melt supply, most likely due to a temporally and spatially limited mantle thermal anomaly.

5.4.3. Remaining Problems

The existence and the amount of translation along the Gastre Fault are strongly debated problems. Large translations of up to 500 km are common in reconstructions (e.g. Rapela and Pankhurst, 1992). However, the results of a comprehensive geological study of the area oppose the existence of a large-scale, intra-continental Gastre Fault zone (von Gosen and Loske, 2004).

If we keep Patagonia fixed to the Colorado plate in our reconstruction, it results in a large crustal overlap between continental eastern South America and Africa, and large gaps between Patagonia and the Falkland Plateau, and across the Agulhas Falkland Fracture Zone. Furthermore, displacement along the Gastre Fault generates space at the paleo-Pacific margin of Gondwana for the Antarctic Peninsula without having to assume large bends along that margin. Torsvik et al. (2010) explain the large movements along the Gastre Fault System and the Agulhas Falkland Fracture Zone as responses to contrasting rollback rates caused by a variable subduction angle along the subduction margin. Our results provide no additional constraints on this possibility.

We assumed an E-W extension/formation of oceanic crust for the formation of the Falkland Plateau, which is difficult to reconcile with the apparent NE-SW strike of the extended margin of East Falkland and of the proposed extinct ridge. More systematic magnetic data with a better areal coverage might facilitate the identification of seafloor spreading anomalies to further refine the kinematic and provide stronger age constraints. In summary, our new crustal model of the Falkland Plateau diminishes the uncertainties of the Jurassic extent of the plateau in Gondwana reconstructions and provides indications about a local emplacement of exceptionally thick oceanic crust during the initial breakup of the Weddell Sea sector.

Acknowledgements

We thank the captain and crew of *RV Polarstern* as well as the geophysical team for their support and assistance during the cruise. We acknowledge the Geomar, Kiel for providing the OBS/H stations. For his support with the software *SOFI2D* we thank Thomas Bohlen.

5.5. Supplementary information - The Falkland Plateau in the context of Gondwana breakup

Here, we describe the methods and present an error analysis, data examples and the ray coverage of the P-wave velocity model. For the western transect, the method is described in greater detail by Schimschal and Jokat (2018). Furthermore we provide the rotation poles of the refined kinematic model.

Method

Data acquisition and processing of the wide-angle seismic data

On East Falkland, six RefTek land stations were deployed at an average spacing of 12 km. The closest distance of any of the land stations to the start of the marine profile was 75 km. Offshore, 39 ocean bottom receivers, provided by GEOMAR, were deployed twice. This resulted in a western and eastern transect. The spacing between stations was 16 km. The seismic source was an array of eight G-Guns with a total volume of 68 l (4160 in³). 3864 shots were generated on the western transect and 5028 shots on the eastern one. The shot interval was 60 s, resulting in an average shot spacing of 150 m. The data were processed using standard procedures including relocation of stations, AGC, filtering and a deconvolution. The processed seismic section of station 37 is shown in Figure 5.4 and of station 66 in Figure 5.5.

Data acquisition and processing of the magnetic data

Along the entire ship track magnetic measurements were carried out by the fix-installed two orthogonal three-component digital fluxgate sensors on *RV Polarstern*. The data were compensated for the effects of induced fields from the ship's hull, corrected for the International Geomagnetic Reference Field (IGRF) and de-spiked. Additional helicopter magnetic data was recorded and allowed the comparison with the shipborne magnetic data.

Modelling of the wide-angle seismic data

Modelling was conducted layer-wise from top to bottom using *RAYINV*R (Zelt and Smith, 1992) together with *PRay* (Fromm, 2016). An additional amplitude modelling using *SOFI2D* (Seismic mOdelling with FInite differences, Bohlen, 2002) provided further constraints for the velocity of the lower crust, where the ray coverage of refracted phases is limited. The synthetic seismogram of station 37 is shown in Figure 5.4 and of station 66 in Figure 5.5. In Figure 5.6 the picks and calculated arrivals of all stations are displayed. The ray coverage of the entire model is shown in Figure 5.7. Error statistics for the velocity model are provided in Table 5.1.

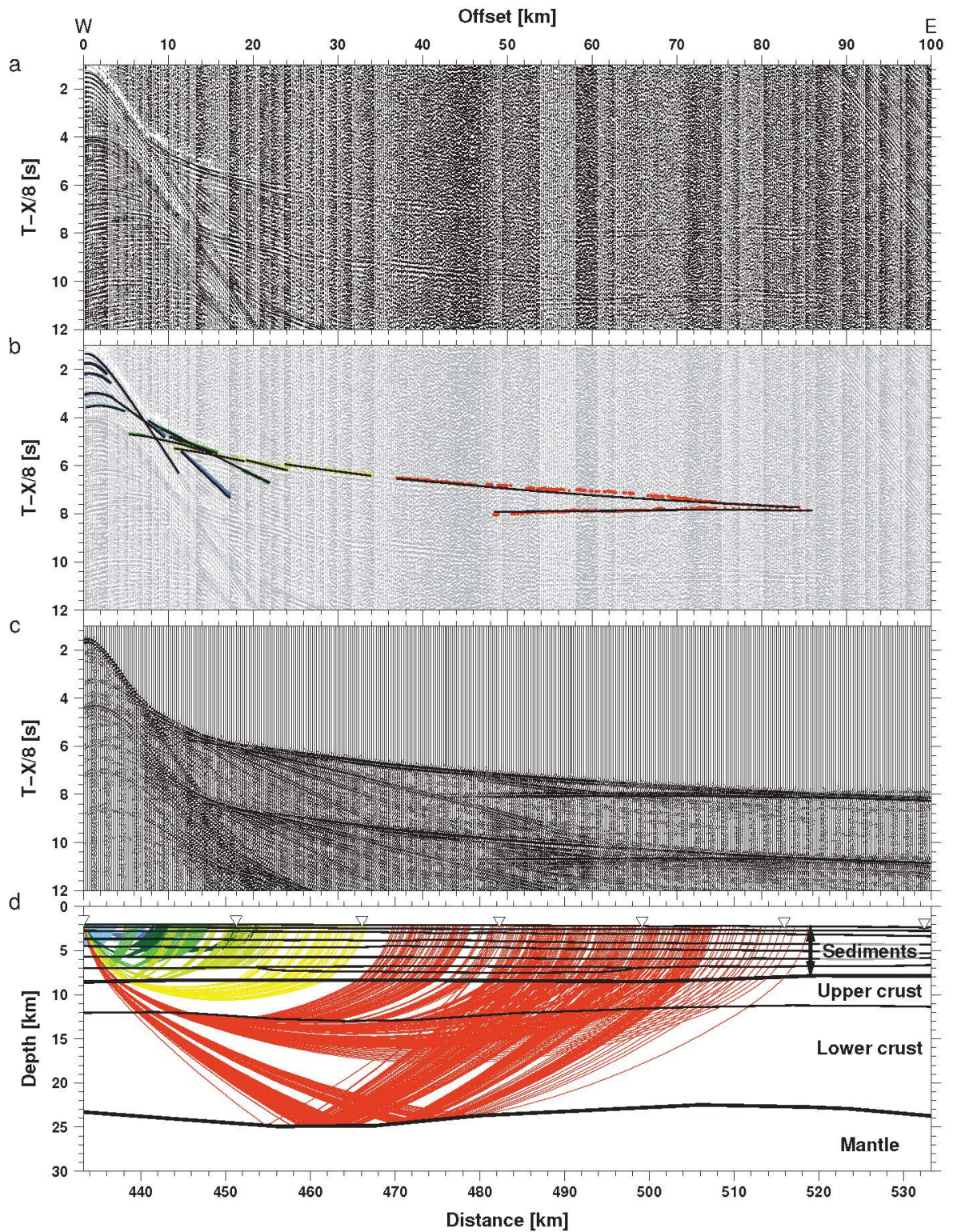


Figure 5.4.: Data example of station 37. (a) Seismic section filtered with a 4-15 Hz bandpass filter, amplified with an AGC of 1 s and displayed with a reduction velocity of 8 km/s. (b) Picked phases and modelled arrivals (black lines), (c) synthetic seismogram and (d) ray coverage of the picks shown in (b).

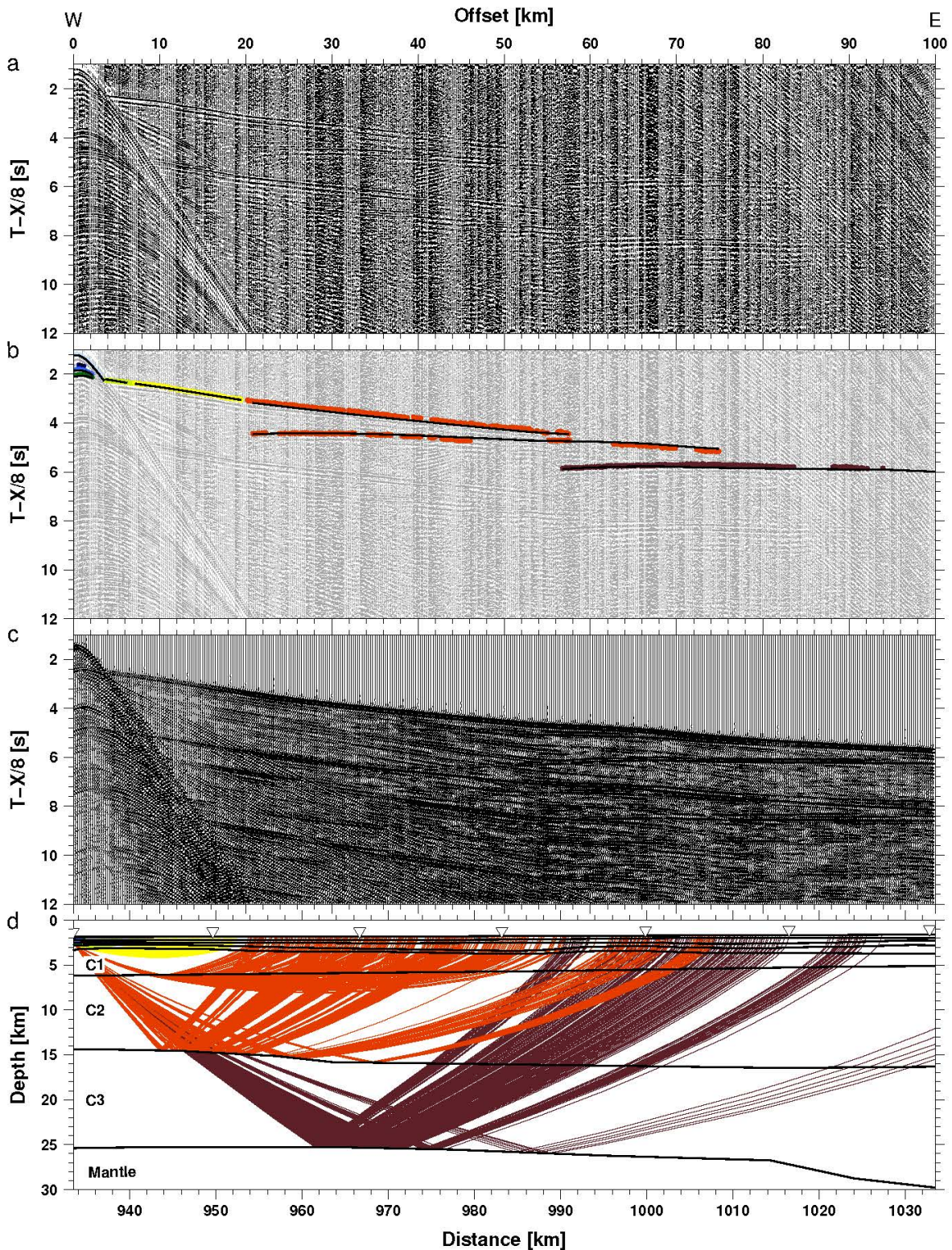


Figure 5.5.: Data example of station 66. (a) Seismic section filtered with a 4-15 Hz bandpass filter, amplified with an AGC of 1 s and displayed with a reduction velocity of 8 km/s. (b) Picked phases and modelled arrivals (black lines), (c) synthetic seismogram and (d) ray coverage of the picks shown in (b).

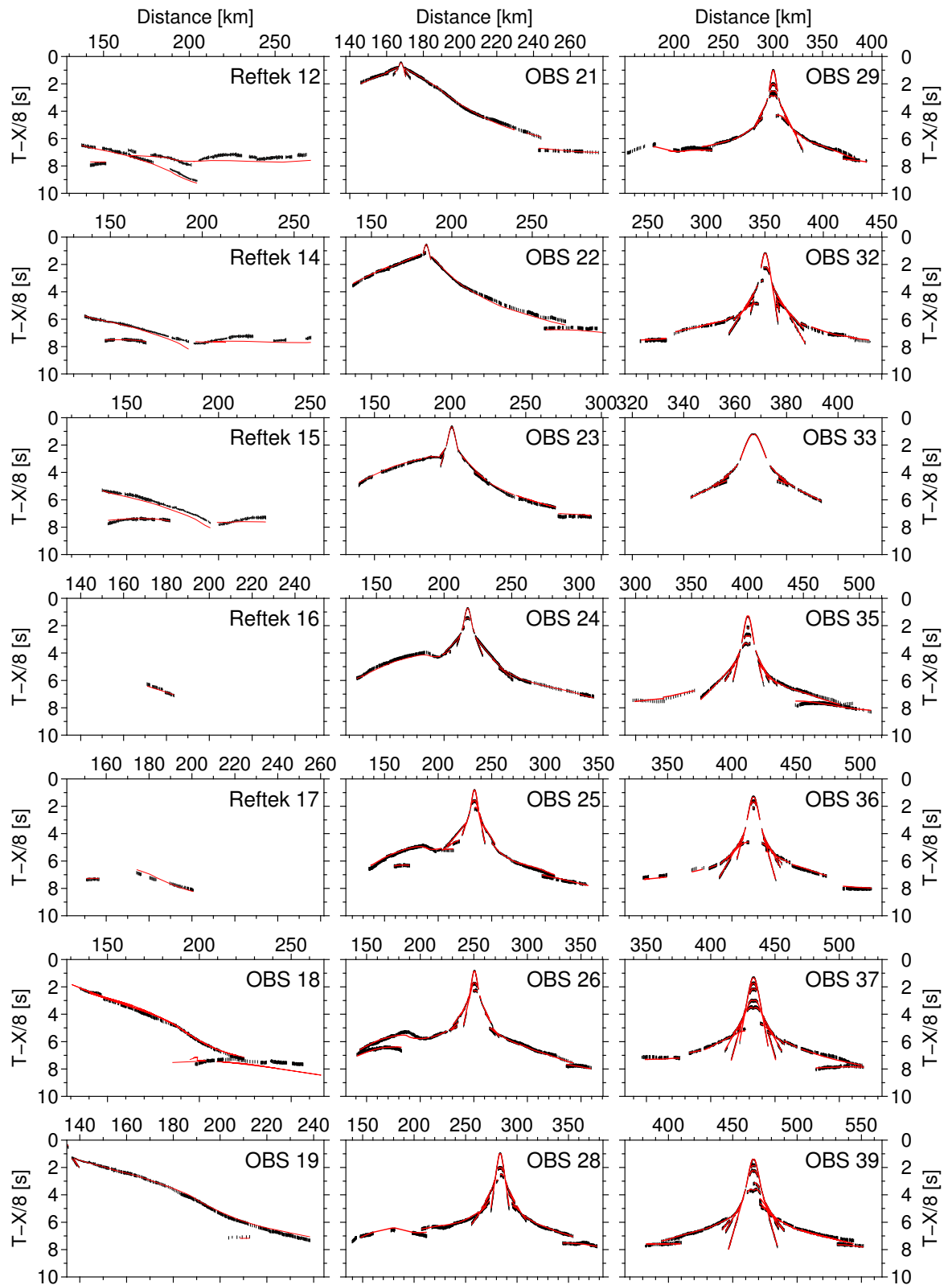


Figure 5.6.: All stations with picked arrivals (shown as black error bars) and modelled arrivals (red).

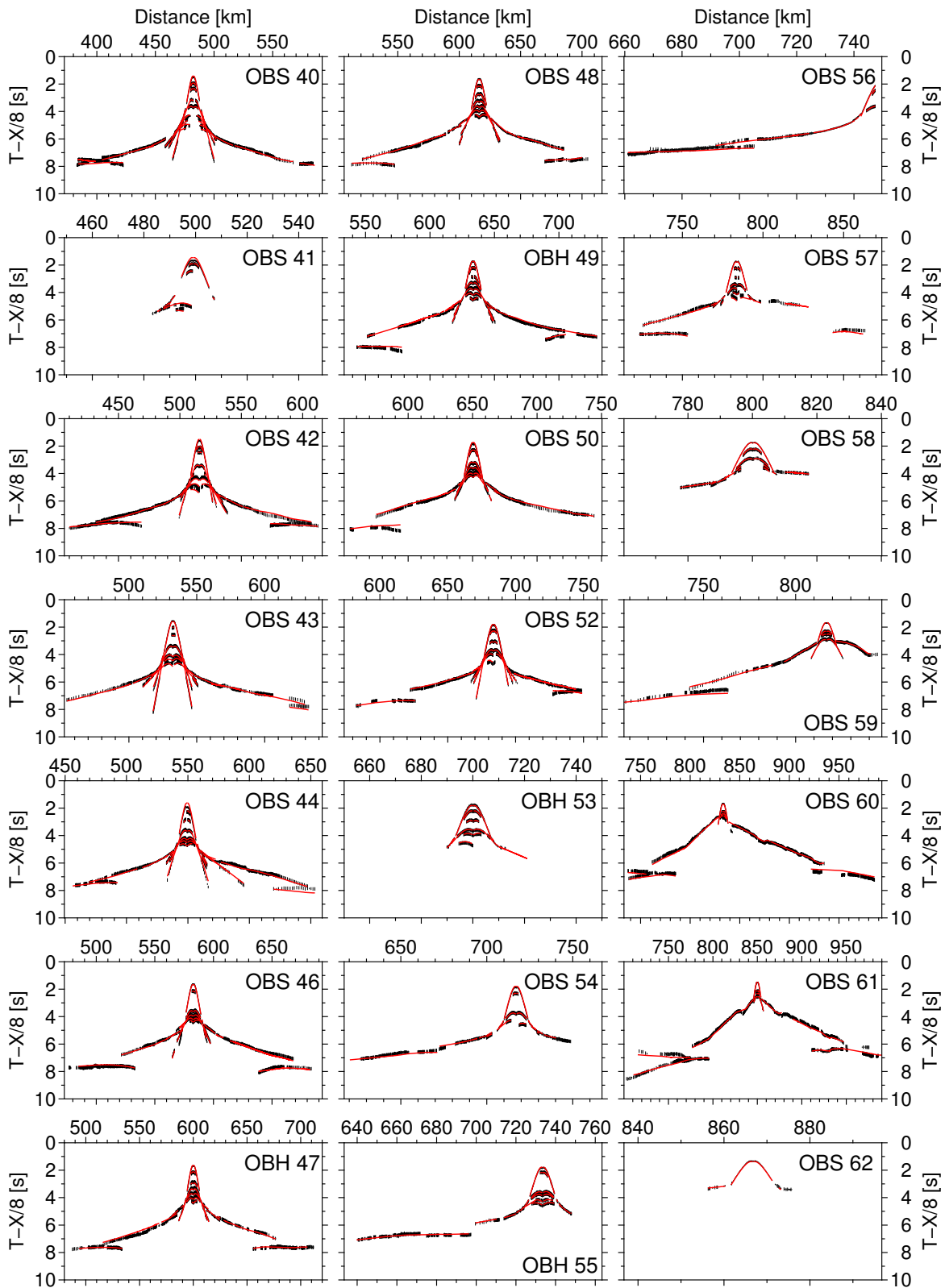


Figure 5.6.: (continued).

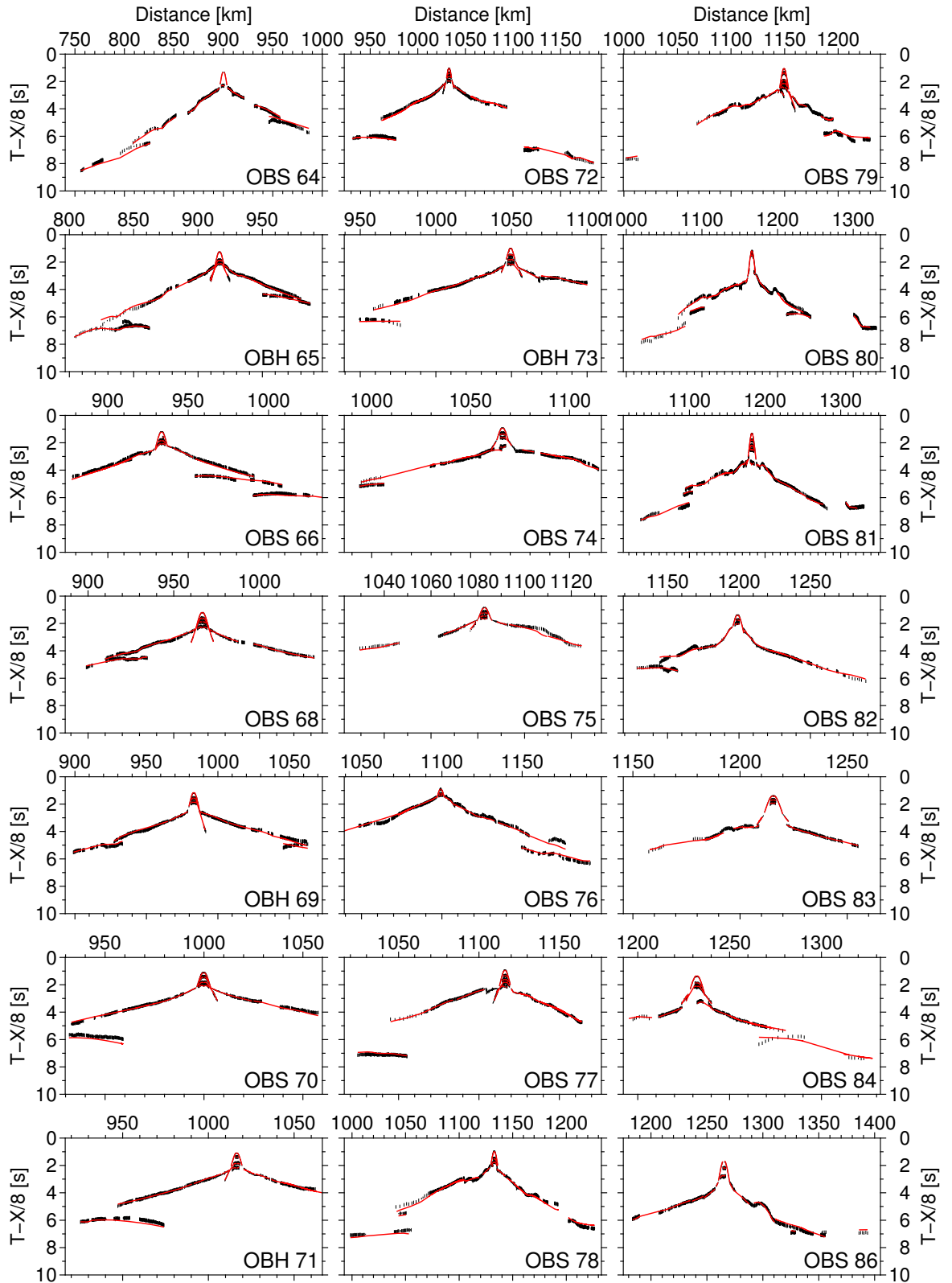


Figure 5.6.: (continued).

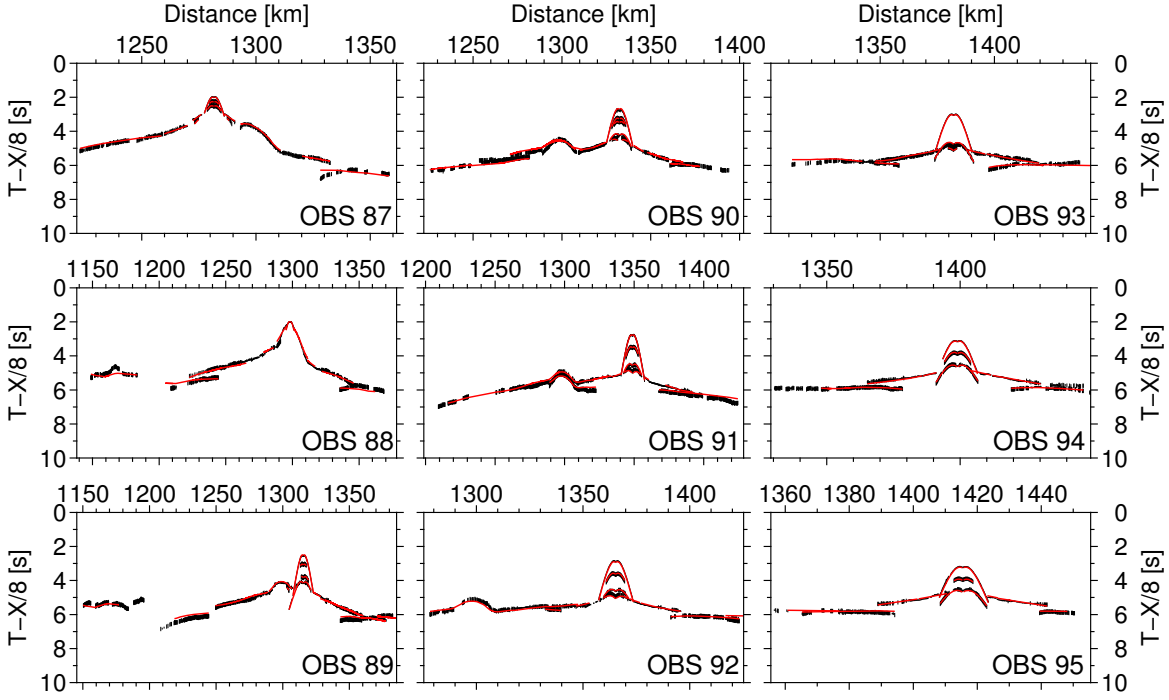


Figure 5.6.: (continued).

Table 5.1.: Summarized error statistics showing the number of observations (No of picks), the root mean square travel time residuals (t_{rms}) and the normalized χ^2 .

| Layer | No of Picks | t_{rms} [ms] | χ^2 |
|--------------------------|-------------|-----------------------|----------|
| Waterwave | 3914 | 57 | 2.115 |
| Sediment phases | 18192 | 57 | 0.761 |
| Crustal phases | 40005 | 101 | 1.557 |
| Mantle (refracted phase) | 1370 | 200 | 5.297 |
| All phases | 63481 | 90 | 1.413 |

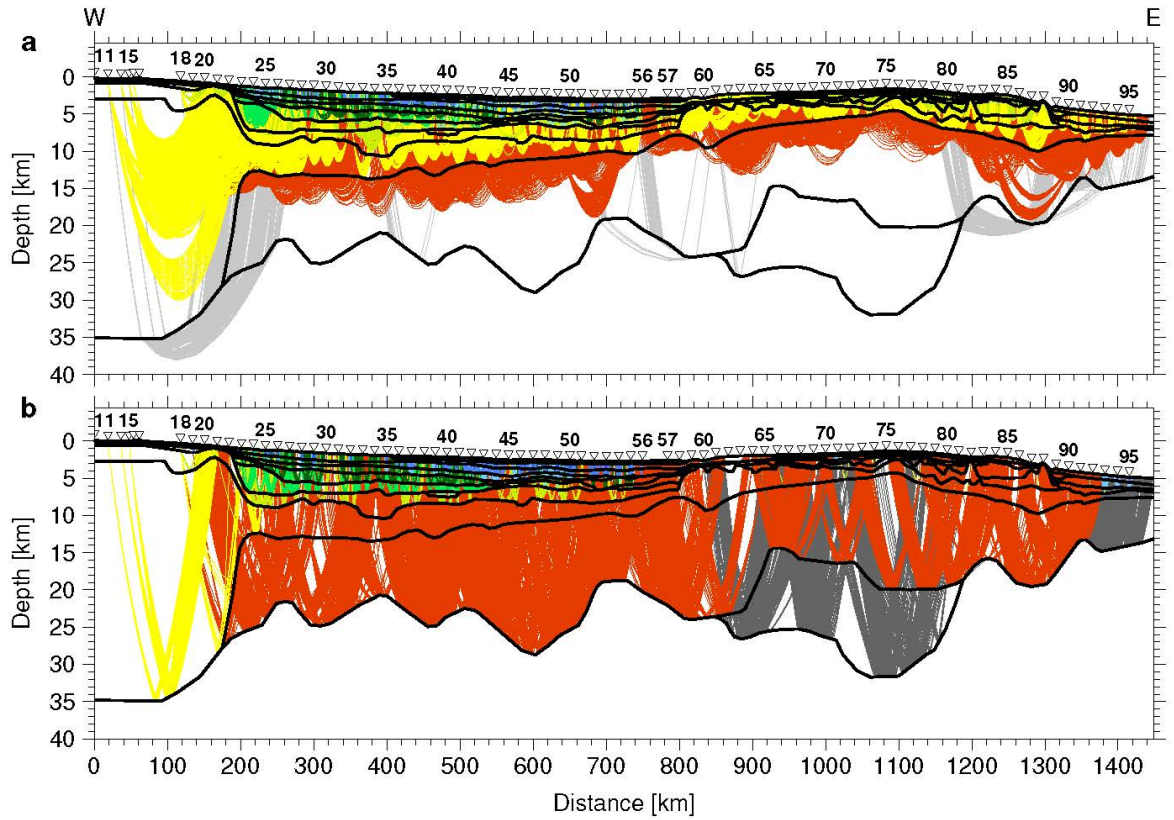


Figure 5.7.: Ray coverage of the entire model in (a) for the refracted phases and in (b) for the reflected phases.

Refined kinematic model

The GPlates software (Boyden et al., 2011) was used for the refined kinematic model. The rotation parameters are given in Table 5.2.

Table 5.2.: Finite rotations for the opening of the Falkland Plateau, the Africa-Antarctica corridor, the Weddell Sea and the South Atlantic Ocean.

| Age (Ogg, 2012) | Lat | Long | Angle | Source |
|--|--------|--------|-------|--------------------------|
| East Antarctica - Southern Africa | | | | |
| 83.64 | -1.17 | -40.52 | 16.92 | C34n, Mueller (2017) |
| 102.00 | -2.32 | -33.32 | 28.09 | CNS, Mueller (2017) |
| 113.00 | -6.74 | -28.95 | 34.57 | CNS, Mueller (2017) |
| 120.00 | -8.77 | -27.49 | 37.48 | CNS, Mueller (2017) |
| 126.12 | -10.41 | -26.02 | 41.09 | M0r, Mueller (2017) |
| 128.89 | -9.55 | -27.19 | 42.30 | M3n, Mueller (2017) |
| 131.02 | -9.36 | -27.58 | 43.01 | M5n, Mueller (2017) |
| 132.68 | -8.86 | -28.44 | 43.21 | M8n, Mueller (2017) |
| 133.73 | -8.93 | -28.71 | 43.65 | M10n, Mueller (2017) |
| 135.62 | -8.89 | -29.17 | 44.42 | M11n, Mueller (2017) |
| 138.34 | -8.99 | -29.57 | 44.96 | M13n, Mueller (2017) |
| 141.03 | -8.58 | -30.20 | 46.64 | M16n, Mueller (2017) |
| 143.29 | -8.20 | -30.20 | 47.86 | M17r, Mueller (2017) |
| 147.34 | -7.41 | -30.99 | 49.17 | M20n.2n, Mueller (2017) |
| 150.56 | -7.00 | -31.46 | 50.30 | M22n.1n, Mueller (2017) |
| 151.79 | -6.74 | -31.71 | 50.88 | M22r, Mueller (2017) |
| 155.70 | -6.45 | -31.96 | 52.67 | M25n, Mueller (2017) |
| 158.24 | -6.55 | -32.30 | 53.59 | M28n.2r, Mueller (2017) |
| 159.50 | -6.63 | -32.42 | 53.87 | M30n, Mueller (2017) |
| 160.83 | -6.70 | -32.57 | 54.23 | M33n.1n, Mueller (2017) |
| 164.10 | -7.02 | -32.97 | 55.05 | M38n.2n, Mueller (2017) |
| 177.00 | -7.79 | -33.86 | 56.72 | Speed-up, Mueller (2017) |
| 182.00 | -7.96 | -33.86 | 56.91 | fit, Mueller (2017) |
| West Antarctica - East Antarctica | | | | |
| 150.0 | 0.0 | 0.0 | 0.0 | this study |
| 178.0 | 10.43 | -27.43 | 0.94 | fit, this study |
| Antarctic Peninsula - West Antarctica | | | | |
| 140.0 | 0.0 | 0.0 | 0.0 | this study |
| 157.0 | -73.55 | -65.70 | 23.04 | fit, this study |

Northern South America - Southern Africa

| | | | | |
|--------|-------|--------|-------|---|
| 83.64 | 61.88 | -34.26 | 33.51 | C34n, Nürnberg and Müller (1991)* |
| 96.0 | 57.46 | -34.02 | 39.79 | Heine et al. (2013) |
| 125.93 | 51.26 | -33.48 | 52.43 | M0r, Heine et al. (2013)** (Crossover to Northwest Africa) |

Northern South America - Northwest Africa

| | | | | |
|--------|-------|--------|-------|---------------------------|
| 125.93 | 52.26 | -34.83 | 51.48 | M0r, Heine et al. (2013)* |
| 130.6 | 50.91 | -34.59 | 52.92 | M4n, Heine et al. (2013)* |
| 132.04 | 50.78 | -34.54 | 53.04 | M7n, Heine et al. (2013)* |
| 140.0 | 50.44 | -34.38 | 53.4 | fit, Heine et al. (2013) |

**Intracontinental Deformations South America
(Parana fixed to northern South America)**

Salado - Parana

| | | | | |
|--------|-------|--------|------|---------------------|
| 124.05 | 0.0 | 0.0 | 0.0 | Heine et al. (2013) |
| 145.0 | 41.16 | -42.00 | 1.22 | fit, this study |

Colorado - Salado

| | | | | |
|--------|-------|--------|------|---------------------|
| 124.05 | 0.0 | 0.0 | 0.0 | Heine et al. (2013) |
| 150.0 | 11.69 | -56.39 | 2.19 | fit, this study |

Patagonia - Colorado

| | | | | |
|-------|--------|--------|------|-----------------|
| 154.0 | 0.0 | 0.0 | 0.0 | this study |
| 178.0 | -10.26 | -64.58 | 6.98 | fit, this study |

Falkland/Malvinas Block - Patagonia

| | | | | |
|-------|-------|--------|-------|-----------------|
| 110.0 | 0.0 | 0.0 | 0.0 | this study |
| 130.0 | 55.62 | 115.37 | -5.17 | this study |
| 139.0 | 55.62 | 115.37 | -5.17 | this study |
| 145.0 | 59.06 | 121.12 | -7.31 | fit, this study |

MEB - Falkland/Malvinas Block

| | | | | |
|-------|--------|--------|-------|-----------------|
| 110.0 | 0.0 | 0.0 | 0.0 | this study |
| 130.0 | -48.17 | -50.59 | -6.92 | this study |
| 135.0 | 48.24 | 123.83 | 2.20 | this study |
| 139.0 | 22.96 | 107.07 | 0.36 | fit, this study |

* ages changed to fit timescale of Ogg (2012)

** timescale changes required minimal adaption of rotation pole

6. The crustal structure of Maurice Ewing Bank from wide-angle seismic data

Claudia Monika Schimschal^a, Wilfried Jokat^{a,b}

^a Alfred Wegener Institute Helmholtz Centre for Polar and Marine Research

^b University of Bremen

6.1. Abstract

The Maurice Ewing Bank is a bathymetric high at the eastern termination of the Falkland Plateau in the South Atlantic Ocean. Its crustal fabric is of interest for plate kinematic reconstructions of the Southern Ocean. On the basis of recently acquired wide-angle seismic and potential field data, a crustal model is established for the Maurice Ewing Bank, the adjacent eastern Falkland Plateau Basin and the western Georgia Basin. According to the model, the Falkland Plateau Basin is floored by thick oceanic crust. An 80 km wide continent-ocean transition zone is located towards the Maurice Ewing Bank. The data indicate that the Maurice Ewing Bank is composed of continental crust of up to 29 km thickness. Its western part shows fast crustal velocities (> 7.0 km/s) and strong intracrustal reflections. The wide-angle data provide no evidence for strong tectonic or magmatic overprinting of the bank's central portion. The continental crust thins eastwards to 11 km. The oceanic crust of the Georgia Basin is of average thickness (~ 7 km) for its type. Here, ship and airborne magnetic data confirm previously identified Mesozoic spreading anomalies and the onset of oceanic crust formation at M10n (~ 133 Ma) time.

6.2. Introduction

The Falkland Plateau is a bathymetric feature in the South Atlantic Ocean that stretches from the Falkland Islands for more than 1500 km eastward into the Georgia Basin. The shallow (< 2 km) water Maurice Ewing Bank (MEB) terminates the plateau in the east (Figure 6.1). An area of deeper water, the Falkland Plateau Basin, lies between the islands and MEB.

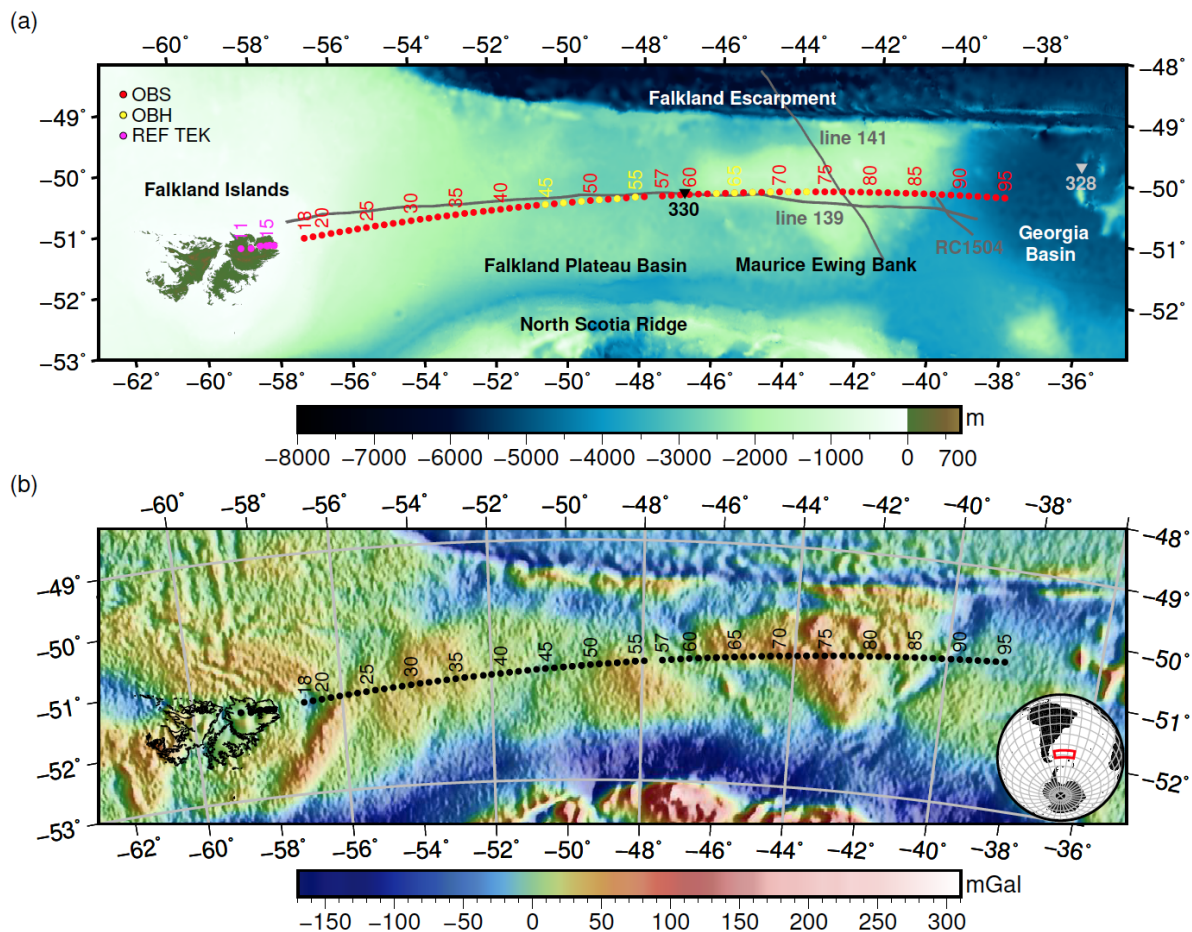


Figure 6.1.: (a) Topographic and bathymetric map of the Falkland Plateau and the Georgia Basin (GEBCO, 2014) with OBS, OBH and land station positions. In addition the seismic reflection lines 139, 141 (Ludwig et al., 1978) and part of profile RC1504 are depicted. Triangles mark the position of the DSDP drill sites 228 and 330. (b) Free-air gravity anomaly map of the Falkland Plateau and the Georgia Basin (Sandwell et al., 2014).

Geophysical and geological information on the composition of MEB is sparse. It was the drilling target of DSDP leg 36 (Barker and Dalziel, 1977) in 1974, and was drilled in 1980 once again during leg 71 (Ludwig and Krasheninnikov, 1983). Continental rocks (gneisses) were drilled at site 330 in 547m, and interpreted as strong evidence for a continental origin (Barker, 1977). Multichannel seismic reflection data (lines 139 and 141) gathered in the 1970s (Ludwig, 1983; Ludwig et al., 1978; Ludwig and Rabinowitz, 1980), provide insights into the sediment structure and the depth of the basement, while only few sound constraints exist on its crustal fabric from sonobuoy data. The only more recent study to address the deeper structure of MEB is a three-dimensional isostatically-compensated density model of the lithosphere (Kimbell and Richards, 2008), designed to fit satellite-derived free-air gravity anomalies. Using a composition- and depth-independent density of 2.85 g/cm^3 , the model implied a $\sim 22 \text{ km}$ thick crust and

the Moho at ~ 25 km depth beneath MEB.

In 2013, wide-angle seismic data were acquired along a west-east oriented profile (AWI-20130010) from East Falkland to the Georgia Basin to provide more detailed constraints on the crustal structure of MEB. Schimschal and Jokat (2018) reported the results of the western transect, which describe the structure of East Falkland and its eastern margin. The study revealed the presence of thick oceanic crust beneath the western Falkland Plateau Basin. Here, we describe in detail the remaining transect over the eastern Falkland Plateau, MEB and the western Georgia Basin. A crustal model is built for the transect by forward modelling of its P-wave arrivals, by additional amplitude modelling, and by modelling of potential field data.

6.3. Geologic Setting

6.3.1. The Falkland Plateau Basin

The Falkland Plateau Basin is filled with sediments of Mid-Jurassic to Mid-Cretaceous age (Lorenzo and Mutter, 1988). Based on seismic reflection data, Lorenzo and Mutter (1988) defined four regional depositional sequences for the sedimentary units in the Falkland Plateau Basin. Three of these sequences are sampled by DSDP drilling. Lorenzo and Mutter (1988) interpreted the bounding unconformities (U1 to U4, Figure 6.2) to originate from (1) an early Paleozoic pediplanation (U2), (2) a post-rift erosional truncation (U3, unsampled by scientific drilling), and (3) erosional ocean currents (U4). In their stratigraphic model U1 represents the top of acoustic basement.

Seismic reflection data revealed a rough and irregular basement topography underneath the Falkland Plateau Basin (Ludwig, 1983). Isolated 30 km wide cone-shaped bodies were interpreted as magmatic edifices. Indications for subaerial lava flows are found south of line 139 in dipping reflectors below basement, which show off-lapping relationships, non-hyperbolic geometries and a decreasing dip towards the south (line 143, Lorenzo and Mutter, 1988).

Evidence for Late Jurassic magmatism is observed in drilled dolerites in a commercial well (61/5-1) southeast of the Falkland Islands (Richards et al., 2013). Later, during the Cretaceous (130 – 139 Ma), the intrusion of sills and extrusion of lavas in the western Falkland Plateau Basin are presumably linked to the initial opening of the South Atlantic Ocean (Richards et al., 2013).

In the west, the basin is bounded by the Falkland Islands. Schimschal and Jokat (2018) classify the eastern margin as a volcanic rifted margin. A 90 km wide continent-ocean transition zone (COT) exists between the continental crust of the Falkland Islands block and the Falkland Plateau Basin. The basin is underlain by up to 20 km thick oceanic crust of probably Late Jurassic age (Schimschal and Jokat, submitted manuscript).

6.3.2. Maurice Ewing Bank

Information about the sedimentary cover of MEB and the geometry of its basement can be inferred from DSDP legs 36 (sites 327, 329, 330) and 71 (sites 511, 512) in combination

with seismic reflection data (Ludwig, 1983). Piston cores together with the DSDP drill data supplement the initial interpretation (Ciesielski and Wise, 1977).

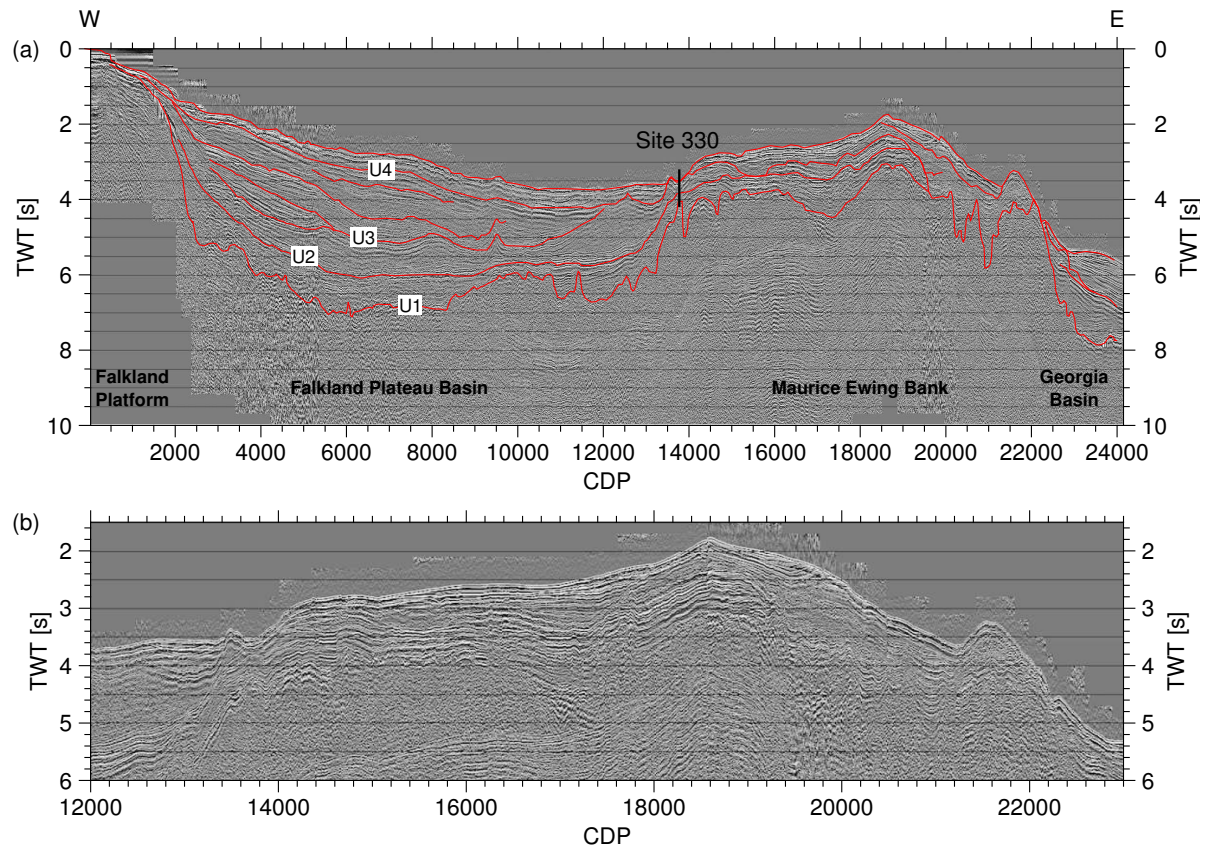


Figure 6.2.: Seismic reflection line 139 (Ludwig et al., 1978) (a) with unconformities (Lorenzo and Mutter, 1988) and in (b) enlarged part of the MEB.

Lorenzo and Mutter (1988) describe how MEB is a basement high over which sediment thicknesses decrease to a minimum of 250 m (line 141). They relate that during the Mid to Late Jurassic, marine transgression resulted in a shelf and basin province. Largely terrigenous sediments were deposited and remained generally undisturbed by any relative movements. Black shales deposited during the Upper Jurassic and Lower Cretaceous point to a period of restricted ocean circulation, attributable to the presence of land barriers to the south and west. MEB subsequently subsided during early Albian times, resulting in enhanced ocean current circulation. Finally, the bank became a site of dominantly pelagic sedimentation (Barker, 1977). Sediments cropping out at the modern seabed near DSDP drill sites represent ages from Late Cretaceous to late Miocene, which Barker (1977) relates to their exposure by significant submarine erosion by strong Neogene currents.

The gneisses, drilled at DSDP site 330, are similar in lithology and composition to the Cape Meredith Complex onshore West Falkland (Barker, 1977). The Cape Meredith rocks date from 1000 – 1100 Ma (Jacobs et al., 1999), significantly older than the

535±66 Ma Rb-Sr date from the MEB gneiss, which Beckinsale et al. (1977) attributed to a hydrothermal event or metamorphic re-crystallization. The shape of the MEB basement is irregular and polygonal, broken up by numerous basins of 10 – 20 km width and 2 – 3 km depth. These basins are asymmetrically V-shaped and interpreted as half-grabens. Steep slopes at the northeast-southwest running margin with the Georgia Basin and along the northern edge of MEB formed by faulting related to post-Middle Jurassic plate motions. The northern margin of the MEB shows a very complex geometry with normal and reverse vertical faults that are accompanied by folding in the lower depositional units (Lorenzo and Mutter, 1988).

6.3.3. Georgia Basin

East of MEB, the water depth increases to 5000 m towards the oceanic Georgia Basin. Single channel seismic reflection data were collected over the basin in preparation for ODP leg 114. From these data, Kristoffersen and LaBrecque (1991) report sediment thicknesses of 1 – 2 s two-way traveltime (TWT), which increase to more than 2.5 s towards the western Georgia Basin. Sedimentary deposits are tectonically undisturbed throughout the basin.

The western and central Georgia Basin was investigated during the DSDP leg 36 (Barker and Dalziel, 1977) with three holes at DSDP drill site 328 (Figure 6.1a). The upper 13.5 m thick sedimentary unit consists of Quaternary to late Miocene diatomaceous ooze with manganese nodules, sand and ice-rafted material with large clasts from the upper Miocene. Below 34 m, late Eocene to late Miocene silty, biogenic siliceous clay was encountered. A decrease in clay content and a lower sedimentation rate compared to the underlying unit, as well as breaks in the stratigraphic record, indicate an increase in bottom current velocities in the late Eocene through the Miocene. The underlying Late Cretaceous or Paleocene to upper Eocene strata comprise siliceous clay and claystones. This 250 m thick unit reveals a fast sedimentation rate, which is probably linked to mid-Cretaceous uplift of the Andean cordillera. In the 471 m deep hole the lowermost drilled unit consists of Upper Cretaceous zeolitic claystone (Barker and Dalziel, 1977).

Magnetic data gathered during the 1976 RRS Shackleton cruise (Barker, 1979) allow identification of the Mesozoic magnetic reversal isochrons M0 to M10 (~125 – 133 Ma) in the western Georgia Basin (Labrecque and Hayes, 1979; Martin et al., 1982). Isochron M10 is located just east of the MEB and profile AWI-20130010 crosses it close to 40° W (OBS 91).

6.4. Data acquisition and data processing

The expedition ANT-XXIX/5 was conducted by the Alfred Wegener Institute for Polar and Marine Research (AWI) with the German icebreaker *Polarstern* from 18th of April until 29th of May 2013. Parallel to the wide-angle experiment with land and ocean bottom stations, magnetic, bathymetry and sediment echosounder data were acquired along the track. Additional magnetic profiles were flown with the ship's helicopter.

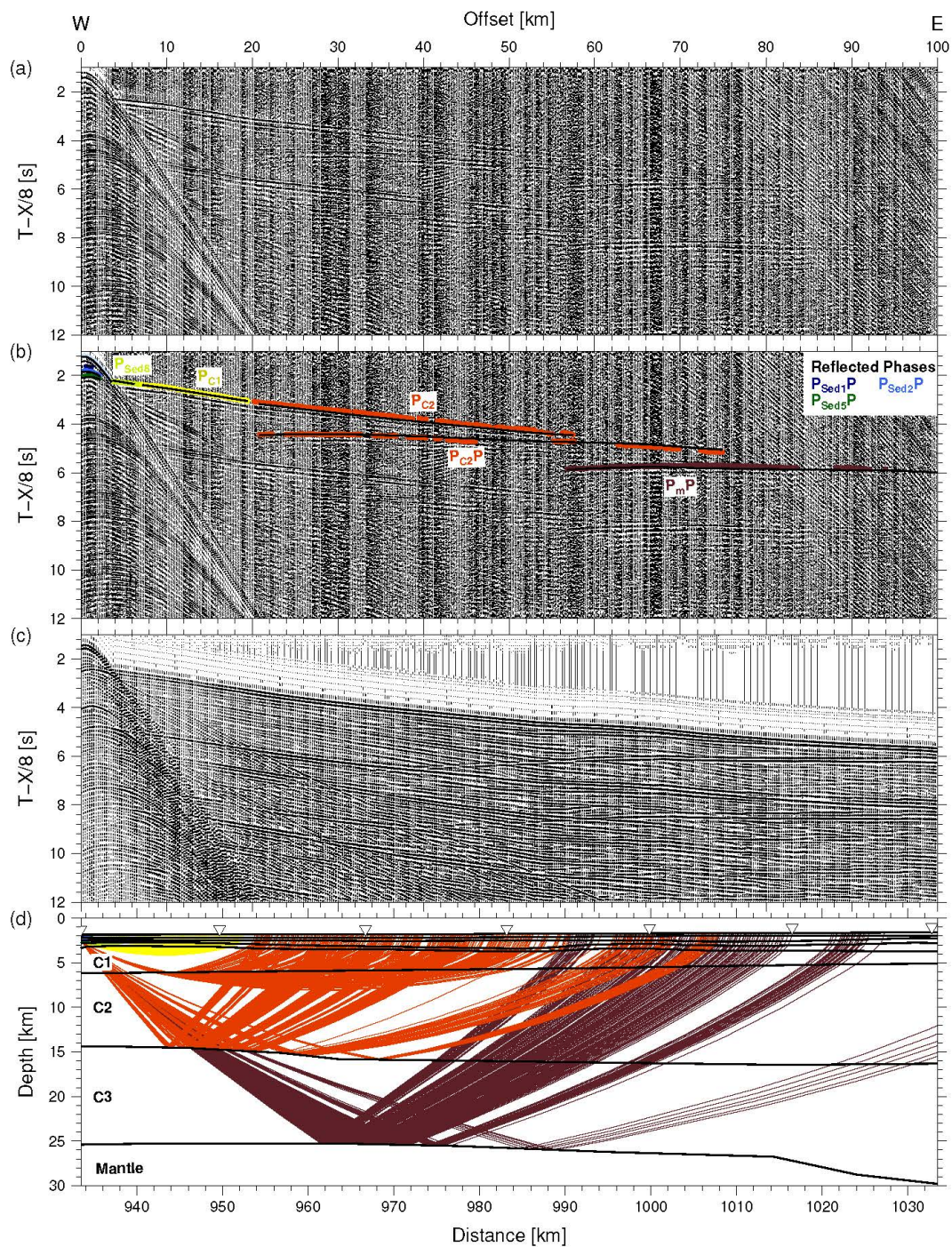


Figure 6.3.: Data example for OBS 66. (a) Seismic section filtered with a 4-15 Hz bandpass filter and displayed with a reduction velocity of 8 km/s. (b) Picked phases with error bars and corresponding phase names. The names of the reflected sediment phases are given in the right corner. The modelled arrivals are plotted as black lines. (c) Synthetic seismogram for OBS 66 calculated with the final P-wave velocity model. (d) Ray paths for picks shown in b. Station positions are marked as triangles.

Unfortunately, it was not possible to acquire seismic reflection data to retrieve information on the geometry of the sediment basin along the profile, because of time and weather constraints (Jokat, 2013).

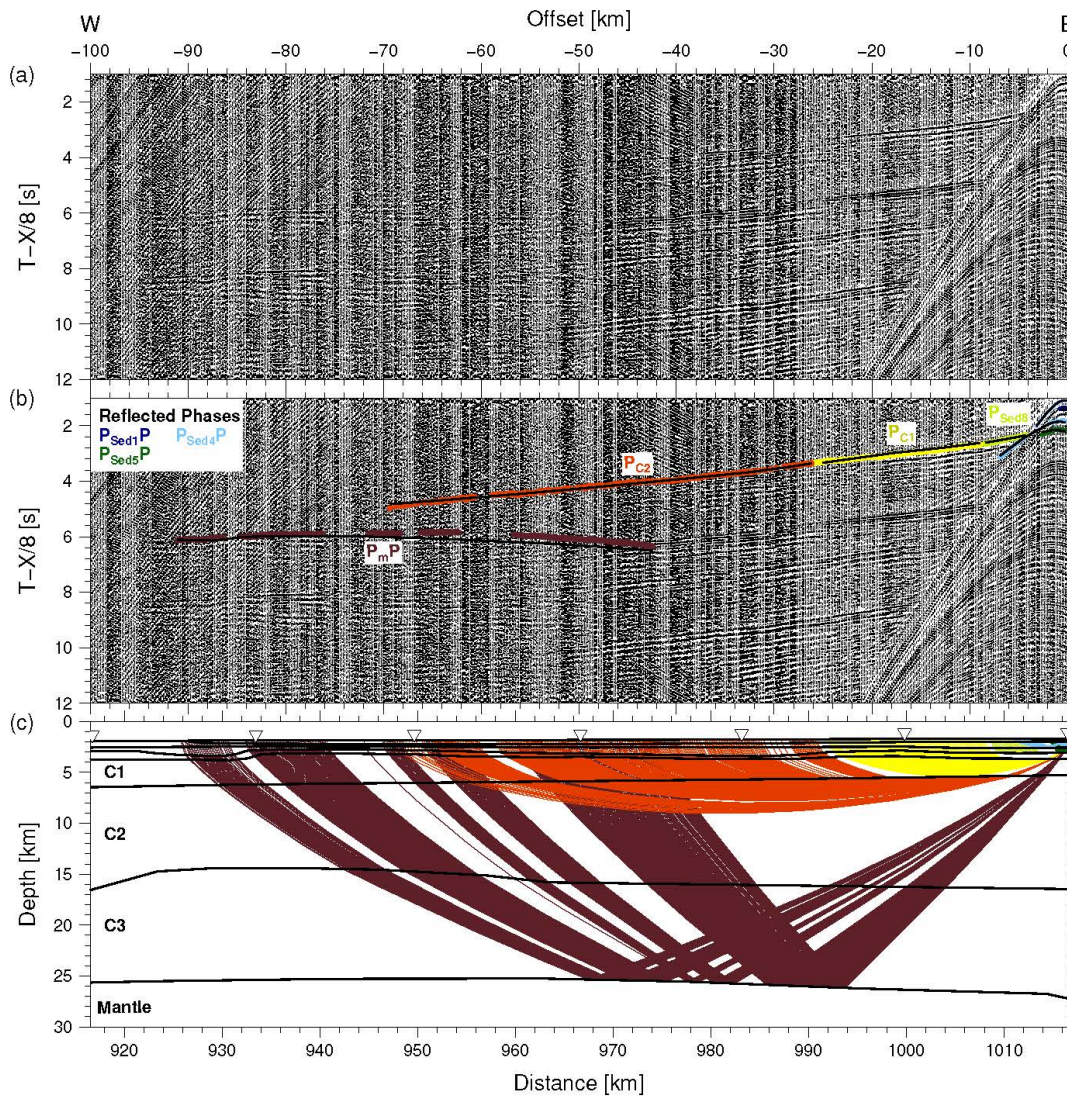


Figure 6.4.: Data example for OBS 71. (a) Seismic section filtered with a 4-15 Hz bandpass filter and displayed with a reduction velocity of 8 km/s. (b) Picked phases with error bars and corresponding phase names. The names of the reflected sediment phases are given in the left corner. The modelled arrivals are plotted as black lines. (c) Ray paths for picks shown in b. Station positions are marked as triangles.

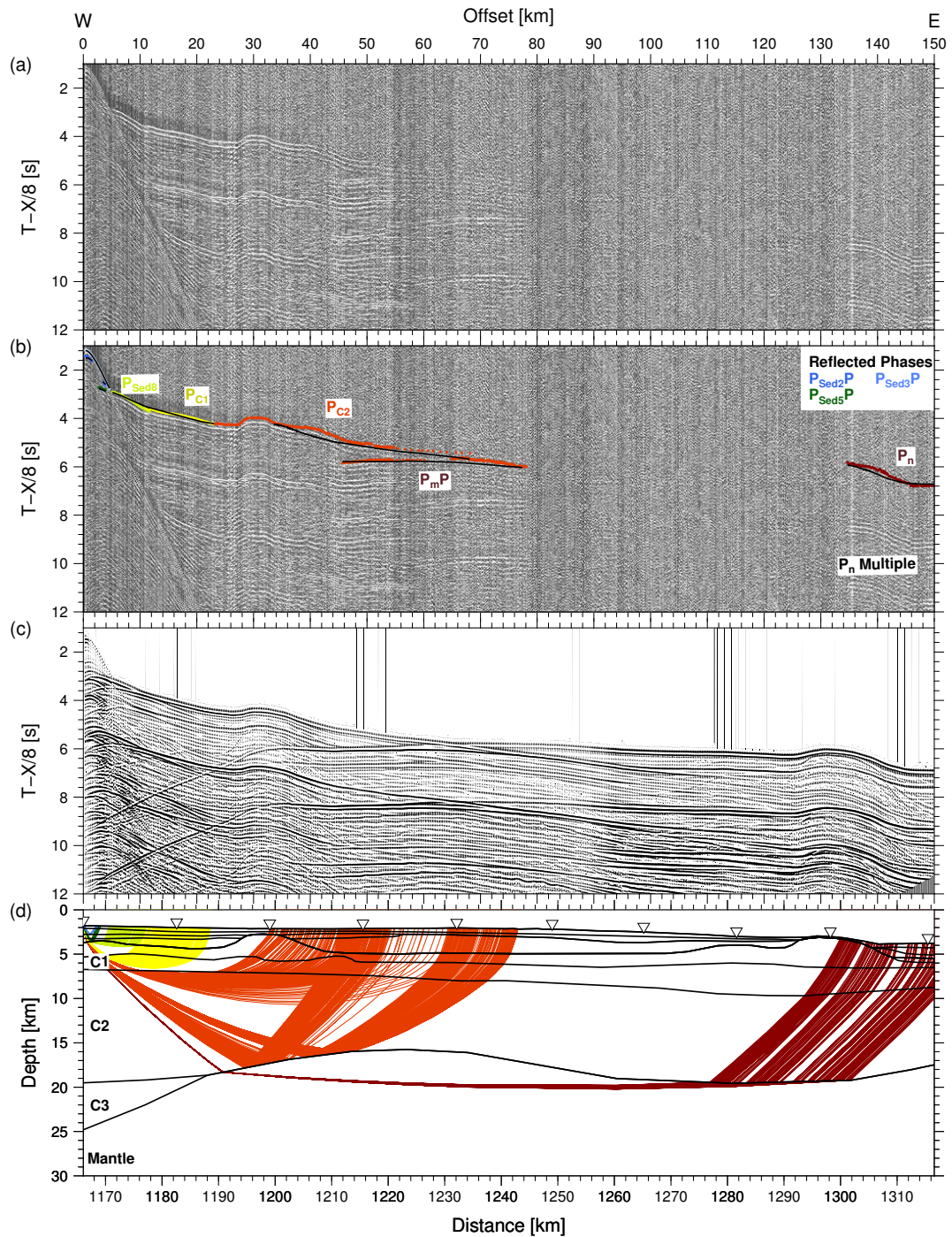


Figure 6.5.: Data example for OBS 80. (a) Seismic section filtered with a 4-15 Hz bandpass filter and displayed with a reduction velocity of 8 km/s. (b) Picked phases with error bars and corresponding phase names. The names of the reflected sediment phases are given in the right corner. The modelled arrivals are plotted as black lines. (c) Synthetic seismogram for OBS 80 calculated with the final P-wave velocity model. (d) Ray paths for picks shown in b. Station positions are marked as triangles.

6.4.1. Seismic refraction data

Wide-angle seismic measurements were conducted along the approximately 1450 km long west-east stretching profile AWI-20130010, which starts onshore East Falkland and terminates east of MEB in the Georgia Basin (Figure 6.1). To investigate the plateau, 39 ocean bottom stations were deployed twice, once each along an eastern and a western profile. The first OBS on the western profile is at station 18. The western profile terminates at station 56, the eastern one starts 33 km further east at station 57. The results of the western profile have been described by Schimschal and Jokat (2018).

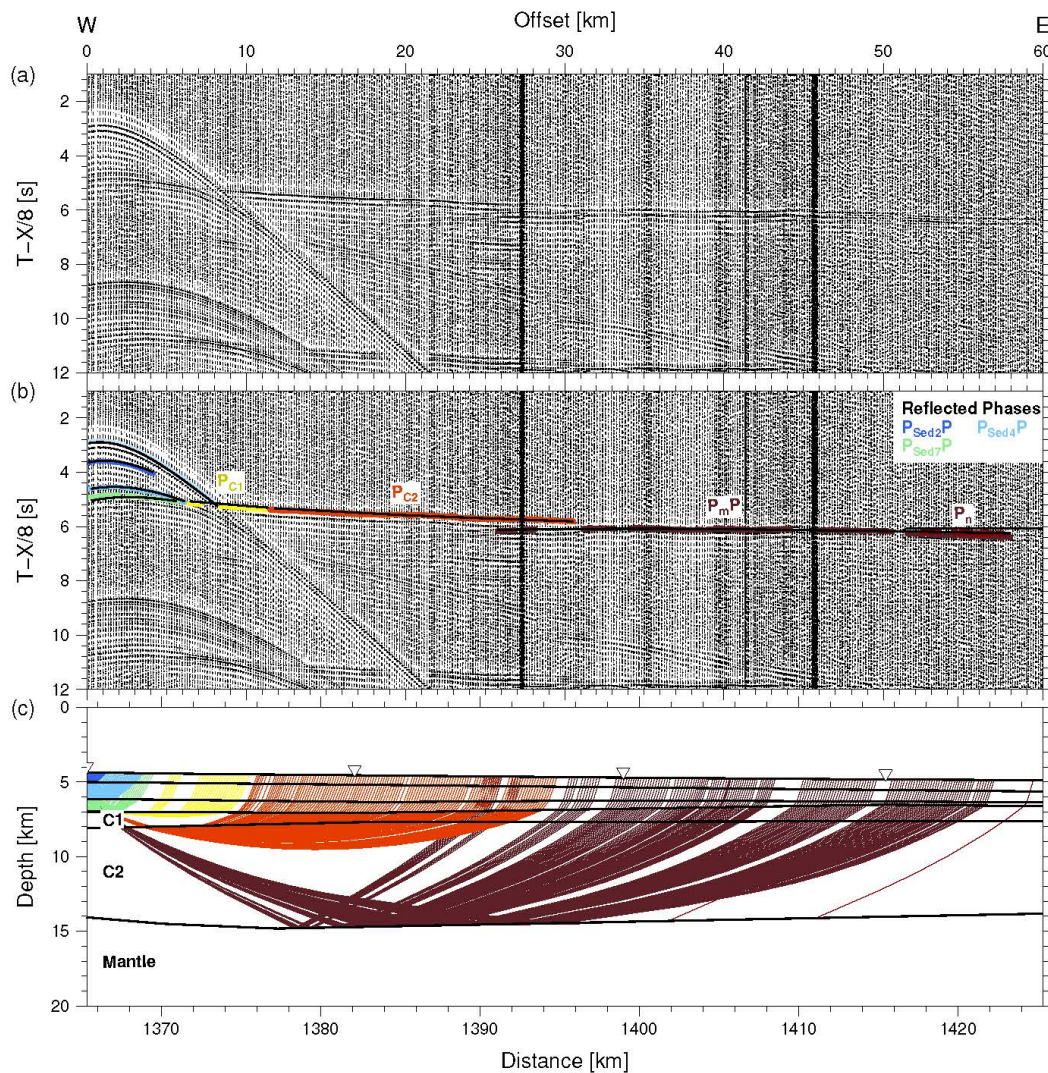


Figure 6.6.: Data example for OBS 92. (a) Seismic section filtered with a 4-15 Hz bandpass filter and displayed with a reduction velocity of 8 km/s. (b) Picked phases with error bars and corresponding phase names. The names of the reflected sediment phases are given in the right corner. The modelled arrivals are plotted as black lines. (c) Ray paths for picks shown in b. Station positions are marked as triangles. Note the different scale compared to Figures 6.3d, 6.4c and 6.5d.

The spacing between the receivers was approximately 16 km. Two different types of stations were used. The 33 ocean bottom seismometers (OBS) were equipped with a hydrophone and a three-component seismometer, while the 6 ocean bottom hydrophones (OBH) recorded the seismic signals only with the hydrophone. The sampling rate for all systems was set to 200 Hz. In total, 5028 shots were generated on the eastern transect and 3864 on the western one, totalling 1300 km of air gun operation. Seismic energy was generated every 60 s with 8 G-Guns with a total volume of 681 (4160 in³). This yields a shot distance of 150 m. All OBS/OBH were recovered, but no data were retained from three stations on the eastern transect. The data were converted to SEG-Y-format and corrected for clock drift. To account for drift during descent to the seafloor, the positions of the OBS/OBH were relocated along the line using direct arrivals. An automatic gain control with a time window of 1 s and a deconvolution filter were applied and the data were bandpass filtered with corner frequencies of 4 Hz and 20 Hz. The data quality is good to very good, with the hydrophone channel having the best data quality for most stations. For MEB stations with very good data quality, phase identification was possible up to an offset of 170 km. Figures 6.3a, 6.4a, 6.5a and 6.6a display the recorded data of stations 66, 71, 80 and 92 with a reduction velocity of 8 km/s.

6.4.2. Potential field data

Airborne magnetic data acquisition was performed by a helicopter launched from *Polarstern* and flying segments parallel to the ship track. The high precision Scintrex Cs3 Cesium vapor magnetometer was towed in an amagnetic bird slung 30 m underneath the helicopter. Profiles were flown ± 10 km off the seismic profile. Additional profiles at 20 km and 5 km separation were acquired as weather permitted. 24 north-south trending tie lines provide for quality control between profiles. During magnetic surveying, the nominal cruise speed of the helicopter was 80 kn (~ 40 m/s) at an altitude of 100 m, and the data were sampled at 10 Hz. The obtained data were corrected for the International Geomagnetic Reference Field (IGRF). Due to the lack of a base station no diurnal correction was applied. Nevertheless, the data of the Port Stanley magnetic observatory (<http://www.geomag.bgs.ac.uk/operations/falklands.html>) show that the diurnal variation on most flight days did not exceed 25 nT. This is considerably smaller than the range of the measured anomalies between -200 nT (km 1310, east of profile AWI-20130010 values decrease to -310 nT) and 185 nT (km 310). The misfits to tie lines are generally less than 10 nT.

Along the entire ship track, additional magnetic measurements were carried out using two permanently-installed three-component digital fluxgate sensors. The three-component data were compensated for the effects of induced fields from the ship's hull via calibration circles. Additionally, the data were IGRF corrected and de-spiked. Cross point analysis with the helicopter magnetic data reveal the ship data to be consistently ~ 150 nT too low compared to the helicopter data. The helicopter data are deemed more reliable, as they are hardly influenced by the induced field from the helicopter. Consequently, we adjusted the ship's data to the helicopter data at their cross points, and linearly interpolated the adjustments between them.

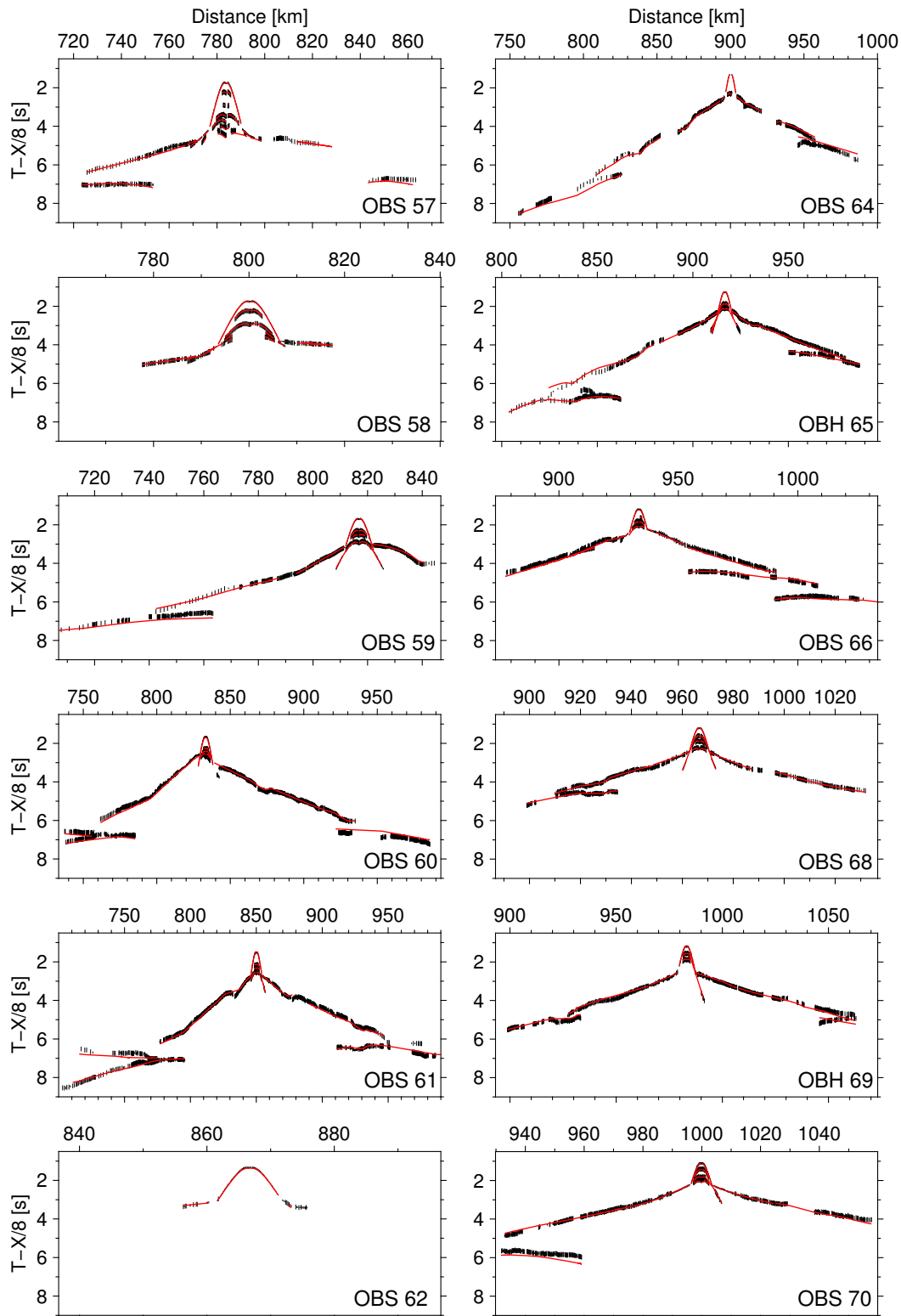


Figure 6.7.: All stations with picked arrivals (shown as black error bars) and modelled arrivals (red).

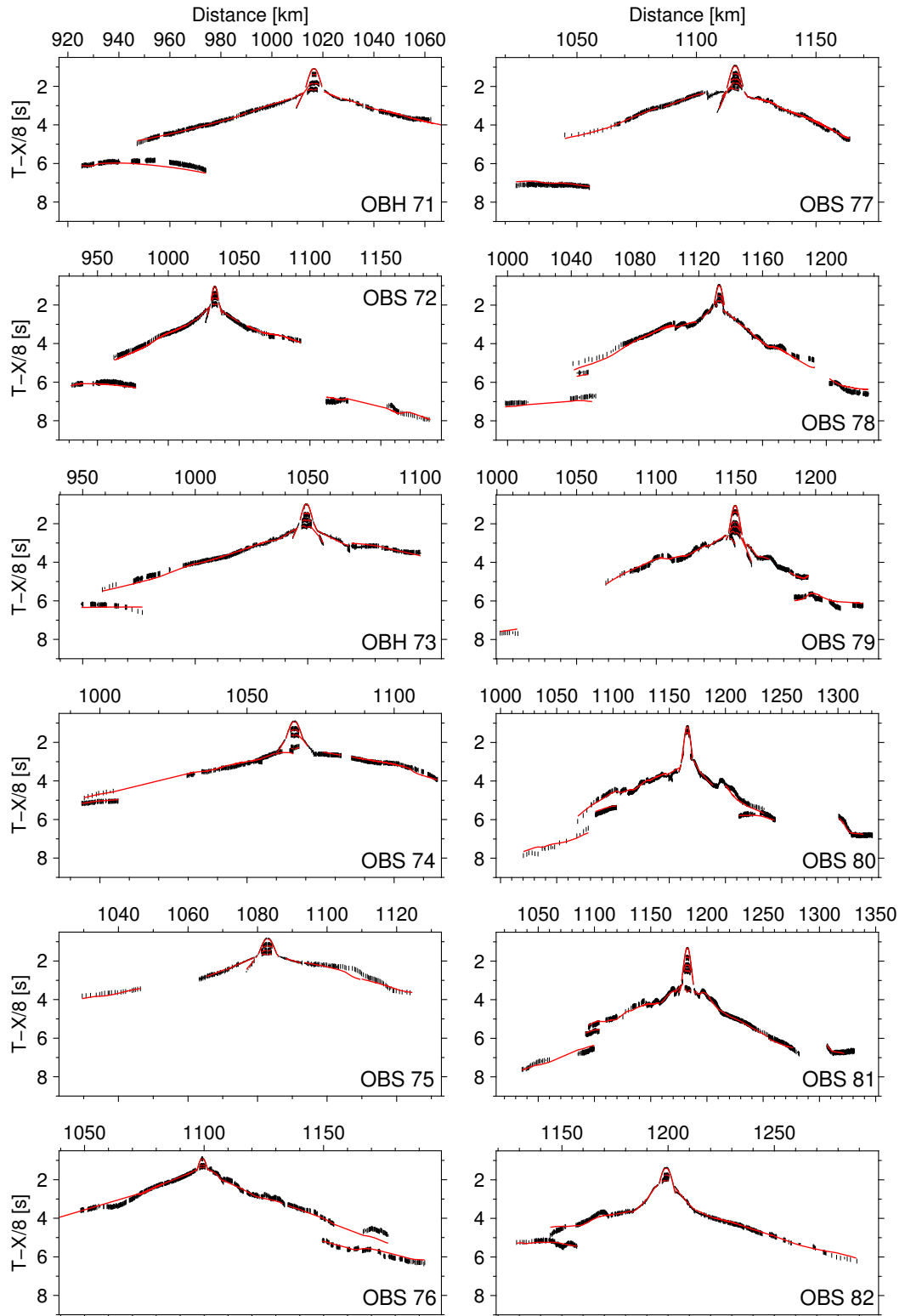


Figure 6.7.: (continued).

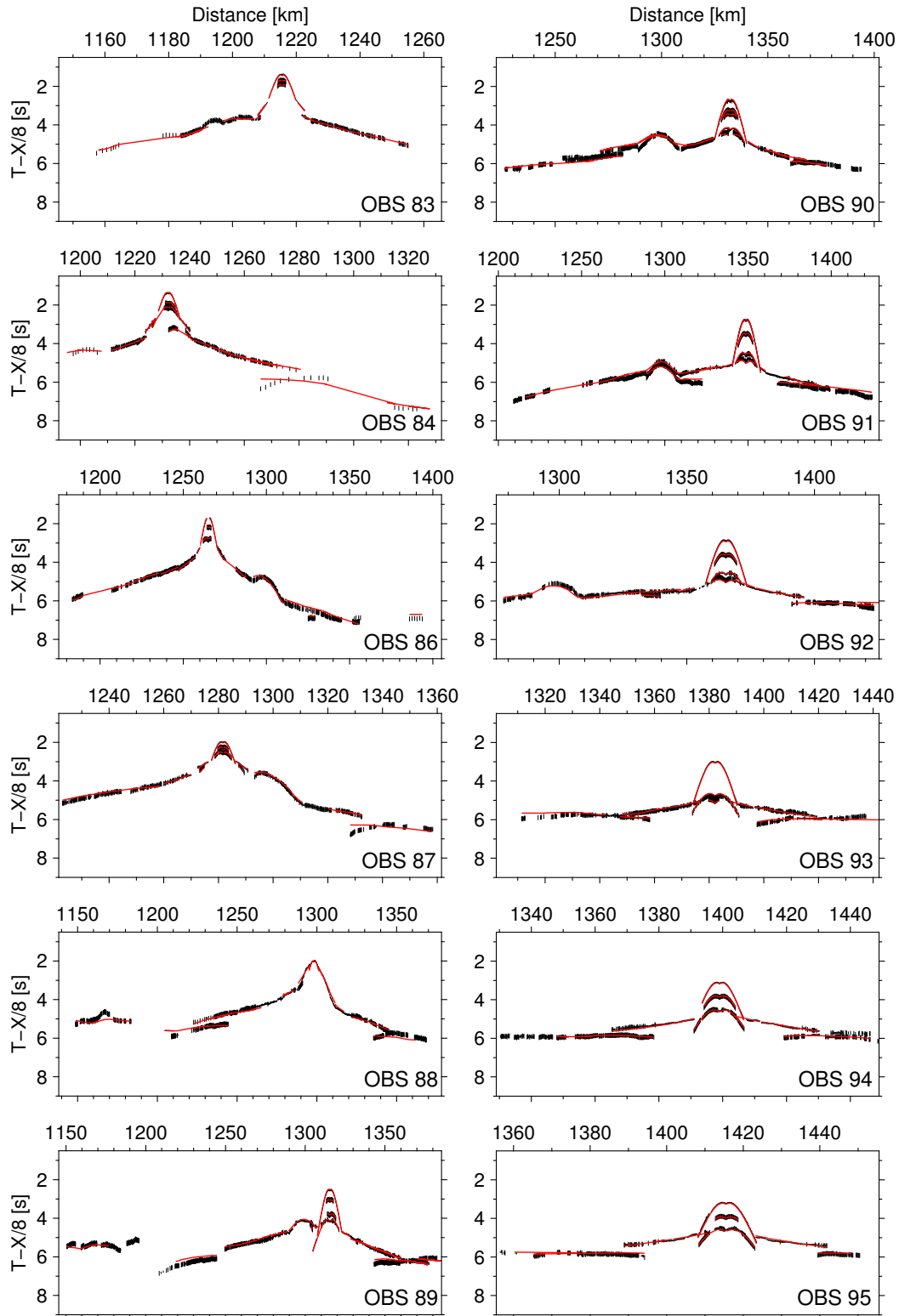


Figure 6.7.: (continued).

6.5. Modelling

6.5.1. Ray tracing

We used the ZP software of B.C. Zelt (<http://www.soest.hawaii.edu/users/bzelt/zp/zp.html>) for picking P-wave arrivals in the seismic record sections. Figures 6.3b, 6.4b, 6.5b and 6.6b show examples of picks in the seismograms of stations 66, 71, 80 and 92. Figure 6.7 displays the picks and calculated arrivals of all stations.

The picks are used to build a model comprising 12 layers (Table 6.1). In the Falkland Plateau Basin, eight sediment layers *Sed1* to *Sed8* can be distinguished. Here, the reflection profile (Ludwig et al., 1978) provided additional constraints. Over MEB, the number of sediment layers varies between one over a local basement high (km 1295 – 1305) and four (km 1100 – 1190). In the Georgia Basin, three sediment layers and an additional sediment body between km 1308 and 1340 were necessary to fit the travel times.

Modelling required just two crustal velocity layers, *C1* and *C2*, beneath the Falkland Plateau Basin and the western part of MEB (km 800 – 860). From km 890 eastwards the crustal fabric is more heterogeneous and, thus, the velocity model of MEB consists of four layers. The oceanic crust of the Georgia Basin consists of two layers. Reflections at the Moho are labelled P_mP and refractions in the mantle P_n .

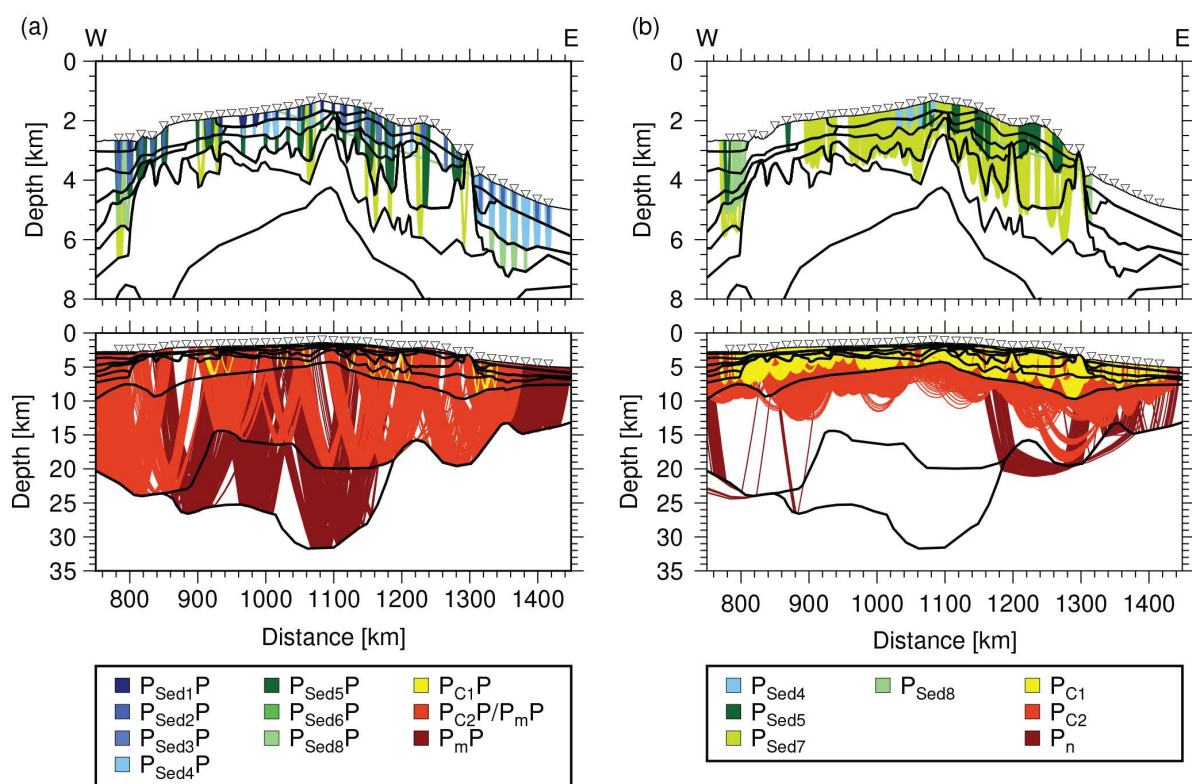


Figure 6.8.: Ray coverage for (a) the reflected phases and (b) for the refracted phases. Station positions (triangles) and layer boundaries (black lines) are marked.

Forward modelling of the P-waves was performed layer-by-layer using *RAYINV*R (Zelt and Smith, 1992) together with *PRay* (Fromm, 2016). In total, 30559 picks were used to determine the model of the eastern transect. Figure 6.8 displays the ray coverages for the reflected (Figure 6.8a) and refracted phases (Figure 6.8b). The upper two sediment layers are only constrained by reflections. Sediment layers at greater depth are defined by reflected and refracted phases. Throughout the model, the uppermost crustal layer *C1* is constrained by refracted phases (P_{C1}). The ray coverage of refracted phases (P_{C2}) in the crustal layer *C2* is limited to the upper ~ 5 km. Underneath MEB, *C3* forms a layer of up to 15 km thickness, which is not covered by refracted phases. The Moho topography is well imaged along the entire transect by reflected phases (P_mP).

Table 6.1.: Statistics of the picked phases. The columns contain the nomenclature of the picked phases, the number of observations of each phase (No of picks), the assigned average pick uncertainty (t_{unc}), the root mean square of the travel time residual (t_{rms}) and the normalized χ^2 .

| Layer | Phase | No of Picks | t_{unc} [ms] | t_{rms} [ms] | χ^2 |
|-----------------------------------|--------------|-------------|----------------|----------------|----------|
| Waterwave | $P_{Water}P$ | 2100 | 42 | 56 | 2.035 |
| Reflection at base of <i>Sed1</i> | $P_{Sed1}P$ | 287 | 117 | 72 | 0.499 |
| Reflection at base of <i>Sed2</i> | $P_{Sed2}P$ | 692 | 123 | 54 | 0.206 |
| Reflection at base of <i>Sed3</i> | $P_{Sed3}P$ | 534 | 120 | 56 | 0.287 |
| Refraction in <i>Sed4</i> | P_{Sed4} | 90 | 53 | 37 | 0.944 |
| Reflection at base of <i>Sed4</i> | $P_{Sed4}P$ | 897 | 90 | 62 | 1.009 |
| Refraction in <i>Sed5</i> | P_{Sed5} | 196 | 53 | 49 | 0.947 |
| Reflection at base of <i>Sed5</i> | $P_{Sed5}P$ | 746 | 109 | 58 | 0.489 |
| Refraction in <i>Sed7</i> | P_{Sed7} | 63 | 58 | 27 | 0.358 |
| Reflection at base of <i>Sed7</i> | $P_{Sed7}P$ | 246 | 105 | 73 | 0.886 |
| Refraction in <i>Sed8</i> | P_{Sed8} | 1618 | 67 | 58 | 1.929 |
| Reflection at base of <i>Sed8</i> | $P_{Sed8}P$ | 158 | 108 | 106 | 1.193 |
| Refraction in <i>C1</i> | P_{C1} | 4953 | 89 | 64 | 0.971 |
| Reflection at base of <i>C1</i> | $P_{C1}P$ | 89 | 93 | 73 | 1.556 |
| Refraction in <i>C2</i> | P_{C2} | 10130 | 100 | 96 | 1.525 |
| Reflection at base of <i>C2</i> | $P_{C2}P$ | 4005 | 109 | 130 | 2.211 |
| Reflection at Moho | P_mP | 3140 | 109 | 130 | 2.034 |
| Refraction in mantle | P_n | 615 | 107 | 131 | 1.809 |
| All stations | all | 30559 | 96 | 95 | 1.532 |

Uncertainties and error analyses

Depth and velocity uncertainties have been determined with the method described by Schlindwein and Jokat (1999). Velocity and boundary knots were perturbed until the calculated travel times were outside the range of assigned uncertainties of the observed data. The perturbations were applied layer-wise and separately for velocities and depths. The depth uncertainty of sediment layers does not exceed ± 100 m on MEB and in

the Georgia Basin. Uncertainties for the sediment velocities over MEB vary between ± 0.1 km/s and ± 0.2 km/s depending on the offset to which phases could be picked. For the Georgia Basin, the velocity uncertainty does not exceed ± 0.1 km/s.

The depth uncertainty for the two upper crustal layers of MEB is only ± 100 m, because of their shallow depth. In the Georgia Basin, the depth uncertainty increases to ± 200 m. The velocity uncertainty for $C1$ and the upper part of $C2$ beneath MEB and the Georgia Basin is estimated at less than ± 0.2 km/s. The lower crustal velocity above the Moho is not constrained by refracted rays, but instead by the move out hyperbolae of reflected phases and by amplitude modelling. The depth uncertainty for the Moho is ± 2.5 km beneath MEB and ± 1.5 km beneath the Georgia Basin.

The normalized χ^2 values and the root mean square (RMS) travel time residuals provide an estimate of model quality. For each layer, the values are given together with the assigned pick uncertainty in Table 6.1. Pick uncertainties range between 42 ms and 123 ms depending on the signal-to-noise ratio. The RMS misfit for the entire model is 95 ms and the normalized χ^2 is 1.53. 1 would be optimum for the normalized χ^2 .

6.5.2. Amplitude modelling

Because of the limited ray coverage, the lower part of the crust is poorly constrained by diving waves. Here, amplitude modelling can provide additional information for the lower crustal velocity structure. Thus, we conducted amplitude modelling using the *SOFI2D* (Seismic mOdelling with FInite differences, Bohlen, 2002) software. The code is based on finite differences (FD) and calculates the wave equation throughout a discretized model. In this way, *SOFI2D* computes the 2-dimensional propagation of P- and SV-waves through a viscoelastic medium. In addition to the wave field, the acoustic impedance is determined at layer boundaries. The code expects input of P- and S-wave velocities and a density model for calculation of the wave field and impedance. Because no clear S-waves are visible in the data, P-wave velocities were converted into S-wave velocities using the simple division by $\sqrt{3}$. Densities are determined according to Barton's rule (Barton, 1986). Because the viscoelastic case is considered, the intrinsic attenuation for P- and S-waves is required and calculated based on Brocher (2008). The P-wave velocity model had to be discretised in order to compute the wave field propagation. This was done with 25 m horizontal and vertical spacing. Computation of the wave field is performed in 1 ms time steps for 30 s. As a source signal, a Ricker wavelet with a centre frequency of 5 Hz was applied. These parameters ensured the stability of the FD code and avoided numerical dispersion effects while keeping the computation time reasonable. The resulting synthetic seismograms were normalized to the maximum amplitudes to enable comparison with the observed ones.

For MEB, the objective of amplitude modelling is to retrieve information about the crustal velocity in the lower crustal layers $C2$ and $C3$ and to facilitate phase identification for far offsets. Clear intracrustal reflections at 15 to 20 km depth (km 925 – 965) mark the top of the lower crustal layer $C3$. The topography at the base of $C3$ (Moho) is imaged by P_mP arrivals, but no diving waves penetrated into the lower crust. The amplitudes of the refracted phase P_{C2} and the reflected phase $P_{C2}P$ are considered

in order to gain information about the velocity contrast at the boundary between the middle ($C2$) and lower crust ($C3$). Synthetic seismograms are calculated for several models. The amplitude trends of three models are displayed in Figure 6.9.

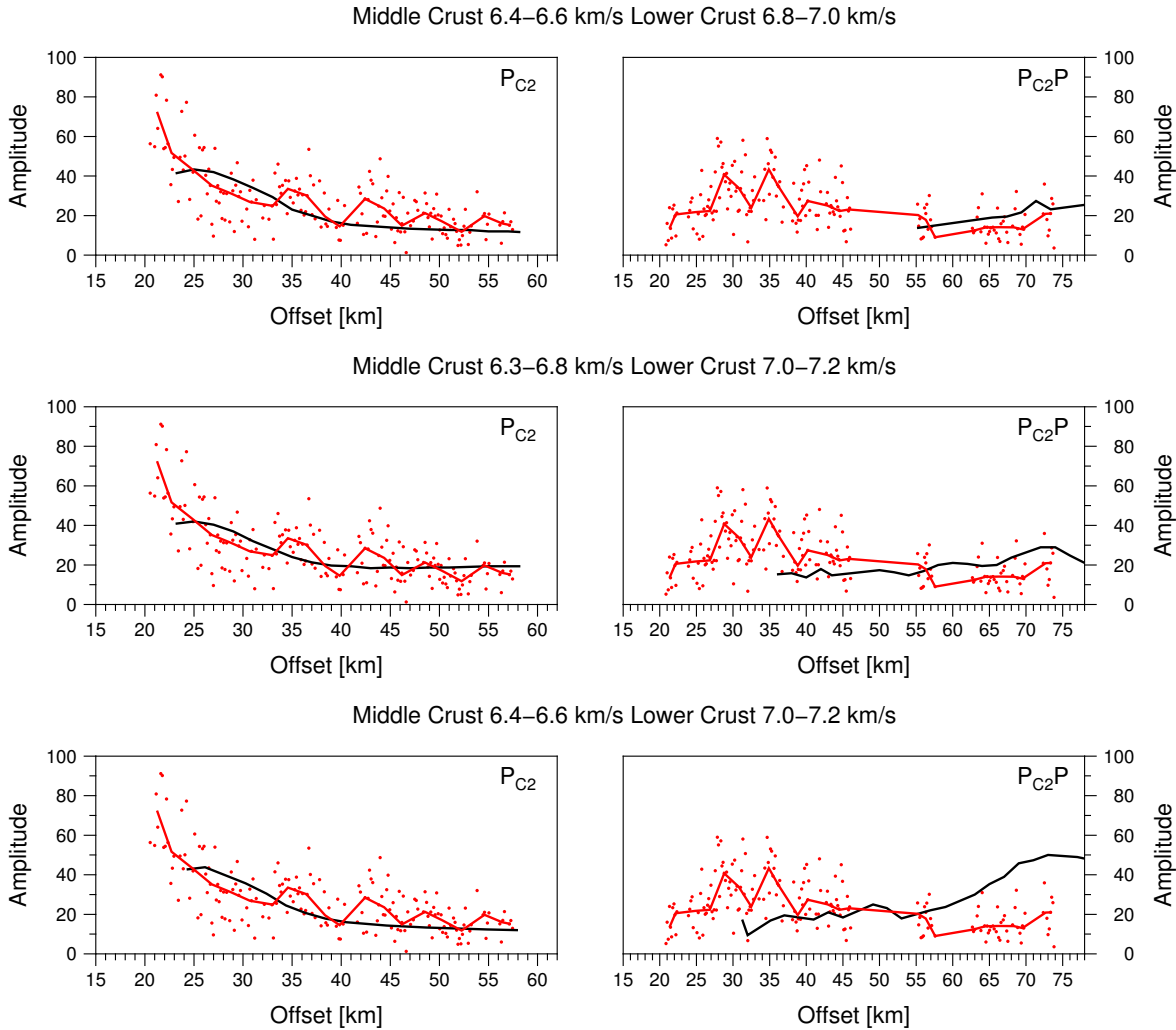


Figure 6.9.: Results of the FD-modelling for OBS 66 for three different velocity models. The left side shows the amplitude trend for the refraction in $C2$ and the right side for the reflection at the base of $C2$. The red line represents the 2 km median of the real amplitudes (red dots). The black line shows the trend of the synthetic amplitudes.

The observed amplitudes of P_{C2} show a clear trend (Figure 6.9 left side, red). All synthetic seismograms reproduce this trend. The observed amplitudes of P_{C2P} (Figure 6.9 right side, red) show generally strong scattering and their trend is less clear than the one of the P_{C2} . P_{C2P} cannot be picked at all in the synthetic seismogram at offsets less than 55 km in the model with a velocity contrast from 6.6 km/s to 6.8 km/s (Figure 6.9 upper panel); this velocity contrast was rejected. A velocity contrast from 6.6 km/s to 7.0 km/s (Figure 6.9 lower panel) was similarly rejected because the calculated amplitude trend

shows clear differences to the observed one between km 55 and 75. The middle panel of Figure 6.9 shows the amplitude trend for a P-wave velocity model with a middle crustal velocity structure increasing between 6.3 km/s and 6.8 km/s, and a lower crustal velocity from 7.0 km/s to 7.2 km/s. Although P_{C2P} cannot be picked in this model's synthetic seismograms for offsets less than 35 km, its velocity structure is favoured because of the similarities of the amplitude trends.

In addition to the comparison of the amplitude trend, the synthetic seismograms can be used to facilitate phase identification for stations with phases at far offsets. Figure 6.5a shows the seismogram from station 80; noise obscures the phases between km 80 and 135. However, between km 135 and 160, a phase is visible at 8.5 to 9 s reduced travel time, which, by comparison with the synthetic seismogram, can be confidently identified as the first multiple of P_n . After shifting the picks by the amount of time between first arrival and first multiple, the phase is explained by the model (black line in Figure 6.5b represents the calculated arrival time from *RAYINVR*).

6.5.3. Gravity modelling

To ensure that the ray tracing model is consistent with the observed gravity field, forward gravity modelling was conducted using *IGMAS+* (Götze, 1978; Schmidt and Götze, 1998). The software package calculates the density response for a 2.5D model. Layers are triangulated between parallel vertical cross sections to form polyhedra to which densities can be assigned for calculation of the gravimetric effect. The geometry of the velocity model was used as input for density modelling.

To avoid edge effects, the model was prolonged east and west by an additional 100 km. Similarly, additional cross sections with the same density configuration as in the main section were introduced 1000 km north and south of the area of interest.

Initial sediment densities were estimated based on Gardner et al. (1985) and adjusted iteratively during the modelling process. Crustal densities were assigned starting from the velocity-density relationship of Christensen and Mooney (1995).

The free-air gravity anomaly was extracted from the satellite derived anomaly map of Sandwell et al. (2014). The observed free-air gravity anomaly varies between a minimum of -15.9 mGal at km 1316 in the COT between the MEB and the Georgia Basin and two areas with maximum values of 68.0 mGal and 70.7 mGal on the MEB (km 1040 and km 1098). To account for lateral density changes, layers were vertically divided into separate blocks.

Error analysis

The standard deviation between the calculated and observed free-air gravity anomaly is 4.6 mGal, considerably smaller than the uncertainty of the gravity modelling method (± 10 mGal, Ljones et al., 2004). Maximum misfits between the observed and calculated free-air gravity anomalies are located in the COTs and in areas with lateral density changes north and south of the profile. Elsewhere, the misfit does not exceed ± 5 mGal. At the COTs between the Falkland Plateau Basin and MEB (km 790 – 820) and between

MEB and the Georgia Basin (km 1300 – 1320), the calculated free-air gravity anomalies are smaller than the observed ones (maximum differences of 11 mGal and 13 mGal). The misfit in these COTs can be related to our usage of blocks with uniform density instead of lateral density gradients. The misfit between km 660 and 750 is related to the source of a strong negative anomaly south of the profile (Figure 6.1b). Over MEB, the biggest difference between observed and calculated anomalies occurs with 16 mGal between km 1010 and 1070. Seismic reflection data (Ludwig et al., 1978) reveal the presence a local basement high 18 km to the south, which is likely to cause the positive free-air gravity anomaly.

6.6. Results

6.6.1. Velocity model

The final P-wave velocity model is displayed in Figure 6.10. Table 6.2 provides an overview of the layers and corresponding velocities. The velocity structure will be described from west to east starting with the sediment layer distribution, and followed by details about the crustal fabric.

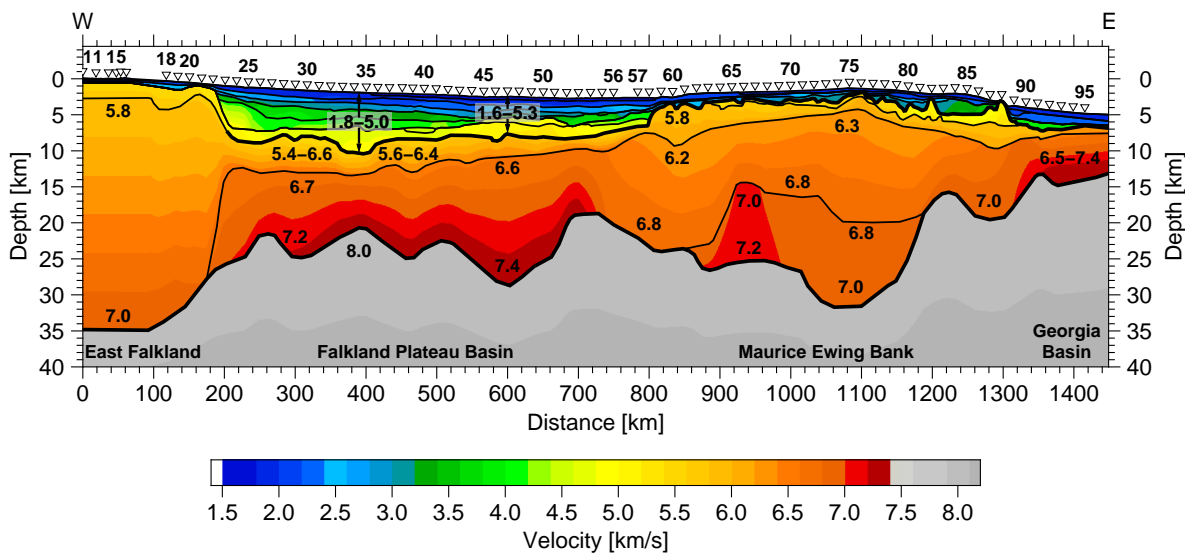


Figure 6.10.: P-wave velocity model of AWI-20130010. The numbers indicate P-wave velocities in km/s. Station positions (triangles) and velocity layer boundaries (black lines) are depicted. Thicker lines indicate the basement and the Moho. The western transect (km 0 – 750, Schimschal and Jokat, 2018) is shown to provide a view on the velocity structure of the entire profile.

Table 6.2.: Layer type and the according velocity (v) and density (ρ) range.

| Basin (km 0 – 800) | | | | |
|---------------------------------------|---------------|-----------------------------------|------------|-----------------------------|
| Layer | Type | Location | v [km/s] | ρ [g/cm ³] |
| <i>Sed1</i> | Sediment | Island and shelf | 1.6 – 1.8 | 1.95 |
| | Sediment | Basin | 1.6 – 1.6 | 1.95 |
| <i>Sed2</i> | Sediment | Island and shelf | 1.8 – 2.1 | 2.05 |
| | Sediment | Basin | 1.7 – 2.1 | 2.05 |
| <i>Sed3</i> | Sediment | Island and shelf | 2.2 – 2.6 | 2.2 |
| | Sediment | Basin | 2.1 – 2.9 | 2.2 |
| <i>Sed4</i> | Sediment | Basin | 2.6 – 3.3 | 2.3 |
| <i>Sed5</i> | Sediment | Basin | 3.4 – 3.9 | 2.2 – 2.54 |
| <i>Sed6</i> | Sediment | Basin (km 200 – 260) | 4.1 – 4.9 | 2.45 |
| | Sediment | Basin | 4.0 – 4.3 | 2.48 |
| <i>Sed7</i> | Sediment | Basin | 4.5 – 4.6 | 2.55 |
| | Intrusions | Basin (km 560 – 680) | 4.5 – 5.0 | 2.65 |
| <i>Sed8</i> | Cont. crust | Island and shelf | 5.5 – 5.7 | 2.58 – 2.65 |
| | Sediment | Basin | 4.6 – 5.0 | 2.70 |
| <i>C1</i> | Cont. crust | Island and shelf | 5.8 – 7.0 | 2.60 |
| | Trans. crust | Profile km 200 – 330 | 5.3 – 6.6 | 2.75 – 2.80 |
| | Oceanic crust | Profile km 330 – 750 | 5.4 – 6.6 | 2.93 |
| <i>C2</i> | Trans. crust | Profile km 200 – 330 | 6.6 – 7.2 | 2.85 – 2.90 |
| | Oceanic crust | Profile km 330 – 750 | 6.6 – 7.4 | 3.05 |
| Mantle | Mantle | Entire profile | 8.0 – 8.2 | 3.40 |
| MEB (km 800 – 1310) | | | | |
| Layer | Type | Location | v [km/s] | ρ [g/cm ³] |
| <i>Sed1</i> | Sediment | central eastern, central western | 1.9 – 2.0 | 1.95 |
| <i>Sed2</i> | Sediment | western, central eastern, eastern | 1.9 – 2.1 | 1.95 – 2.05 |
| <i>Sed3</i> | Sediment | western, central eastern, eastern | 2.0 – 2.4 | 2.00 – 2.40 |
| <i>Sed4</i> | Sediment | central eastern, eastern | 2.4 – 2.5 | 2.10 |
| <i>Sed5</i> | Sediment | above basement all segments | 2.4 – 3.6 | 2.10 – 2.45 |
| <i>Sed8</i> | Cont. crust | km 885 – 1320 | 4.8 – 5.7 | 2.55 – 2.75 |
| <i>C1</i> | Cont. crust | entire MEB | 5.5 – 6.2 | 2.70 |
| <i>C2</i> | Cont. crust | entire MEB | 6.2 – 6.8 | 2.85 |
| <i>C3</i> | Cont. crust | km 855 – 1190 | 6.8 – 7.2 | 2.90 |
| Georgia Basin (km 1310 – 1449) | | | | |
| Layer | Type | Location | v [km/s] | ρ [g/cm ³] |
| <i>Sed2</i> | Sediment | Basin | 1.8 – 1.9 | 2.20 |
| <i>Sed3</i> | Sediment | km 1310 – 1340 | 2.1 – 2.2 | 2.00 |
| <i>Sed4</i> | Sediment | Basin | 2.2 – 2.5 | 2.40 |
| <i>Sed7</i> | Sediment | Basin | 3.9 – 4.0 | 2.42 |
| <i>C1</i> | Oceanic crust | Basin | 5.8 – 6.4 | 2.90 |
| <i>C2</i> | Oceanic crust | Basin | 6.5 – 7.4 | 3.02 – 3.20 |

Velocity structure of the sediments

The Falkland Plateau Basin (km 200 – 800)

In the Falkland Plateau Basin eight sediment layers are introduced in our velocity model (Figure 6.11) and the layer nomenclature is given in Figure 6.12b.

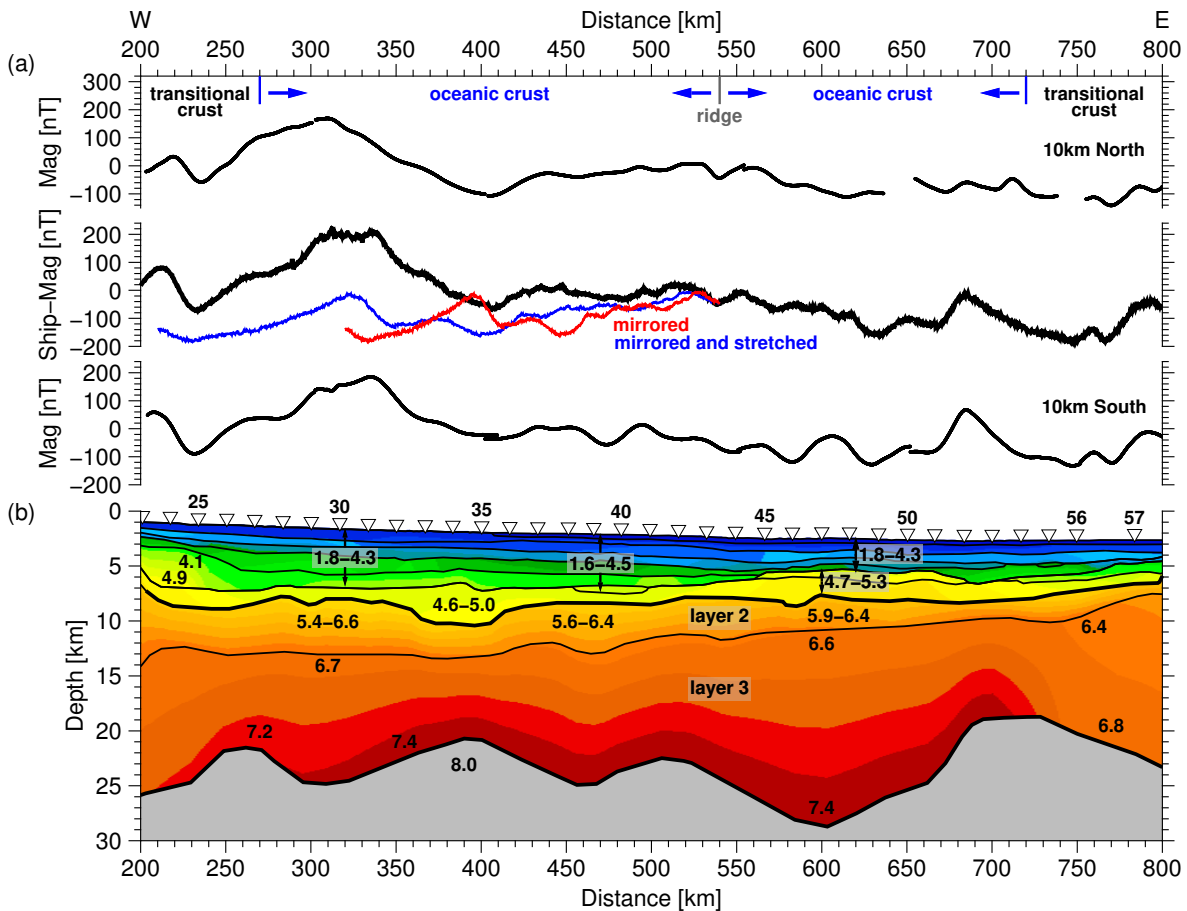


Figure 6.11.: The Falkland Plateau Basin. (a) Magnetic anomaly data along profile AWI-20130010 and 10 km north and south to the profile. The ship data is mirrored to show that the anomaly trend is symmetric around the spreading ridge at km 540 when applying a stretching factor of 1.5. (b) Velocity model with station positions (triangles). The color scale is the same as in Figure 6.10.

In total, the sediment thickness ranges between 4.1 km close to the basin's eastern margin (km 783 – 798) and a maximum of 8.4 km in the west at km 396 close to the Falkland Islands. Velocities range from 1.6 km/s in *Sed1* to 5.3 km/s above basement in *Sed8* between km 550 and 700. Elsewhere in the basin, sediment velocities do not exceed 5.0 km/s. The basement lies at 7.8 to 10.4 km depth. For the Falkland Plateau Basin, Figure 6.12a displays the seismic reflection data of line 139 (Ludwig et al., 1978) combined with the P-wave velocity model converted into TWT.

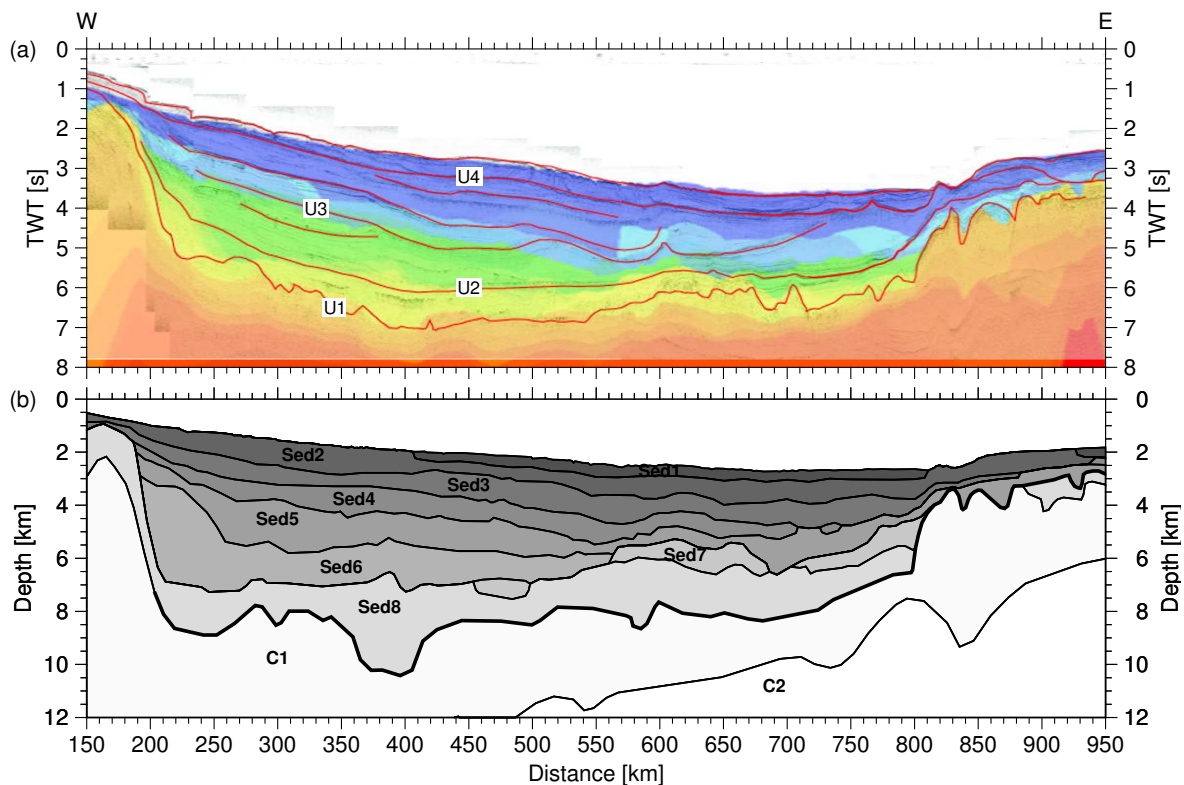


Figure 6.12.: (a) Seismic reflection line 139 (Ludwig et al., 1978) combined with the P-wave velocity model in TWT. The unconformities (Lorenzo and Mutter, 1988) are plotted in red. The color scale is the same as in Figure 6.10. (b) Nomenclature of the sediment layers above the crustal layers *C1* and *C2*.

Maurice Ewing Bank (km 800 – 1320)

The velocity model for MEB is enlarged and plotted in Figure 6.13b. MEB is characterized by a basement high with pronounced basement topography. Sediment thickness varies over the small basins and highs of this topography, ranging between a maximum of ~ 3 km (km 1210 – 1270) and a minimum of 300 m (km 1295 – 1300). As well as this thickness variation, the sediment velocity structure varies such that the number of model sediment layers ranges between four in some basement depressions (km 1105 – 1195, 1200 – 1222) and one over a local basement high (km 1292 – 1306). Table 6.2 provides an overview on these model sediment layers.

On western MEB (km 810 – 935), the velocity in the uppermost sediment unit is 2.0 km/s. Below, a thin (200 m) layer is observed between km 810 and 880 with a velocity of 2.2 km/s. The lowermost, up to 1.1 km thick sediment unit, has a velocity of 2.4 km/s. On the central western MEB (km 935 – 1095), three sediment layers can be identified with velocities from 1.9 km/s in the uppermost layer to 3.0 km/s at basement. Between km 1095 and 1104, sediments thin to 500 m on a local basement high with only two velocity layers (1.9 km/s and 3.1 km/s). East of the basement high (central eastern MEB, km 1104 – 1195), four sediment layers exist with velocities from 1.9 km/s to 3.1 km/s. Be-

tween km 1195 and 1205, sediment layers are reduced to two with velocities of 1.9 km/s and 2.1 km/s on a basement high. Sediments are modelled over eastern MEB (km 1205 – 1290) using four layers. The maximum sediment thickness over MEB, 3 km, is reached here. MEB is terminated by a basement high (km 1290 – 1320), which is covered by only one sediment layer (1.9 km/s, 100 m thick).

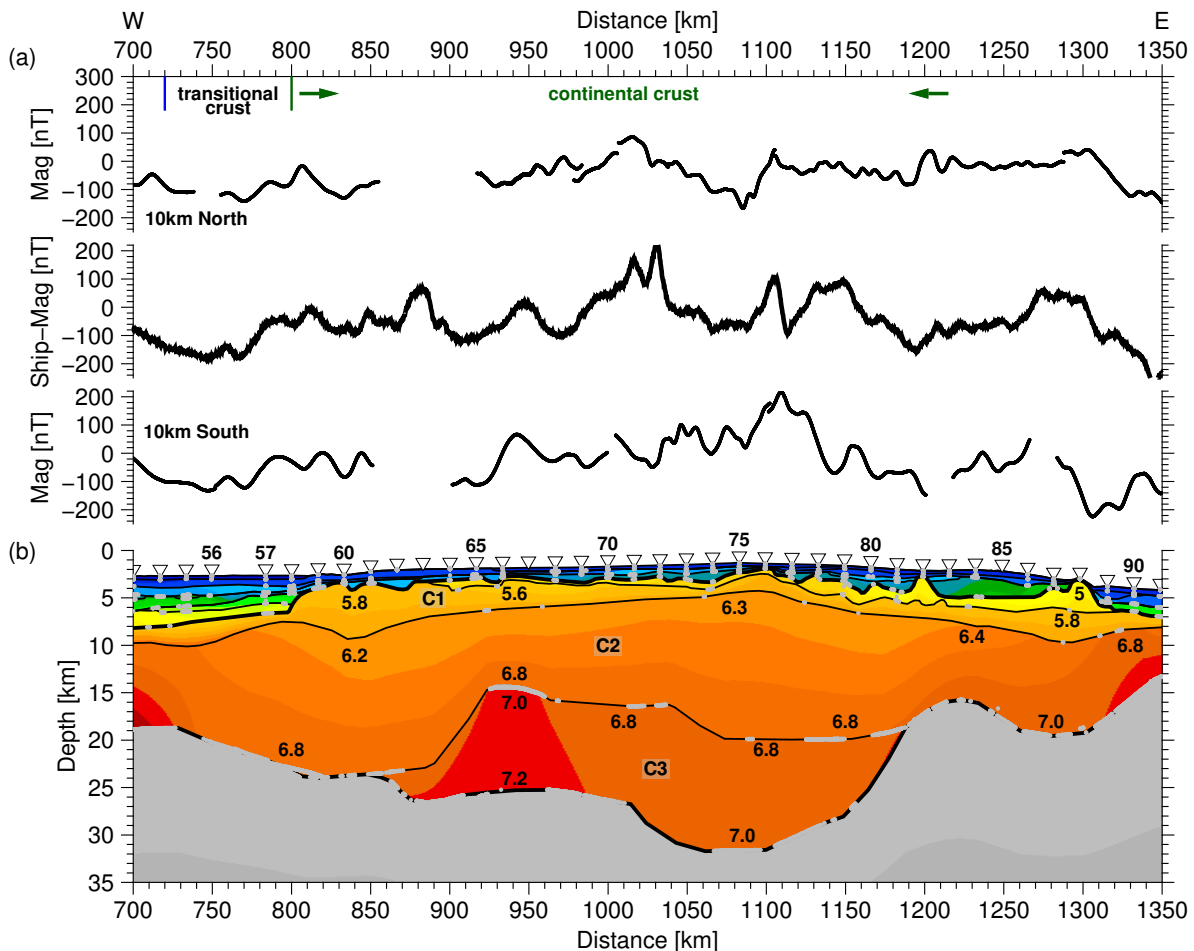


Figure 6.13.: Maurice Ewing Bank. (a) Magnetic anomaly data along profile AWI-20130010 and 10 km north and south to the profile. (b) Velocity model with station positions (triangles). The color scale is the same as Figure 6.10. The numbers indicate P-wave velocities in km/s. Parts of layer boundaries that are constrained by reflections are plotted as thick grey line.

The Georgia Basin (km 1310 – 1449)

Four sediment layers are present in the Georgia Basin (Figure 6.14a) with a total thickness of 1.6 to 2.9 km. The uppermost 600 m thick layer has a velocity of 1.8 km/s and exists from the eastern rim of MEB all the way into the basin. Close to the MEB margin, a narrow sediment layer, that is just 30 km wide (Figure 6.14a, km 1309 – 1339) with

a velocity of 2.1 km/s and a maximum thickness of 800 m, is modelled. The underlying layer has velocities of between 2.2 km/s and 2.4 km/s. It is only 300 m thick close to the MEB margin, but increases eastwards to a maximum of 1.1 km at km 1340 – 1449. The velocity in the layer above basement is 3.9 km/s. Its thickness reaches a maximum of 1.0 km at km 1355, and decreases towards the east and west.

Seismic reflection profile RC1504 (Figures 6.1a; 6.14b) crosses profile AWI-20130010 east of MEB (km 1300) and provides additional more detailed information on the sediment structure. In the upper half of RC1504, flat-lying, layered sediments are visible for 2.2 s TWT. The lower part rests on basement with little topography and has no internal reflections.

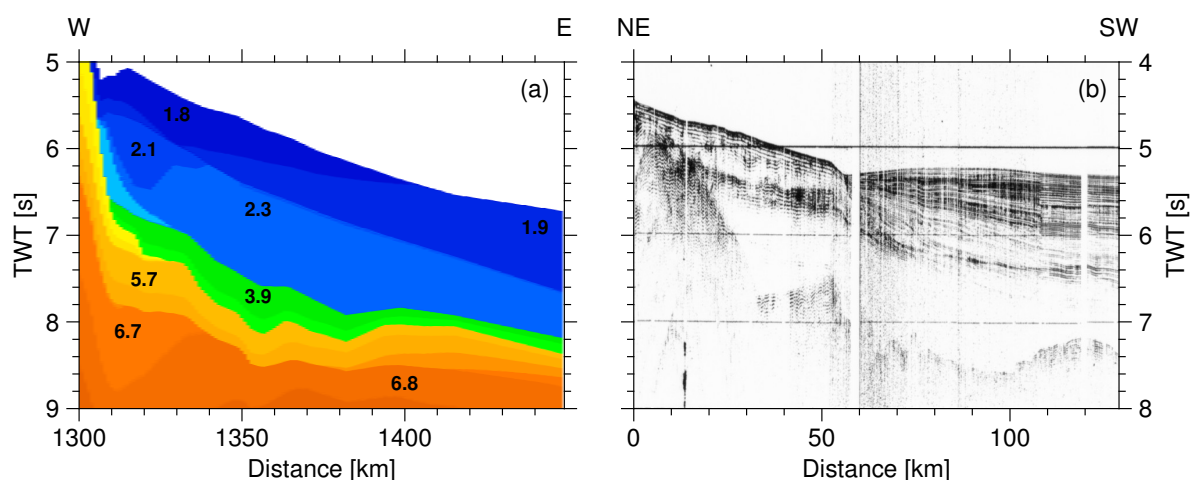


Figure 6.14.: Sediments in the Georgia Basin. (a) Part of the velocity model of AWI-20130010 in TWT. The color scale is the same as in Figure 6.10. The numbers indicate P-wave velocities in km/s. (b) Seismic reflection data of the Georgia Basin (profile RC1504). Although both profile cross approximately at km 1300 (km 0 of the plotted segment of RC1504), different time segments have to be plotted to fit the bathymetry.

The crustal structure

Oceanic crust in the Falkland Plateau Basin (km 270 – 720)

The oceanic crust in this part of the transect was already described by Schimschal and Jokat (2018). Thus, their results are only summarized here to emphasize the crustal differences compared to the COT (km 720 – 800) and MEB. The crust beneath the Falkland Plateau Basin shows characteristics of thick igneous crust (Figure 6.11b). The upper crustal oceanic layer 2 is between 1.5 and 4.2 km thick and shows a vertical velocity gradient of 0.2 s^{-1} with velocities from $\sim 5.6 \text{ km/s}$ at its top to $\sim 6.5 \text{ km/s}$ at its base. No reflections are present at the base of layer 2 and no velocity discontinuity exists between layers 2 and 3. Layer 3 ranges in thickness between 7.3 and 11.7 km, except for at km 530 – 670, where it reaches a maximum of 17.5 km. The velocity gradient of layer 3 is

0.05 s^{-1} to 0.1 s^{-1} less than that of layer 2. Velocities range from $\sim 6.6\text{ km/s}$ at its top to 7.4 km/s at the Moho. The Moho has a distinct topography and lies at 19 to 29 km depth. It shallows towards the MEB (km 688 – 730). All P_n arrivals indicate a mantle velocity of 8.0 km/s for the entire model.

COT between the Falkland Plateau Basin and the MEB (km 720 – 800)

In the COT, the crust consists of two velocity layers. The thickness of the upper layer, $C1$, decreases to a minimum of 1 km at km 800. Here, $C2$ is 16 km thick. The total crustal thickness increases eastwards from 8 km at km 720 to 17 km at km 800. Velocities range between 5.8 km/s and 6.8 km/s at the Moho.

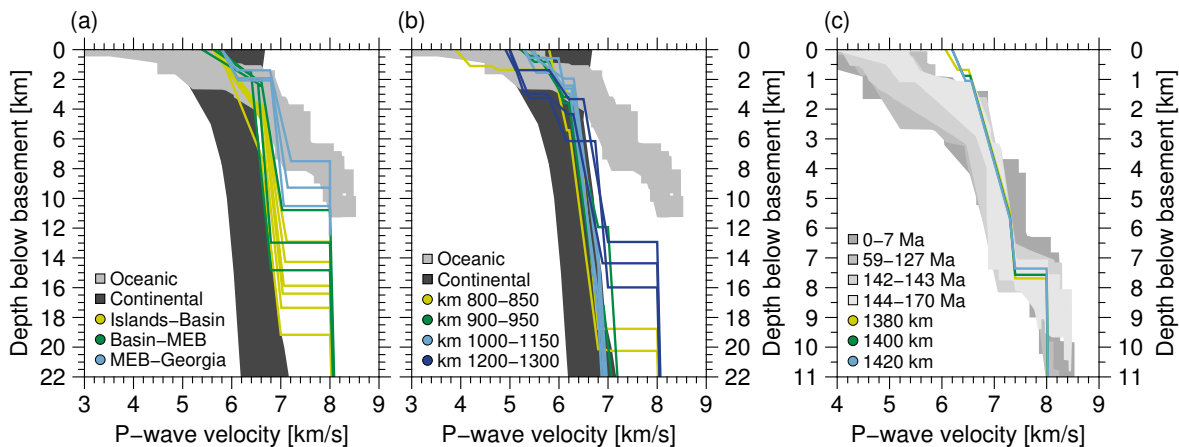


Figure 6.15.: Velocity-depth functions for average oceanic (White et al., 1992) and continental crust (Christensen and Mooney, 1995) with (a) 1D-velocity functions from the COTs of profile AWI-20130010 and (b) Maurice Ewing Bank. (c) Functions for average oceanic crust of the Atlantic Ocean and the corresponding ages (White and McKenzie, 1995) with 1D-velocity functions from the Georgia Basin.

In Figure 6.15a the velocity distributions for normal oceanic crust of the Atlantic Ocean (White et al., 1992) and continental crust (Christensen and Mooney, 1995) are plotted together with velocity functions from the western COT of MEB. Oceanic crust is characterized by a two-layered velocity structure with a steeper gradient in the upper layer (layer 2) and a shallower one in the lower layer (layer 3). Layer 2 is composed of extrusive basaltic lavas and dykes. On average, layer 3 accounts for two-thirds of the volume of oceanic crust and consists of intrusive gabbroic rocks (White et al., 1992). Despite the gradient change between layers 2 and 3, there is no sharp velocity discontinuity.

Despite its two-layer structure, it is obvious that the velocity distribution in the COT of western MEB does not match that of oceanic crust. With a maximum velocity of 6.8 km/s , lower crustal velocities are considerably slower than in the oceanic part of the transect (km 270 – 720). The volume contrast between $C1$ and $C2$ is not typical for oceanic crust as $C1$ is considerably thinner than $C2$ (1 km to 16 km). Velocities decrease eastwards from the onset of the COT towards MEB. In the COT, velocities are faster

than for continental crust until km 775. Here, the velocity-depth distribution resembles the range typical of continental crust.

At km 800, the basement topography changes markedly and resembles that of the eastern edge of the Falkland Plateau Basin. With the continental termination of the COT thus tentatively set to km 800, the width of the COT is 80 km.

MEB's continental crust (km 800 – 1320)

While the velocity structure beneath the oceanic Falkland Plateau Basin is comparably homogenous along the line, the stronger variations in velocity, thickness and number of layers betray a more heterogeneous crustal fabric beneath MEB. Consistent with this, the data reveal intracrustal reflections (Figure 6.13b). In contrast to the basin fabric, up to four crustal layers are needed to explain the observed data.

MEB's overall crustal velocity structure can be divided into five different segments: In the west (km 800 – 850), just two crustal layers exist and the maximum velocity is 6.8 km/s. Further east (km 925 – 965), we observe four crustal layers with strong reflections between *C2* and *C3*. Although these reflections disappear almost completely east of km 965, *C2* and *C3* maintain their depths and thicknesses (km 965 – 1015). Between km 1015 and 1190 the Moho deepens to 32 km. By km 1223 the crustal thickness decreases again to 11 km, east of which only three crustal layers are necessary for the model (km 1190 – 1320).

The uppermost crustal layer (*Sed8*, km 886 – 1320) has velocities from 5.2 km/s at its top to 5.7 km/s at its base. The layer reflects the strong basement topography and forms the local basement highs, which influences the sedimentary deposition.

The underlying crustal layer (*C1*) shows minor undulations at its top (velocities from 5.6 km/s), but is comparably smooth at its base (6.2 km/s). The next crustal layer *C2* returns velocities between 6.2 km/s at its upper boundary and 6.8 km/s at its base over the central part of the MEB. Towards the east, the velocity at the base of *C2* increases to 7.2 km/s at km 1220.

The data require that a fourth crustal velocity layer (*C3*) be added between km 855 and 1190. Its upper boundary is marked by strong reflections between km 925 and 965. Here, amplitude modelling reveals a velocity contrast from 6.8 km/s at the base of *C2* to 7.0 km/s at the top of *C3*. *C3* is not covered by refracted phases, but reflections (P_mP) at its base (Moho) are clearly visible. Move out hyperbolae from these reflections enable the calculation of an interval velocity for *C3* that indicates a velocity of 7.2 km/s at the Moho. East of km 955, a few stations show reflections at the top of *C3*, but these are by far not as distinct as further west. Here, no velocity contrast is needed or assumed at the boundary between *C2* and *C3*. Between km 955 and 1335, lower crustal velocities are slower than in the western part of *C3*, ranging from 6.8 km/s at its top to 7.0 km/s at its base. Moho depth beneath MEB ranges between 32 km (km 1060 – 1100) and 15.8 km (km 1223).

Figure 6.15b compares the velocity-depth distribution of MEB to those of normal oceanic and continental crust. The velocity-depth functions from MEB are clearly in the same range as for normal continental crust, with the exception of those velocity-depth func-

tions between km 1200 to 1300.

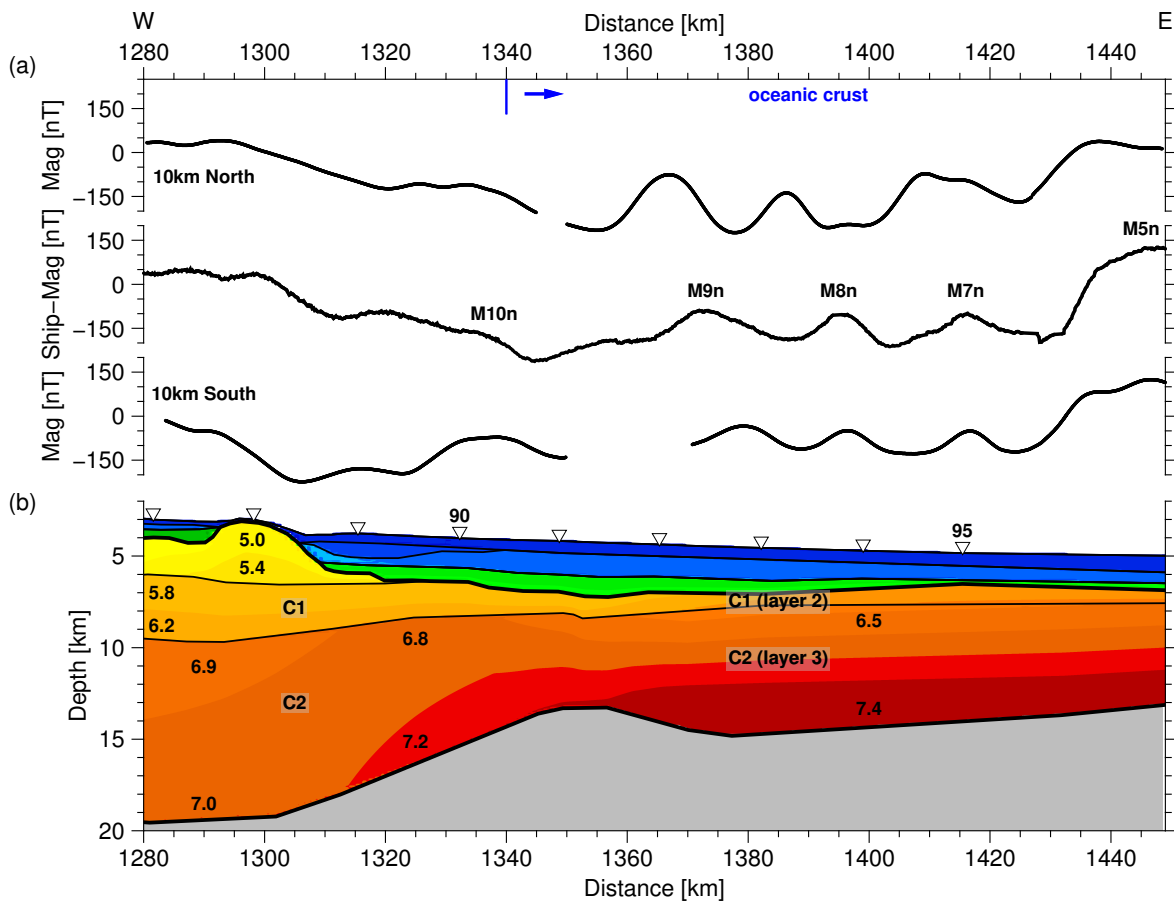


Figure 6.16.: The Georgia Basin. (a) Magnetic anomaly data along profile AWI-20130010 and 10 km north and south to the profile. The beginning of each track was shifted along the distance axis in order to match the anomaly data gathered by ship. (b) Velocity model with station positions (triangles). The color scale is the same as in Figure 6.10. The numbers indicate P-wave velocities in km/s.

MEB COT towards the Georgia Basin

The crustal thickness is considerably thinner (minimum 11 km) between km 1200 and 1300 than for the remaining MEB. Although clearly not in the usual range of continental velocities (Figure 6.15b, Christensen and Mooney, 1995), the velocity structure still shows some characteristics of continental crust, with its three layers, the velocity discontinuity at 6 km depth, and distinct basement topography featuring a double-peaked high at km 1270 – 1310. Without high quality seismic reflection data, it cannot be concluded if the crust is of exclusively continental composition or can be characterized already as transitional.

East of this segment, the model needs just two crustal velocity layers (Figure 6.16b).

The total crustal thickness is 10.5 km at km 1320 and decreases to 6 km at km 1350. Velocities range between 5.8 km/s and 6.1 km/s in *C1*, and between 6.8 km/s and 7.2 km/s in *C2*. Although the velocity-depth distribution is in the same range as that of oceanic crust (Figure 6.15a), the velocity discontinuity between the two layers is not characteristic of oceanic crust. We interpret these signals as clear indicators of a COT, whose termination at km 1340 correlates with the first magnetic reversal isochron (M10, Martin et al., 1982).

Oceanic crust of the Georgia Basin (km 1340 – 1449)

Figure 6.16 shows the velocity model for the Georgia Basin and Figure 6.15c the corresponding velocity-depth functions. The top surface of the upper crustal layer, *C1* (oceanic layer 2), shows only minor undulations. Its velocities range from 5.8 km/s to 6.4 km/s, and its thickness varies between 600 m (km 1382) and 1.1 km (km 1415). Beneath the Georgia Basin, the entire lower crustal layer *C2* (oceanic layer 3) shows velocities from 6.5 km/s to 7.4 km/s and is ~ 7 km thick. The Moho rises from 13.3 km (km 1349 – 1357) to 14.8 km at km 1377. A comparison with the velocity-depth distribution compiled for the Atlantic Ocean (Figure 6.15c) indicates that the crustal thickness is the same as the global average for normal oceanic crust and the velocity gradients indicate a differentiation into an upper oceanic layer 2 and a lower oceanic layer 3. The velocity gradient of the basin's layer 2 is less than that for average oceanic crust (0.2 s^{-1} compared to 1.0 s^{-1} , White et al., 1992). In average oceanic crust layer 2 accounts for 30% of the total crustal thickness and is ~ 2.4 km thick (White et al., 1992). In the Georgia Basin layer 2 is considerably thinner (maximum 1.1 km) and accounts only for ~ 15 % of the total crustal thickness.

6.6.2. Density model

Densities modelled for the sediments of the Falkland Plateau Basin range between 1.95 g/cm^3 in the uppermost layer and 2.7 g/cm^3 above basement (Figure 6.17c, Table 6.2). Beneath the Falkland Plateau Basin, layers 2 and 3 have average densities of 2.93 g/cm^3 and 3.05 g/cm^3 (Schimschal and Jokat, 2018). Eastwards, a block with an intermediate crustal density of 2.95 g/cm^3 is situated between the basin and the MEB (km 750 – 790). Sediment densities over MEB vary between 1.95 g/cm^3 for the uppermost layer and 2.45 g/cm^3 in the central part above basement (km 980 – 1080). The upper crustal layer (here *Sed8*) has a density of 2.55 g/cm^3 in the west (km 890 – 995), 2.75 g/cm^3 in the central part (km 995 – 1140) and 2.65 g/cm^3 in the east (km 1140 – 1320). The density of *C1* beneath MEB is 2.7 g/cm^3 and for *C2* it is 2.85 g/cm^3 . While the velocity model does not require body *C3* to exist in the western part of MEB (dashed line in Figure 6.17c), the density model requires greater densities with depth than *C2* exhibits. To account for this, we simply extended *C3* and its density of 2.9 g/cm^3 westwards so that it composes the lower ~ 9 km of the crust here. This is reasonable considering that density can be expected to increase with depth, and that the velocities of *C2* and *C3* at the Moho are in most places closely comparable (6.8 km/s and 7.0 km/s). Between km 1184 and 1260 an additional body with a density of 2.9 g/cm^3

had to be introduced at 15 to 20 km depth. Figure 6.18 shows the effect of the body in the calculated free-air gravity anomaly. This body can be interpreted as crystallized melt, which could not be resolved by the wide-angle seismic method because of the limitations of ray tracing in areas with topography. In the Georgia Basin, sediment densities

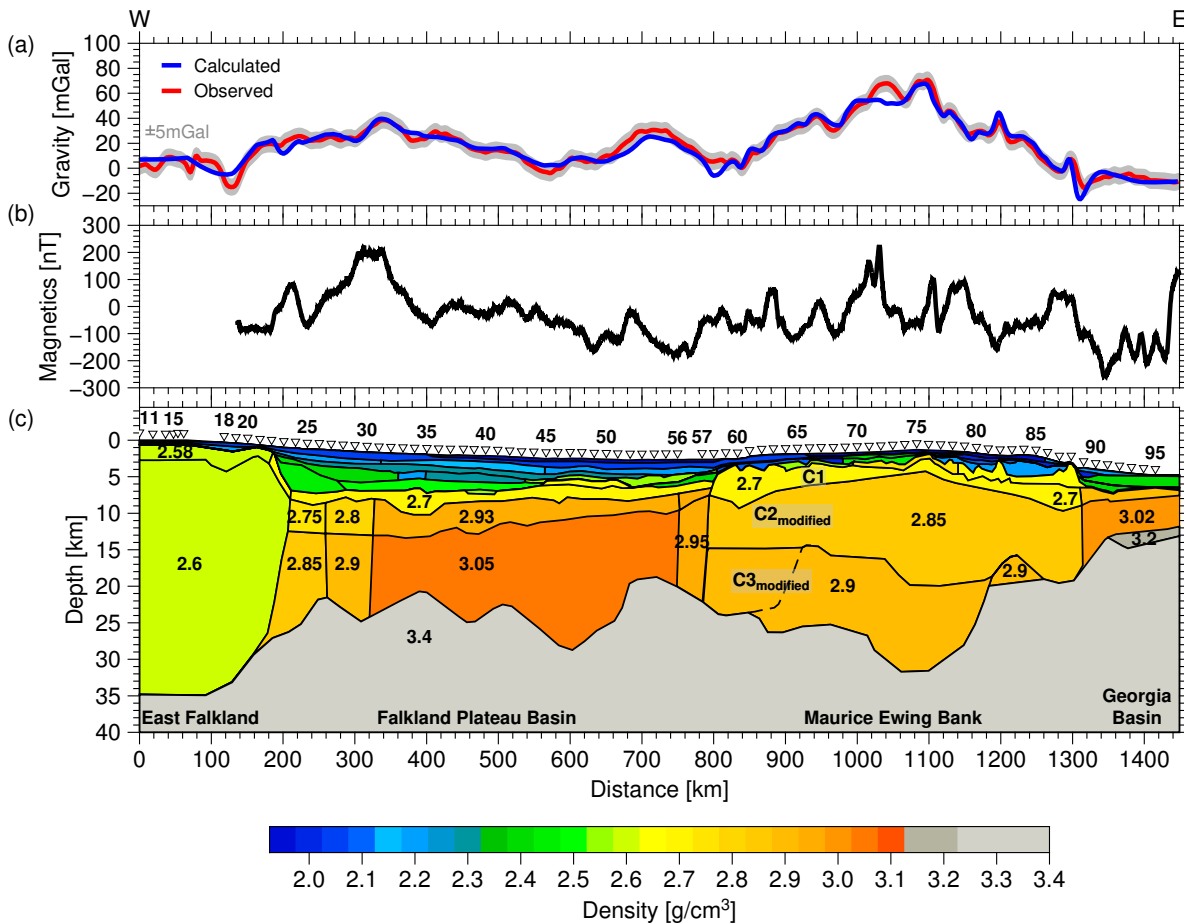


Figure 6.17.: (a) Observed free-air gravity anomaly from the Sandwell et al. (2014) grid and free-air gravity anomaly calculated with *IGMAS+*. (b) Magnetic anomaly data gathered with the Fluxgate magnetometer aboard *Polarstern* along profile AWI-20130010. (c) Density model along AWI-20130010. The numbers indicate the density in g/cm^3 . The dashed line indicates the boundary of *C3* in the velocity model. The western transect (km 0 – 750, Schimschal and Jokat, 2018) is shown to provide a view on the density structure of the entire profile.

range from 2.0 g/cm^3 to 2.42 g/cm^3 . No additional crustal body was introduced in the COT between MEB and the Georgia Basin. In the Georgia Basin, layer 2 has a density of 2.9 g/cm^3 . Layer 3 is divided into two layers along the 7.3 km/s contour line. The upper, 5 km thick, layer has a density of 3.02 g/cm^3 and the lower one 3.2 g/cm^3 . The density of the mantle is 3.4 g/cm^3 throughout the model.

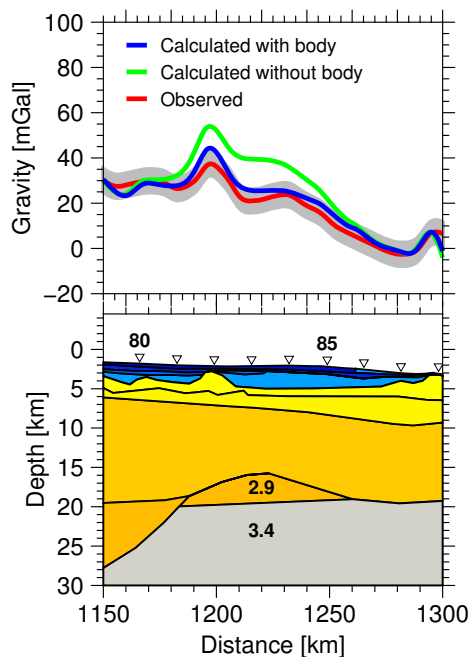


Figure 6.18: The effects of the additional density body (indicated with the density of 2.9 g/cm^3) in the free-air gravity anomaly (blue line) compared to the free-air gravity anomaly without the additional body (green line).

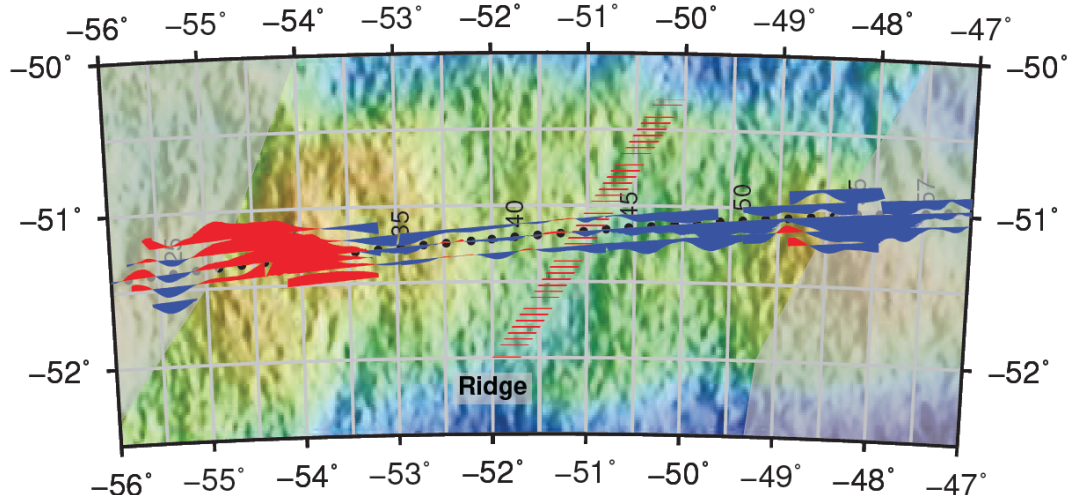


Figure 6.19.: Free-air gravity anomaly (Sandwell et al., 2014) map of the Falkland Plateau Basin with the magnetic anomaly data. Grey areas indicate the extent of continental and transitional crust.

6.6.3. Magnetic anomaly data

Along the entire profile, the magnetic data acquired with the *Polarstern*'s fluxgate magnetometers (Figure 6.17b) show strong magnetic anomalies, which likely mark major structural changes along the profile. Across the continental shelf east of East Falkland the magnetic anomaly has almost constant values of around -100 nT . This reveals that no structural changes occur between km 130 – 180.

With the onset of the COT at km 180 (Schimschal and Jokat, 2018), the magnetic

anomaly increases to 80 nT at km 212 (Figure 6.11a). At the end of the COT at km 270, a plateau between a negative anomaly in the west (maximum at km 245) and a positive anomaly in the east (km 305 – 340) is observed.

A wide strong positive anomaly at km 300 – 350 (~ 220 nT) coincides with the onset of oceanic crust and is also evident in the parallel helicopter borne magnetic profiles (Figures 6.11a, 6.19). Between km 410 and 620 the magnetic anomaly profile shows minor undulations that has a distinct pattern reminiscent of positive and negative spreading anomalies. This pattern is also seen in the helicopter profiles parallel to the ship track (Figures 6.11a, 6.19). Another anomaly peak is situated at the eastern end of the oceanic crust between km 670 and 710. Here, values increase from -130 nT to -20 nT. The COT

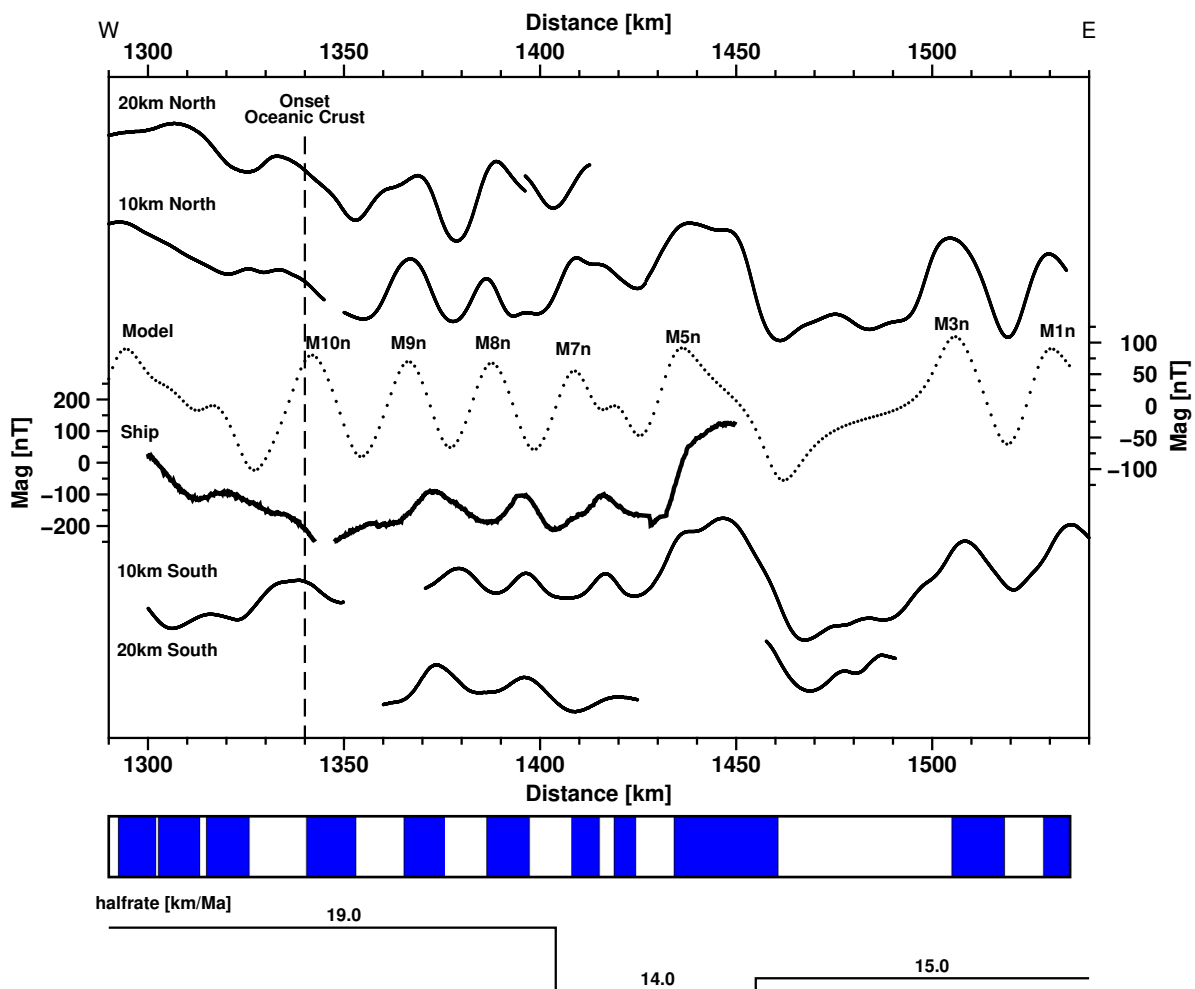


Figure 6.20.: Magnetic anomaly data and spreading model for the Georgia Basin. The beginning of each track was shifted along the distance axis in order to match the anomalies.

between the Falkland Plateau Basin and MEB is characterized by a distinct negative anomaly (-180 nT) in both the ship's and airborne magnetic anomaly data.

Schimschal and Jokat (submitted manuscript) reported that an extinct spreading ridge exists on the Falkland Plateau. In the free-air gravity map of Figure 6.19, it is visible as a southwest-northeast trending linear gravity anomaly that crosses our profile between OBS 43 and 44. The magnetic anomaly pattern at each side of this feature is only symmetrical if those parts east of the ridge are stretched by a factor of 1.5 (blue, Figure 6.11a). The data east and west of the ridge correlate between km 210 and 760. The negative anomalies at the western and eastern terminations of the basin (km 220 – 260 and km 740 – 750) are probably caused by the contrasts between transitional and oceanic crust. Schimschal and Jokat (submitted manuscript) estimated the age of rifting to be between 178 and 154 Ma. The upper limit is based on the age of a Jurassic dyke swarm and the lower limit by the age of sediments above basement in an industry well southeast of the Falkland Islands.

On the continental MEB, the anomaly pattern is irregular with several positive and negative anomalies. The maximum is situated at km 1030 (226 nT).

An anomaly that Labrecque and Hayes (1979) interpreted as isochron M10 marks the onset of oceanic crust in the Georgia Basin (Figure 6.20). On our profile, this magnetic anomaly reaches a minimum value of -260 nT. Magnetic modelling was conducted using the MATLAB-based program MODMAG (Mendel et al., 2005). The synthetic data confirm the identification of spreading anomalies published by Labrecque and Hayes (1979). The magnetic anomaly data from expedition ANT-XXIX/5 show anomalies M10n to M1n. The spreading velocity is 19 km/Myr after continental breakup at 133 Ma. Between 132 and 130 Ma (timescale of Gradstein et al., 2004 the half spreading rate is 14 km/Myr. At 130 Ma it increases to 15 km/Myr.

The geological interpretation that resulted from the velocity and density models and the magnetic anomaly data is plotted in Figure 6.21.

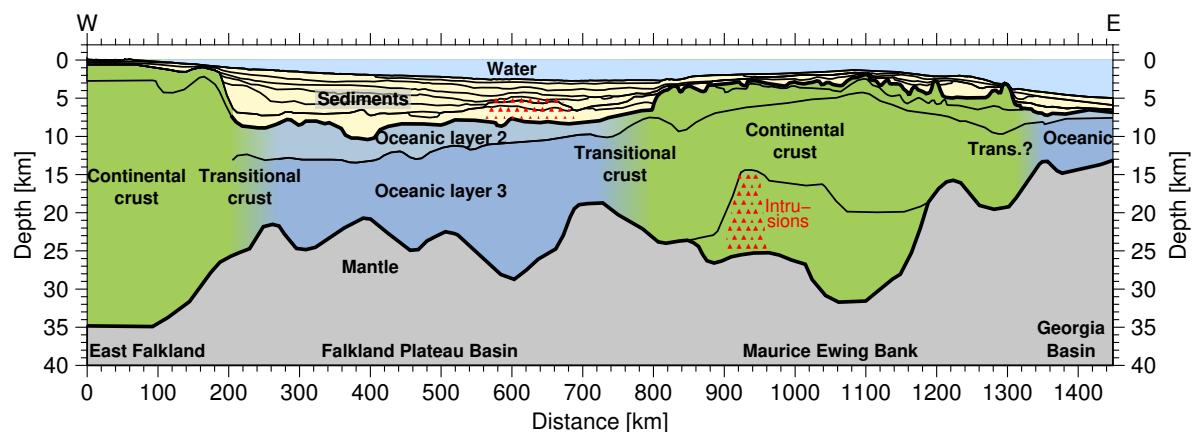


Figure 6.21.: Geological interpretation of profile AWI-20130010. The western transect (km 0 – 750, Schimschal and Jokat, 2018) is shown to provide a view on the entire profile.

6.7. Discussion

6.7.1. Sediments in the Falkland Plateau Basin

Lorenzo and Mutter (1988) described in detail the sediments of the Falkland Plateau Basin using several regional seismic reflection profiles in combination with dredge-haul results and DSDP data. They identified four depositional sequences, which are truncated by major unconformities (U1 to U4). These unconformities are plotted in red in Figures 6.2 and 6.12a. Table 6.3 provides an overview of the geological setting, the corresponding age and the velocity of each unconformity.

The uppermost sequence, above the unconformity U4, consists of pelagic drift deposits of early Paleogene age. The deposits are several hundred meters thick and are widespread over the whole plateau. Drilling on MEB revealed diatomaceous, nannofossil, calcareous and zeolitic oozes (Lorenzo and Mutter, 1988). In the Falkland Plateau Basin, our velocity model indicates that this unit is 500 m thick along the profile. In the west of the basin (km 180 – 405), the sequence has faster velocities (1.8 km/s) than in its eastern part (km 405 – 800; 1.6 km/s).

The underlying unit is erosionally truncated by unconformity U4, across which a 10 Myrs-long hiatus was identified at the drill site. Erosion was the work of vigorous ocean currents near the time of Cretaceous/Tertiary boundary (Lorenzo and Mutter, 1988). In the eastern half of the profile, U4 correlates with the velocity discontinuity between *Sed1* and *Sed2*. In the west (to km 405) no clear velocity jump can be identified.

The sedimentary unit between unconformities U3 and U4 has not been sampled by scientific drilling. Its seismic pattern and context shows that the unit likely consists of mid-Cretaceous pelagic sediments that were influenced by ocean current activity. Lorenzo and Mutter (1988) depicted two reflectors in between U3 and U4. The upper reflector is identical with the velocity layer boundary between *Sed2* and *Sed3* (2.0 km/s to 2.2 km/s). Between km 200 and 400, the lower one coincides with the layer boundary *Sed3* to *Sed4* (2.5 km/s to 2.7 km/s).

Unconformity U3 is not correlatable to any surface in the DSDP holes, but is depicted by Lorenzo and Mutter's (1988) data as truncating several lens-shaped bodies. Between km 380 and 480, U3 coincides with a velocity jump from 2.9 km/s to 3.3 km/s and further eastwards (from km 510 to 650) with one from roughly 2.6 km/s to 3.0 km/s.

The acoustic pattern of the unit between unconformities U3 and U2 shows laterally incoherent parallel reflectors and is erosionally truncated by U3. Its velocities are faster (~ 3.5 km/s) in the west (to km 620) than in the east (< 3.2 km/s; km 620 – 800).

The lowermost unit above basement (U1) is terminated at the top by unconformity U2, a result of early Paleozoic pediplanation. According to Lorenzo and Mutter (1988) U2 spans a period of 30 Myrs from Portlandian to Late Neocomian and marks the end of important tectonic activity on the plateau as major normal faulting diminishes below U2. Drilling returned the same black shales from above and below the unconformity. U2 locally correlates (e.g. at km 250 – 300 and 480 – 540) with velocity jumps from 3.9 km/s and 3.4 km/s to 4.1 km/s (*Sed5* to *Sed6*).

The lowermost unit shows strong parallel reflectors in the basin. At DSDP drill site 330,

Jurassic sediments lie unconformably on basement and show a fining-upwards tendency, which was interpreted to be the effect of the site's gradual isolation from terrestrial influence. The upper part consists of undisturbed laminated shales, indicative of restricted ocean-bottom circulation at the MEB (Lorenzo and Mutter, 1988). Contrasting velocities in this unit at DSDP drill site 330 (2.6 km/s) compared to the rest of the basin (4.9 km/s) show that the drilled sediments in this unit on MEB are not representative of the entire basin. In the Falkland Plateau Basin, the high velocities and densities (2.7 g/cm³) indicate that the sediments are highly compacted or in the early stages of burial metamorphosis. Between km 550 and 670, velocities above basement exceed 5.0 km/s and might be related to the presence of intercalated volcanic intrusions. In summary, the unconformities identified by Lorenzo and Mutter (1988) generally correlate well with velocity discontinuities.

Table 6.3.: The unconformities (U) with the corresponding geological units, ages and velocities and their profile km.

| U | Geological setting | Age | Velocity and km |
|-------|---|--|---|
| U4 | Erosional truncation creating a 10 Myrs hiatus | Cretaceous/Tertiary boundary (~66 Ma) | <i>Sed1</i> (1.6 km/s) to <i>Sed2</i> (1.9 km/s) km 400-750 |
| U3-U4 | Pelagic sediments that are influenced by ocean current activity | Mid-Cretaceous (~100 Ma) | Two reflectors: Lower one <i>Sed3</i> (2.5 km/s) to <i>Sed4</i> (2.7 km/s) km 180-400; Upper one <i>Sed2</i> (2.0 km/s) to <i>Sed3</i> (2.2 km/s) |
| U3 | Post-rift erosional truncation of several lense-shaped bodies | ? (Unsampled by scientific drilling) | <i>Sed4</i> (2.9 km/s) to <i>Sed5</i> (3.3 km/s) km 380-480, <i>Sed3</i> (2.6 km/s) to <i>Sed4</i> (~3.0 km/s) km 510-650 |
| U2-U3 | Laterally incoherent parallel reflectors | ? | |
| U2 | Pediplanation | Period of 30 Myrs from Portlandian to Late Neocomian (~152 Ma–~129 Ma) | <i>Sed5</i> (3.9 km/s) to <i>Sed6</i> (4.1 km/s) km 250-300 and <i>Sed5</i> (3.4 km/s) to <i>Sed6</i> (4.1 km/s) km 480-540 |
| U1-U2 | Unconformably deposited sediments with a fining upwards tendency, upper part undisturbed laminated shales | Jurassic | |
| U1 | Basement | | ~4.8 km/s to ~5.5 km/s |

6.7.2. Crustal fabric of the Falkland Islands and the western MEB

Although the Falkland Islands and MEB were situated close together during the Jurassic, their crustal structures differ markedly. The part of the Falkland Islands that is covered by seismic rays shows a homogenous velocity structure. The crust consists of a 1.3 to 2.8 km thick upper layer overlying a main layer of up to 32 km thickness (Schimschal and Jokat, 2018). The crustal structure of MEB is more variable.

We interpret the central part of MEB between km 1020 and 1150 to be the only segment that is not stretched or magmatically intruded. Here, the continental crust is similarly homogenous to that beneath the Falkland Islands. Crustal velocities at top basement range between 5.4 km/s at the islands and 5.5 km/s at MEB, and increase in both locations to 7.0 km/s at the Moho. The maximum crustal thickness is 34 km beneath the Falkland Islands and 29 km beneath MEB. Weak intra-crustal reflections are evident at 20 km depth beneath MEB, but none are observed beneath the islands. It is not clear if this results from the limited number of rays underneath the islands or if none are present.

The density of the crust beneath MEB is on average 10% denser than beneath the Falkland Islands (Figure 6.17c). This can be explained by the presence of magmatic intrusions. Although dykes are present throughout the Falkland Islands, magmatism did not influence the imaged velocity structure of East Falkland to any great extent. In contrast, intrusions can be interpreted to have strongly modified the crust beneath MEB at km 900 – 990. Here, velocities exceed 7.0 km/s in a lower crustal layer whose top surface is strongly reflective.

In summary, the velocity structure of the crust at MEB is more variable than that below the easternmost part of the Falkland Islands. This is due to intensive magmatic intrusions into the MEB continental crust and more extensive crustal stretching.

Falkland Island/MEB COTs towards the Falkland Plateau Basin

Towards the Falkland Plateau Basin, the crust of the Falkland Islands thins from 35 to 26 km over a distance of 90 km. The crust of the conjugate MEB margin (km 810 – 1015) is, at ~22 km, thinner than in its central part (up to 29 km, km 1020 – 1150), but does not show a sharp decrease in crustal thickness close to the COT. Based on the small number of magnetic profiles available, seafloor spreading in the Falkland Plateau Basin seems to have been asymmetric (Figure 6.11), with more oceanic crust generated west of the spreading ridge. Systematic areal magnetic data are needed to provide better constraints to test this conclusion.

Crustal thinning, in contrast, affected a wider area of MEB than of the Falkland Islands, leading to contrasting continental crustal velocity structures. The two COTs, nonetheless, are remarkably similar in width (km 200 – 270 and km 720 – 800, Figure 6.10), and show closely comparable velocity structures. In contrast to the continental blocks, the basement topography is flat in both transition zones.

6.7.3. Eastern MEB continental margin towards the Georgia Basin

The velocity-depth structure of the COT between MEB and the Georgia Basin differs markedly to its counterparts at the margins of the Falkland Plateau Basin (Figure 6.15a). The eastern margin of MEB (km 1200 – 1300) consists of highly stretched continental crust, which is significantly thinner (10 – 16 km) than the western margin of MEB (~ 22 km). It is unclear if this part of the crust can already be considered as transitional. The last basement high of MEB is encountered at km 1310 (Figure 6.16), and the first correlatable magnetic isochron lies at km 1340 (Figure 6.20). Between km 1310 and 1340 the crust is not typical for oceanic crust because a velocity contrast is visible between the two crustal layers (Figure 6.15a).

The eastern margin of MEB was affected by strong shearing when Antarctica moved southward along a transcurrent fault from ~ 182 Ma onwards along eastern Africa (Livermore and Hunter, 1996). Oceanic accretion, by now between the South American and African plates following the rupture of West Gondwana, started by 133 Ma. The oceanic crusts in the Georgia Basin and in the Falkland Plateau Basin show similar velocity structures for oceanic layers 2 and 3, and the same maximum velocity of 7.4 km/s. However, the crustal thickness in the Falkland Plateau Basin is abnormally thick and variable, at 10.5 – 20 km, locally more than twice as thick as in the Georgia Basin. In contrast to the Falkland Plateau Basin, the Moho in the Georgia Basin is flat.

6.7.4. Igneous activity of the Falkland Plateau Basin and processes

Is the Falkland Plateau Basin a Large Igneous Province?

Considering its unusually thick oceanic crust, the question arises if the Falkland Plateau Basin can be considered as a Large Igneous Province (LIP) and, if so, what were the driving processes for the formation of such thick crust.

The term LIP was originally introduced by Coffin and Eldholm (1991) and describes large areas with massive emplacement of extrusive and intrusive rocks producing a magmatic crust with thicknesses of 20 – 40 km (Coffin and Eldholm, 1994). LIPs do not form in the same way as normal oceanic crust, which is the result of steady-state decompression melting of ‘normal’ mantle at ‘normal’ seafloor spreading centres. In contrast, LIPs are generated by magmatic pulses that cover areas of at least $1 \cdot 10^5$ km² with a volume of more than $1 \cdot 10^5$ km³ (Bryan and Ernst, 2008).

The areal extent of the oceanic part of the Falkland Plateau is $\sim 1.5 \cdot 10^5$ km², similar to the southern Mozambique Ridge ($\sim 1.45 \cdot 10^5$ km²), which is also interpreted as a LIP (Fischer et al., 2016). Assuming an average crustal thickness of 15.5 km, the volume of the oceanic part of the Falkland Plateau is $\sim 23 \cdot 10^5$ km³. Thus, the estimated size and volume fulfil the definition of a LIP.

Further constraints for classification as a LIP concern the duration of magmatism and the volumetric volcanic output rate. LIPs are formed predominantly during a short-lived main pulse (often < 1 Myrs), during which most ($> 75\%$) of the total magmatic volume is emplaced. After this, an intrusion-dominated regime lasts over the total active lifetime of 10 – 30 Myrs (Karlstrom and Richards, 2011). Schimschal and Jokat (submitted

manuscript) suggest rifting and subsequent seafloor spreading of the Falkland Plateau Basin lasted 24 Myrs. A varying magma production rate might explain the variable topography of the Moho, but there are no indications for an initial short-lived magmatic pulse.

White et al. (2006) calculated a time-averaged volumetric volcanic output rate of $9 \cdot 10^5 \text{ km}^3/\text{Myr}$ for oceanic plateaus from published data. Assuming full spreading rates at the Falkland Plateau Basin of $33.3 - 39.2 \text{ km/Myr}$ (Schimschal and Jokat, submitted manuscript), a 350 km long spreading ridge (Figure 6.19), and a crustal thickness of $10.3 - 17.5 \text{ km}$, magma production rates varied between a minimum of $1.2 \cdot 10^5 \text{ km}^3/\text{Myr}$ and a maximum of $2.4 \cdot 10^5 \text{ km}^3/\text{Myr}$, far less than in the LIP estimates of White et al. (2006). Although the areal extent and volume of the Falkland Plateau fulfil the definition of a LIP, the typical short-lived magmatic pulse cannot be confirmed. The thick crust, thus, might have been formed along a ‘normal’ spreading centre in a region with enhanced melt supply.

A spreading centre at which exceptionally thick oceanic crust is currently forming crosses Iceland. Foulger et al. (2003) describe the characteristics of the crustal velocity structure beneath the Iceland transverse ridge and introduced the term Icelandic-type crust. In their model, the upper crust resembles layer 2, but even on its own is considerably thicker ($7 \pm 1 \text{ km}$) than average oceanic crust. The lower crustal layer begins, where the velocity gradient changes (usually at $V_p \sim 6.5 \text{ km/s}$) and has a thickness of $15 - 30 \pm 5 \text{ km}$. The oceanic crust of the Falkland Plateau reveals similar seismic velocities and total thicknesses. However, in contrast to Icelandic-type crust the thickness of layer 2 is, at a maximum of 4.2 km , considerably thinner.

Process of crustal formation

The similarities with Iceland invite speculations about the role of a mantle thermal anomaly in the production of thick oceanic crust in the Falkland Plateau Basin. Four factors are important in the formation of igneous crust by melt generation along a spreading centre (Parkin and White, 2008): 1. mantle temperature, 2. mantle composition, 3. presence of volatiles and water in the mantle, and 4. upwelling rate of mantle rocks. Of all these factors, temperature may be the most important, with a change of 5% (e.g. 50°C higher than the average of 1300°C) calculated to double the melt volume (Bown and White, 1994). Higher temperature melting should also result in magnesium-enriched melts, leading to crustal lithologies with above-average seismic velocities. Trumbull et al. (2002) showed for the Namibian volcanic margin that mantle temperatures of 1440°C to 1560°C result in crustal velocities of 7.1 km/s to 7.4 km/s . Active upwelling, in contrast, may lead to enhanced melting and thicker crust without influencing lithology or crustal velocities. During active convection through the melt region, the melt composition remains rather unchanged and therefore the seismic velocities do not vary much (Parkin and White, 2008).

Kelemen and Holbrook (1995) separated the effects of active upwelling and temperature anomalies by plotting the theoretical velocity of the igneous section against its thickness. The graph of total igneous thickness, h , versus seismic P-wave velocity, V_p , (Korenaga

et al., 2000) in Figure 6.22 shows the effect of the main possible processes on crustal thickness and velocity.

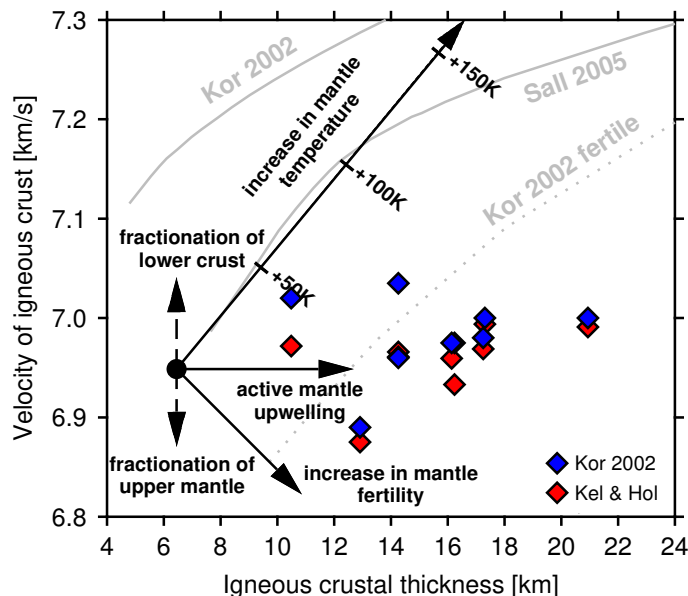


Figure 6.22.: Theoretical igneous crustal thickness versus velocity of igneous crust generated by passive mantle upwelling calculated by Sallarès et al. (2005) [Sall 2005] and Korenaga et al. (2002) [Kor 2002]. The curves are representative for a pressure of 230 MPa and a temperature of 150°C. Solid lines are for normal pyrolytic mantle and the dashed line for fertile mantle. The filled circle shows the value for average oceanic crust (White et al., 1992) and the arrows indicate how mantle temperature, active upwelling and the mantle fertility influence the igneous crustal velocity and thickness. The effects of fractionation of the lower crust and fractionation of the upper mantle oppose each other and are of similar scale, so this will be neglected here (after Parkin and White, 2008). For the crust beneath the Falkland Plateau Basin the velocity of the igneous crust is calculated with the method of Korenaga et al. (2002) (Kor 2002, blue rectangles) and Kelemen and Holbrook (1995) (Kel & Hol, red rectangles).

Upper crustal velocity is strongly influenced by pores and cracks, which are not considered in the theoretical curves. Instead, V_p refers to the bulk crustal velocity, which is calculated in two different ways for the Falkland Plateau in Figure 6.22. In the first, following Kelemen and Holbrook (1995), all velocities slower than 6.8 km/s are set to 6.8 km/s, and V_p is calculated as the average of these and all faster velocities. In the second, following Korenaga et al.'s (2002) argument that the steeper gradient of layer 2 reflects pervasive porosity and fracturing, V_p is calculated from the average velocity of layer 3 alone. V_p estimates for the Falkland Plateau Basin were completed using both methods for every 50 km between km 250 and 650. While the method of Korenaga et al. (2002) (blue rectangles, Figure 6.22) results in higher bulk crustal velocities than that of Kelemen and Holbrook (1995) (red rectangles, Figure 6.22), both methods show a

similar trend. From this trend, the h - V_p diagram indicates that active mantle upwelling of rocks whose temperature did not exceed 1350°C can explain the crustal thickness signals of the Falkland Plateau Basin. Consistent with this, Hole et al. (2015) report that the chemical composition of a Jurassic dyke (182.3 ± 1.5 Ma) on Weddell Island (2 km west of West Falkland) is indicative of decompression melting of mantle with a potential temperatures below 1450°C .

Active upwelling of the mantle can be linked to the Jurassic position of the Falkland Plateau in the back-arc environment of the Paleo-Pacific subduction zone. Martin (2007) classified the Falkland Plateau Basin as a back-arc basin that opened in response to roll-back of the hinge of the paleo-Pacific subduction zone at the western margin of Gondwana. Several theories exist to explain the initiation of spreading ridges in back-arc basins (e.g. active or passive diapirism, stepwise migration, Karig, 1974). Toksöz and Bird (1977) propose the driving mechanism is convective circulation in the mantle wedge above the subducted slab. Convection-driven upwelling of the upper mantle would explain the observed active upwelling component without high temperatures that our data indicate. Subduction influence on the formation of oceanic crust in the Falkland Plateau Basin can also be inferred from the asymmetry of seafloor spreading there (factor of 1.5, Schimschal and Jokat, submitted manuscript), a phenomenon that is often observed for spreading ridges in back-arc basins (Barker and Hill, 1980).

The crustal thickness of the Falkland Plateau is certainly influenced by enhanced melt supply, which also fed the Karroo, Ferrar and Chon Aike volcanic provinces (Schimschal and Jokat, submitted manuscript). This study shows that a mantle thermal anomaly was not the only component driving enhanced melting as southwest Gondwana fragmented, but that active mantle upwelling also played at least a local role. Regions of oceanic crust that formed contemporaneously and/or nearby the Falkland Plateau Basin can be used as constraints on the timing and extent of enhanced melt supply. The Weddell Rift in the Weddell Sea lay just to the south of the Falkland Plateau, opening at around the same time (160 to 147 Ma compared to 166 to 154 Ma). In its southern continuation, Jokat and Herter (2016) reported on a 160 km wide corridor of up to 20 km thick oceanic crust below the Filchner Ronne Shelf. Northeast of the Falkland Plateau, opening of the Mozambique Basin also started in the Early Jurassic (~ 178 Ma), but resulted in oceanic crust of average thickness (Mueller and Jokat, 2017). In the late Jurassic, the regional extensional regime changed from approximately east-west to north-south and led to the emplacement of normal-thickness oceanic crust in the Weddell Sea from 147 Ma onwards (Jokat et al., 2004, König and Jokat, 2006). In summary, enhanced melt supply was spatially and temporary limited to the area and time of the development of the Falkland Plateau Basin and Weddell Rift.

6.7.5. Conclusions

Modelling of wide-angle seismic data in combination with potential field data show the crustal structure of the Falkland Plateau, MEB and the eastern Georgia Basin. MEB is a continental fragment characterized by strong basement topography lying at 3 – 5 km depth beneath a variable sediment thicknesses of 0.3 – 3 km. MEB consists of two to

four crustal layers with velocities varying in the range from 5.0 km/s at basement to 7.2 km/s at the Moho. Western MEB shows clear intra-crustal reflections and crustal velocities higher than 7.0 km/s, related to the presence of intrusions. The central part of the MEB is in contrast not strongly tectonically or magmatically overprinted and its crust is up to 29 km thick. The eastern 250 km of the MEB consist of highly stretched continental crust of 11 – 16 km thickness. The average crustal density of the MEB is 2.83 g/cm³, which is 10 % higher than the density of the Falkland Islands. This shows that the MEB was more strongly intruded by breakup-related melts than the Falkland Islands. For the Georgia Basin, magnetic anomaly modelling confirms the presence of isochrons M10n to M1n east of MEB. Half-spreading rates there ranged between 14 and 19 km/Myr. In contrast to the crust of the Falkland Plateau Basin, the oceanic crust of the Georgia Basin is of average crustal thickness with high lower crustal velocities of up to 7.4 km/s. The crustal thickness and velocity structure of the Falkland Plateau Basin was formed in an environment with enhanced melt supply and under the influence of the Paleo-Pacific subduction zone.

7. Conclusions

The main objective of this thesis was to determine the crustal structure of the Falkland Plateau and provide new insights into the initial fit and breakup of Gondwana. In this chapter, I summarize my main results and address the research questions from section 1.3.

What is the crustal thickness and composition of the entire Falkland Plateau?

The velocity and density models together with the magnetic anomalies provided sound results for the interpretation of the crustal composition of the plateau. East Falkland is underlain by 34 km thick continental crust. Eastwards, the basement dips steeply and forms the Falkland Plateau Basin. Beneath the basin, 11 to 20 km thick oceanic crust is present above a pronounced Moho topography. The MEB is an up to 29 km thick continental fragment. The Georgia Basin consists of 7.1 km thick oceanic crust, which is typical for this crustal type.

How far does the Falkland Islands' continental basement extend?

The crustal model shows that continental basement is present for up to 120 km east of the coast. The termination of the islands' continental crust coincides with major magnetic and free-air gravity anomalies.

If there is oceanic crust beneath the Falkland Plateau Basin, what is the structure of the continental margin and the COT?

Towards the Falkland Plateau Basin, the continental crustal thickness decreases from 34 km to 17 km. The thickness of the oceanic crust beneath the basin, the presence of dykes onshore and sills offshore and the identification of SDRs in the basin (Barker, 1999) lead to the conclusion that the eastern Falkland margin is a volcanic rifted margin. Modelled velocities and densities and the magnetic anomalies indicate the presence of a 90 km wide COT with velocities intermediate between the continental and oceanic ones. Towards the MEB, the COT is of similar structure and its extent is tentatively set to 80 km. New high resolution seismic reflection data would enable a more precise determination of the extent of the COT and could prove the presence of SDRs as proposed by Barker (1999). Nevertheless, my model provides insights into the crustal thickness and velocities of the margin and the COTs.

Is there evidence for a high lower crustal velocity body underneath the plateau?

Fast velocities of 7.4 km/s are present in a diffuse layer above Moho. However, there is no evidence that this layer forms a discrete high velocity lower crustal body underneath

the Falkland Plateau Basin.

Is the MEB a volcanic structure or extended continental crust?

The MEB is a continental fragment with strong basement topography. Parts of the MEB are magmatically intruded. The central part is up to 29 km thick and not magmatically or tectonically overprinted.

How does the transition from the MEB to the oceanic Georgia Basin look like?

The eastern 130 km of the MEB are highly stretched continental crust or transitional crust. 40 km east of the last basement high, magnetic anomaly isochron M10n marks the onset of oceanic crust of the Georgia Basin.

What kind of β factor (stretching) can be calculated to constrain the maximum extension of the plateau?

In total, the pre-rift extent of the Falkland Plateau was ~ 520 km shorter than today. Most of the lengthening was achieved by igneous crustal growth in the oceanic Falkland Plateau Basin and, to a lesser extent, its COTs and the COT of the eastern MEB. The likelihood of significant crustal growth by magmatism makes the calculation of a β factor for reconstruction of the Falkland Plateau mostly meaningless.

Which age model is supported by the new magnetic investigations for the Georgia Basin?

Marine magnetic anomaly modelling supports previous interpretations (Labrecque and Hayes, 1979; Martin et al., 1982) of the onset of oceanisation at M10n times (133 Ma). The spreading velocity was 19 km/Myr after continental breakup. Between 132 and 130 Ma, the half spreading rate was 14 km/Myr. At 130 Ma, it increased to 15 km/Myr.

One important question was initially not asked, but emerged after modelling of the data showed the oceanic crustal thickness beneath the Falkland Plateau Basin:

What was the driving force behind the exceptionally thick oceanic crust?

During crustal formation of the Falkland Plateau Basin, the area was located in a back-arc position behind the Paleo-Pacific subduction zone. Onshore magmatism of the Chon Aike and Karoo-Ferrar provinces and the dykes onshore the Falkland Islands reveal that the area was influenced by enhanced melt supply during the Jurassic. Thus, the reason for the unusually thick oceanic crust was a mantle thermal anomaly or unusual fertile mantle in combination with the position in a back-arc environment.

Implications for the breakup of Gondwana

The knowledge of the crustal structure of the Falkland Plateau enables a reassessment of the initial fit and breakup of Gondwana for the area.

What was the initial fit of Gondwana in the Falkland Plateau's area?

The MEB and the Falkland/Malvinas block formed one continuous geologic feature during the Early Jurassic. The MEB was located between the African and the East Antarctic plate, just north of the Weddell Sea region. The Patagonian sub-plate was located closer to the Falkland Islands than today, considering crustal extension in the Malvinas Basin. This, together with the smaller extent of the Falkland Plateau prior to spreading and the geological requirement for the islands to have been positioned originally southeast of South Africa, results in the requirement for a large displacement along the Gastre Fault. To accommodate this, it is necessary to consider that the Antarctic Peninsula must have been rotated compared to its present-day position.

Which age constraints can be deduced for the breakup of Gondwana?

In the absence of clear marine magnetic anomalies in the Falkland Plateau Basin, I estimated the timing of rifting and seafloor spreading from the age of sediments overlying the basement, the timing of onshore magmatism and the timing of rifting in regions adjacent to the plateau. According to these considerations, rifting started at ~ 178 Ma and oceanic crust accreted between ~ 166 Ma and ~ 154 Ma.

Are there indications for the processes that led to continental desintegration?

The oceanic crustal thickness beneath the Falkland Plateau Basin shows that unusually fertile mantle or a mantle thermal anomaly was present during crustal formation. The influence of mantle thermal anomalies on continental breakup is addressed by numerous studies (e.g. Storey, 1995). This study confirms that continental breakup can occur in the presence of enhanced melt supply.

Although it was not one of my research questions, I would like to comment on the proposed rotation of the Falkland Islands block. Previous studies, focussing primarily on geologic features, regard the Weddell Sea region as an amalgamation of micro plates (e.g. Dalziel et al., 2013). These models comprise long-distance translations and rotations of continental blocks including the 180° clockwise rotation of the Falkland Islands. In the Weddell Sea region, repeated geophysical studies using different techniques failed to find evidence for the complicated plate boundary processes that must have accompanied such events (e.g. Eagles and Vaughan, 2009; Ferris et al., 2000; Jordan et al., 2017; King and Bell, 1996; Studinger and Miller, 1999). Instead, the region is interpreted to host a broad Jurassic extensional province. Taken in isolation, the crustal model of the Falkland Plateau does not supply direct evidence to favour or dismiss rotation of the Falkland Islands block. When applied with other geophysical constraints from the Weddell Sea, however, the resulting Gondwana reconstruction shows that large translations and rotations of crustal blocks are unlikely.

During this thesis, I derived the first crustal model for the Falkland Plateau. I included these findings in a new model for the initial fit and breakup of Gondwana.

8. Outlook

I could answer several research questions in my thesis. Here, I would like to address a range of remaining problems.

The crustal structure of the Falkland Plateau

Continental and oceanic crust are reliably identified on the basis of the velocity and density model and the magnetic anomalies. For a more precise determination of the onset of the COTs, however, further seismic reflection data should be acquired or, in the case of industry data, made available. These data would help to identify SDRs on both margins of the Falkland Plateau Basin. On the MEB, the acquisition of new seismic reflection data is planned to evaluate proposed drill sites for the International Ocean Discovery Program (IODP; leg 862-Pre). These new data will target Paleogene sediments. However, it could still prove valuable in determining the onset of the COT and basement structure of the MEB. Another issue is that profile AWI-20130010 covers the entire Falkland Plateau in east-west direction, but not the northern and southern part of the plateau. South of the Falkland Escarpment, previous studies identified continental crustal blocks. Here, it would be interesting to verify this interpretation with new data and, if present, determine the extent of continental crust.

The spreading ridge and direction of spreading of the Falkland Plateau Basin

For the reconstruction of Gondwana, I supposed an east-west extension and formation of the crust of the Falkland Plateau Basin. However, the extended margin of East Falkland and the proposed extinct spreading ridge both strike northeast-southwest, implying a northwest-southeast directed opening of the Falkland Plateau. In my Gondwana reconstruction, such an opening direction would result in overlap between the Patagonian and Colorado sub-plates. More systematic magnetic data with a better areal coverage might improve the identification of seafloor spreading anomalies and the extinct spreading ridge. During the austral summer 2017/2018, AWI acquired new aeromagnetic data with one of its two Polar aircrafts. These new data sets might provide better constraints on the issue of seafloor spreading direction.

The age of the oceanic crust of the Falkland Plateau Basin

New magnetic data could also provide stronger constraints on the age of oceanic crust in the Falkland Plateau Basin. According to my current age model, oceanic crust formed during the Jurassic Quiet Zone, suggesting that clearly-identifiable magnetic reversal anomalies should be absent. The thickness of sediments might further diminish magnetic amplitudes. Despite this, the currently available magnetic anomaly data show that a strong, positive anomaly (180 nT) characterizes the transition from continental

to oceanic crust east of East Falkland and weaker anomalies are present in the basin. Thus, the identification of distinct marine magnetic anomalies might be possible in the recently acquired magnetic data.

Age constraints could also be obtained from dating the sediments at drill sites. The sediment thickness and water depth prevents drilling into the sediments overlying the basement in the Falkland Plateau Basin. At the MEB, it is questionable if the planned IODP drill sites will provide information about the sediments overlying the basement as the target depth is only 200 m and the focus is on sediments of Paleogene age. Close to the Falkland Islands, several commercial drill sites exist (e.g. well 61/5-1, Loligo). The publication of these data sets could further improve the age dating of the sediments in the vicinity of the islands.

The Gastre Fault

Numerous reconstructions incorporate large (up to 500 km) displacements of terranes along the Gastre Fault (e.g. König and Jokat, 2006; Macdonald et al., 2003; Marshall, 1994; Rapela and Pankhurst, 1992; Torsvik et al., 2010). This avoids crustal overlap between continental eastern South America and Africa, and large gaps between Patagonia and the Falkland Plateau, and across the Agulhas Falkland Fracture Zone. However, no evidence for a large-scale, intra-continental Gastre Fault zone could be found in a comprehensive geological study of the area (von Gosen and Loske, 2004). To gain new constraints on this issue extensive new data sets are needed that either better constrain the kinematic model or provide new insights into the geology of Patagonia.

The driving forces for continental breakup

This thesis proposes a mechanism for the development of exceptionally thick oceanic crust, that involves decompression melting of anomalously warm and/or fertile mantle rocks. Further research is needed to investigate whether and how such conditions might also influence the progress of continental breakup, for example by interactions between regional magmatism and stress regimes. Furthermore, the role of the Paleo-Pacific subduction zone should be considered. The presence of a nearby subduction zone certainly influenced the crustal formation of the Falkland Plateau area, but what role might it have played in continental breakup? Further research is needed to answer this and related questions.

References

- Adie, R. (1952). The position of the Falklands Islands in a reconstruction of Gondwana. *Geological Magazine*, 89:401–410.
- Aldiss, D. T. and Edwards, E. J. (1999). The Geology of the Falkland Islands. *British Geological Survey Technical Report, WC/99/10*.
- Altenbernd, T., Jokat, W., Heyde, I., and Damm, V. (2015). Geophysical evidence for the extent of crustal types and the type of margin along a profile in the northeastern Baffin Bay. *Journal of Geophysical Research: Solid Earth*, 120(11):7337–7360.
- Baker, H. A. (1922). Geological investigations in the Falkland Islands. *Proceedings of the Geological Society, London*, 1093:12–15.
- Baristead, N., Anka, Z., di Primio, R., Rodriguez, J. F., Marchal, D., and Dominguez, F. (2013). New insights into the tectono-stratigraphic evolution of the Malvinas Basin, offshore of the southernmost Argentinean continental margin. *Tectonophysics*, 604:280–295.
- Barker, P. F. (1977). Correlations between Sites on the Eastern Falkland Plateau by Means of Seismic Reflection Profiles, Leg 36, DSDP. In *Initial Reports of the Deep Sea Drilling Project, 36*. U.S. Government Printing Office.
- Barker, P. F. (1979). The history of ridge-crest offset at the Falkland-Agulhas Fracture Zone from a small-circle geophysical profile. *Geophysical Journal of the Royal Astronomical Society*, 59(1):131–145.
- Barker, P. F. (1999). Evidence for a volcanic rifted margin and oceanic crustal structure for the Falkland Plateau Basin. *Journal of the Geological Society*, 156(5):889–900.
- Barker, P. F. and Dalziel, I. W. D. (1977). *Initial Reports of the Deep Sea Drilling Project*, volume 36 of *Initial Reports of the Deep Sea Drilling Project*. U.S. Government Printing Office.
- Barker, P. F. and Hill, I. A. (1980). Asymmetric spreading in back-arc basins. *Nature*, 285(5767):652–654.
- Barton, P. J. (1986). The relationship between seismic velocity and density in the continental crust - a useful constraint? *Geophysical Journal International*, 87(1):195–208.

- Bauer, K., Neben, S., Schreckenberger, B., Emmermann, R., Hinz, K., Fechner, N., Gohl, K., Schulze, A., Trumbull, R. B., and Weber, K. (2000). Deep structure of the Namibia continental margin as derived from integrated geophysical studies. *Journal of Geophysical Research*, 105(B11):25829.
- Becker, K., Franke, D., Schnabel, M., Schreckenberger, B., Heyde, I., and Krawczyk, C. M. (2012). The crustal structure of the southern Argentine margin. *Geophysical Journal International*, 189(3):1483–1504.
- Becker, K., Franke, D., Trumbull, R., Schnabel, M., Heyde, I., Schreckenberger, B., Koopmann, H., Bauer, K., Jokat, W., and Krawczyk, C. M. (2014). Asymmetry of high-velocity lower crust on the South Atlantic rifted margins and implications for the interplay of magmatism and tectonics in continental breakup. *Solid Earth*, 5(2):1011–1026.
- Beckinsale, R., Tarney, J., Darbyshire, D., and Humm, M. (1977). Re-Sr and K-Ar Age Determinations on Samples of the Falkland Plateau Basement at Site 330, DSDP. In *Initial Reports of the Deep Sea Drilling Project, 36*, pages 923–927. U.S. Government Printing Office.
- Ben-Avraham, Z., Hartnady, C., and Malan, J. (1993). Early tectonic extension between the Agulhas Bank and the Falkland Plateau due to the rotation of the Lafonia microplate. *Earth and Planetary Science Letters*, 117(1-2):43–58.
- Bohlen, T. (2002). Parallel 3-D viscoelastic finite difference seismic modelling. *Computers and Geosciences*, 28(8):887–899.
- Bohlen, T., De Nil, D., Daniel, K., and Jetschny, S. (2015). SOFI2D, seismic modeling with finite differences 2D - elastic and viscoelastic version, User’s Guide. pages 1–50.
- Borissova, I., Coffin, M. F., Charvis, P., and Operto, S. (2003). Structure and development of a microcontinent: Elan Bank in the southern Indian Ocean. *Geochemistry, Geophysics, Geosystems*, 4(9):1–16.
- Bown, J. W. and White, R. S. (1994). Variation with spreading rate of oceanic crustal thickness and geochemistry. *Earth and Planetary Science Letters*, 121(3-4):435–449.
- Boyden, J. A., Müller, R. D., Gurnis, M., Torsvik, T. H., Clark, J. A., Turner, M., Ivey-Law, H., Watson, R. J., and Cannon, J. S. (2011). Next-generation plate-tectonic reconstructions using GPlates. In Keller, G. R. and Baru, C., editors, *Geoinformatics*, pages 95–114. Cambridge University Press, Cambridge.
- Brocher, T. M. (2008). Compressional and Shear-Wave Velocity versus Depth Relations for Common Rock Types in Northern California. *Bulletin of the Seismological Society of America*, 98(2):950–968.

- Bry, M., White, N., Singh, S., England, R., and Trowell, C. (2004). Anatomy and formation of oblique continental collision: South Falkland basin. *Tectonics*, 23(4):1–20.
- Bryan, S. E. and Ernst, R. E. (2008). Revised definition of Large Igneous Provinces (LIPs). *Earth-Science Reviews*, 86(1-4):175–202.
- Carlson, R. L. and Raskin, G. S. (1984). Density of the ocean crust. *Nature*, 311(5986):555–558.
- Charvis, P. and Operto, S. (1999). Structure of the Cretaceous Kerguelen Volcanic Province (southern Indian Ocean) from wide-angle seismic data. *Journal of Geodynamics*, 28(1):51–71.
- Christensen, N. I. and Mooney, W. D. (1995). Seismic velocity structure and composition of the continental crust: A global view. *Journal of Geophysical Research*, 100(B6):9761.
- Ciesielski, P. F. and Wise, S. W. (1977). Geologic history of the Maurice Ewing Bank of the Falkland Plateau (southwest Atlantic sector of the Southern Ocean) based on piston and drill cores. *Marine Geology*, 25(1-3).
- Coffin, M. and Eldholm, O. (1991). Large Igneous Provinces: JOI/USSAC Workshop Report. Technical report, University of Texas at Austin Institute for Geophysics (Technical Report 114).
- Coffin, M. and Eldholm, O. (1994). Large igneous provinces: crustal structure, dimensions, and external consequences. *Reviews of Geophysics*, (93):1–36.
- Curtis, M. L. and Hyam, D. M. (1998). Late Palaeozoic to Mesozoic structural evolution of the Falkland Islands: a displaced segment of the Cape Fold Belt. *Journal of the Geological Society*, 155(1):115–129.
- Dalziel, I. W. D. and Lawver, L. A. (2001). The lithospheric setting of the West Antarctic ice sheet. *The West Antarctic Ice Sheet: Behaviour and Environment, Antarctic Research Series*, 77:29 – 44.
- Dalziel, I. W. D., Lawver, L. A., Norton, I. O., and Gahagan, L. M. (2013). The Scotia Arc: Genesis, Evolution, Global Significance. *Annual Review of Earth and Planetary Sciences*, 41(1):767–793.
- Darwin, C. (1846). On the geology of the Falkland Islands. *Quarterly Journal of the Geological Society of London*, 2:267–274.
- De Beer, J. and Meyer, R. (1984). Geophysical characteristics of the Namaqua-Natal Belt and its boundaries, South Africa. *Journal of Geodynamics*, 1(3-5):473–494.

- Eagles, G. and Vaughan, A. P. M. (2009). Gondwana breakup and plate kinematics: Business as usual. *Geophysical Research Letters*, 36(10):L10302.
- Ehlers, B. M. and Jokat, W. (2009). Subsidence and crustal roughness of ultra-slow spreading ridges in the northern North Atlantic and the Arctic Ocean. *Geophysical Journal International*, 177(2):451–462.
- Eldholm, O., Skogseid, J., Planke, S., and Gladchenko, T. P. (1995). *Volcanic Margin Concepts*, pages 1–16. Springer Netherlands, Dordrecht.
- Ewing, J. I., Ludwig, W. J., Ewing, M., and Eittreim, S. L. (1971). Structure of the Scotia Sea and Falkland Plateau. *Journal of Geophysical Research*, 76(29):7118.
- Ferris, J., Vaughan, A., and Storey, B. (2000). Relics of a complex triple junction in the Weddell Sea embayment, Antarctica. *Earth and Planetary Science Letters*, 178(3-4):215–230.
- Fischer, M. D., Uenzelmann-Neben, G., Jacques, G., and Werner, R. (2016). The Mozambique Ridge: a document of massive multi-stage magmatism. *Geophysical Journal International*, pages 449–467.
- Flueh, E. R. and Bialas, J. (1996). A digital, high data capacity ocean bottom recorder for seismic investigations. *Underwater Systems Design*, 18(3):18–20.
- Foulger, G. R., Du, Z., and Julian, B. R. (2003). Icelandic-type crust. *Geophysical Journal International*, 155(2):567–590.
- Fromm, T. (2016). PRay - A graphical user interface for interactive visualization and modification of rayinvr models. *Journal of Applied Geophysics*, 124:1–3.
- Funck, T., Andersen, M. S., Neish, J. K., and Dahl-Jensen, T. (2008). A refraction seismic transect from the Faroe Islands to the Hatton-Rockall Basin. *Journal of Geophysical Research: Solid Earth*, 113(12):1–25.
- Gardner, G., Gardner, L., and Gregory, A. (1985). Formation velocity and density: the diagnostic basics for stratigraphic traps. *Geophysics*, 50(11):2085–2095.
- GEBCO (2014). General Bathymetric Chart of the Oceans; International Hydrographic Organization (IHO) and the Intergovernmental Oceanographic Commission (IOC) of UNESCO.
- Ghidella, M. E., Lawver, L. A., and Gahagan, L. M. (2007). Break-up of Gondwana and opening of the South Atlantic; review of existing plate tectonic models. *Open-File Report - U. S. Geological Survey*, 055:5p.
- Gohl, K. and Uenzelmann-Neben, G. (2001). The crustal role of the Agulhas Plateau, southwest Indian Ocean: Evidence from seismic profiling. *Geophysical Journal International*, 144(3):632–646.

- Gohl, K., Uenzelmann-Neben, G., and Grobys, N. (2011). Growth and dispersal of a Southeast African large igneous province. *South African Journal of Geology*, 114(3-4):379–386.
- Götze, H. J. (1978). Ein numerisches Verfahren zur Berechnung der gravimetrischen Feldgrößen dreidimensionaler Modellkörper. *Archiv für Meteorologie, Geophysik und Bioklimatologie Serie A*, 27(2):195–215.
- Gradstein, J., Ogg, A. G., and Smith, A. (2004). A Geologic Time Scale 2004. *Cambridge University Press, Cambridge*.
- Greenroyd, C. J., Peirce, C., Rodger, M., Watts, A. B., and Hobbs, R. W. (2008). Demerara Plateau - The structure and evolution of a transform passive margin. *Geophysical Journal International*, 172(2):549–564.
- Greenway, M. E. (1972). The geology of the Falkland Islands. *British Antarctic Survey Scientific Reports*, 76:42 pp.
- Halle, T. G. (1911). On the geological structure and history of the Falkland Islands. *Bulletin of the Geological Institution of the University of Uppsala*, 11:115–229.
- Heine, C., Zoethout, J., and Müller, R. D. (2013). Kinematics of the South Atlantic rift. *Solid Earth*, 4(2):215–253.
- Hermann, T. and Jokat, W. (2013). Crustal structures of the Boreas Basin and the Knipovich Ridge, North Atlantic. *Geophysical Journal International*, 193(3):1399–1414.
- Hermann, T. and Jokat, W. (2016). Crustal structure off Kong Oscar Fjord, East Greenland: Evidence for focused melt supply along the Jan Mayen Fracture Zone. *Tectonophysics*, 691:110–119.
- Hinz, K. (1981). A hypothesis on terrestrial catastrophes wedges of very thick oceanward dipping layers beneath passive continental margins; their origin and palaeoenvironmental significance. *Geologisches Jahrbuch*, E2:3–28.
- Hinz, K., Mutter, J. C., Zehnder, C. M., and Group, N. S. (1987). Symmetric conjugation of continent-ocean boundary structures along the Norwegian and East Greenland margins. *Mar. Petrol. Geol.*, 3:166–187.
- Hole, M. J., Ellam, R. M., Macdonald, D. I. M., and Kelley, S. P. (2015). Gondwana break-up related magmatism in the Falkland Islands. *Journal of the Geological Society*, 173(1):108–126.
- Hübscher, C., Jokat, W., and Miller, H. (1996). Crustal structures of Antarctica's continental margin in the eastern Weddell Sea. In *Storey, B., King, E., Livermore, R. (eds.). Weddell Sea Tectonics and Gondwana Breakup*, pages 165–174. Geological Society Special Publication, Vol 108.

- Hunter, R. J., Johnson, A. C., and Aleshkova, N. D. (1996). Aeromagnetic data from the southern Weddell Sea embayment and adjacent areas: synthesis and interpretation. *Geological Society, London, Special Publications*, 108(1):143–154.
- Jacobs, J., Thomas, R. J., Armstrong, R. A., and Henjes-Kunst, F. (1999). Age and thermal evolution of the Mesoproterozoic Cape Meredith Complex, West Falkland. *Journal of the Geological Society*, 156(5):917–928.
- Jokat, W. (2013). The Expedition of the Research Vessel "Polarstern" to the Antarctic in 2013 (ANT-XXIX/5). *Reports on Polar and Marine Research*.
- Jokat, W., Boebel, T., König, M., and Meyer, U. (2003a). Timing and geometry of early Gondwana breakup. *Journal of Geophysical Research*, 108(B9).
- Jokat, W. and Herter, U. (2016). Jurassic failed rift system below the Filchner-Ronne Shelf, Antarctica: New evidence from geophysical data. *Tectonophysics*, 688:65–83.
- Jokat, W., Ritzmann, O., Reichert, C., and Hinz, K. (2004). Deep crustal structure of the continental margin off the Explora Escarpment and in the Lazarev Sea, East Antarctica. *Marine Geophysical Researches*, 25(3-4):283–304.
- Jokat, W., Ritzmann, O., Schmidt-Aursch, M. C., Drachev, S., Gauger, S., and Snow, J. (2003b). Geophysical evidence for reduced melt production on the Arctic ultraslow Gakkel mid-ocean ridge. *Nature*, 423(6943):962–965.
- Jokat, W. and Schmidt-Aursch, M. C. (2007). Geophysical characteristics of the ultraslow spreading Gakkel Ridge, Arctic Ocean. *Geophysical Journal International*, 168(3):983–998.
- Jordan, T., Ferraccioli, F., and Leat, P. (2017). New geophysical compilations link crustal block motion to Jurassic extension and strike-slip faulting in the Weddell Sea Rift System of West Antarctica. *Gondwana Research*, 42:29–48.
- Jourdan, F., Féraud, G., Bertrand, H., and Watkeys, M. K. (2007). From flood basalts to the inception of oceanization: Example from the $^{40}\text{Ar}/^{39}\text{Ar}$ high-resolution picture of the Karoo large igneous province. *Geochemistry, Geophysics, Geosystems*, 8(2).
- Karig, D. E. (1974). Evolution of Arc Systems in the Western Pacific. *Annual Review of Earth and Planetary Sciences*, 2(1):51–75.
- Karlstrom, L. and Richards, M. (2011). On the evolution of large ultramafic magma chambers and timescales for flood basalt eruptions. *Journal of Geophysical Research: Solid Earth*, 116(8):1–13.
- Kelemen, P. B. and Holbrook, W. S. (1995). Origin of thick, high-velocity igneous crust along the U.S. East Coast Margin. *Journal of Geophysical Research: Solid Earth*, 100(B6):10077–10094.

- Kimbell, G. S. and Richards, P. C. (2008). The three-dimensional lithospheric structure of the Falkland Plateau region based on gravity modelling. *Journal of the Geological Society*, 165(4):795–806.
- King, E. C. and Bell, A. C. (1996). New seismic data from the Ronne Ice Shelf, Antarctica. *Geological Society, London, Special Publications*, 108(1):213–226.
- Klingelhoefer, F., Lafoy, Y., Collot, J., Cosquer, E., Géli, L., Nouzé, H., and Vially, R. (2007). Crustal structure of the basin and ridge system west of New Caledonia (southwest Pacific) from wide-angle and reflection seismic data. *Journal of Geophysical Research: Solid Earth*, 112(11):1–18.
- König, M. (2005). *Processing of shipborne magnetometer data and revision of the timing and geometry of the Mesozoic break-up of Gondwana*. PhD thesis, University of Bremen, Germany.
- König, M. and Jokat, W. (2006). The Mesozoic breakup of the Weddell Sea. *Journal of Geophysical Research: Solid Earth*, 111(12):1–28.
- König, M. and Jokat, W. (2010). Advanced insights into magmatism and volcanism of the Mozambique Ridge and Mozambique Basin in the view of new potential field data. *Geophysical Journal International*, 180(1):158–180.
- Korenaga, J., Holbrook, W. S., Kent, G., Kelemen, P., Detrick, R. S., Larsen, H.-C., Hopper, J., and Dahl-Jensen, T. (2000). Crustal structure of the southeast Greenland margin from joint refraction and reflection seismic tomography. *Journal of Geophysical Research*, 105:21591.
- Korenaga, J., Kelemen, P. B., and Holbrook, W. S. (2002). Methods for resolving the origin of large igneous provinces from crustal seismology. *Journal of Geophysical Research*, 107(B9):2178.
- Kristoffersen, Y. and LaBrecque, J. (1991). On the Tectonic History and Origin of the Northeast Georgia Rise (Synthesis). In *Proceedings of the Ocean Drilling Program, 114 Scientific Reports*, volume 114, pages 23–38. Ocean Drilling Program.
- Labrecque, J. L. and Hayes, D. E. (1979). Seafloor spreading history of the Agulhas Basin. *Earth and Planetary Science Letters*, 45(2):411–428.
- Livermore, R. A. and Hunter, R. J. (1996). Mesozoic seafloor spreading in the southern Weddell Sea. *Geological Society, London, Special Publications*, 108(1):227–241.
- Ljones, F., Kuwano, A., Mjelde, R., Breivik, A., Shimamura, H., Murai, Y., and Nishimura, Y. (2004). Crustal transect from the North Atlantic Knipovich Ridge to the Svalbard Margin west of Hornsund. *Tectonophysics*, 378(1):17–41.

- Lohr, T. and Underhill, J. R. (2015). Role of rift transection and punctuated subsidence in the development of the North Falkland Basin. *Petroleum Geoscience*, 21(2-3):85–110.
- Lorenzo, J. M. and Mutter, J. C. (1988). Seismic stratigraphy and tectonic evolution of the Falkland/Malvinas Plateau. *Revista Brasileira de Geociências*, 18:843–846.
- Lorenzo, J. M. and Wessel, P. (1997). Flexure across a continent-ocean fracture zone: the northern Falkland/Malvinas Plateau, South Atlantic. *Geo-Marine Letters*, 17:110–118.
- Ludwig, W. and Krasheninnikov, V. (1983). *Initial Reports of the Deep Sea Drilling Project, 71*, volume 71 of *Initial Reports of the Deep Sea Drilling Project*. U.S. Government Printing Office.
- Ludwig, W. J. (1983). Geologic Framework of the Falkland Plateau. In *Ludwig W.J., Krasheninnikov V.A. et al. (Eds.), Initial Reports of the Deep Sea Drilling Project, Pt. 1 71*. Washington, DC, pages 281–293. US Government Printing Office.
- Ludwig, W. J. and Rabinowitz, P. D. (1980). Seismic stratigraphy and structure of Falkland Plateau. *AAPG Bull.*, 64(5): 742.
- Ludwig, W. J. and Rabinowitz, P. D. (1982). The collision complex of the North Scotia Ridge. *Journal of Geophysical Research*, 87(B5):3731.
- Ludwig, W. J., Windisch, C. C., Houtz, R., and Ewing, J. I. (1978). Structure of Falkland Plateau and Offshore Tierra del Fuego, Argentina. *Geological and Geophysical investigations of continental margins*, pages 125–137.
- Macdonald, D., Gomez-Perez, I., Franzese, J., Spalletti, L., Lawver, L., Gahagan, L., Dalziel, I., Thomas, C., Trewin, N., Hole, M., and Paton, D. (2003). Mesozoic breakup of SW Gondwana: Implications for regional hydrocarbon potential of the southern South Atlantic. *Marine and Petroleum Geology*, 20(3-4):287–308.
- Marshall, J. E. A. (1994). The Falkland Islands: a key element in Gondwana paleogeography. *Tectonics*, 13(2):499–514.
- Martin, A. K. (2007). Gondwana breakup via double-saloon-door rifting and seafloor spreading in a backarc basin during subduction rollback. *Tectonophysics*, 445(3-4):245–272.
- Martin, A. K., Goodlad, S. W., Hartnady, C., and du Plessis, A. (1982). Cretaceous palaeopositions of the Falkland Plateau relative to southern Africa using mesozoic seafloor spreading anomalies. *Deep Sea Research Part B. Oceanographic Literature Review*, 30(6):457.
- Mendel, V., Munschy, M., and Sauter, D. (2005). MODMAG, a MATLAB program to model marine magnetic anomalies. *Computers and Geosciences*, 31(5):589–597.

- Mercier de Lépinay, M., Loncke, L., Basile, C., Roest, W. R., Patriat, M., Maillard, A., and De Clarens, P. (2016). Transform continental margins - Part 2: A worldwide review. *Tectonophysics*, 693:96–115.
- Mitchell, C., Taylor, G. K., Cox, K. G., and Shaw, J. (1986). Are the Falkland Islands a rotated microplate? *Nature*, 319(6049):131–134.
- Mjelde, R., Breivik, A., Raum, T., Mittelstaedt, E., Ito, G., and Faleide, J. (2008). Magmatic and tectonic evolution of the North Atlantic. *Journal of the Geological Society*, 165(1):31–42.
- Mosar, J., Lewis, G., and Torsvik, T. H. (2002). North Atlantic sea-floor spreading rates: Implications for the Tertiary development of inversion structures of the Norwegian-Greenland Sea. *Journal of the Geological Society*, 159(5).
- Mueller, C. O. (2017). *The Central Mozambique continental margin - Its tectonic evolution as the centrepiece of the initial Gondwana break-up*. PhD thesis, University of Bremen, Germany.
- Mueller, C. O. and Jokat, W. (2017). Geophysical evidence for the crustal variation and distribution of magmatism along the central coast of Mozambique. *Tectonophysics*, 712-713:684–703.
- Mueller, C. O., Jokat, W., and Schreckenberger, B. (2016). The crustal structure of Beira High, central Mozambique-Combined investigation of wide-angle seismic and potential field data. *Tectonophysics*, 683:233–254.
- Mussett, A. E. and Taylor, G. K. (1994). ^{40}Ar - ^{39}Ar ages for dykes from the Falkland Islands with implications for the break-up of southern Gondwanaland. *Journal of the Geological Society*, 151(1):79–81.
- Nürnberg, D. and Müller, R. D. (1991). The tectonic evolution of the South Atlantic from Late Jurassic to present. *Tectonophysics*, 191(1-2):27–53.
- Ogg, J. G. (2012). Geomagnetic Polarity Time Scale. *The Geologic Time Scale 2012*, 1-2:85–113.
- Parkin, C. J. and White, R. S. (2008). Influence of the Iceland mantle plume on oceanic crust generation in the North Atlantic. *Geophysical Journal International*, 173(1):168–188.
- Parsiegla, N., Gohl, K., and Uenzelmann-Neben, G. (2008). The Agulhas Plateau: structure and evolution of a Large Igneous Province. *Geophysical Journal International*, 174(1):336–350.
- Parsiegla, N., Stankiewicz, J., Gohl, K., Ryberg, T., and Uenzelmann-Neben, G. (2009). Southern African continental margin: Dynamic processes of a transform margin. *Geochemistry, Geophysics, Geosystems*, 10(3).

- Pérez-Díaz, L. and Eagles, G. (2014). Constraining South Atlantic growth with seafloor spreading data. *Tectonics*, 33(9):1848–1873.
- Platt, N. H. and Philip, P. R. (1995). Structure of the southern Falkland Islands continental shelf: initial results from new seismic data. *Marine and Petroleum Geology*, 12(7):759–771.
- Rapela, C. W. and Pankhurst, R. J. (1992). The granites of northern Patagonia and the Gastre Fault System in relation to the break-up of Gondwana. *Geological Society, London, Special Publications*, 68(1):209–220.
- Richards, P. C., Gatliff, R. W., Quinn, M. F., Fannin, N. G. T., and Williamson, J. P. (1996). The geological evolution of the Falkland Islands continental shelf. *Geological Society, London, Special Publications*, 108(1):105–128.
- Richards, P. C., Stone, P., Kimbell, G. S., McIntosh, W. C., and Phillips, E. R. (2013). Mesozoic magmatism in the Falkland Islands (South Atlantic) and their offshore sedimentary basins. *Journal of Petroleum Geology*, 36(1):61–73.
- Sallarès, V., Charvis, P., Flueh, E. R., and Bialas, J. (2005). Seismic structure of the Carnegie ridge and the nature of the Galápagos hotspot. *Geophysical Journal International*, 161(3):763–788.
- Sandwell, D. T., Müller, R. D., Smith, W. H. F., Garcia, E., and Francis, R. (2014). New global marine gravity model from CryoSat-2 and Jason-1 reveals buried tectonic structure. *Science (New York, N.Y.)*, 346(6205):65–7.
- Schimschal, C. M. and Jokat, W. (2018). The crustal structure of the continental margin east of the Falkland Islands. *Tectonophysics*, 724-725:234–253.
- Schimschal, C. M. and Jokat, W. (submitted). The Falkland Plateau in the context of Gondwana breakup. *submitted to Gondwana Research*.
- Schindwein, V. and Jokat, W. (1999). Structure and evolution of the continental crust of northern east Greenland from integrated geophysical studies. *Journal of Geophysical Research: Solid Earth*, 104(B7):15227–15245.
- Schmidt, S. and Götze, H.-J. (1998). Interactive visualization and modification of 3D-models using GIS-functions. *Physics and Chemistry of the Earth*, 23(3):289–295.
- Schmidt-Aursch, M. (2003). The crustal structure of the East Greenland Fjord Region between the Precambrian shield and the recent mid-oceanic ridges: Results from seismic and gravity modelling, PhD Thesis. *Reports on polar and marine research 451*, pages 1–145.
- Shorttle, O., MacLennan, J., and Lambart, S. (2014). Quantifying lithological variability in the mantle. *Earth and Planetary Science Letters*, 395(April):24–40.

- Stone, P. (2008). Charles Darwin in the Falkland Islands, 1833 & 1834. *Falkland Islands Journal*, 9(2):15–23.
- Stone, P. (2016). Geology reviewed for the Falkland Islands and their offshore sedimentary basins, South Atlantic Ocean. *Earth and Environmental Science Transactions of the Royal Society of Edinburgh*, 106(02):115–143.
- Stone, P., Kimbell, G. S., and Richards, P. C. (2009). Rotation of the Falklands microplate reassessed after recognition of discrete Jurassic and Cretaceous dyke swarms. *Petroleum Geoscience*, 15(3):279–287.
- Stone, P., Richards, P. C., Kimbell, G. S., Esser, R. P., and Reeves, D. (2008). Cretaceous dykes discovered in the Falkland Islands: implications for regional tectonics in the South Atlantic. *Journal of the Geological Society*, 165(1):1–4.
- Storey, B. C. (1995). The role of mantle plumes in continental breakup: case histories from Gondwanaland. *Nature*, 377(6547):301–308.
- Storey, B. C. and Kyle, P. R. (1997). An active mantle mechanism for Gondwana breakup. *South African Journal of Geology Geology*, 100:283–290.
- Studinger, M. and Miller, H. (1999). Crustal structure of the Filchner-Ronne shelf and Coats Land, Antarctica, from gravity and magnetic data: Implications for the breakup of Gondwana. *Journal of Geophysical Research-Solid Earth*, 104(B9):20379–20394.
- Tassone, A., Lodolo, E., Menichetti, M., Yagupsky, D., and Vilas, J. F. (2008). Seismostratigraphic and structural setting of the Malvinas Basin and its southern margin (Tierra del fuego Atlantic offshore). *Geologica Acta*, 6(1):55–67.
- Taylor, G. K. and Shaw, J. (1982). The Falkland Islands: New palaeomagnetic data and their origin as a displaced terrane from Southern Africa. In *Hillhouse, J. W. (ed.) Deep structure and past kinematics of accreted terranes. Geophysical Monographs*, volume 50, page 294 pp. American Geophysical Union.
- Thistlewood, L., Leat, P. T., Millar, I. L., Storey, B. C., and Vaughan, A. P. M. (1997). Basement geology and Palaeozoic-Mesozoic mafic dykes from the Cape Meredith Complex, Falkland Islands: a record of repeated intracontinental extension. *Geological Magazine*, 134(03):355–367.
- Toksöz, M. N. and Bird, P. (1977). Formation and evolution of marginal basins and continental plateaus. In Talwani, M. and Pitman, W. C., editors, *Island Arcs, Deep Sea Trenches and Back-Arc Basins*, 1, pages 379–393.
- Torsvik, T. H., Rouse, S., and Smethurst, M. A. (2010). A new scheme for the opening of the South Atlantic Ocean and the dissection of an Aptian salt basin. *Geophysical Journal International*, 183(1):29–34.

- Trumbull, R. B., Sobolev, S. V., and Bauer, K. (2002). Petrophysical modeling of high seismic velocity crust at the Namibian volcanic margin. In *Special Paper 362: Volcanic Rifted Margins*, volume 362, pages 221–230. Geological Society of America.
- Vogt, U., Makris, J., O'Reilly, B. M., Hauser, F., Readman, P. W., Jacob, a. W. B., and Shannon, P. M. (1998). The Hatton Basin and continental margin: Crustal structure from wide-angle seismic and gravity data. *Journal of Geophysical Research*, 103(B6):12545.
- von Gosen, W. and Loske, W. (2004). Tectonic history of the Calcatapul Formation, Chubut province, Argentina, and the "Gastre fault system". *Journal of South American Earth Sciences*, 18(1):73–88.
- Wegener, A. (1922). *Die Entstehung der Kontinente und Ozeane*. Braunschweig: Friedrich Vieweg & Sohn, 3rd edition.
- White, R. and McKenzie, D. (1989). Magmatism at rift zones: The generation of volcanic continental margins and flood basalts. *Journal of Geophysical Research*, 94(B6):7685.
- White, R. S. and McKenzie, D. (1995). Mantle plumes and flood basalts. *Journal of Geophysical Research: Solid Earth*, 100(B9):17543–17585.
- White, R. S., McKenzie, D., and O'Nions, R. K. (1992). Oceanic crustal thickness from seismic measurements and rare earth element inversions. *Journal of Geophysical Research*, 97(B13):19683.
- White, R. S. and Smith, L. K. (2009). Crustal structure of the Hatton and the conjugate east Greenland rifted volcanic continental margins, NE Atlantic. *Journal of Geophysical Research: Solid Earth*, 114(2):1–28.
- White, R. S., Smith, L. K., Roberts, A. W., Christie, P. A. F., Kuszniir, N. J., Roberts, a. M., Healy, D., Spitzer, R., Chappell, A., Eccles, J. D., Fletcher, R., Hurst, N., Lunnon, Z., Parkin, C. J., and Tymms, V. J. (2008). Lower-crustal intrusion on the North Atlantic continental margin. *Nature*, 452(7186):460–464.
- White, S. M., Crisp, J. A., and Spera, F. J. (2006). Long-term volumetric eruption rates and magma budgets. *Geochemistry, Geophysics, Geosystems*, 7(3).
- Zelt, C. a. and Smith, R. B. (1992). Seismic travelttime inversion for 2-D crustal velocity structure. *Geophysical Journal International*, 108(1):16–34.

A. Appendix

Stations of profile AWI-20130010.

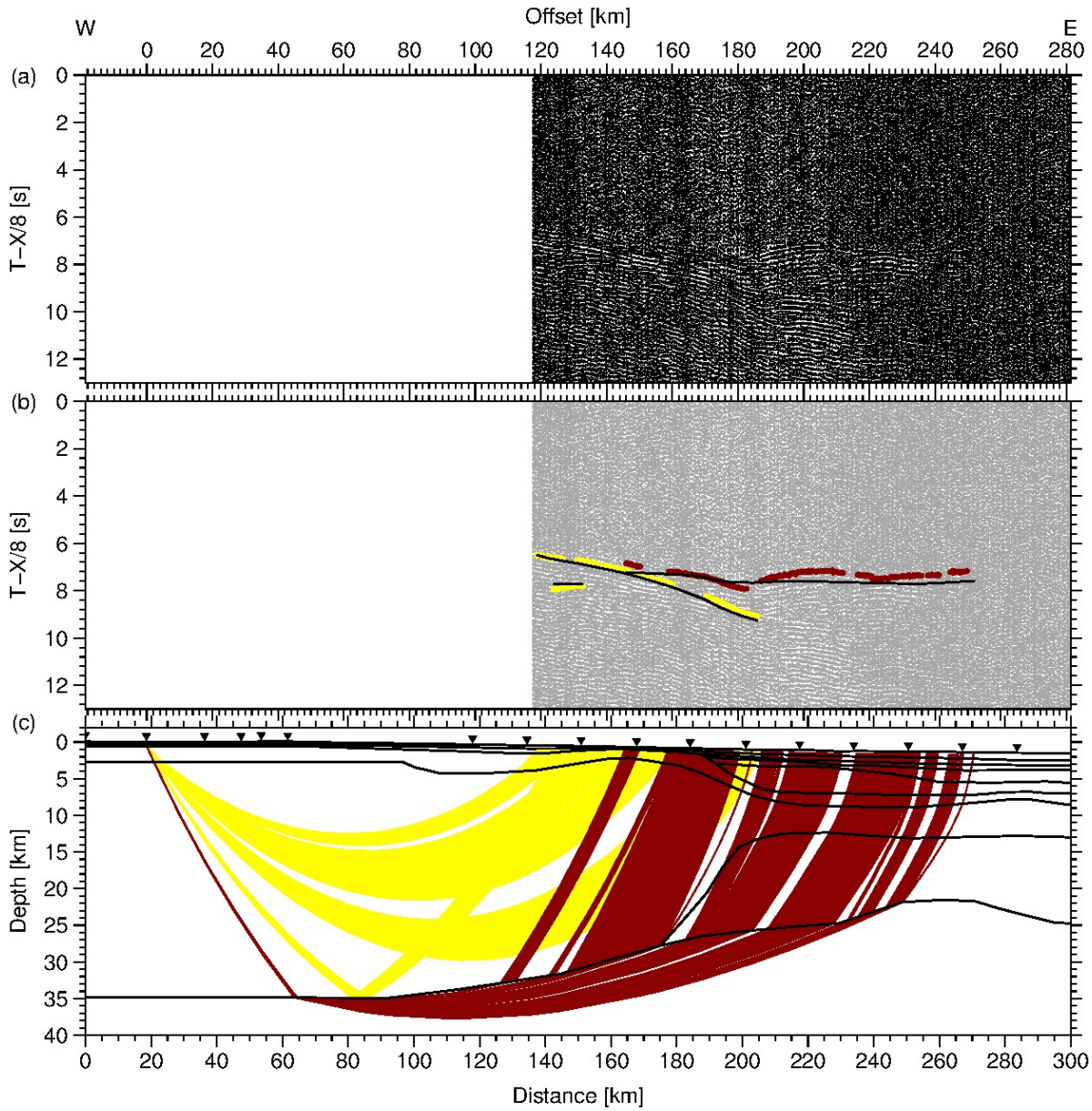


Figure A1.: Data example for land station 12. (a) Seismic section filtered with a 4-15 Hz bandpass filter and displayed with a reduction velocity of 8 km/s. (b) Picked phases with error bars and corresponding phase names. The modelled first arrivals are plotted as black lines. (c) Ray path for picks shown in (b). Station positions are marked as triangles.

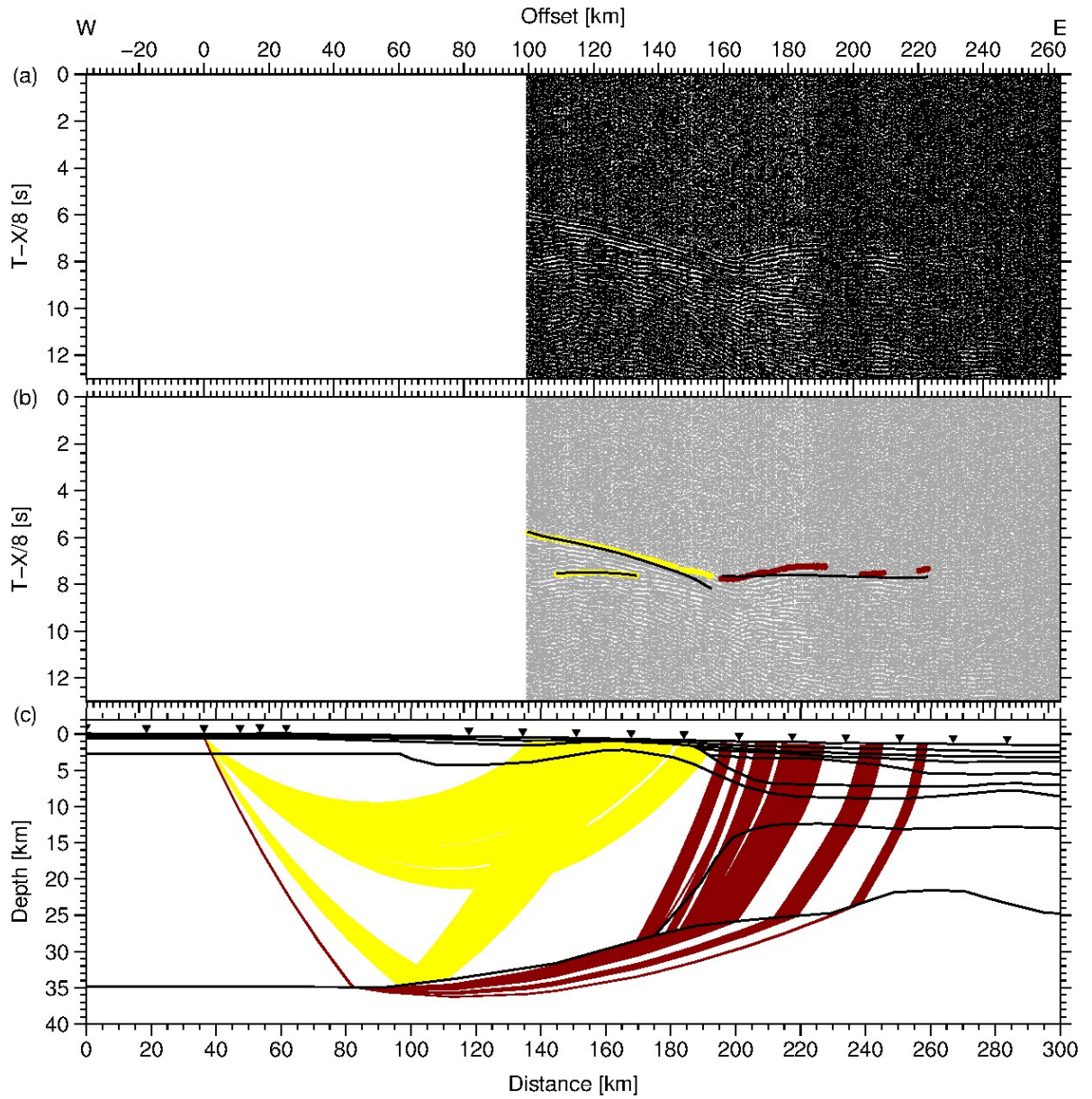


Figure A2.: Data example for land station 14. (a) Seismic section filtered with a 4-15 Hz bandpass filter and displayed with a reduction velocity of 8 km/s. (b) Picked phases with error bars and corresponding phase names. The modelled first arrivals are plotted as black lines. (c) Ray path for picks shown in (b). Station positions are marked as triangles.

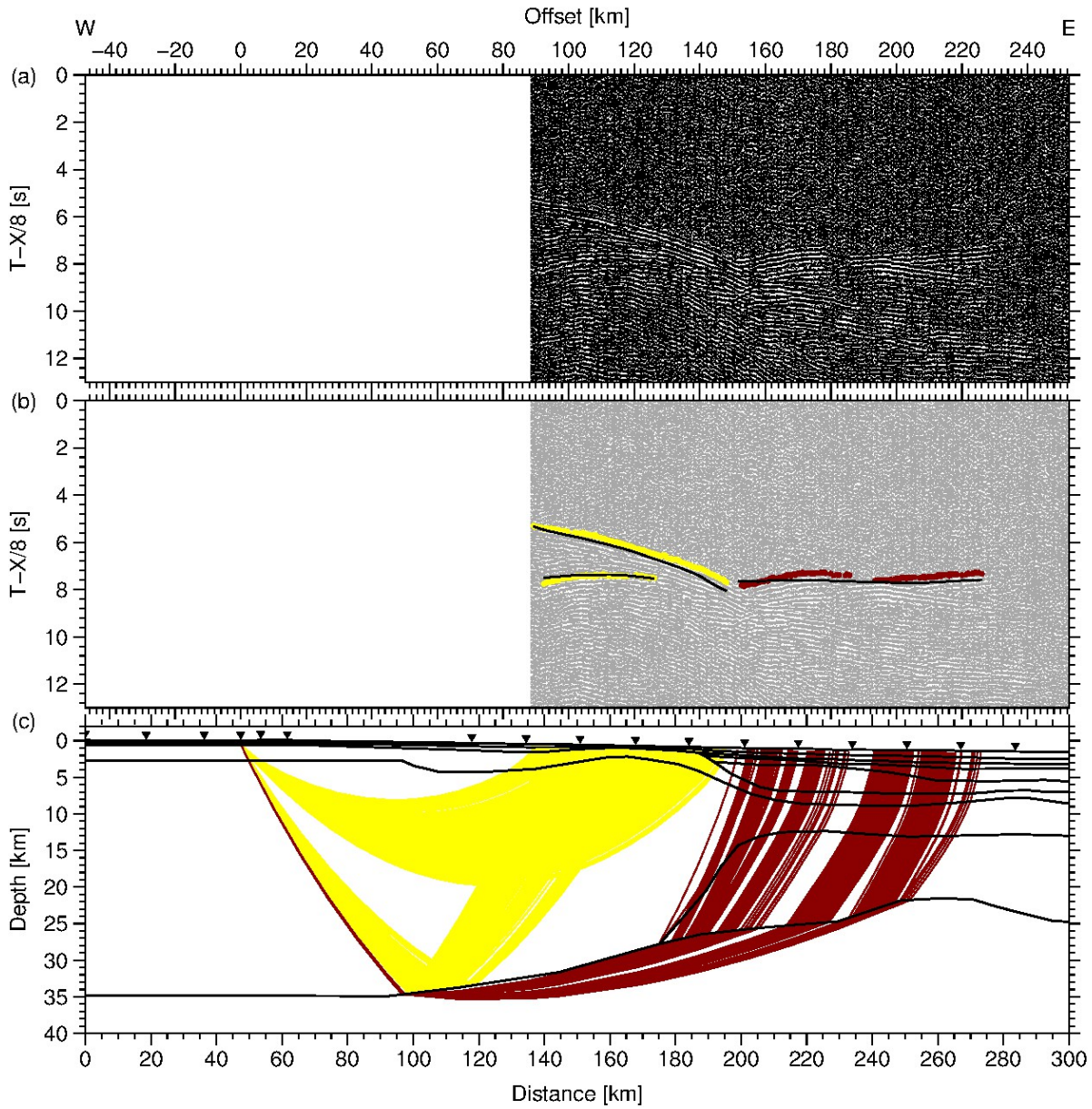


Figure A3.: Data example for land station 15. (a) Seismic section filtered with a 4-15 Hz bandpass filter and displayed with a reduction velocity of 8 km/s. (b) Picked phases with error bars and corresponding phase names. The modelled first arrivals are plotted as black lines. (c) Ray path for picks shown in (b). Station positions are marked as triangles.

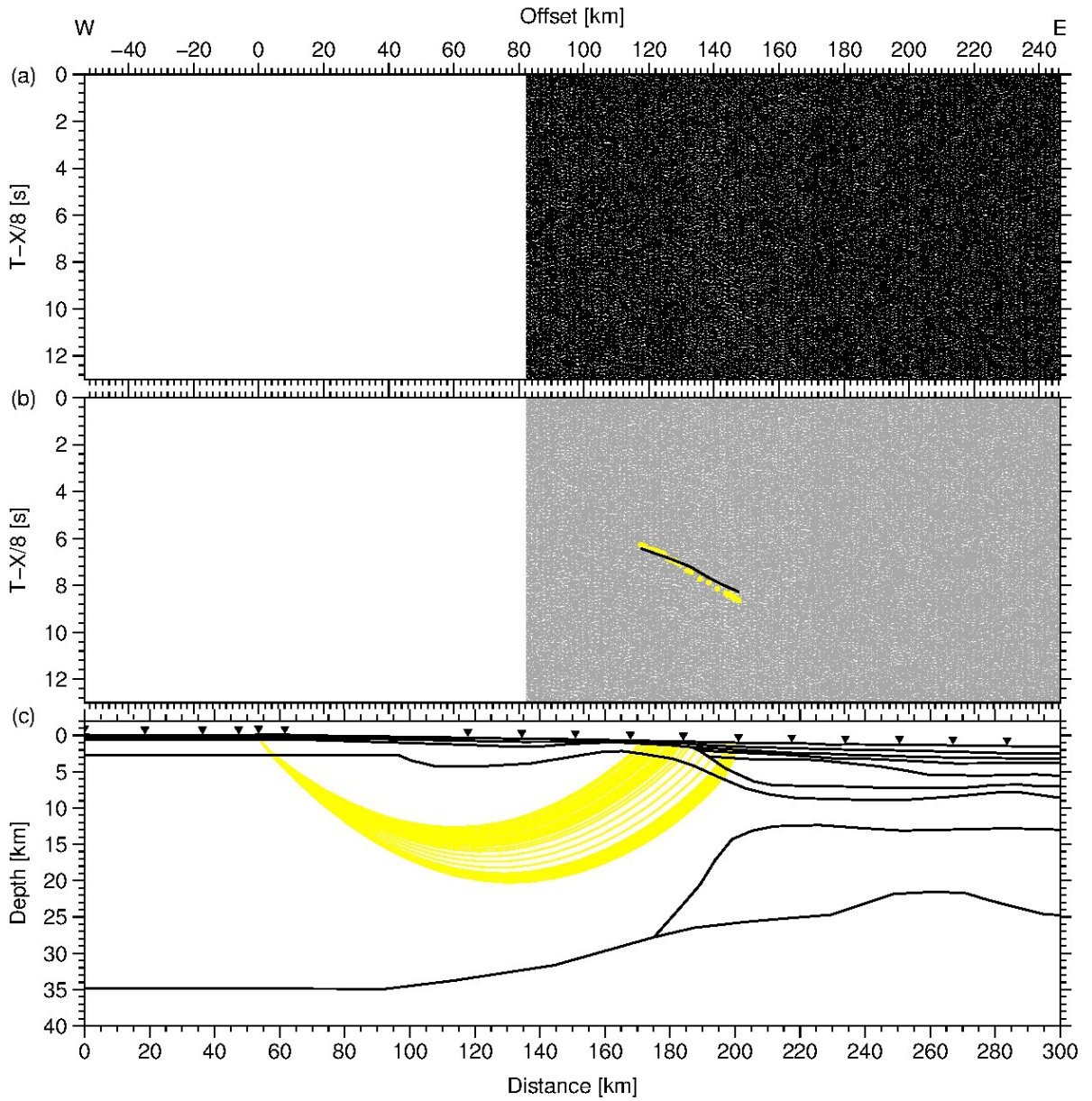


Figure A4.: Data example for land station 16. (a) Seismic section filtered with a 4-15 Hz bandpass filter and displayed with a reduction velocity of 8 km/s. (b) Picked phases with error bars and corresponding phase names. The modelled first arrivals are plotted as black lines. (c) Ray path for picks shown in (b). Station positions are marked as triangles.

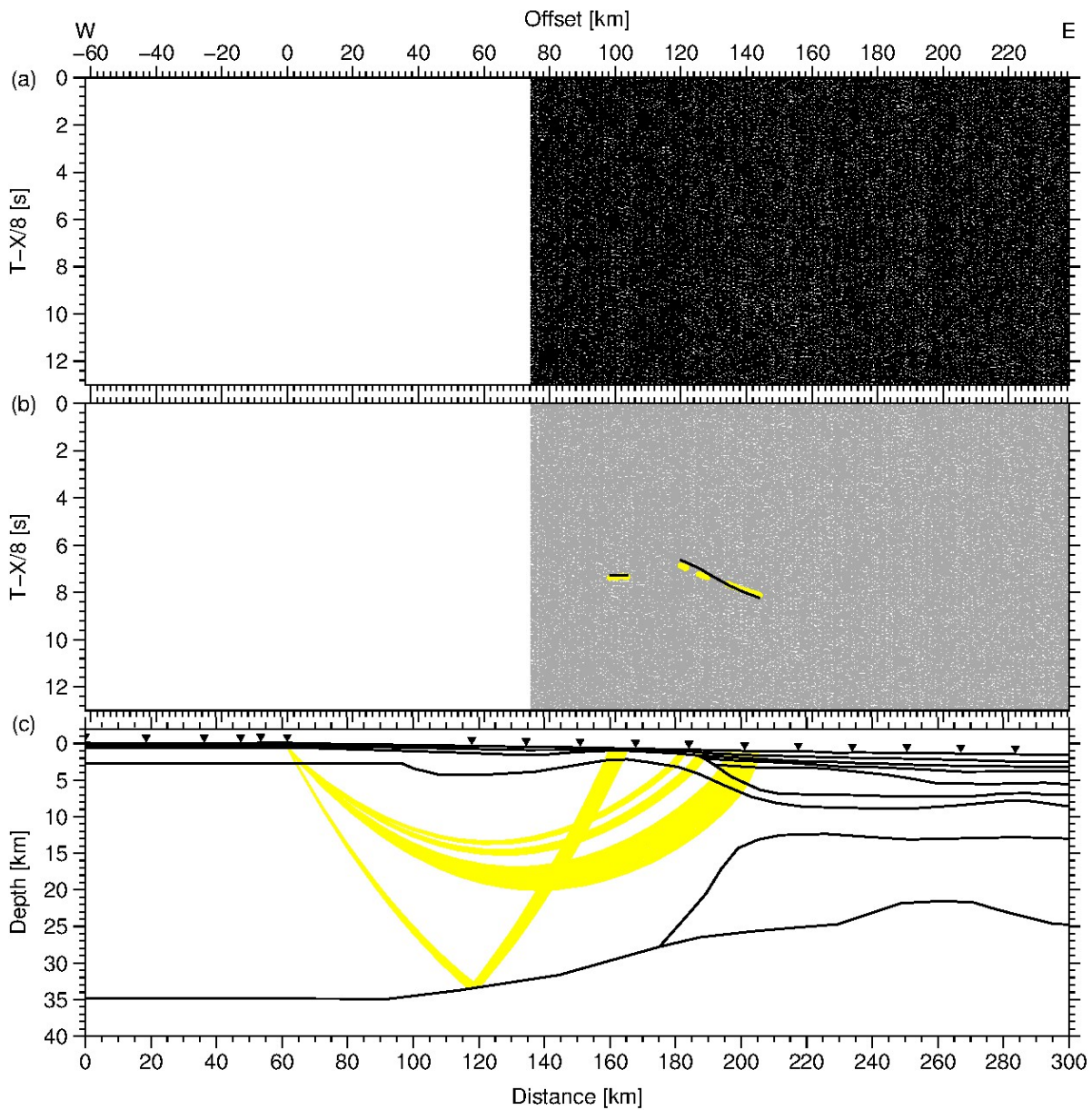


Figure A5.: Data example for land station 17. (a) Seismic section filtered with a 4-15 Hz bandpass filter and displayed with a reduction velocity of 8 km/s. (b) Picked phases with error bars and corresponding phase names. The modelled first arrivals are plotted as black lines. (c) Ray path for picks shown in (b). Station positions are marked as triangles.

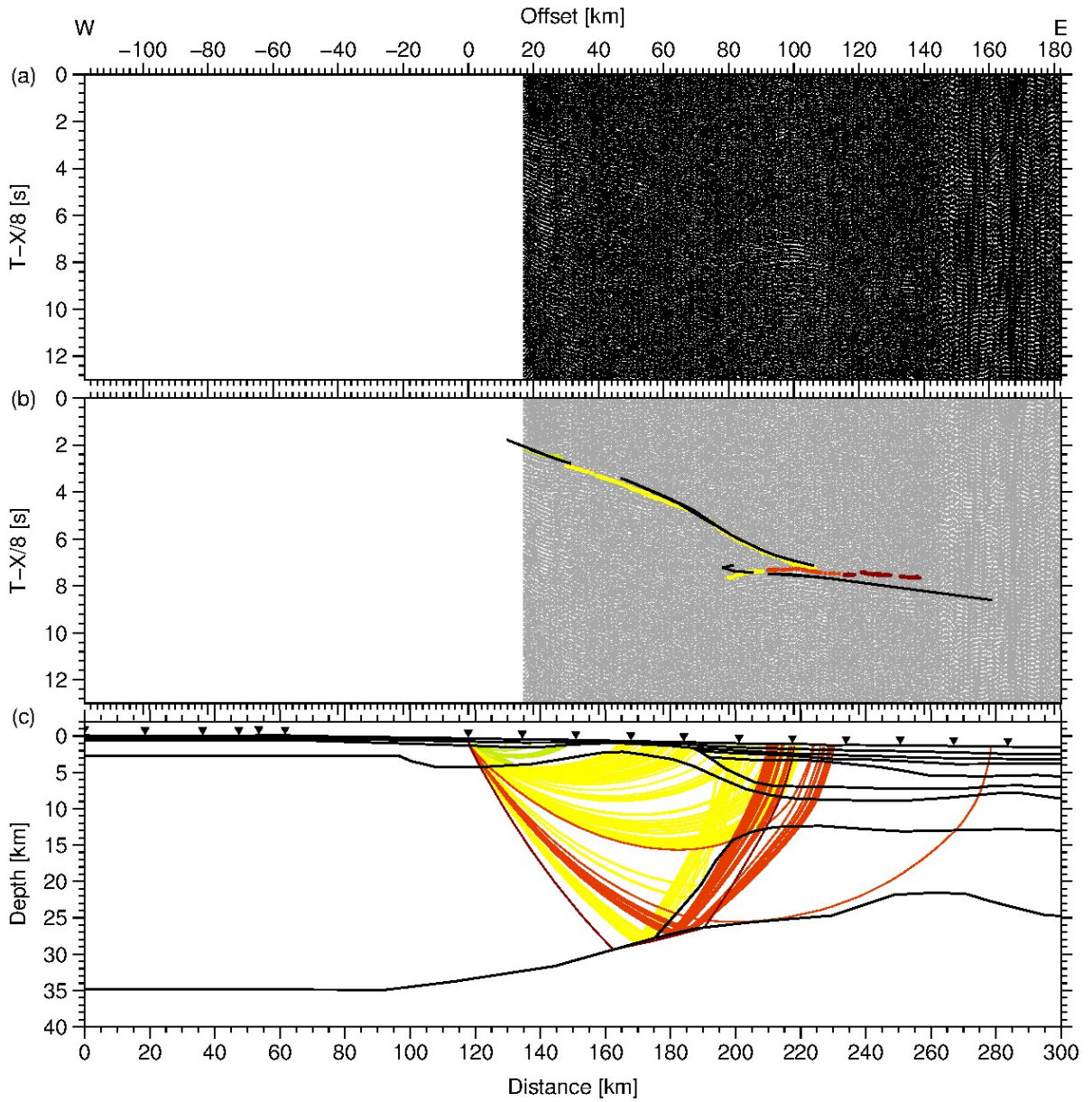


Figure A6.: Data example for OBS 18. (a) Seismic section filtered with a 4-15 Hz bandpass filter and displayed with a reduction velocity of 8 km/s. (b) Picked phases with error bars and corresponding phase names. The modelled first arrivals are plotted as black lines. (c) Ray path for picks shown in (b). Station positions are marked as triangles.

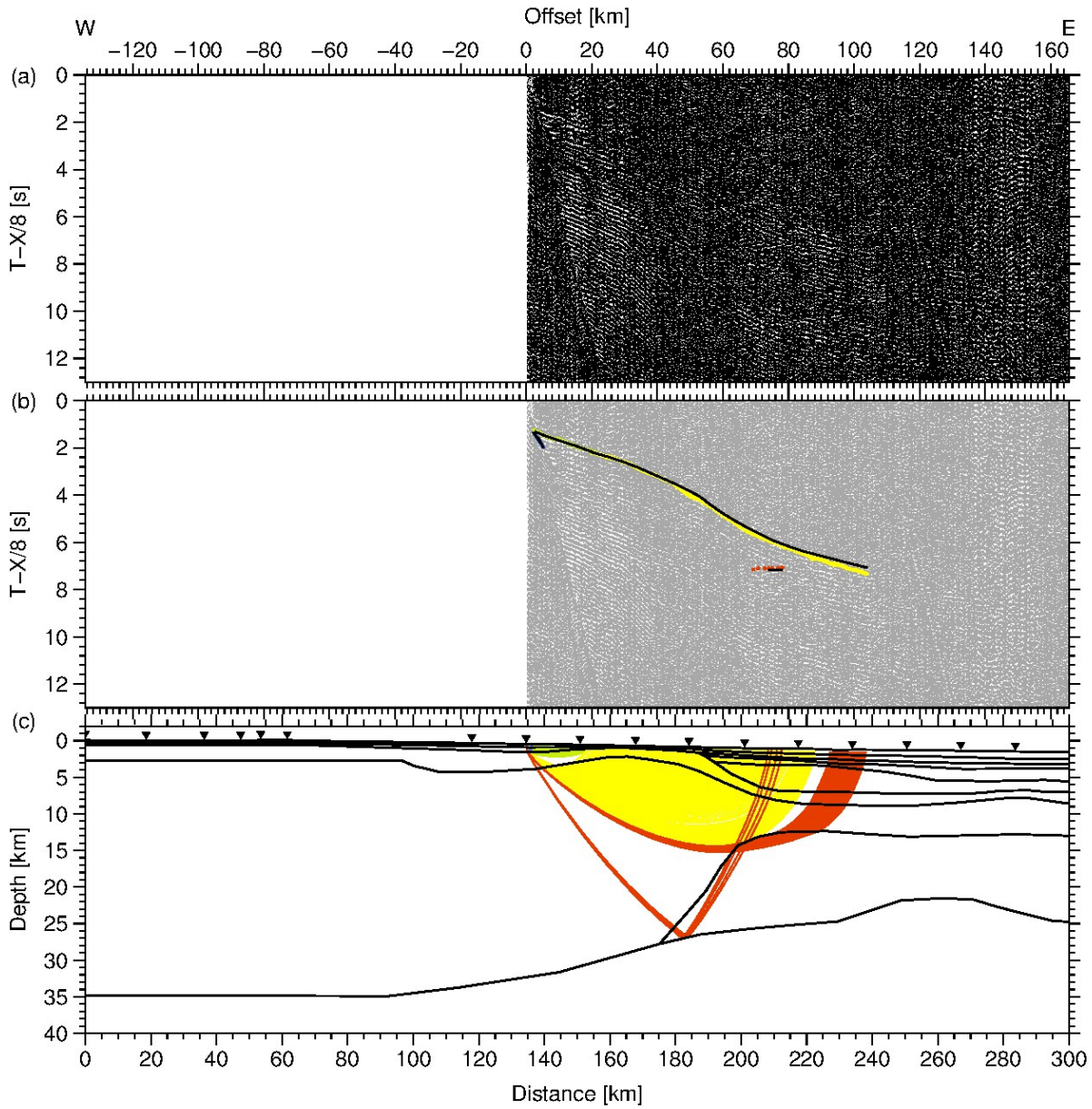


Figure A7.: Data example for OBS 19. (a) Seismic section filtered with a 4-15 Hz bandpass filter and displayed with a reduction velocity of 8 km/s. (b) Picked phases with error bars and corresponding phase names. The modelled first arrivals are plotted as black lines. (c) Ray path for picks shown in (b). Station positions are marked as triangles.

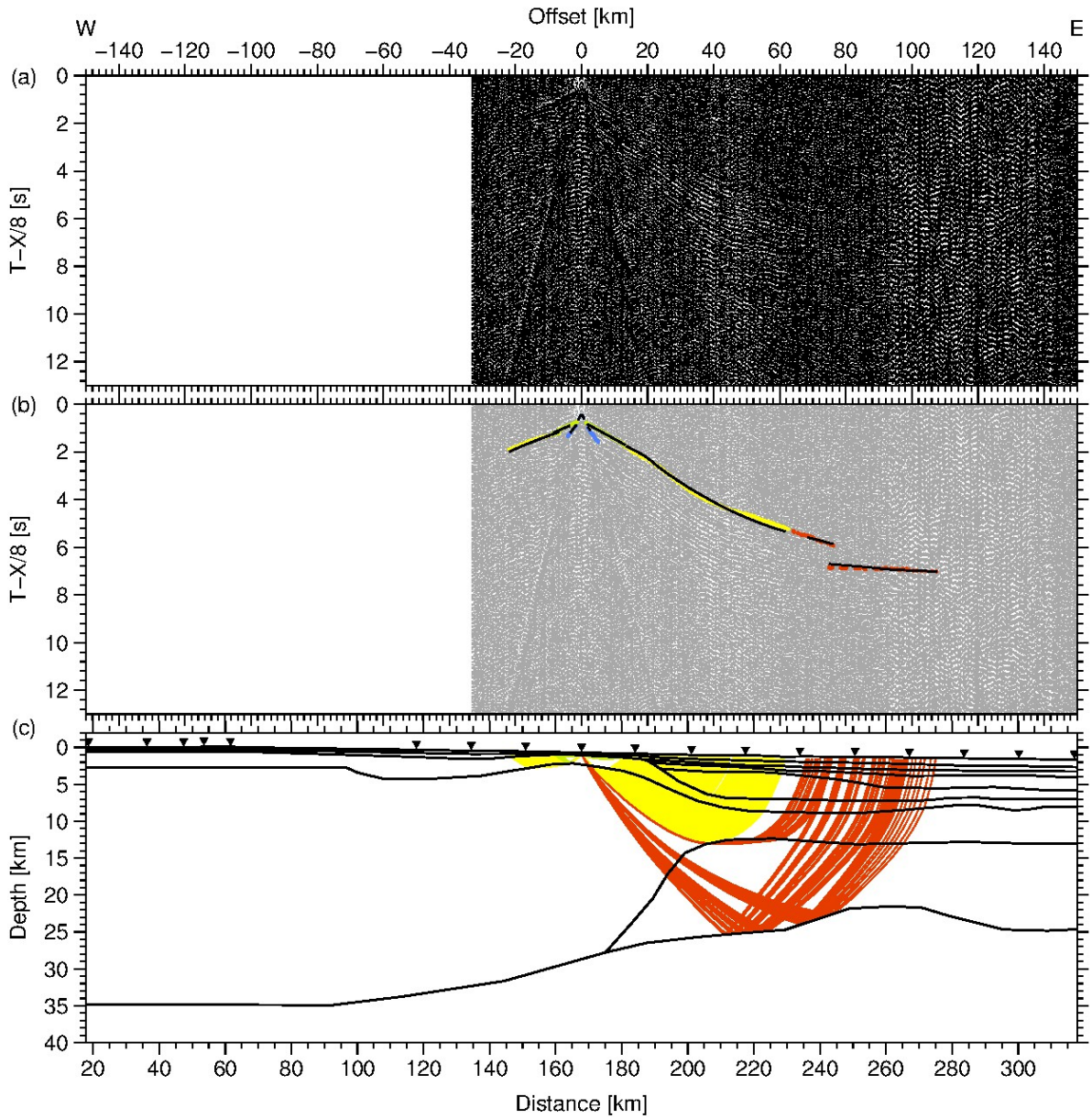


Figure A8.: Data example for OBS 21. (a) Seismic section filtered with a 4-15 Hz bandpass filter and displayed with a reduction velocity of 8 km/s. (b) Picked phases with error bars and corresponding phase names. The modelled first arrivals are plotted as black lines. (c) Ray path for picks shown in (b). Station positions are marked as triangles.

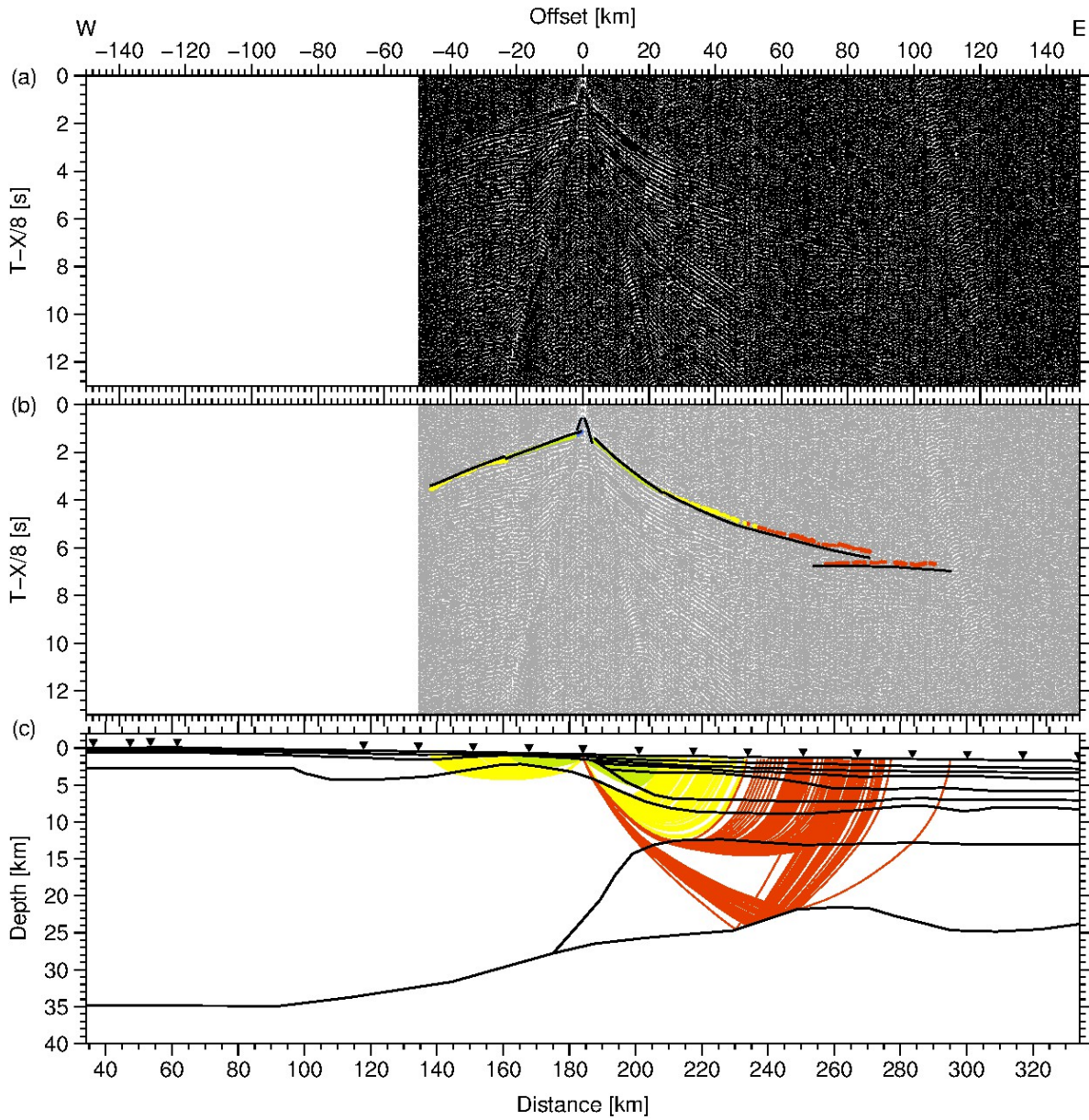


Figure A9.: Data example for OBS 22. (a) Seismic section filtered with a 4-15 Hz bandpass filter and displayed with a reduction velocity of 8 km/s. (b) Picked phases with error bars and corresponding phase names. The modelled first arrivals are plotted as black lines. (c) Ray path for picks shown in (b). Station positions are marked as triangles.

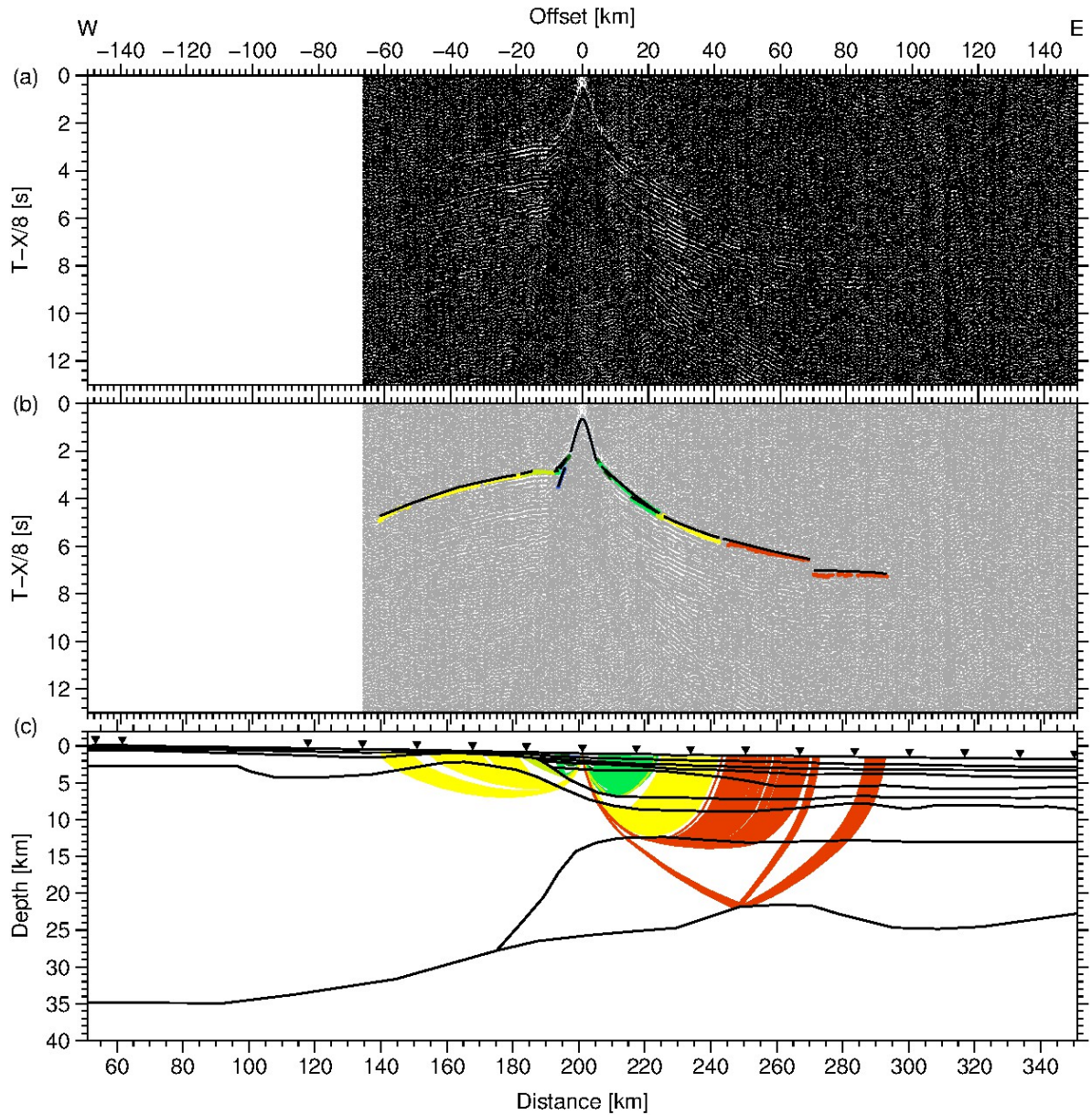


Figure A10.: Data example for OBS 23. (a) Seismic section filtered with a 4-15 Hz bandpass filter and displayed with a reduction velocity of 8 km/s. (b) Picked phases with error bars and corresponding phase names. The modelled first arrivals are plotted as black lines. (c) Ray path for picks shown in (b). Station positions are marked as triangles.

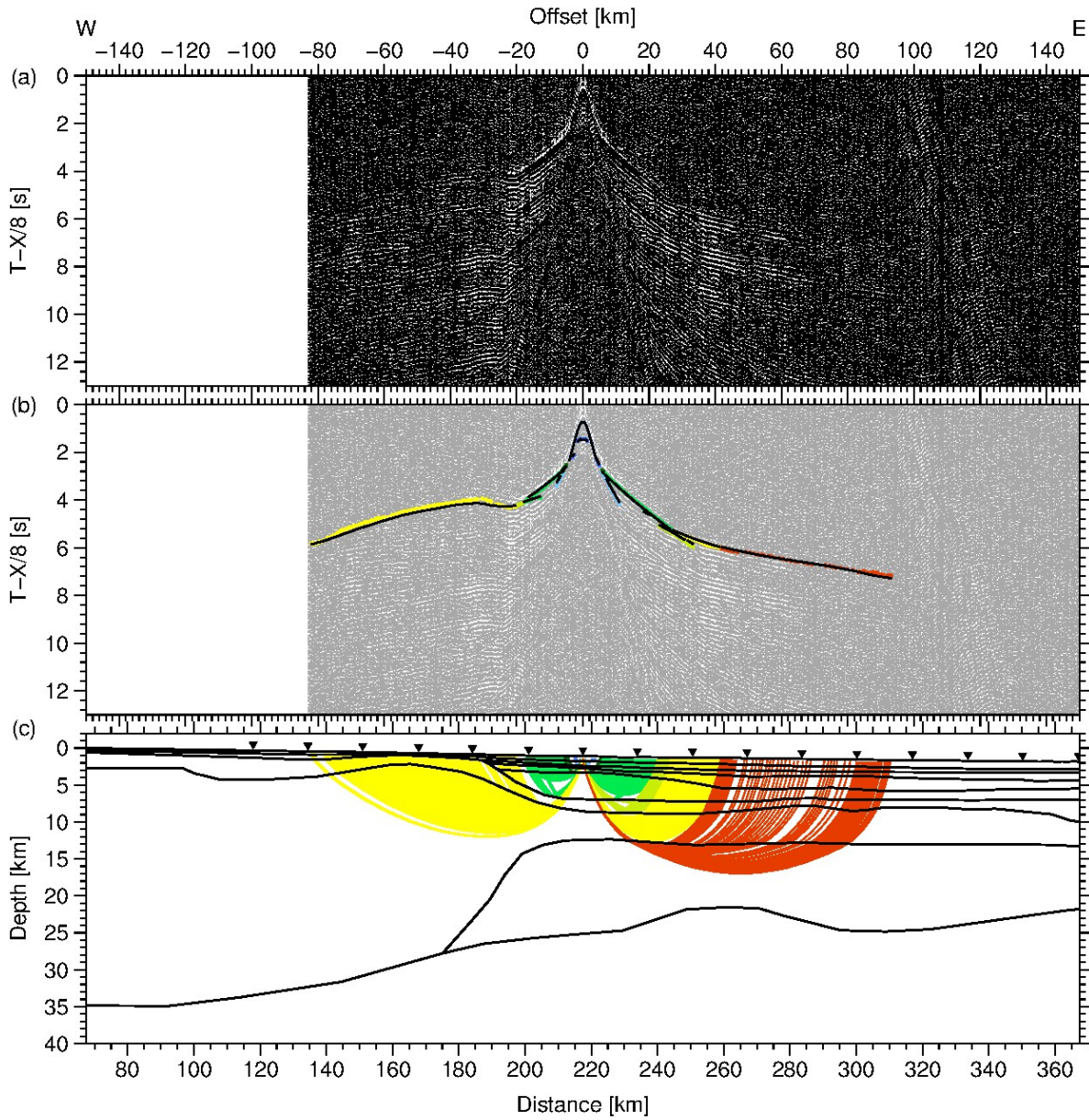


Figure A11.: Data example for OBS 24. (a) Seismic section filtered with a 4-15 Hz bandpass filter and displayed with a reduction velocity of 8 km/s. (b) Picked phases with error bars and corresponding phase names. The modelled first arrivals are plotted as black lines. (c) Ray path for picks shown in (b). Station positions are marked as triangles.

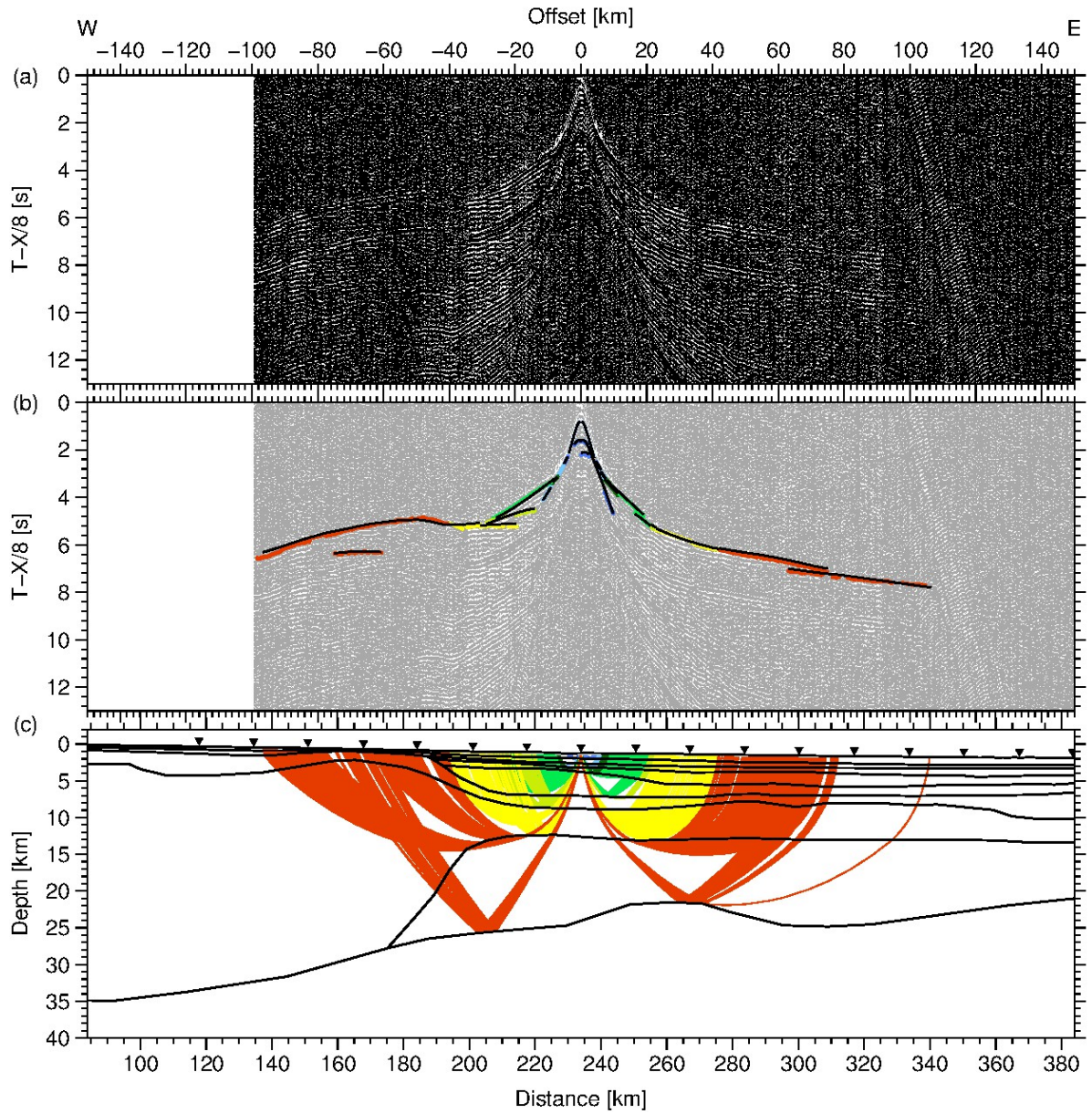


Figure A12.: Data example for OBS 25. (a) Seismic section filtered with a 4-15 Hz bandpass filter and displayed with a reduction velocity of 8 km/s. (b) Picked phases with error bars and corresponding phase names. The modelled first arrivals are plotted as black lines. (c) Ray path for picks shown in (b). Station positions are marked as triangles.

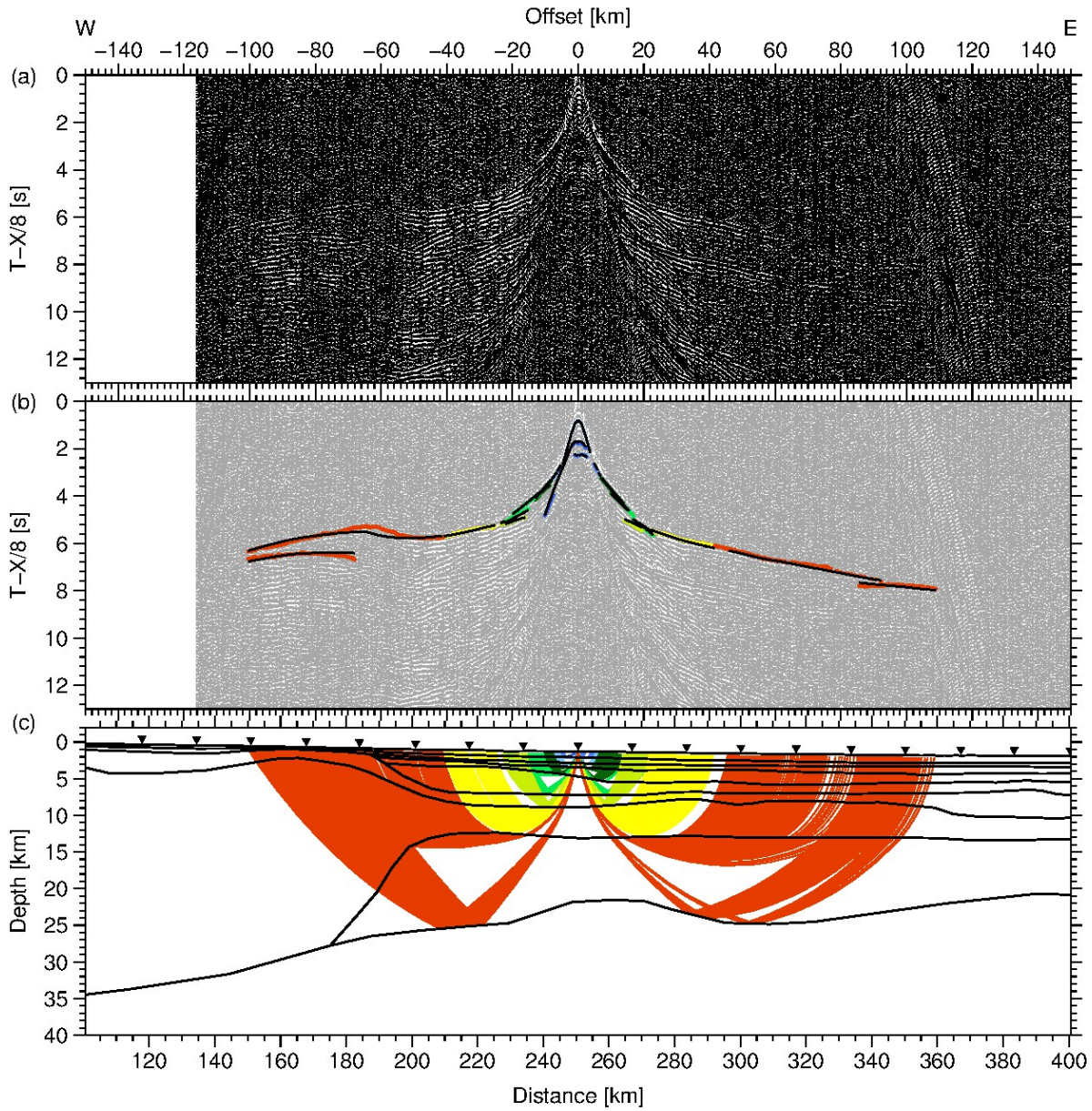


Figure A13.: Data example for OBS 26. (a) Seismic section filtered with a 4-15 Hz bandpass filter and displayed with a reduction velocity of 8 km/s. (b) Picked phases with error bars and corresponding phase names. The modelled first arrivals are plotted as black lines. (c) Ray path for picks shown in (b). Station positions are marked as triangles.

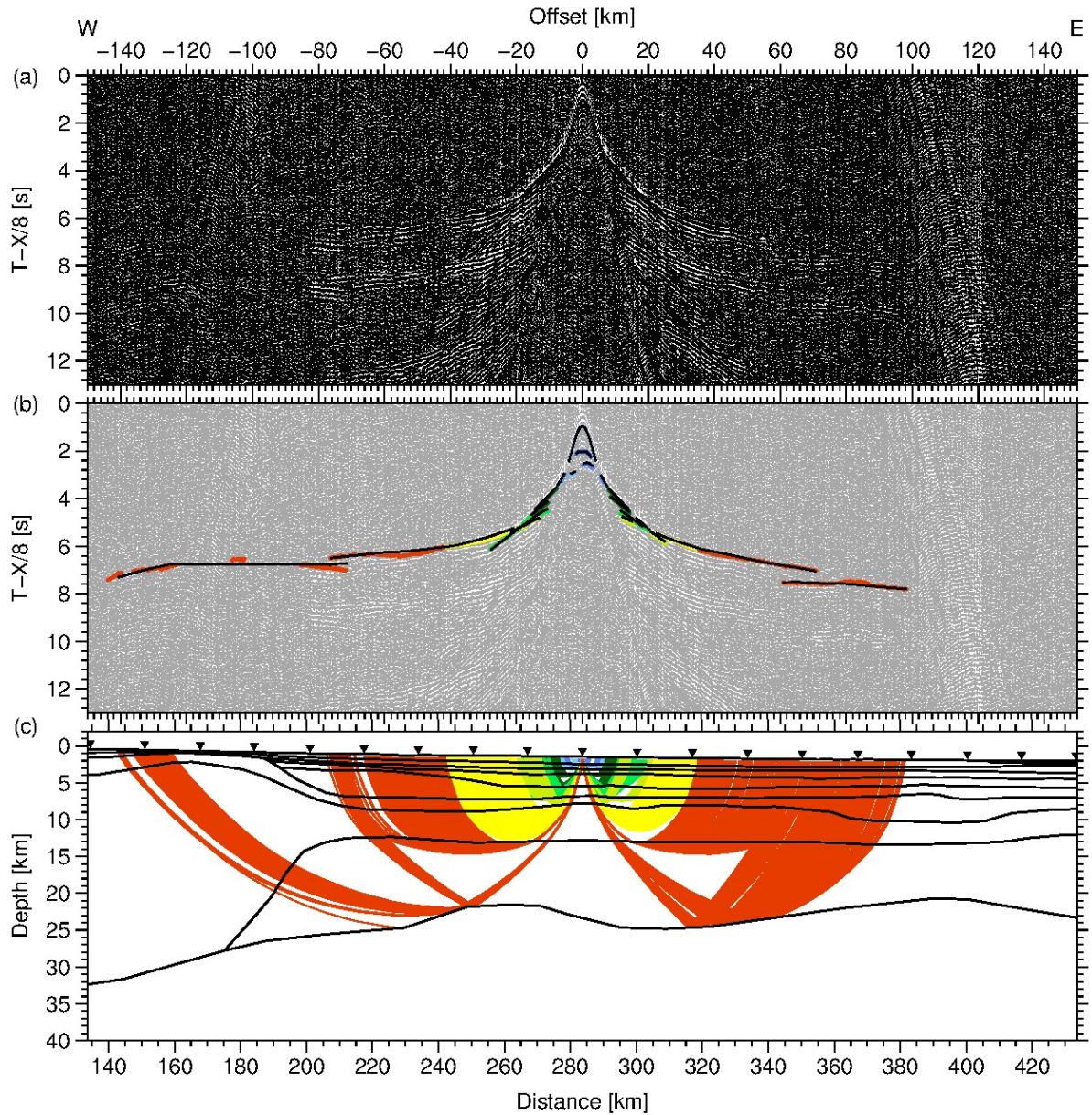


Figure A14.: Data example for OBS 28. (a) Seismic section filtered with a 4-15 Hz bandpass filter and displayed with a reduction velocity of 8 km/s. (b) Picked phases with error bars and corresponding phase names. The modelled first arrivals are plotted as black lines. (c) Ray path for picks shown in (b). Station positions are marked as triangles.

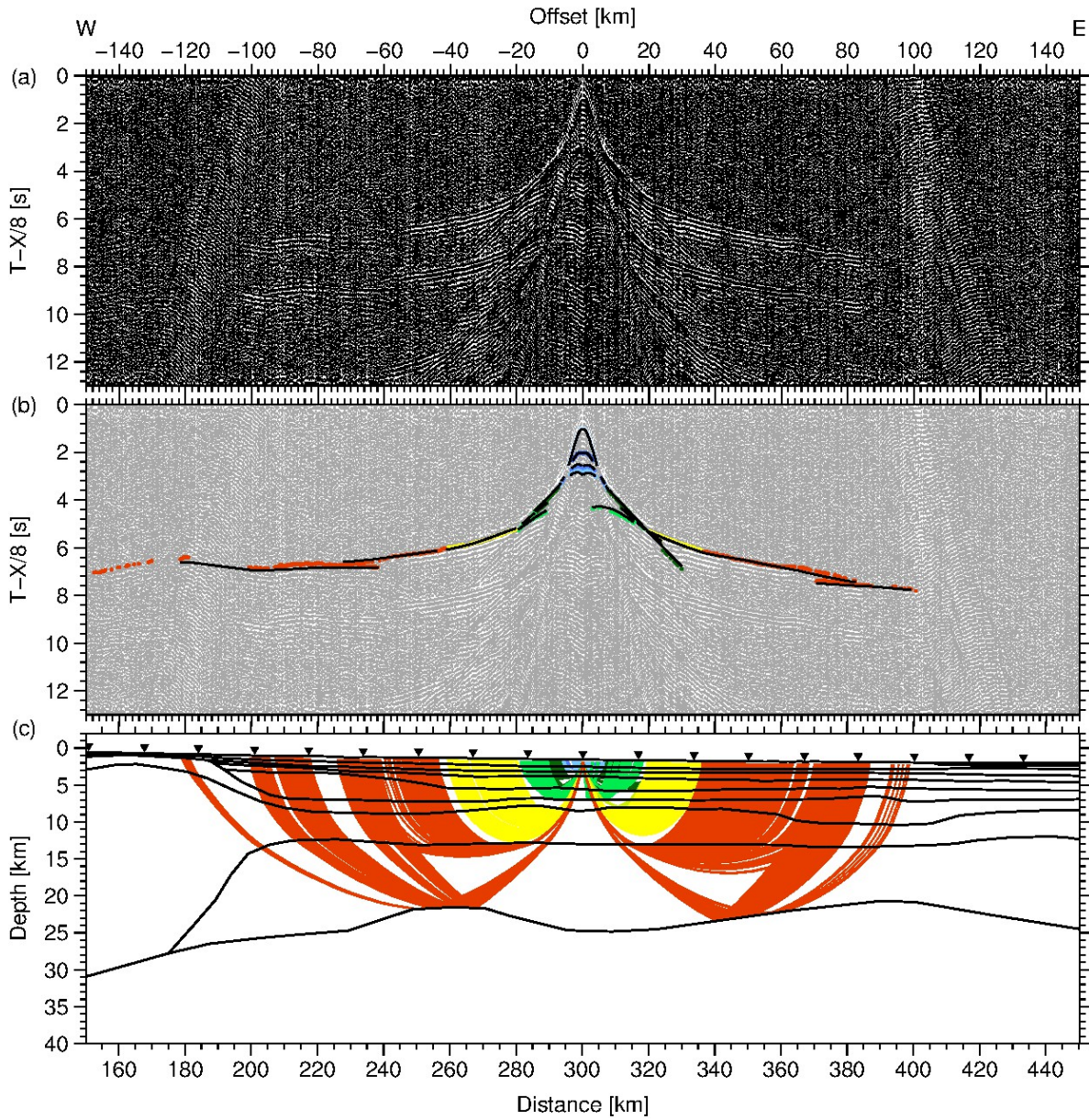


Figure A15.: Data example for OBS 29. (a) Seismic section filtered with a 4-15 Hz bandpass filter and displayed with a reduction velocity of 8 km/s. (b) Picked phases with error bars and corresponding phase names. The modelled first arrivals are plotted as black lines. (c) Ray path for picks shown in (b). Station positions are marked as triangles.

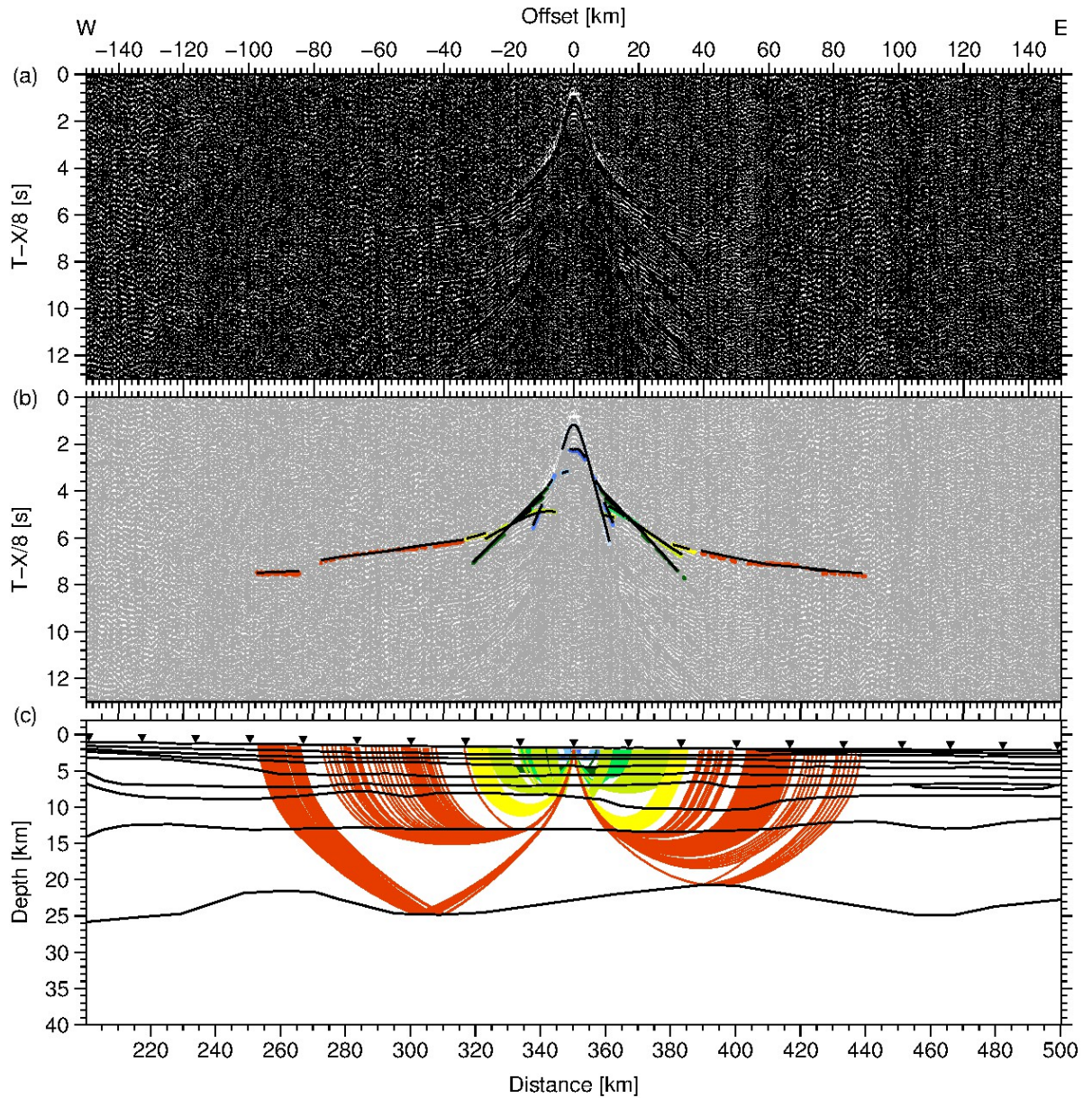


Figure A16.: Data example for OBS 32. (a) Seismic section filtered with a 4-15 Hz bandpass filter and displayed with a reduction velocity of 8 km/s. (b) Picked phases with error bars and corresponding phase names. The modelled first arrivals are plotted as black lines. (c) Ray path for picks shown in (b). Station positions are marked as triangles.

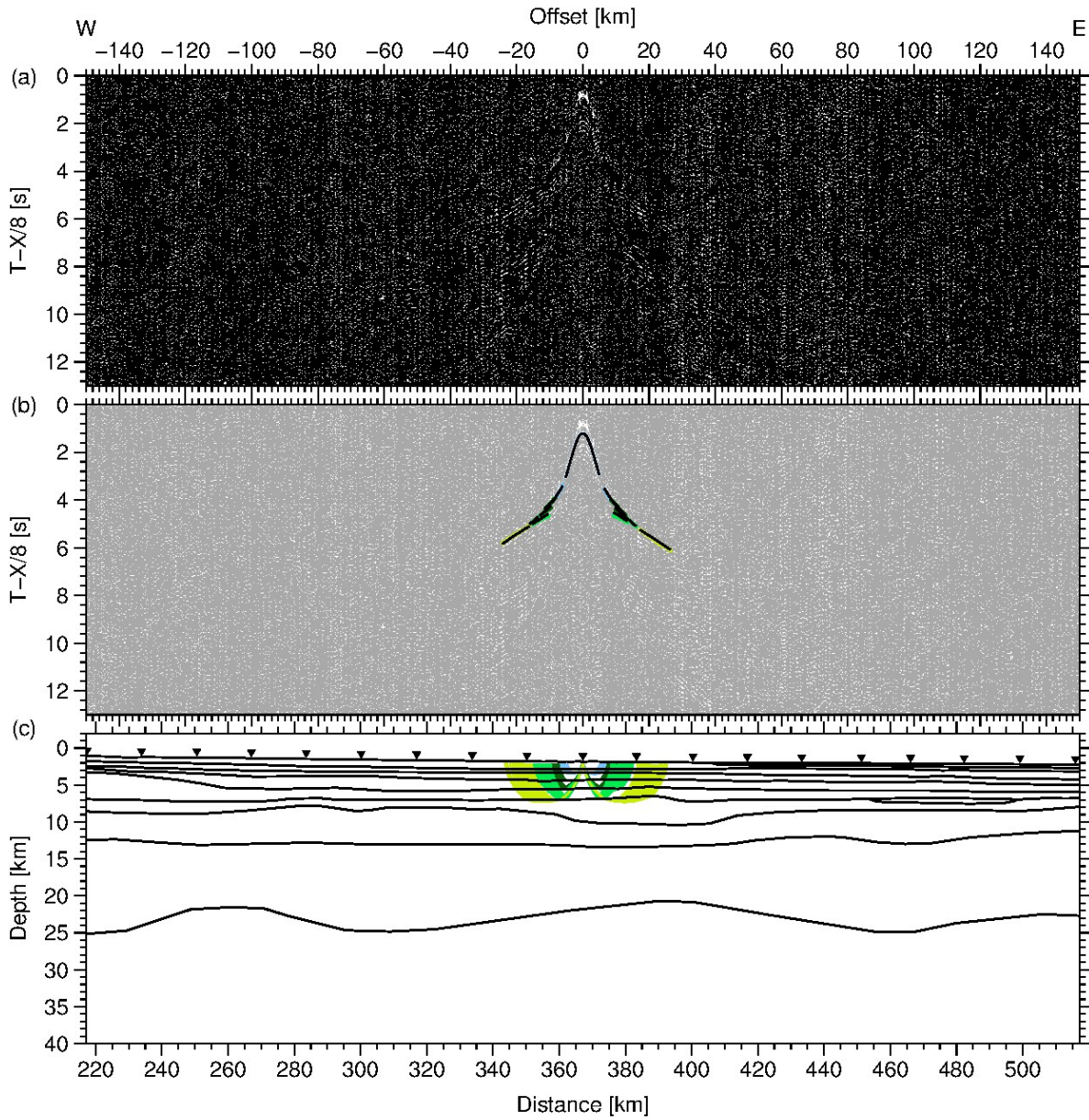


Figure A17.: Data example for OBS 33. (a) Seismic section filtered with a 4-15 Hz bandpass filter and displayed with a reduction velocity of 8 km/s. (b) Picked phases with error bars and corresponding phase names. The modelled first arrivals are plotted as black lines. (c) Ray path for picks shown in (b). Station positions are marked as triangles.

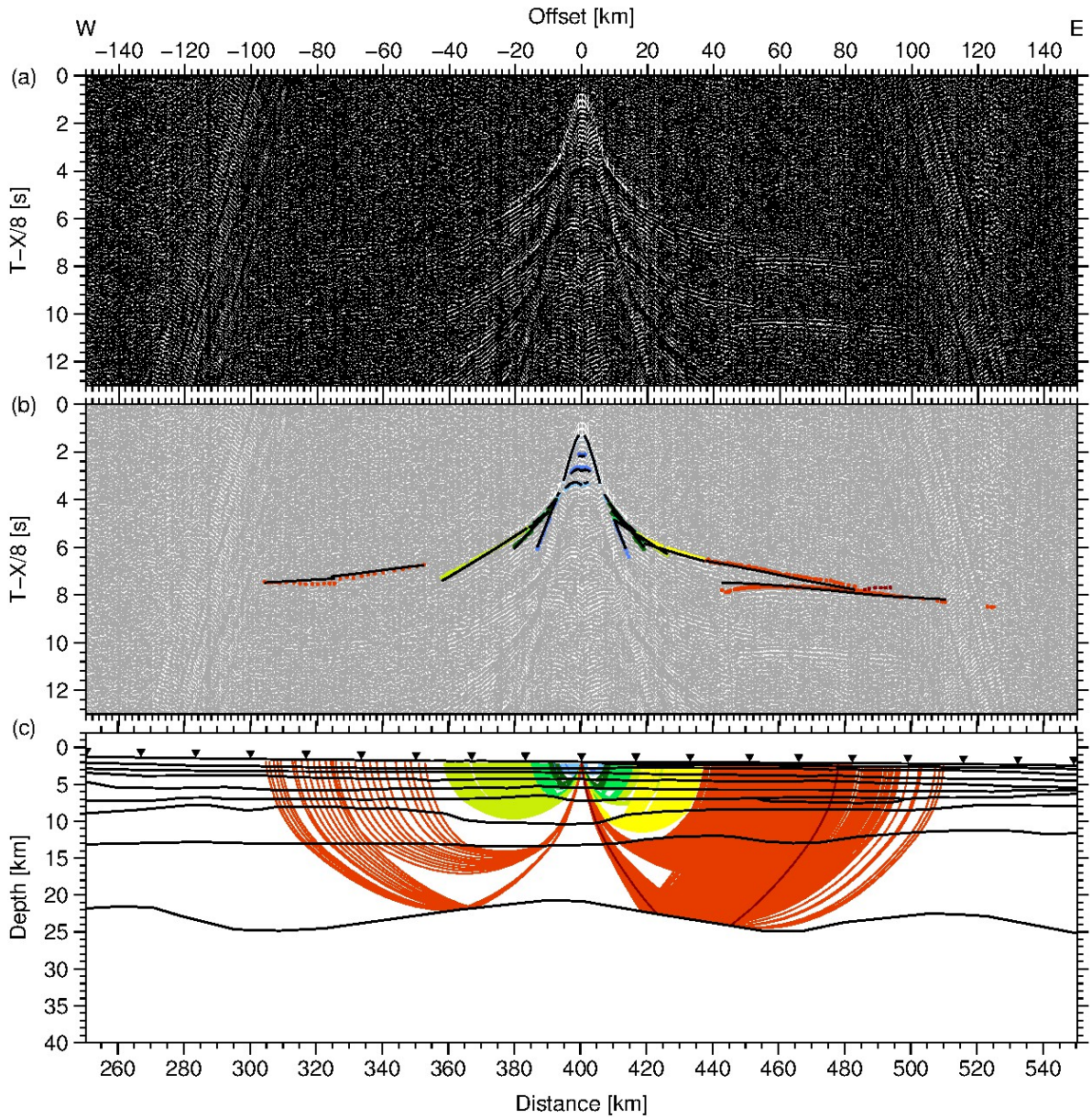


Figure A18.: Data example for OBS 35. (a) Seismic section filtered with a 4-15 Hz bandpass filter and displayed with a reduction velocity of 8 km/s. (b) Picked phases with error bars and corresponding phase names. The modelled first arrivals are plotted as black lines. (c) Ray path for picks shown in (b). Station positions are marked as triangles.

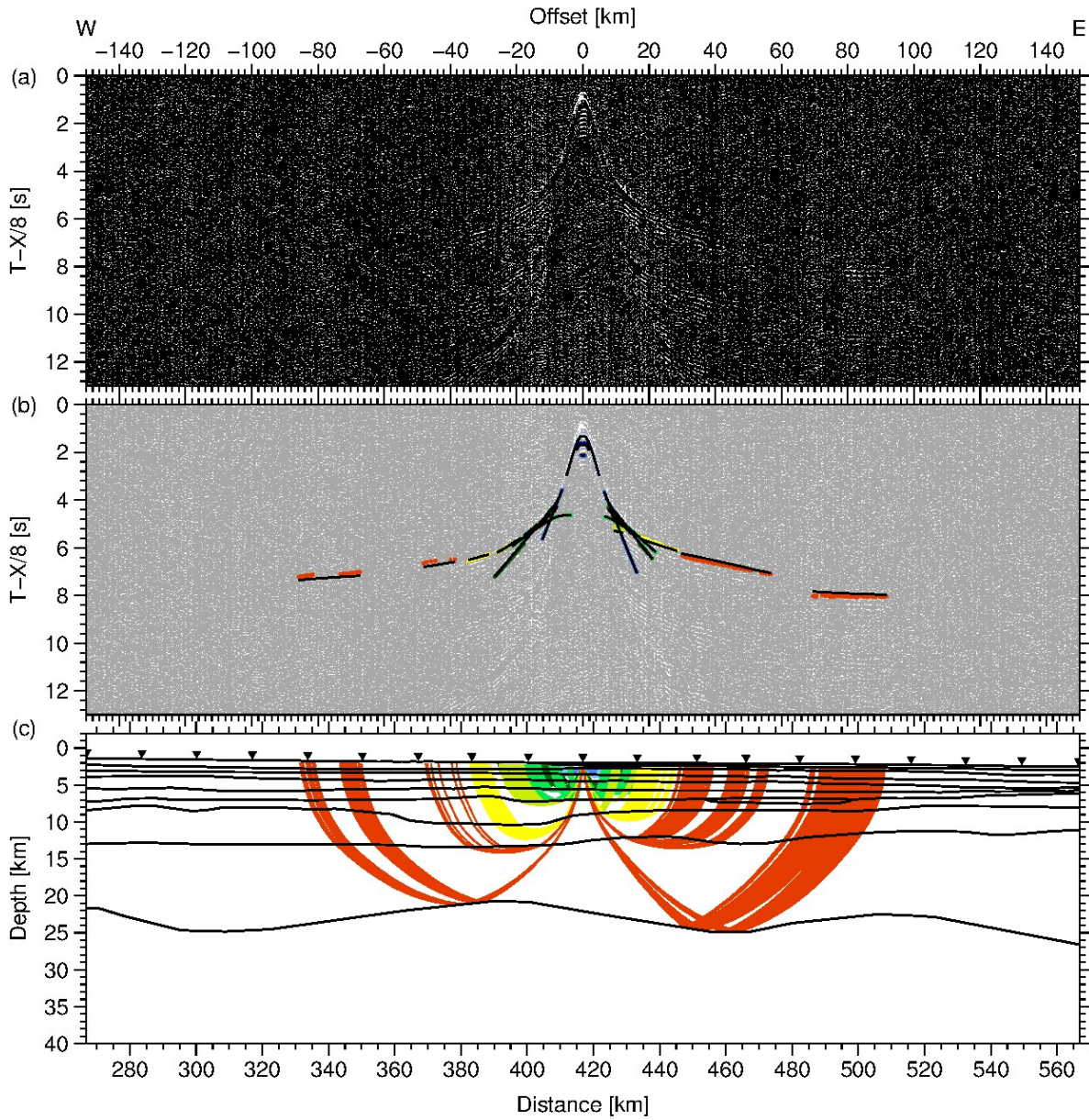


Figure A19.: Data example for OBS 36. (a) Seismic section filtered with a 4-15 Hz bandpass filter and displayed with a reduction velocity of 8 km/s. (b) Picked phases with error bars and corresponding phase names. The modelled first arrivals are plotted as black lines. (c) Ray path for picks shown in (b). Station positions are marked as triangles.

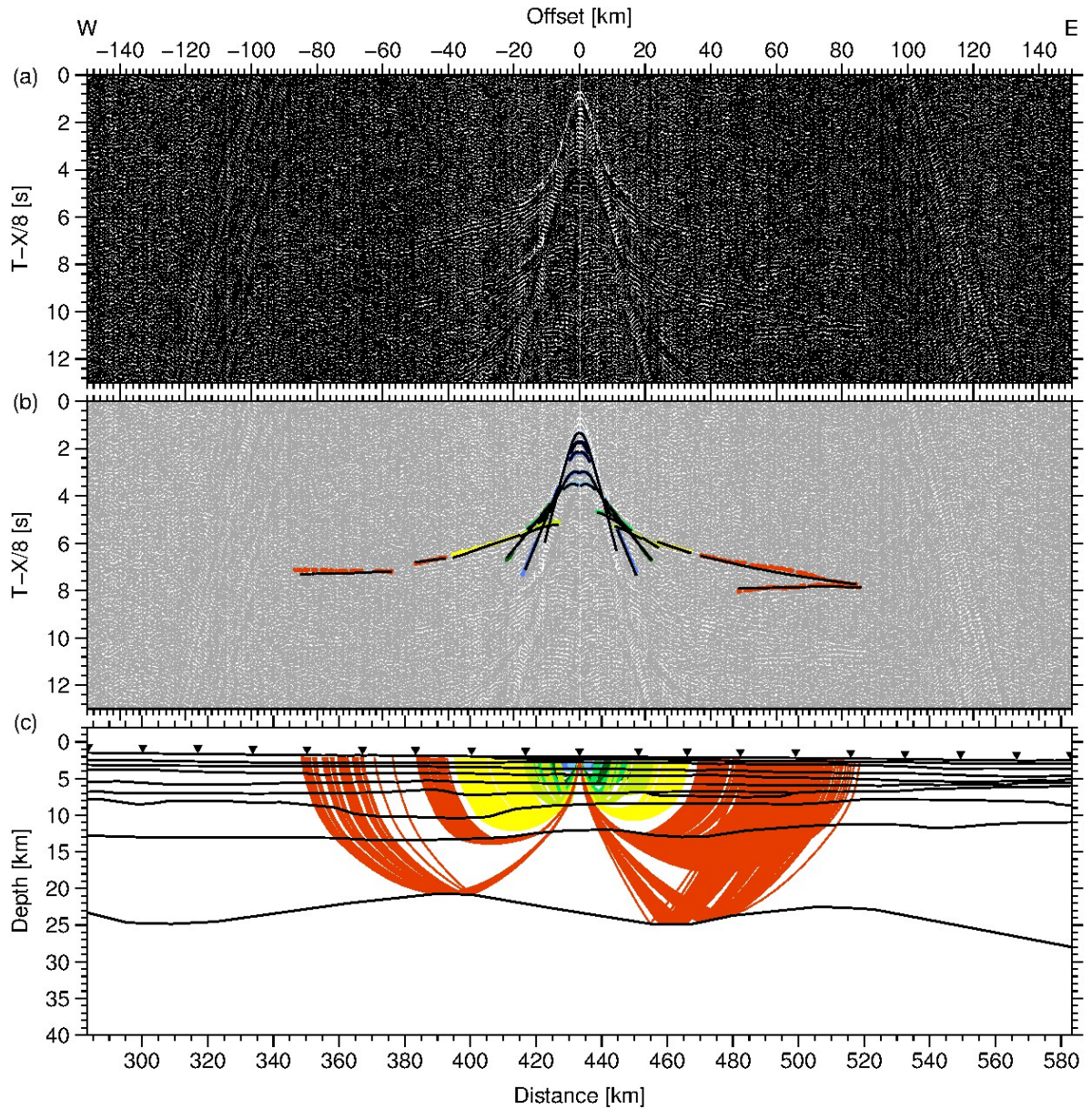


Figure A20.: Data example for OBS 37. (a) Seismic section filtered with a 4-15 Hz bandpass filter and displayed with a reduction velocity of 8 km/s. (b) Picked phases with error bars and corresponding phase names. The modelled first arrivals are plotted as black lines. (c) Ray path for picks shown in (b). Station positions are marked as triangles.

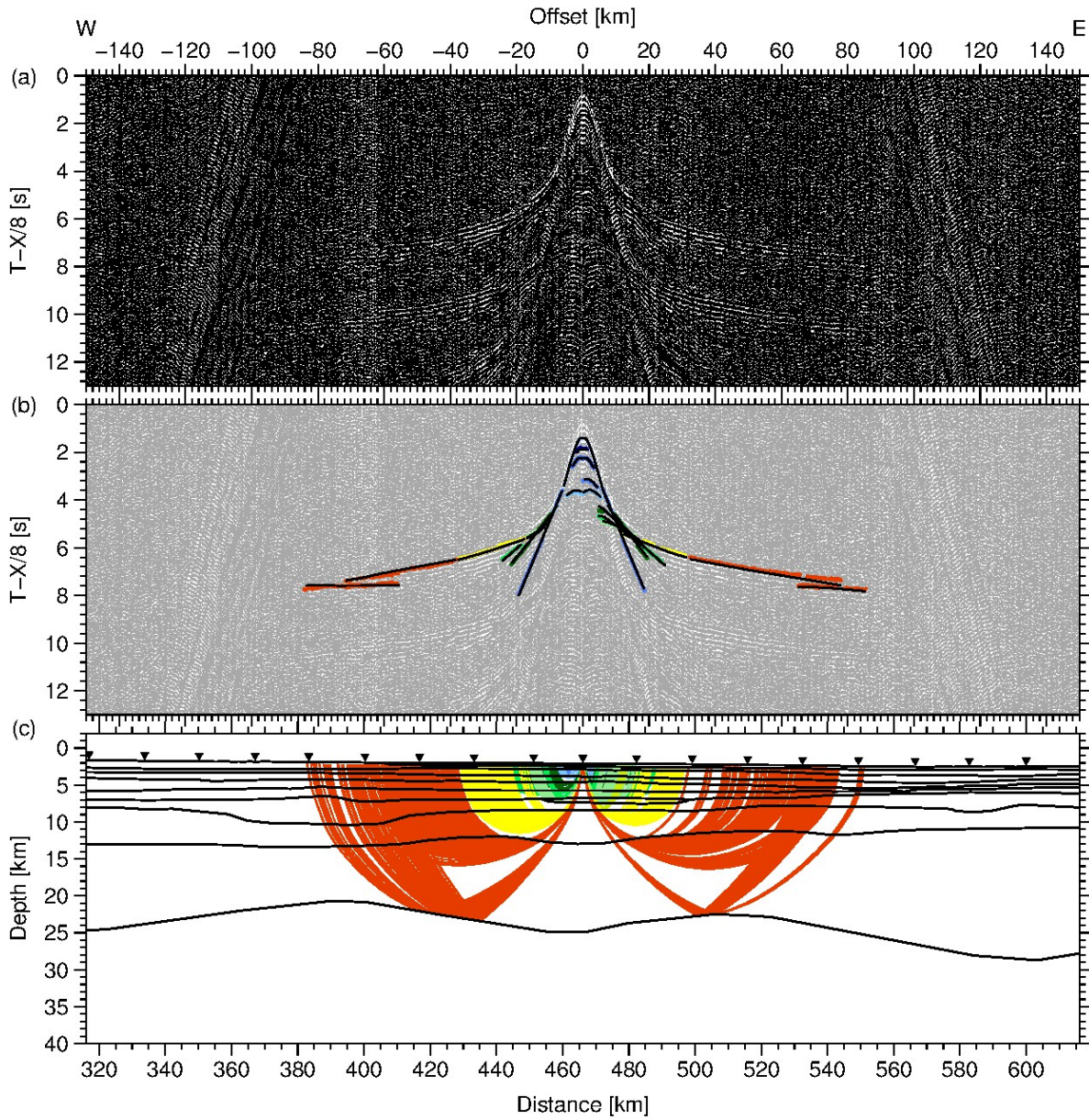


Figure A21.: Data example for OBS 39. (a) Seismic section filtered with a 4-15 Hz bandpass filter and displayed with a reduction velocity of 8 km/s. (b) Picked phases with error bars and corresponding phase names. The modelled first arrivals are plotted as black lines. (c) Ray path for picks shown in (b). Station positions are marked as triangles.

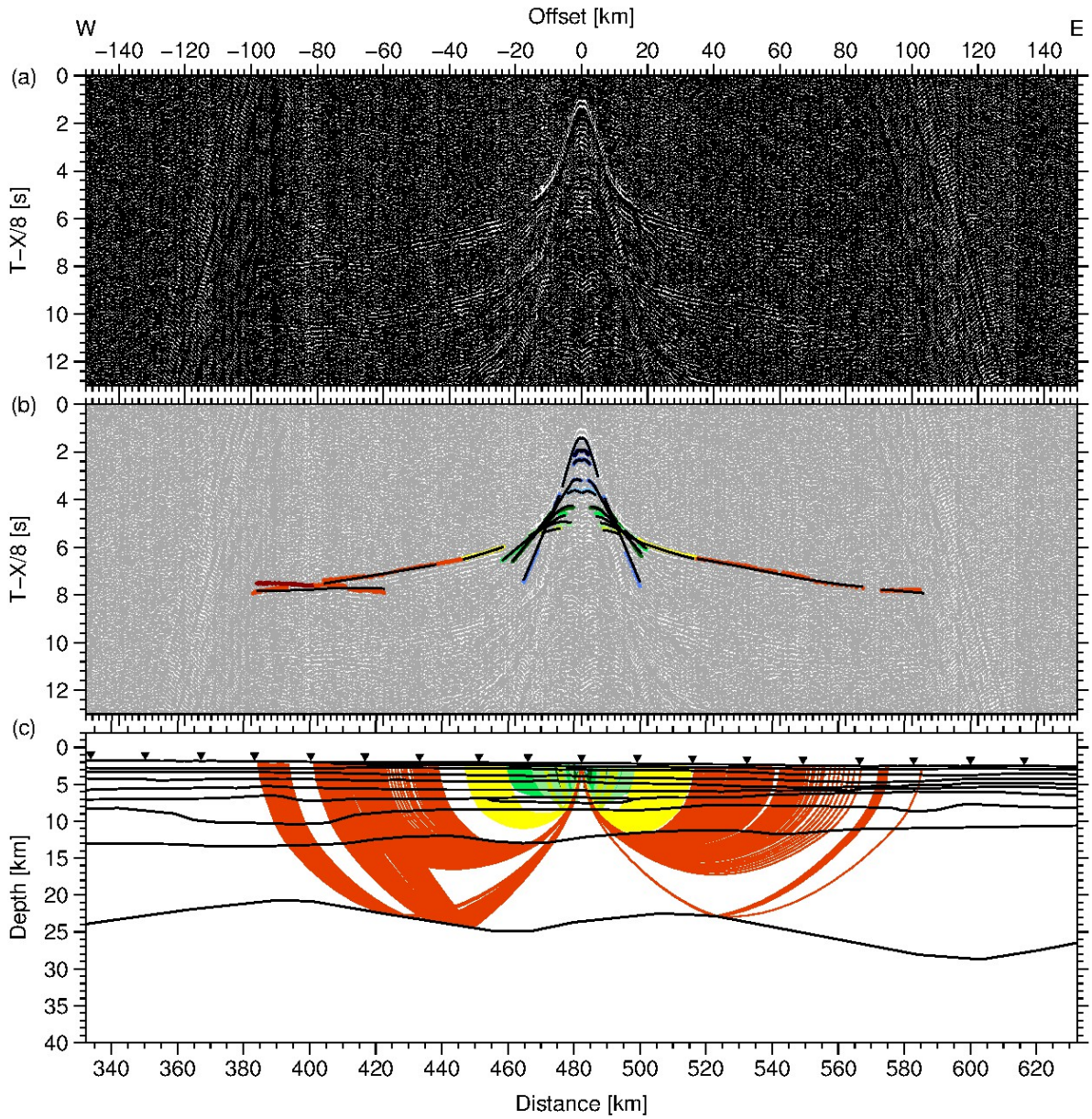


Figure A22.: Data example for OBS 40. (a) Seismic section filtered with a 4-15 Hz bandpass filter and displayed with a reduction velocity of 8 km/s. (b) Picked phases with error bars and corresponding phase names. The modelled first arrivals are plotted as black lines. (c) Ray path for picks shown in (b). Station positions are marked as triangles.

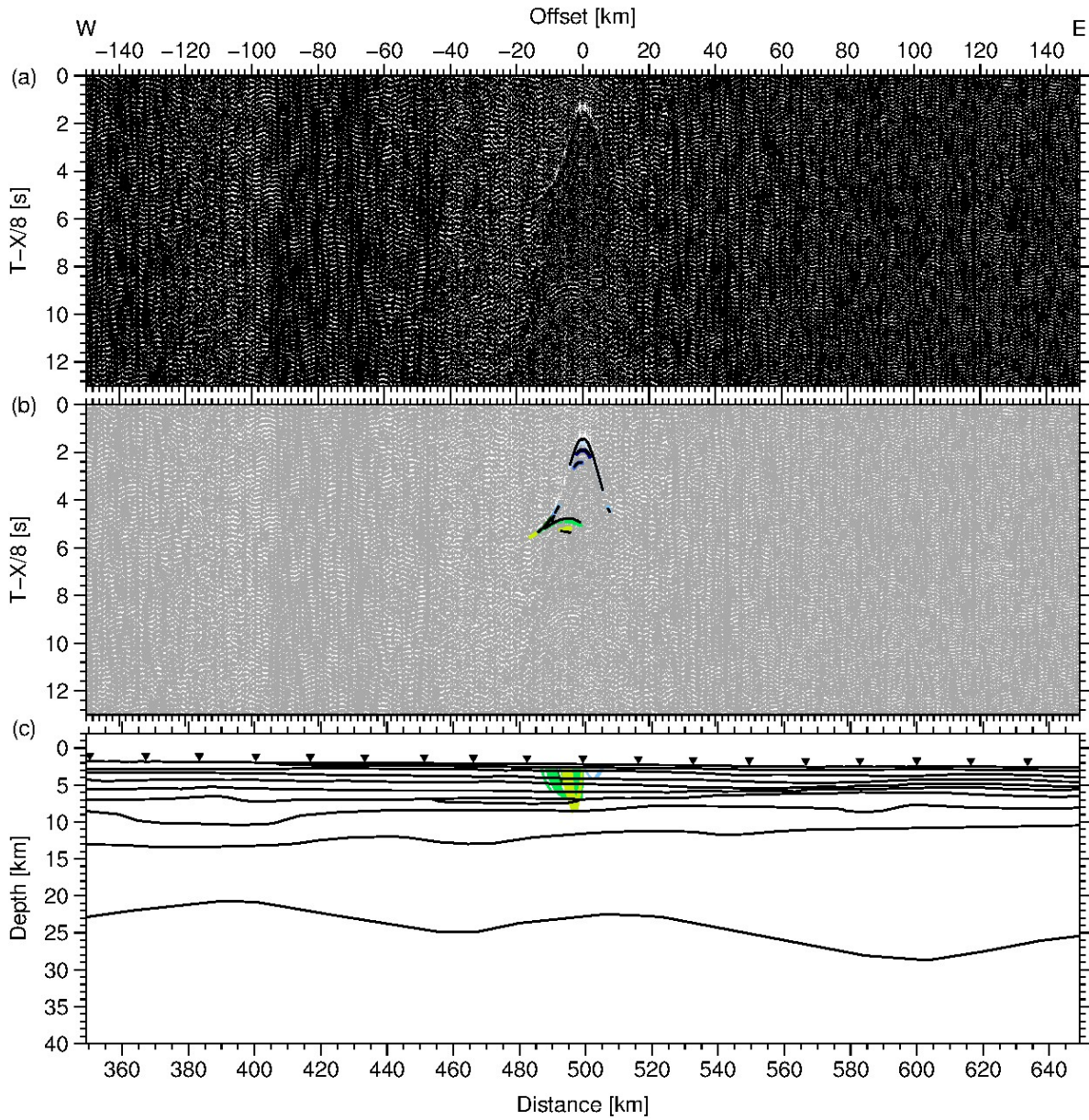


Figure A23.: Data example for OBS 41. (a) Seismic section filtered with a 4-15 Hz bandpass filter and displayed with a reduction velocity of 8 km/s. (b) Picked phases with error bars and corresponding phase names. The modelled first arrivals are plotted as black lines. (c) Ray path for picks shown in (b). Station positions are marked as triangles.

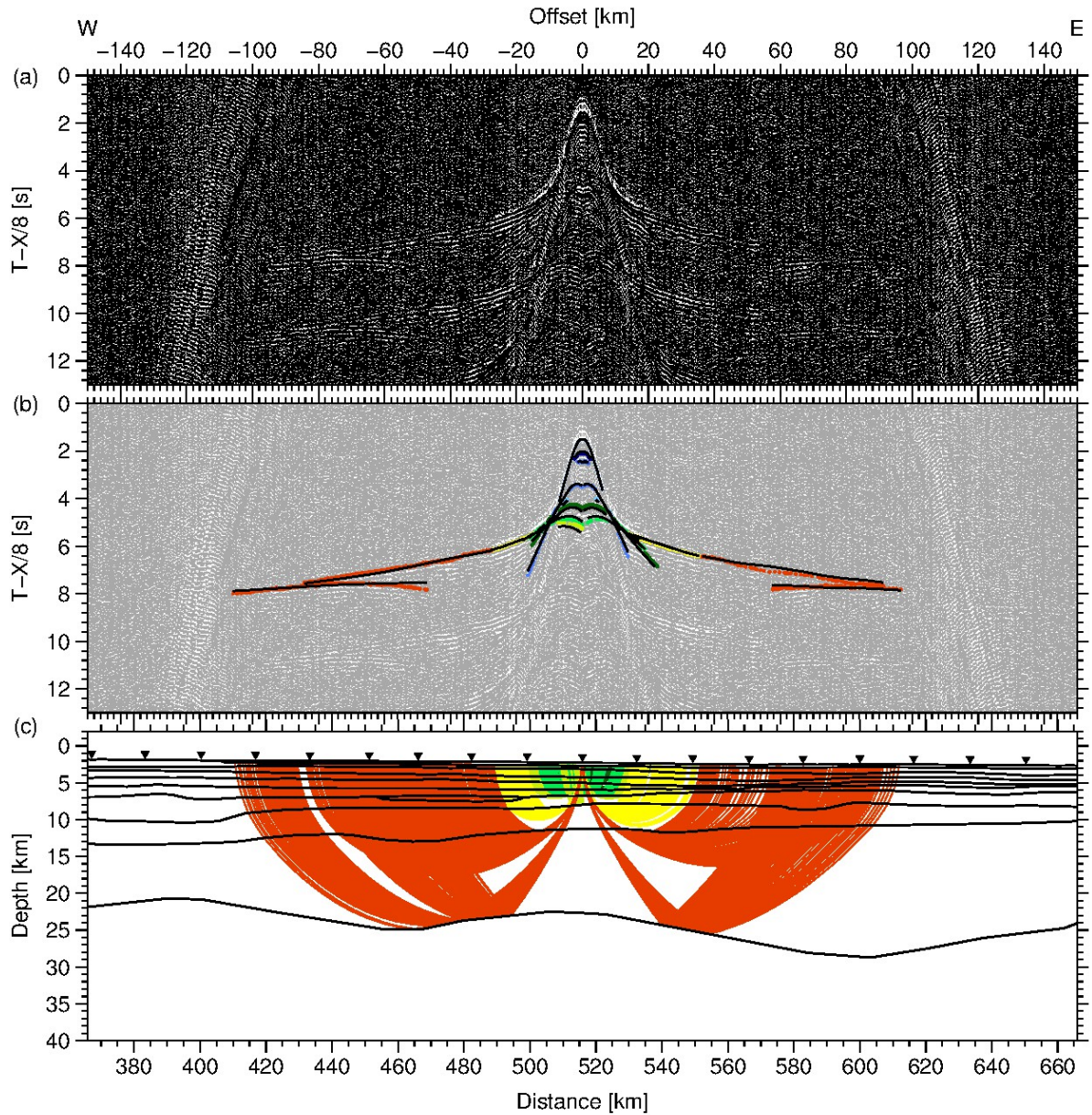


Figure A24.: Data example for OBS 42. (a) Seismic section filtered with a 4-15 Hz bandpass filter and displayed with a reduction velocity of 8 km/s. (b) Picked phases with error bars and corresponding phase names. The modelled first arrivals are plotted as black lines. (c) Ray path for picks shown in (b). Station positions are marked as triangles.

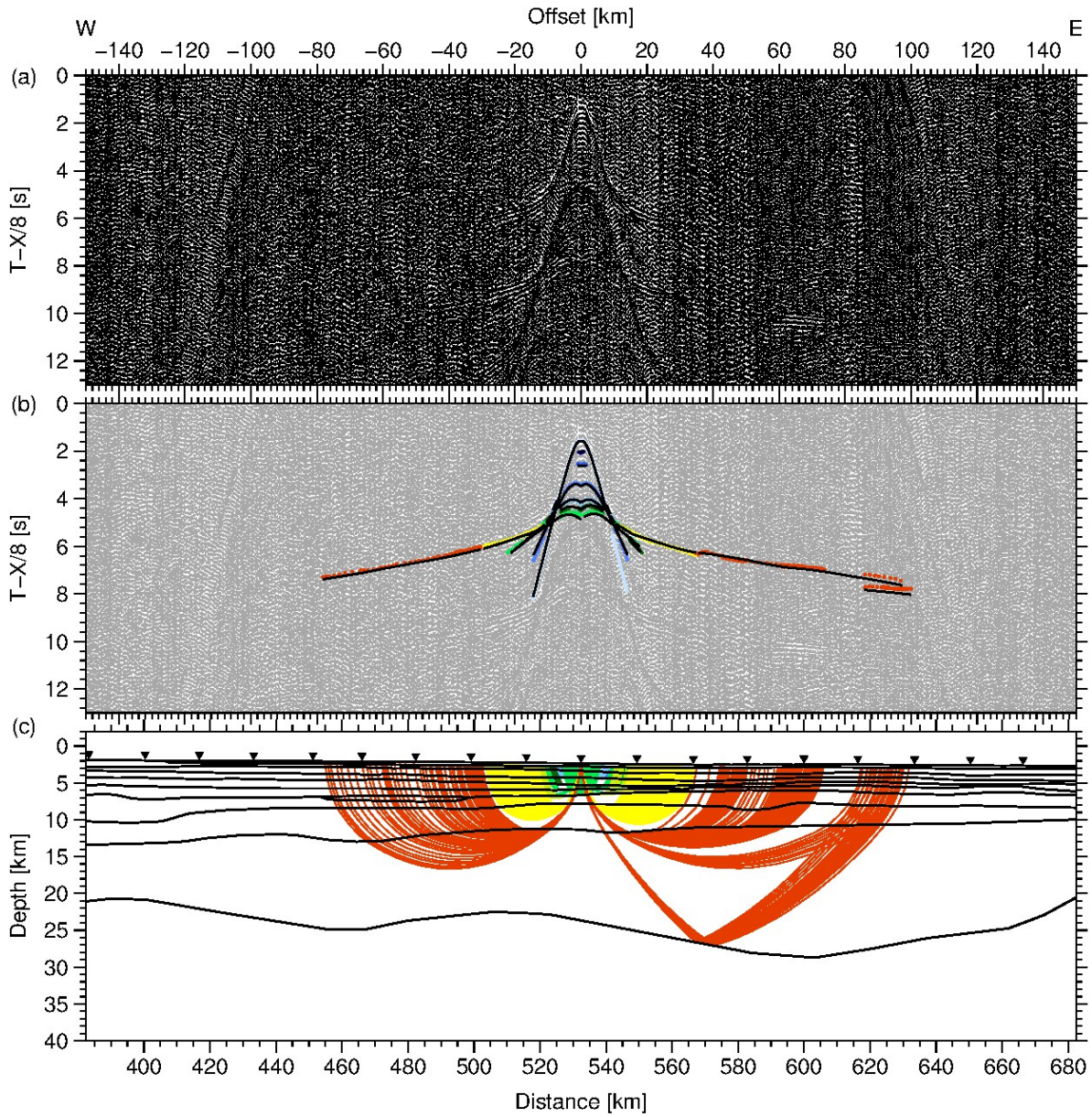


Figure A25.: Data example for OBS 43. (a) Seismic section filtered with a 4-15 Hz bandpass filter and displayed with a reduction velocity of 8 km/s. (b) Picked phases with error bars and corresponding phase names. The modelled first arrivals are plotted as black lines. (c) Ray path for picks shown in (b). Station positions are marked as triangles.

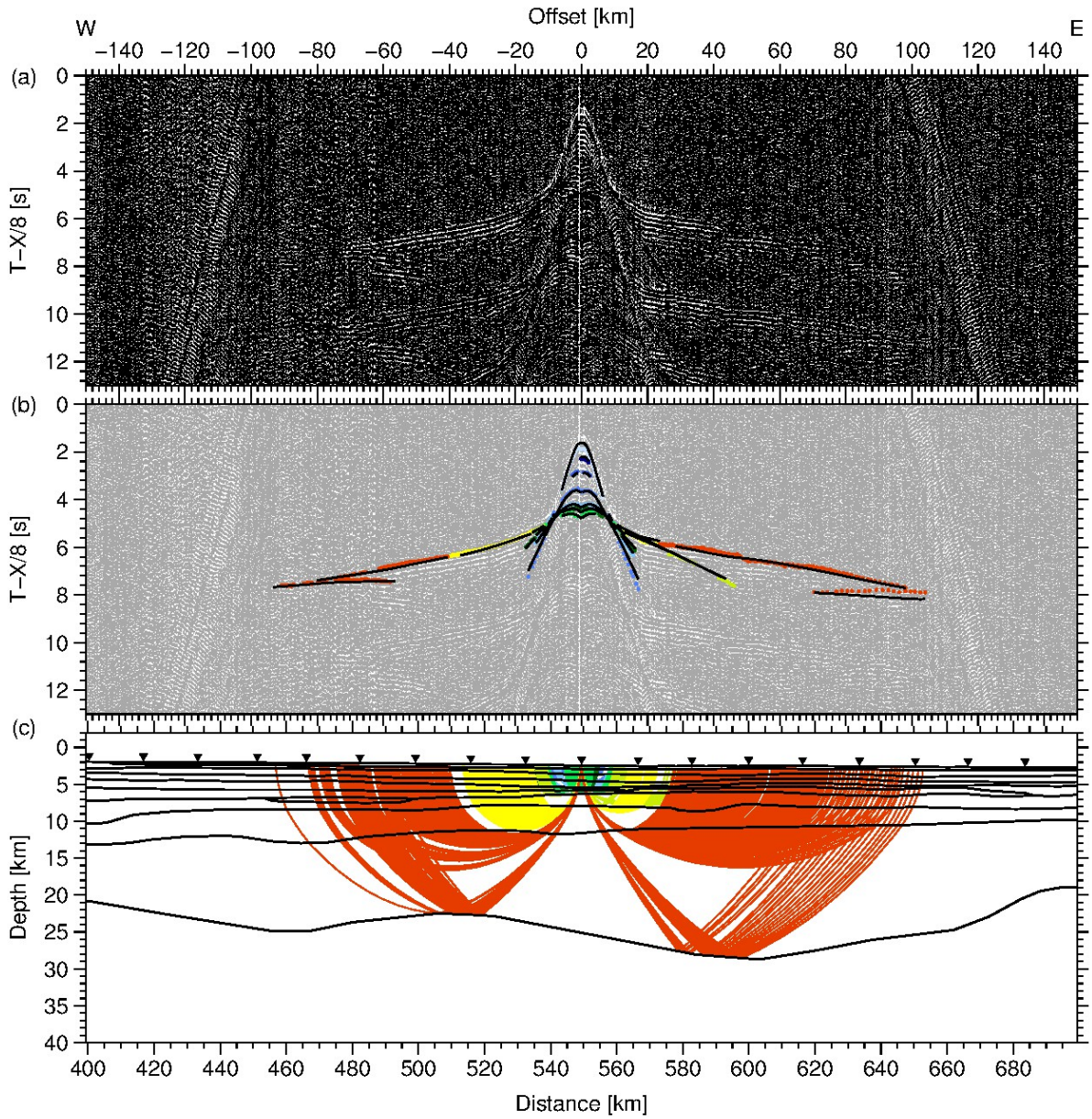


Figure A26.: Data example for OBS 44. (a) Seismic section filtered with a 4-15 Hz bandpass filter and displayed with a reduction velocity of 8 km/s. (b) Picked phases with error bars and corresponding phase names. The modelled first arrivals are plotted as black lines. (c) Ray path for picks shown in (b). Station positions are marked as triangles.

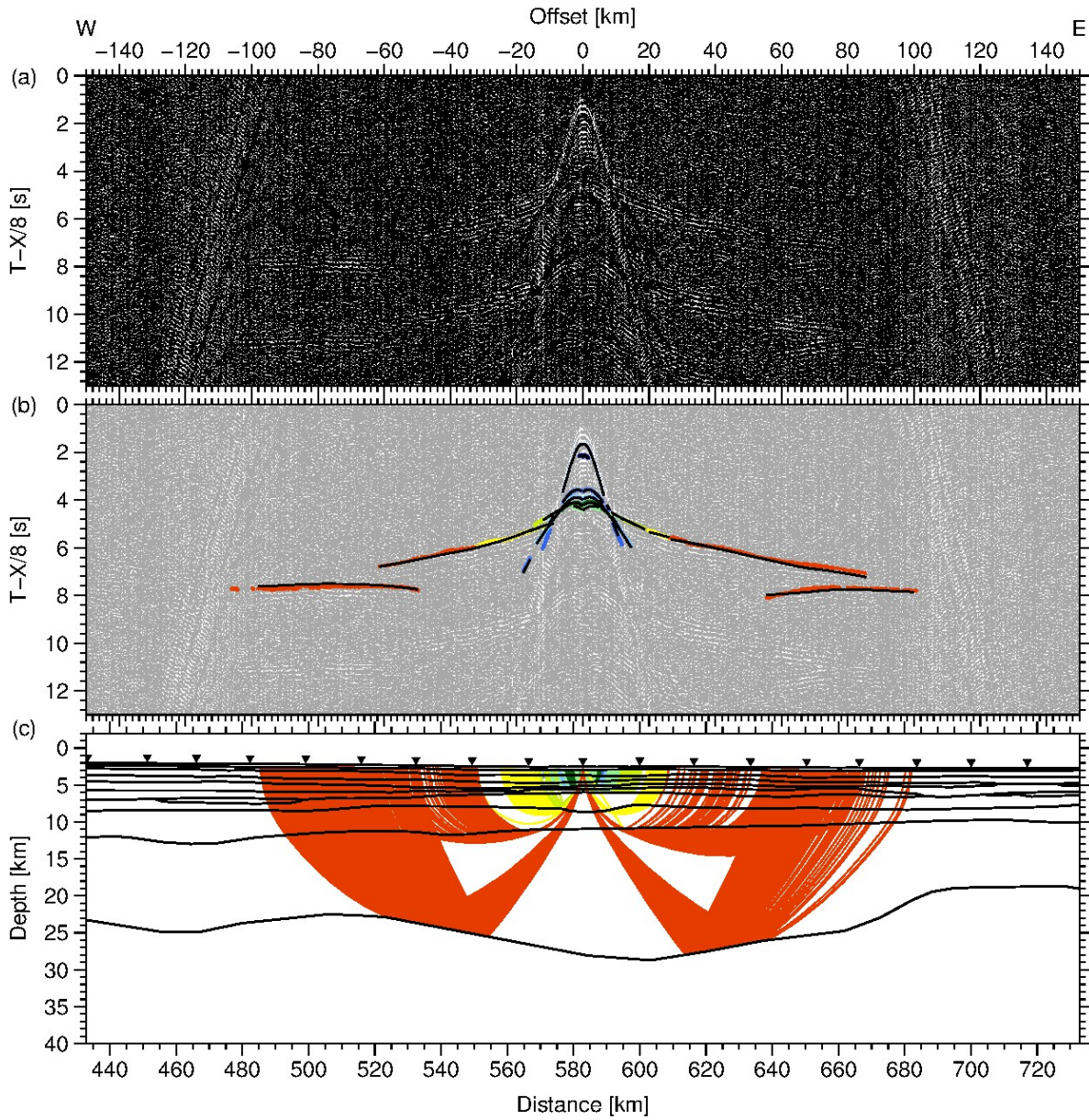


Figure A27.: Data example for OBS 46. (a) Seismic section filtered with a 4-15 Hz bandpass filter and displayed with a reduction velocity of 8 km/s. (b) Picked phases with error bars and corresponding phase names. The modelled first arrivals are plotted as black lines. (c) Ray path for picks shown in (b). Station positions are marked as triangles.

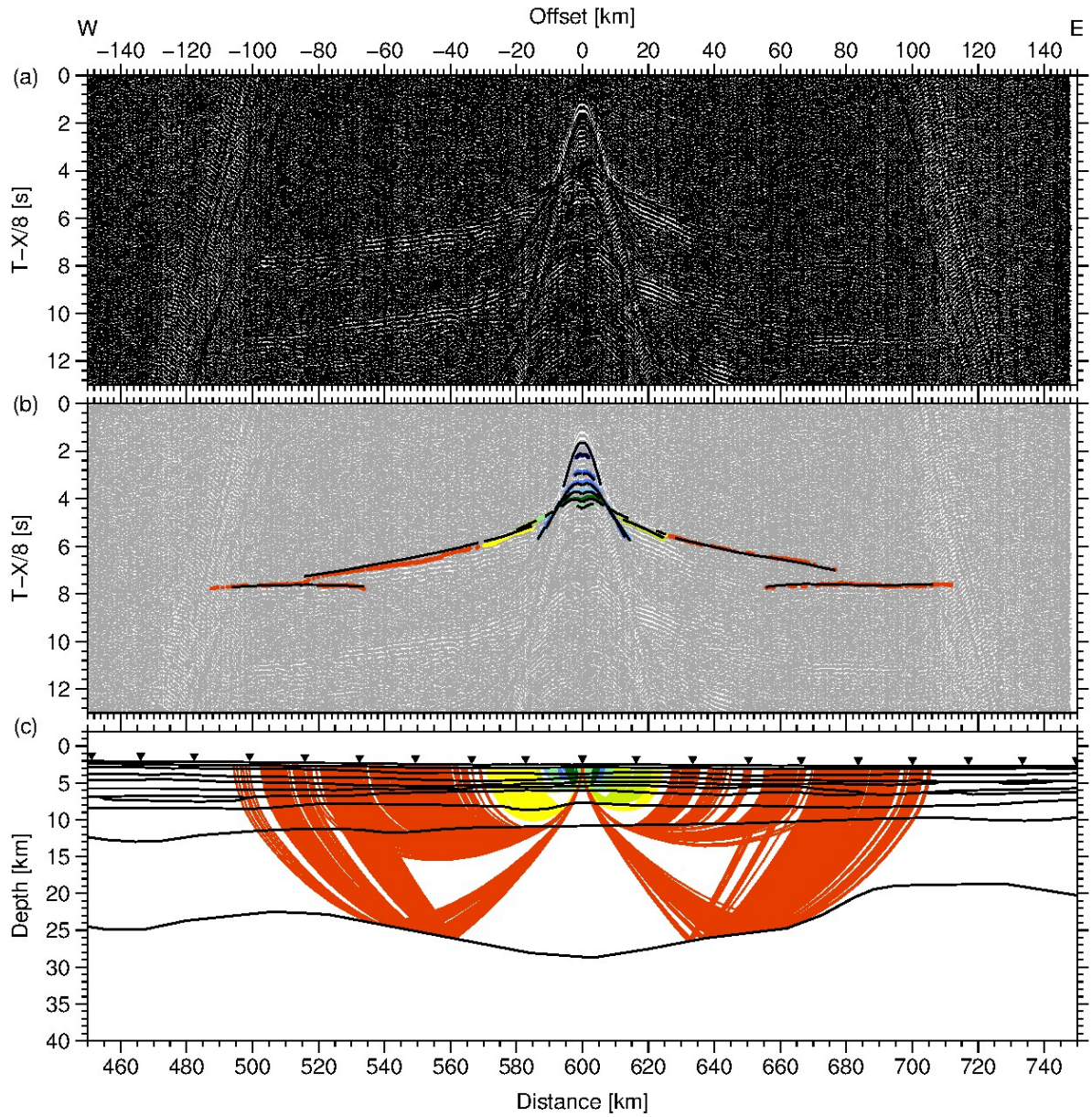


Figure A28.: Data example for OBH 47. (a) Seismic section filtered with a 4-15 Hz bandpass filter and displayed with a reduction velocity of 8 km/s. (b) Picked phases with error bars and corresponding phase names. The modelled first arrivals are plotted as black lines. (c) Ray path for picks shown in (b). Station positions are marked as triangles.

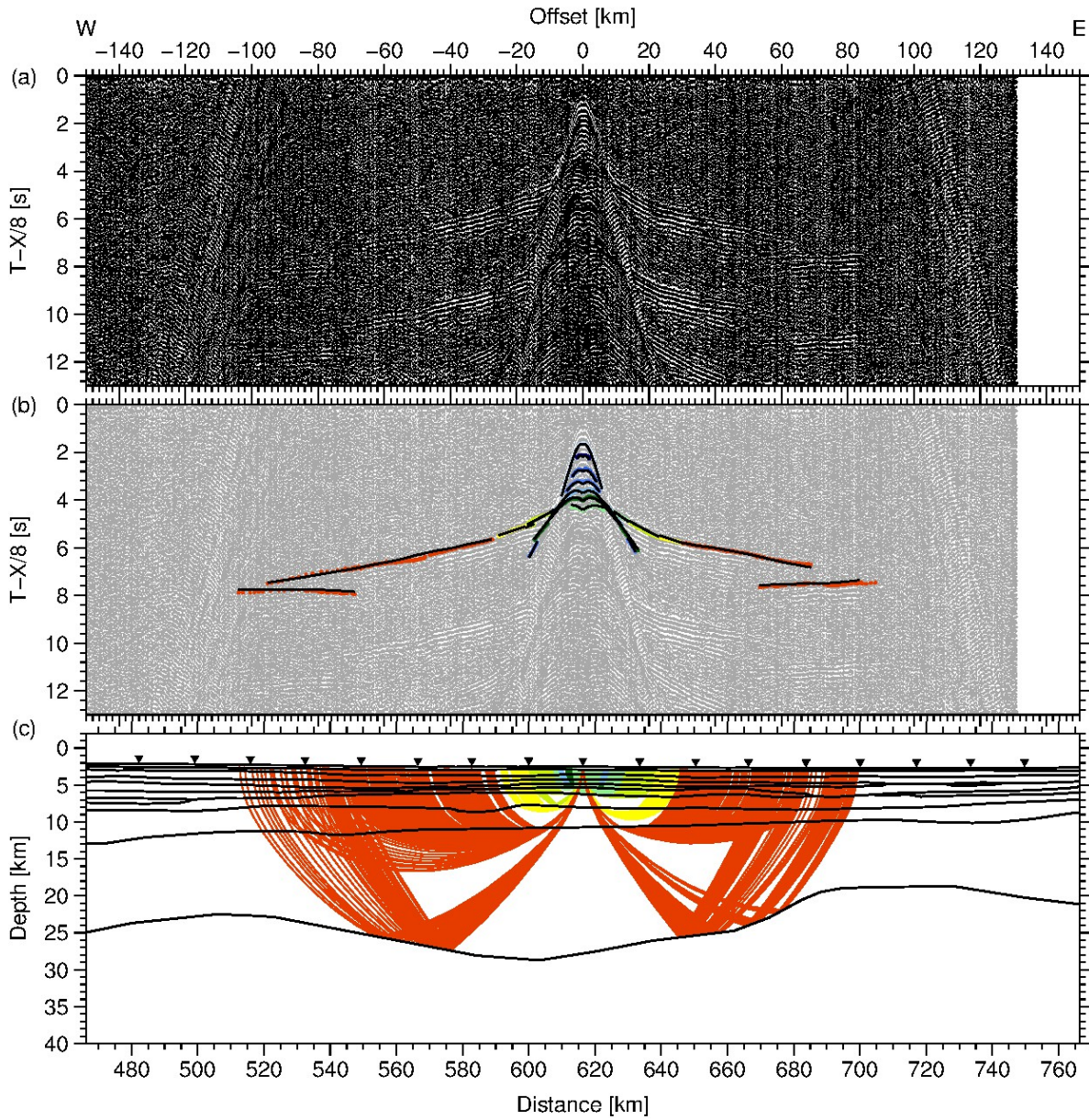


Figure A29.: Data example for OBS 48. (a) Seismic section filtered with a 4-15 Hz bandpass filter and displayed with a reduction velocity of 8 km/s. (b) Picked phases with error bars and corresponding phase names. The modelled first arrivals are plotted as black lines. (c) Ray path for picks shown in (b). Station positions are marked as triangles.

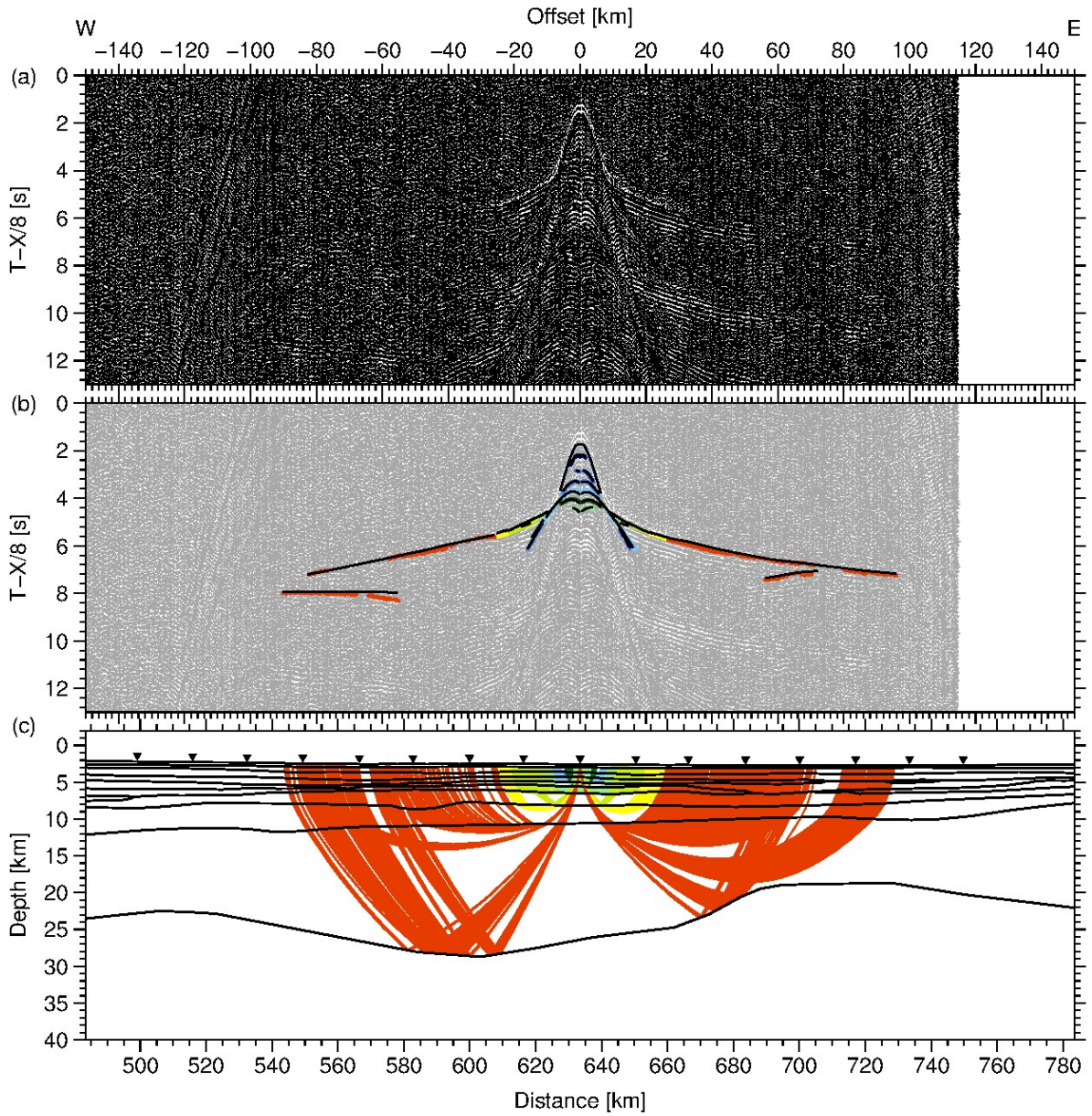


Figure A30.: Data example for OBH 49. (a) Seismic section filtered with a 4-15 Hz bandpass filter and displayed with a reduction velocity of 8 km/s. (b) Picked phases with error bars and corresponding phase names. The modelled first arrivals are plotted as black lines. (c) Ray path for picks shown in (b). Station positions are marked as triangles.

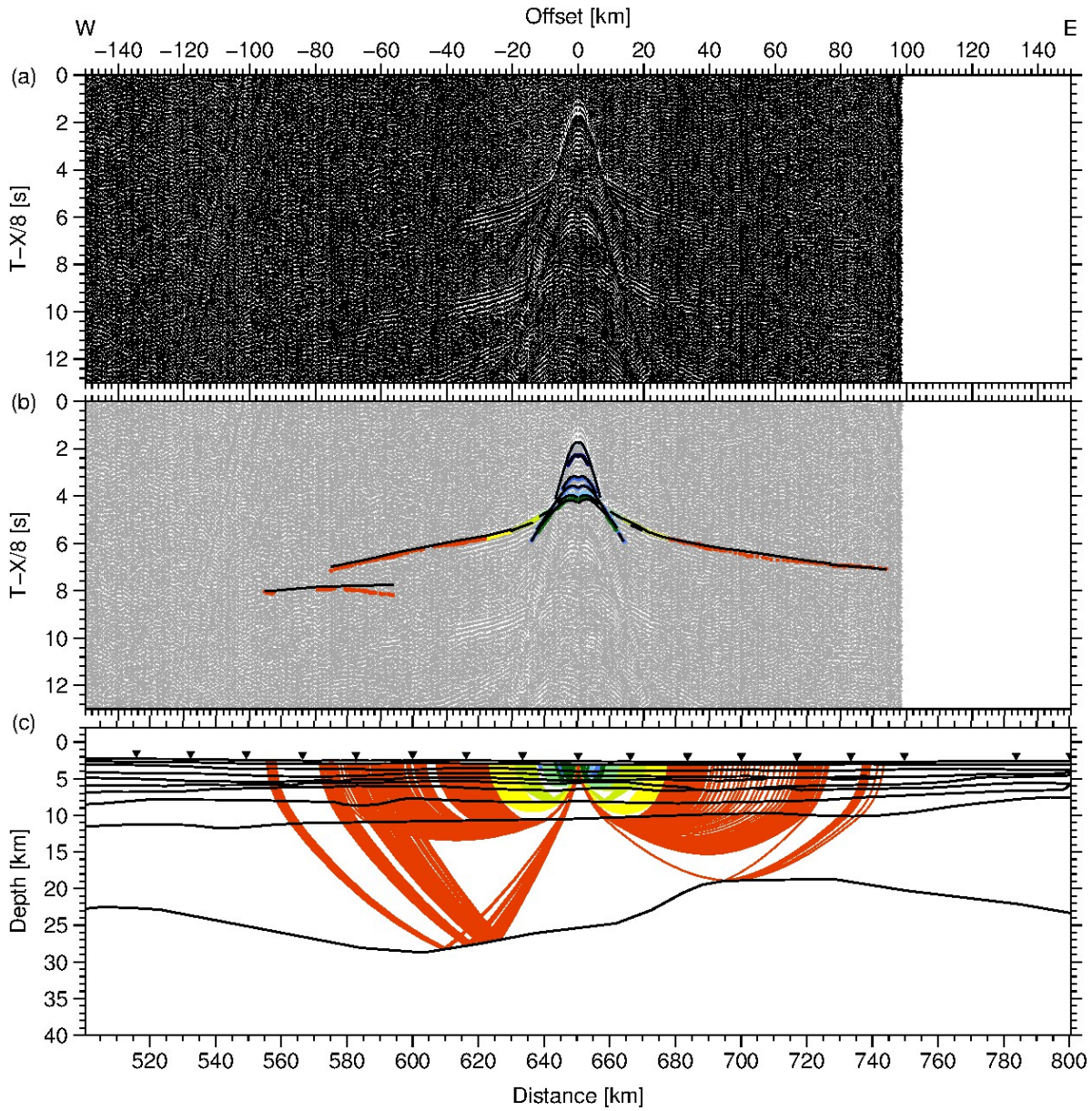


Figure A31.: Data example for OBS 50. (a) Seismic section filtered with a 4-15 Hz bandpass filter and displayed with a reduction velocity of 8 km/s. (b) Picked phases with error bars and corresponding phase names. The modelled first arrivals are plotted as black lines. (c) Ray path for picks shown in (b). Station positions are marked as triangles.

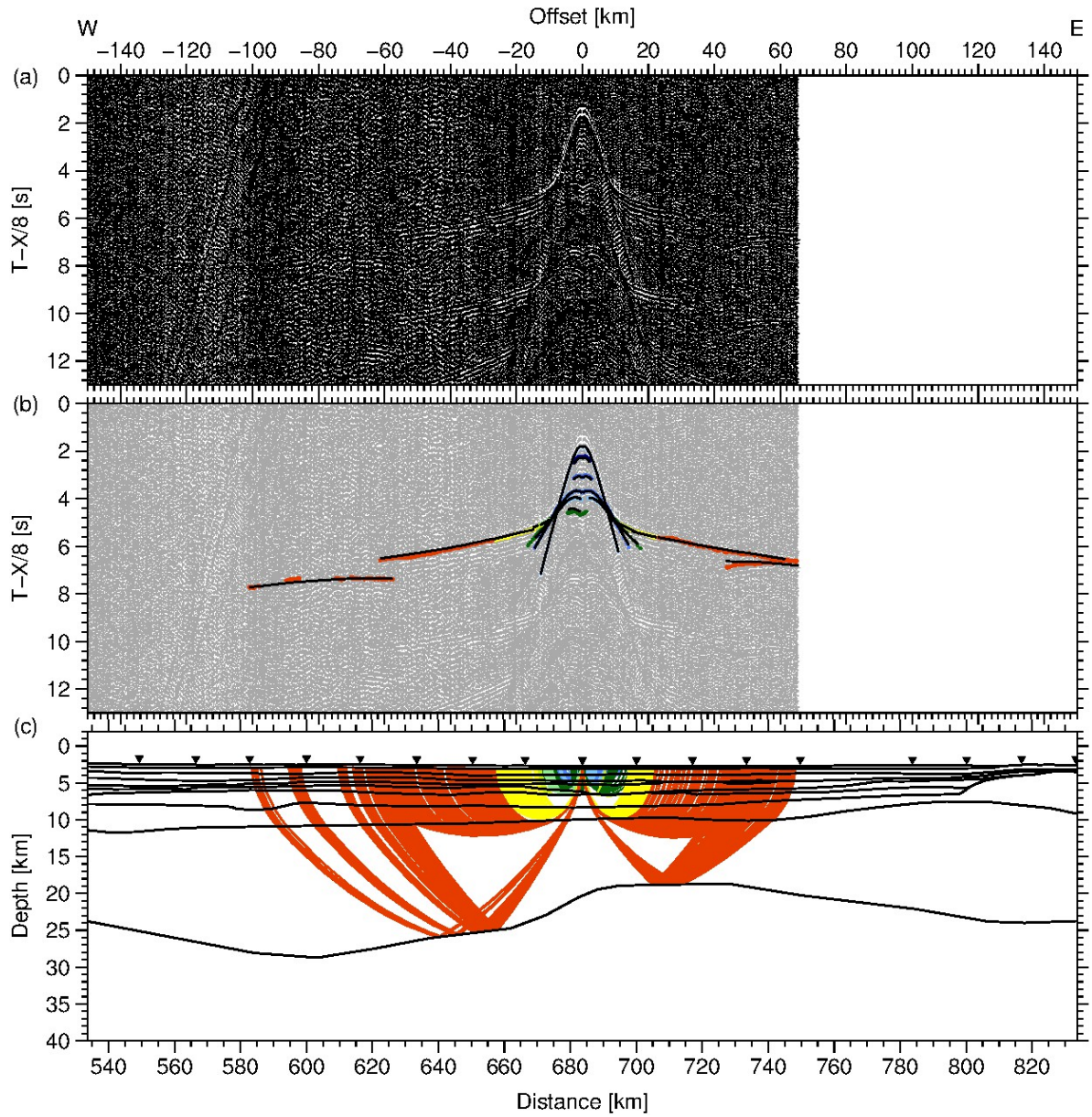


Figure A32.: Data example for OBS 52. (a) Seismic section filtered with a 4-15 Hz bandpass filter and displayed with a reduction velocity of 8 km/s. (b) Picked phases with error bars and corresponding phase names. The modelled first arrivals are plotted as black lines. (c) Ray path for picks shown in (b). Station positions are marked as triangles.

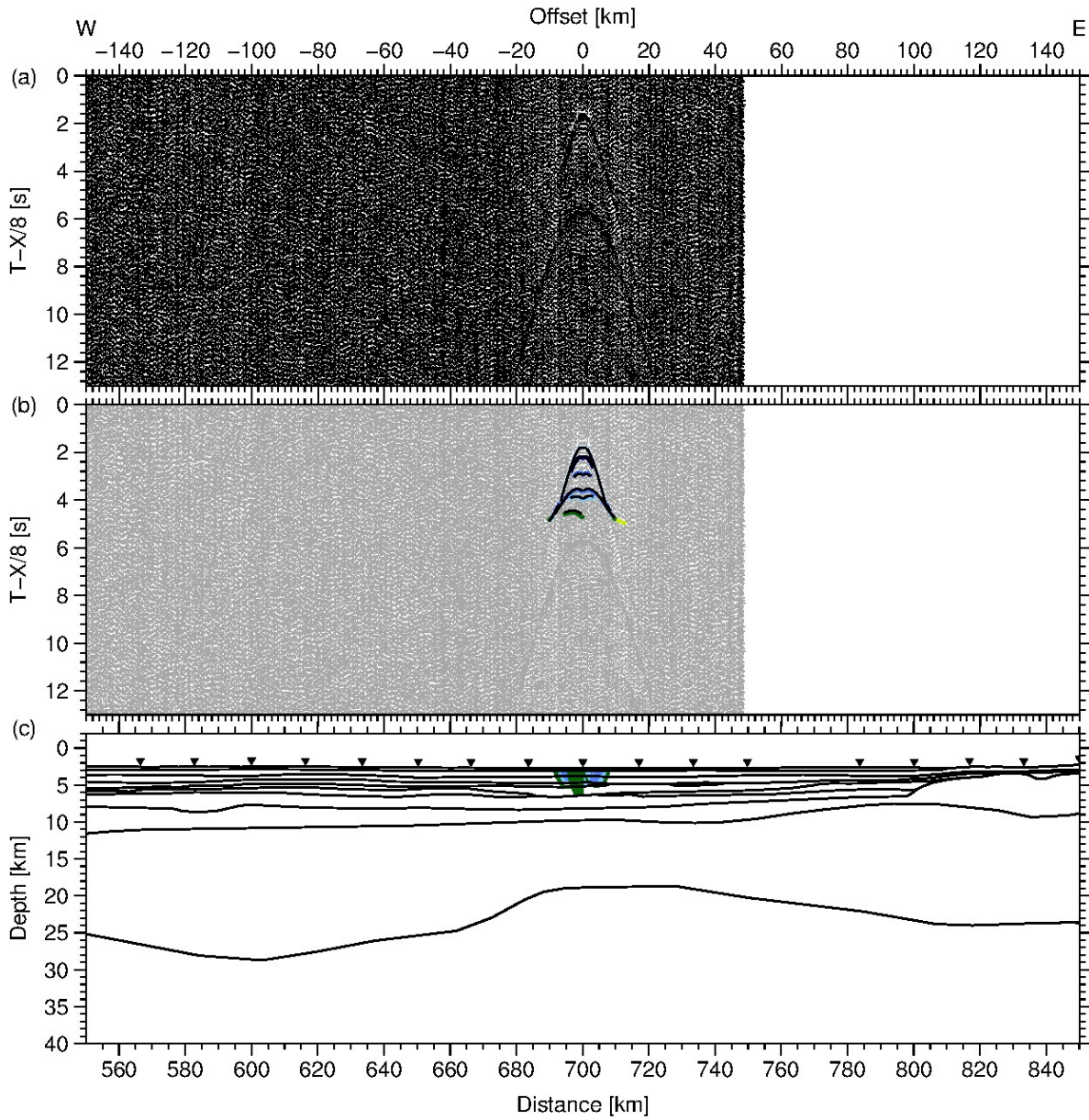


Figure A33.: Data example for OBS 53. (a) Seismic section filtered with a 4-15 Hz bandpass filter and displayed with a reduction velocity of 8 km/s. (b) Picked phases with error bars and corresponding phase names. The modelled first arrivals are plotted as black lines. (c) Ray path for picks shown in (b). Station positions are marked as triangles.

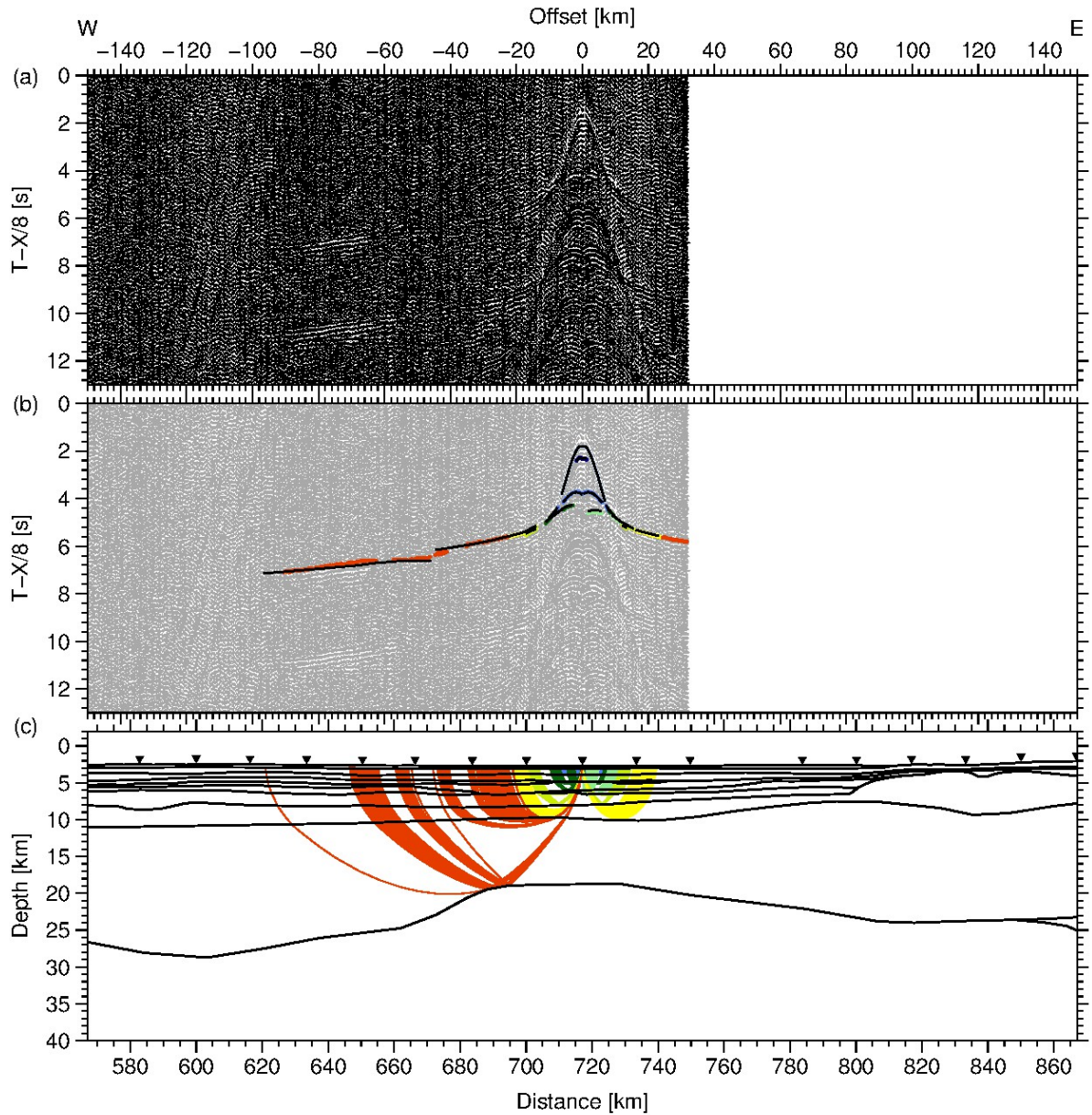


Figure A34.: Data example for OBS 54. (a) Seismic section filtered with a 4-15 Hz bandpass filter and displayed with a reduction velocity of 8 km/s. (b) Picked phases with error bars and corresponding phase names. The modelled first arrivals are plotted as black lines. (c) Ray path for picks shown in (b). Station positions are marked as triangles.

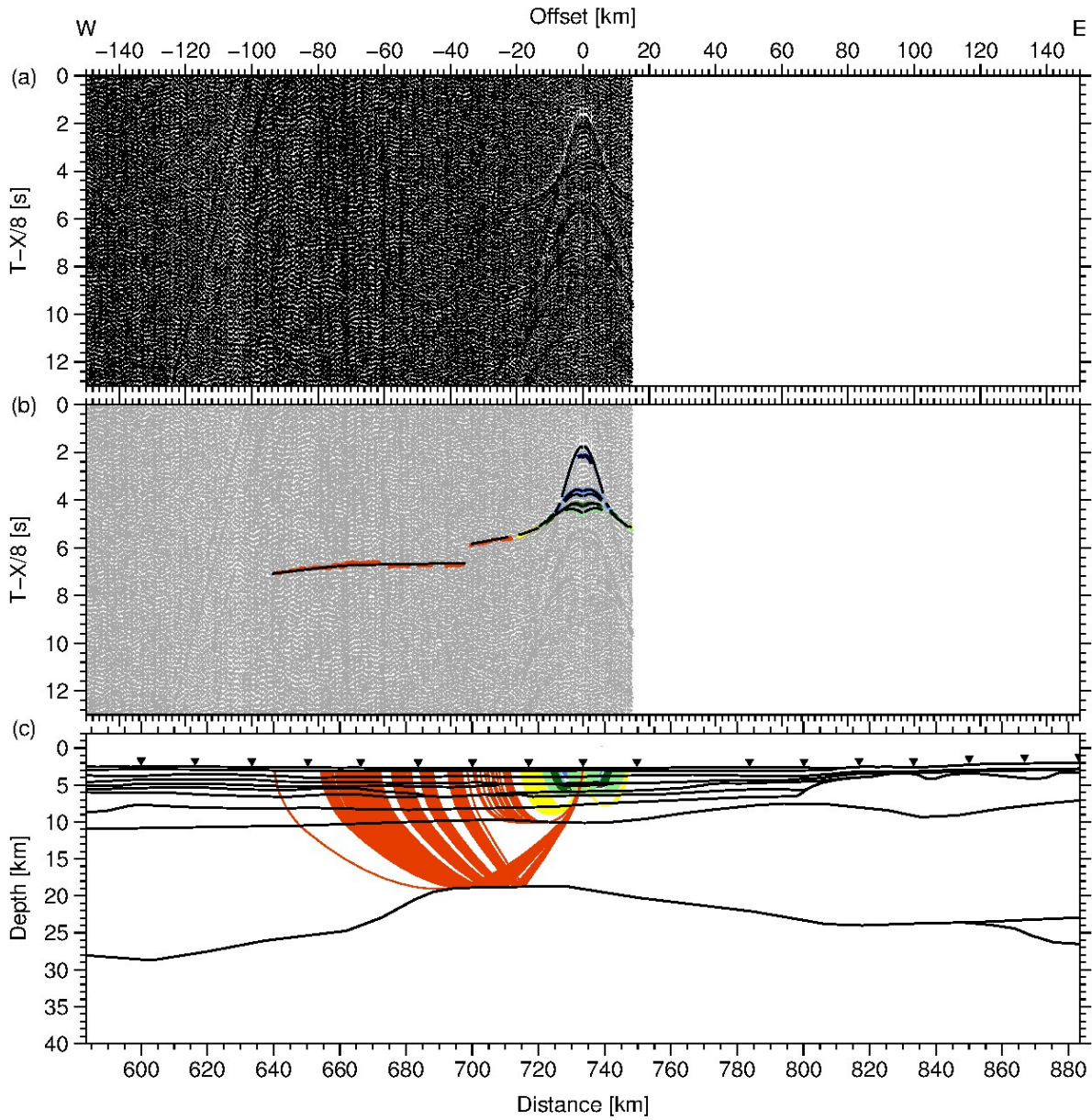


Figure A35.: Data example for OBH 55. (a) Seismic section filtered with a 4-15 Hz bandpass filter and displayed with a reduction velocity of 8 km/s. (b) Picked phases with error bars and corresponding phase names. The modelled first arrivals are plotted as black lines. (c) Ray path for picks shown in (b). Station positions are marked as triangles.

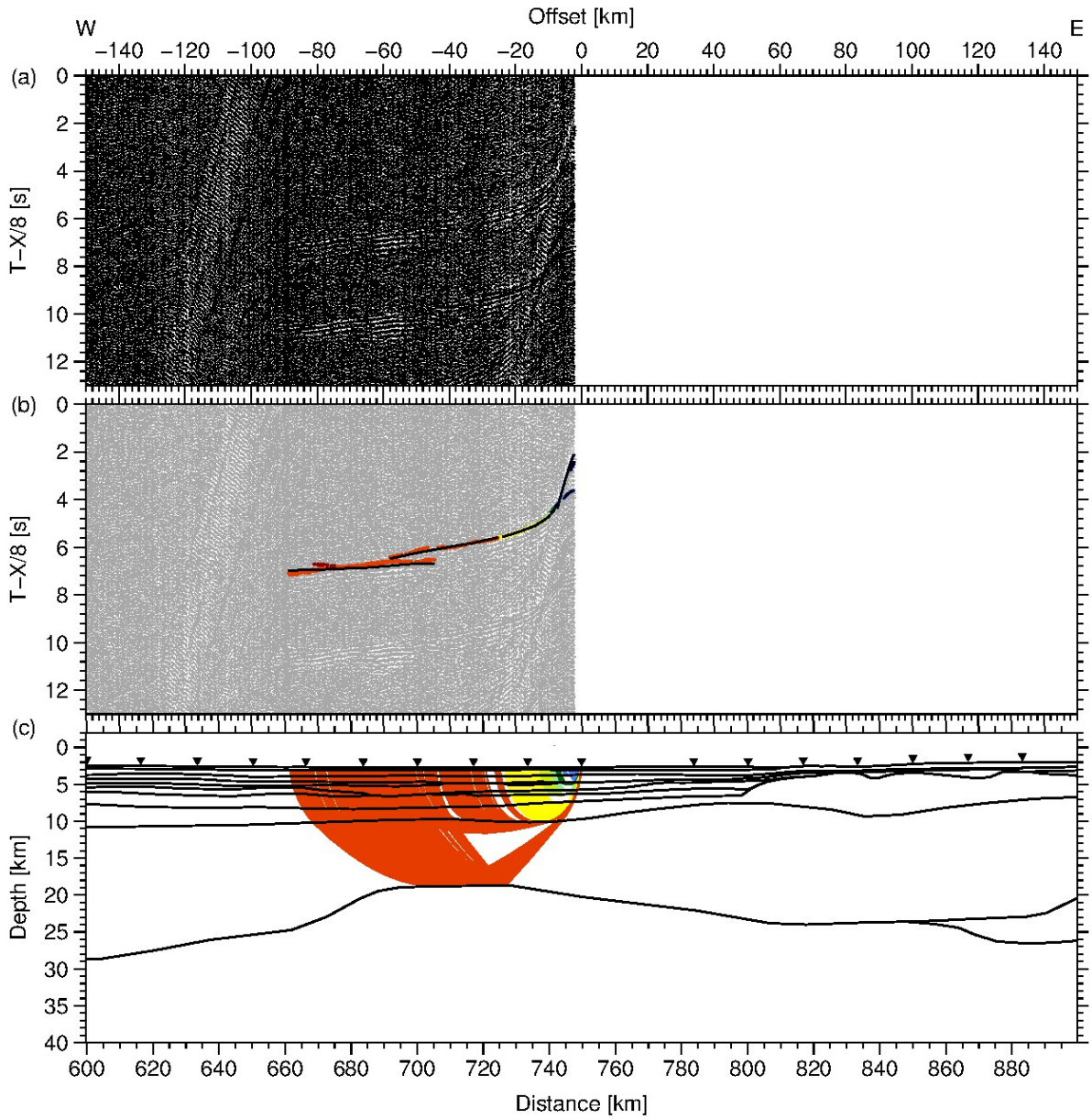


Figure A36.: Data example for OBS 56. (a) Seismic section filtered with a 4-15 Hz bandpass filter and displayed with a reduction velocity of 8 km/s. (b) Picked phases with error bars and corresponding phase names. The modelled first arrivals are plotted as black lines. (c) Ray path for picks shown in (b). Station positions are marked as triangles.

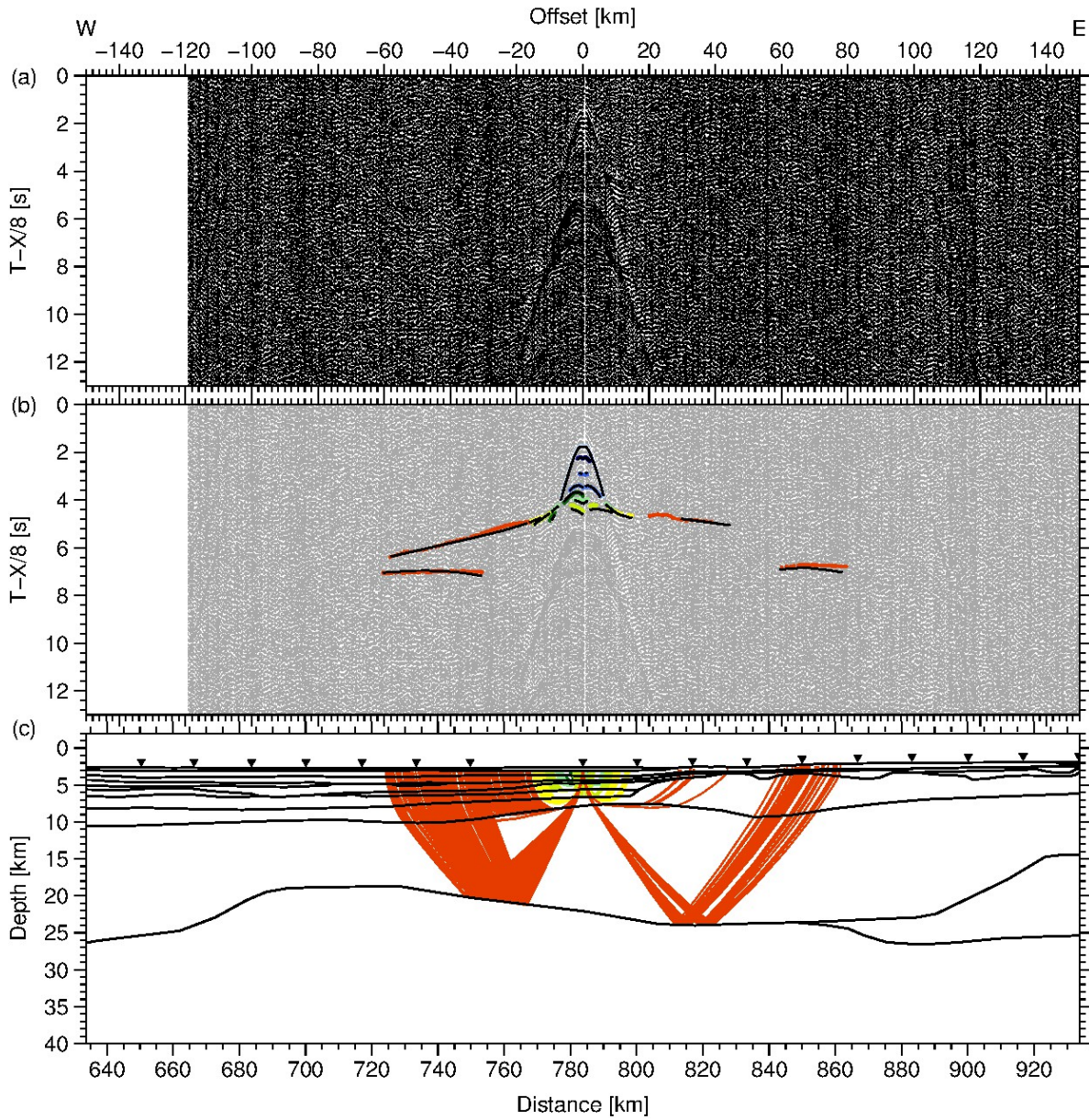


Figure A37.: Data example for OBS 57. (a) Seismic section filtered with a 4-15 Hz bandpass filter and displayed with a reduction velocity of 8 km/s. (b) Picked phases with error bars and corresponding phase names. The modelled first arrivals are plotted as black lines. (c) Ray path for picks shown in (b). Station positions are marked as triangles.

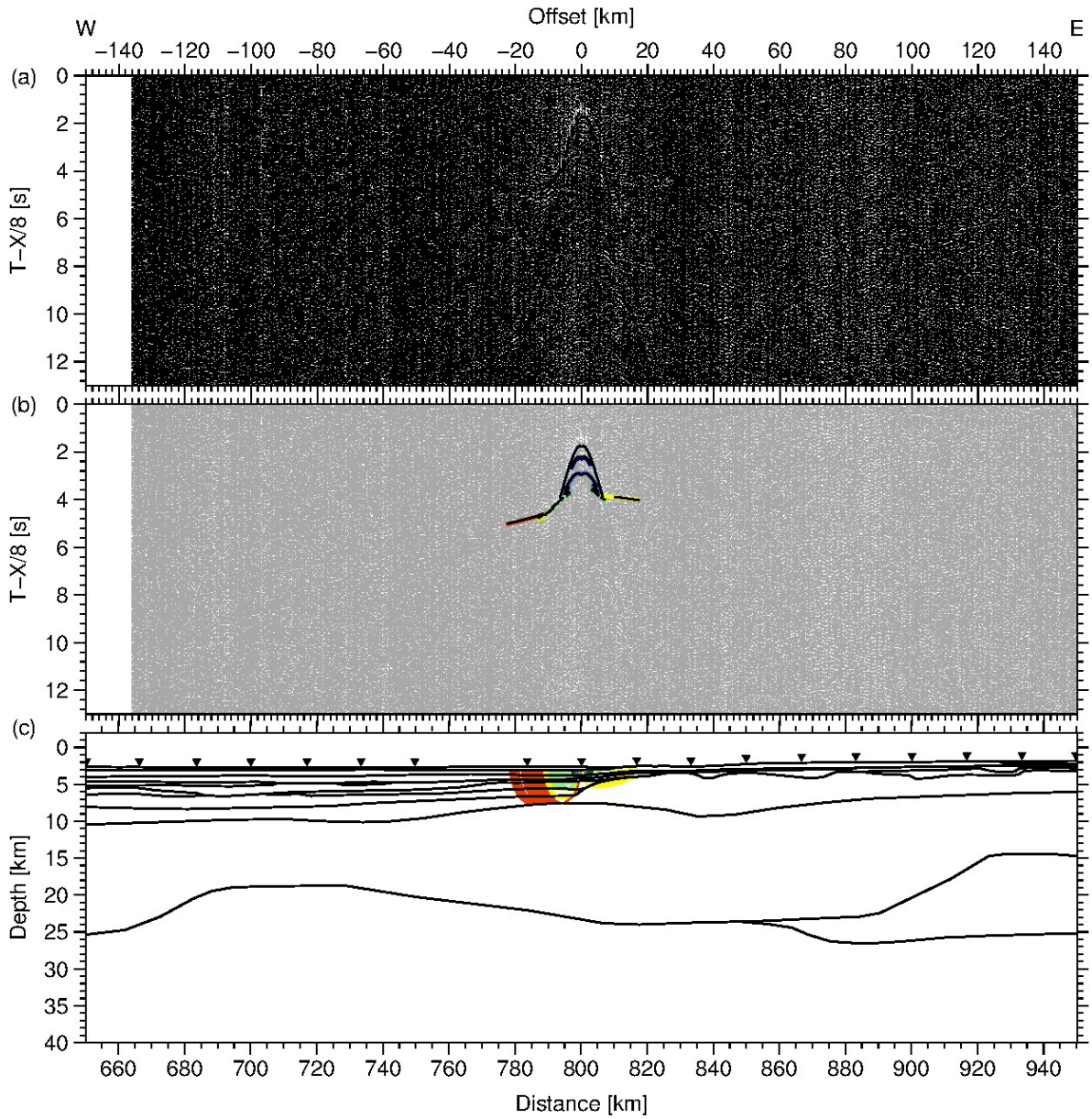


Figure A38.: Data example for OBS 58. (a) Seismic section filtered with a 4-15 Hz bandpass filter and displayed with a reduction velocity of 8 km/s. (b) Picked phases with error bars and corresponding phase names. The modelled first arrivals are plotted as black lines. (c) Ray path for picks shown in (b). Station positions are marked as triangles.

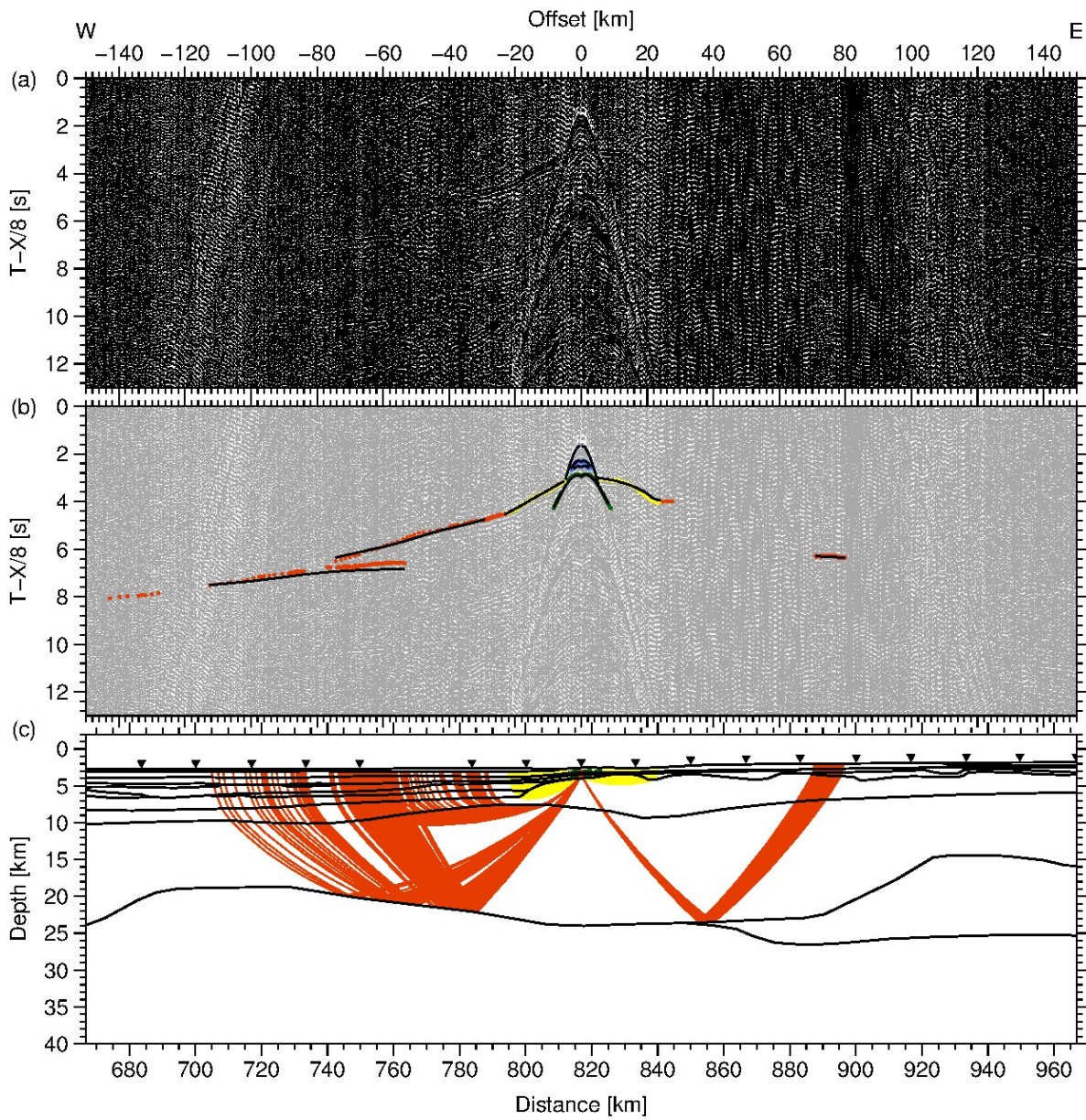


Figure A39.: Data example for OBS 59. (a) Seismic section filtered with a 4-15 Hz bandpass filter and displayed with a reduction velocity of 8 km/s. (b) Picked phases with error bars and corresponding phase names. The modelled first arrivals are plotted as black lines. (c) Ray path for picks shown in (b). Station positions are marked as triangles.

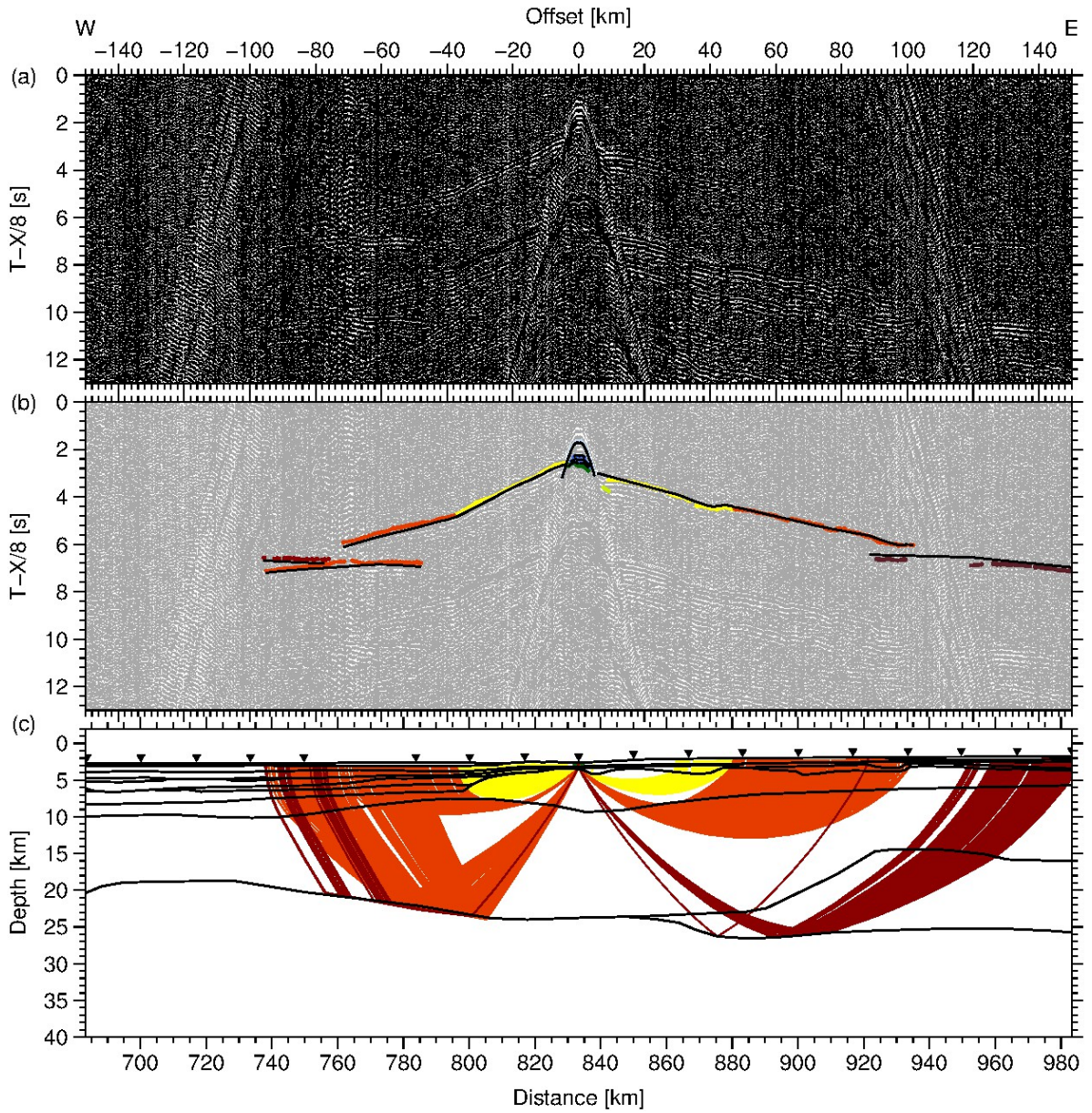


Figure A40.: Data example for OBS 60. (a) Seismic section filtered with a 4-15 Hz bandpass filter and displayed with a reduction velocity of 8 km/s. (b) Picked phases with error bars and corresponding phase names. The modelled first arrivals are plotted as black lines. (c) Ray path for picks shown in (b). Station positions are marked as triangles.

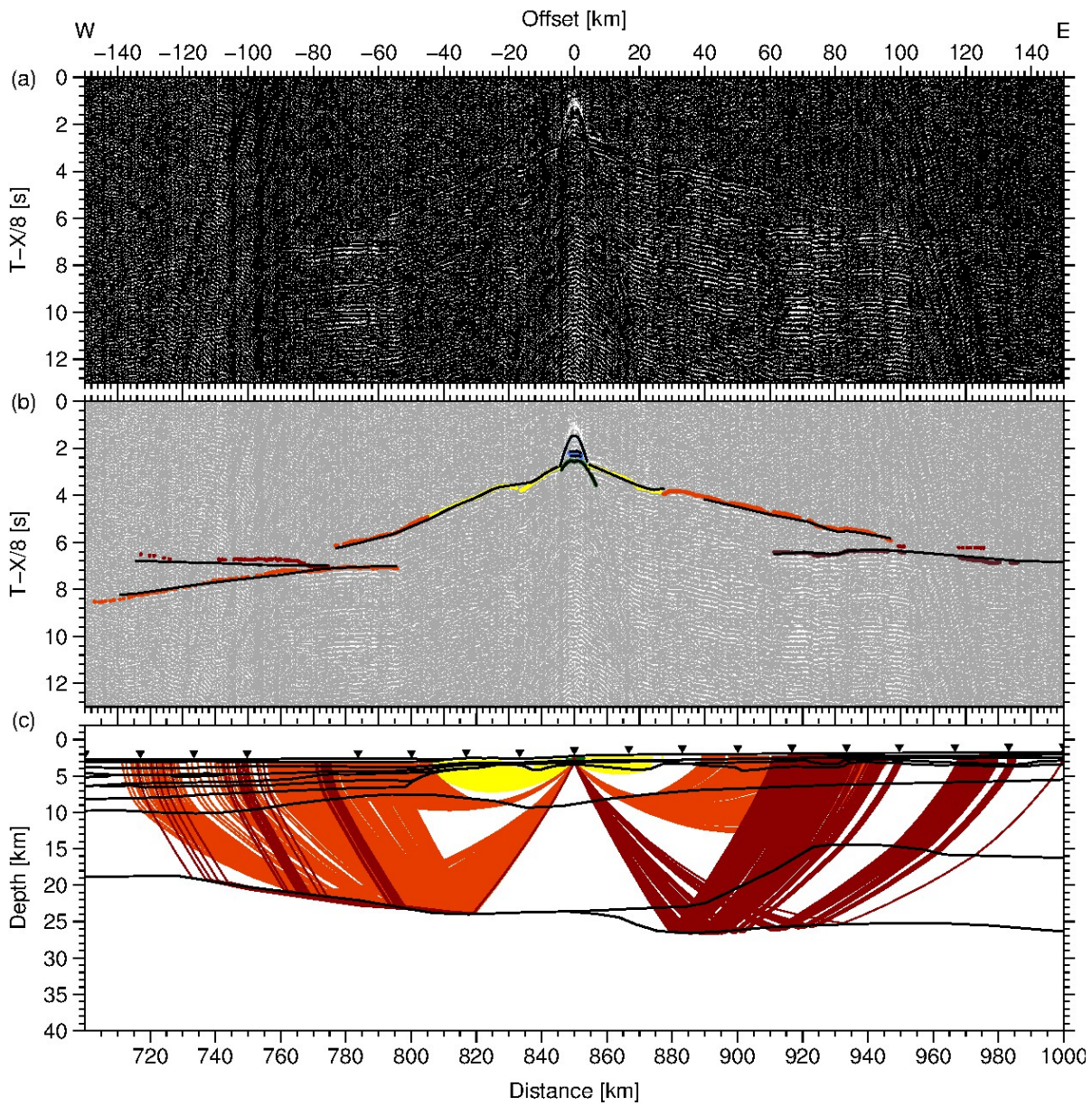


Figure A41.: Data example for OBS 61. (a) Seismic section filtered with a 4-15 Hz bandpass filter and displayed with a reduction velocity of 8 km/s. (b) Picked phases with error bars and corresponding phase names. The modelled first arrivals are plotted as black lines. (c) Ray path for picks shown in (b). Station positions are marked as triangles.

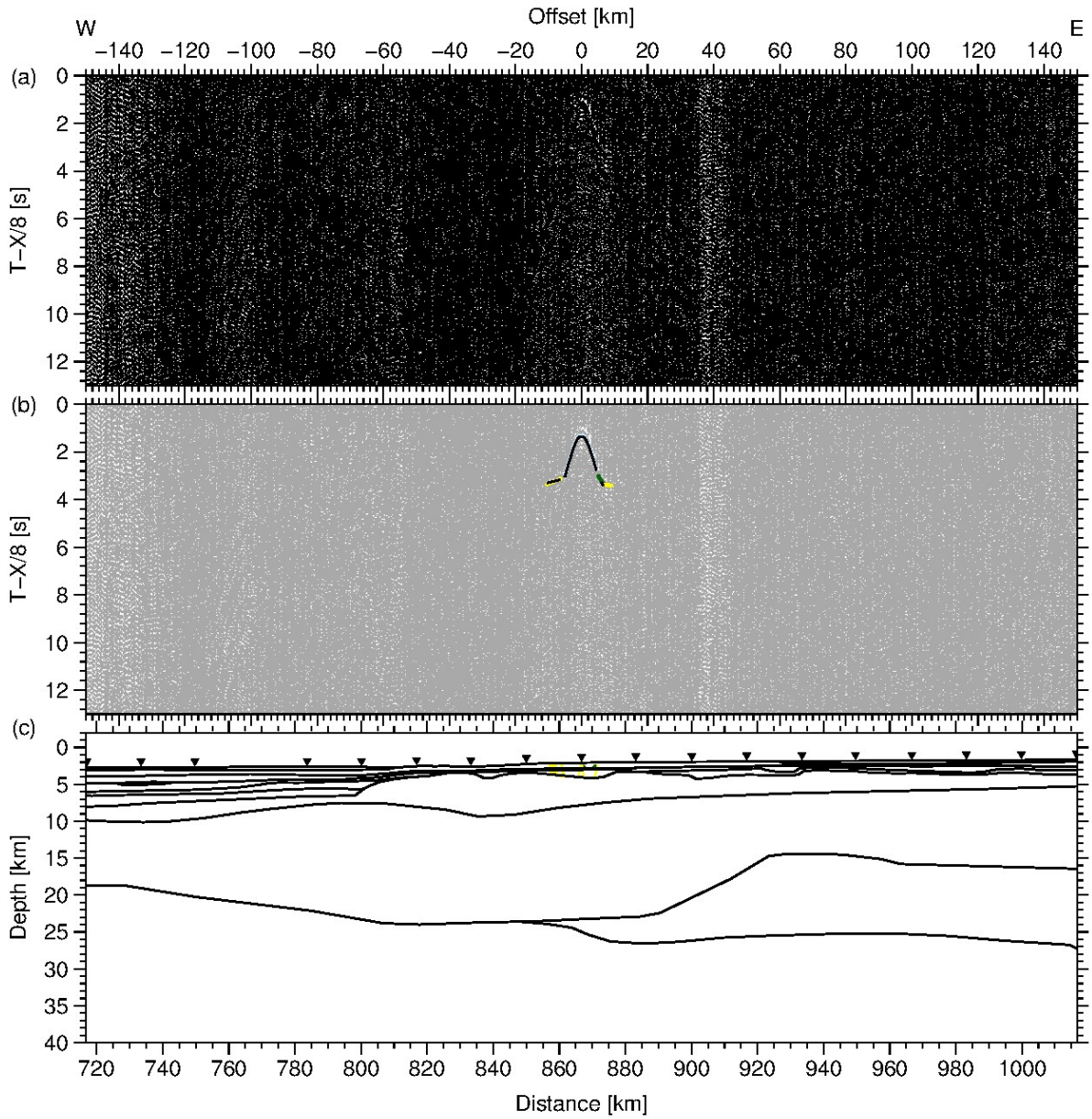


Figure A42.: Data example for OBS 62. (a) Seismic section filtered with a 4-15 Hz bandpass filter and displayed with a reduction velocity of 8 km/s. (b) Picked phases with error bars and corresponding phase names. The modelled first arrivals are plotted as black lines. (c) Ray path for picks shown in (b). Station positions are marked as triangles.

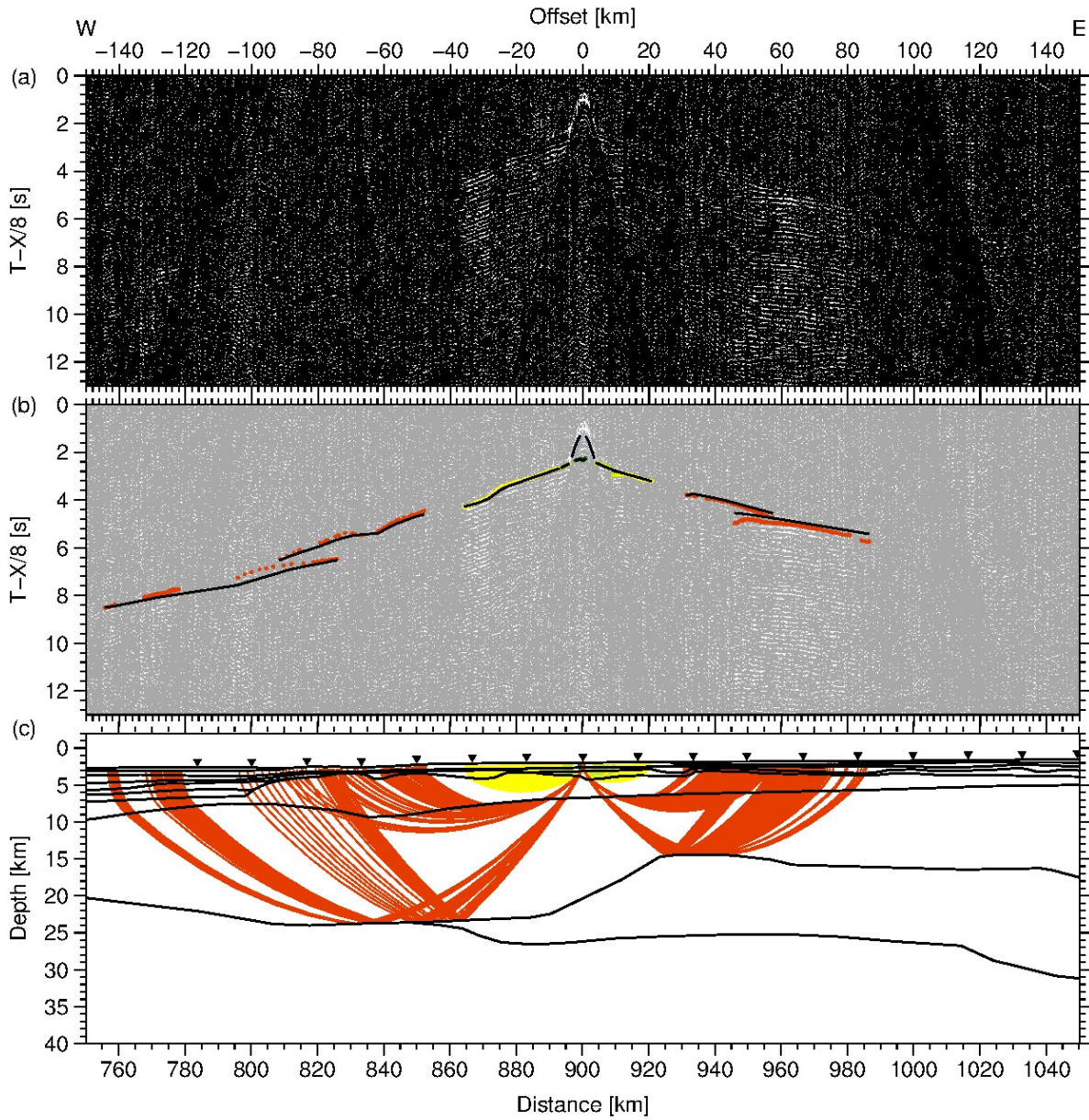


Figure A43.: Data example for OBS 64. (a) Seismic section filtered with a 4-15 Hz bandpass filter and displayed with a reduction velocity of 8 km/s. (b) Picked phases with error bars and corresponding phase names. The modelled first arrivals are plotted as black lines. (c) Ray path for picks shown in (b). Station positions are marked as triangles.

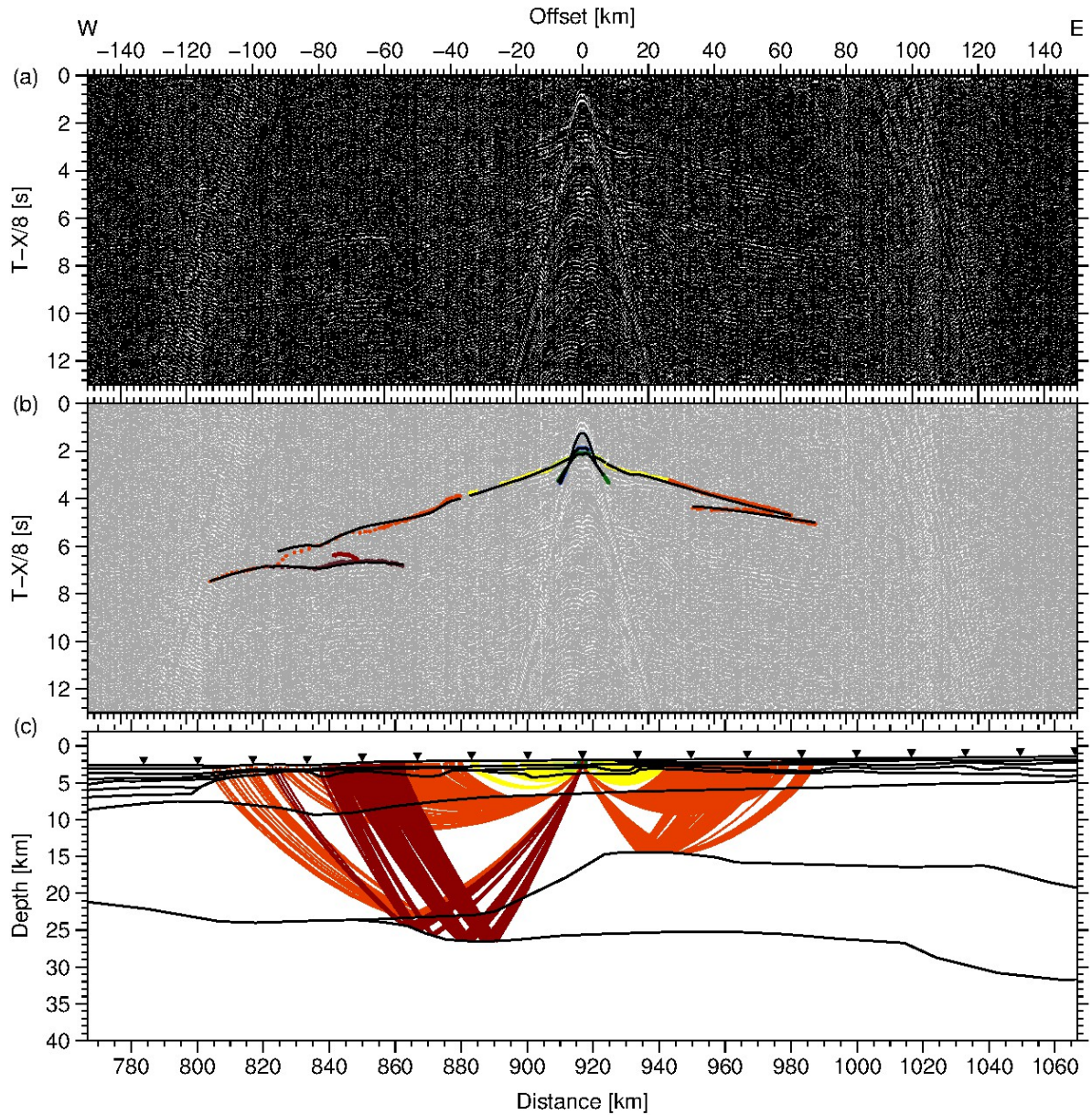


Figure A44.: Data example for OBH 65. (a) Seismic section filtered with a 4-15 Hz bandpass filter and displayed with a reduction velocity of 8 km/s. (b) Picked phases with error bars and corresponding phase names. The modelled first arrivals are plotted as black lines. (c) Ray path for picks shown in (b). Station positions are marked as triangles.

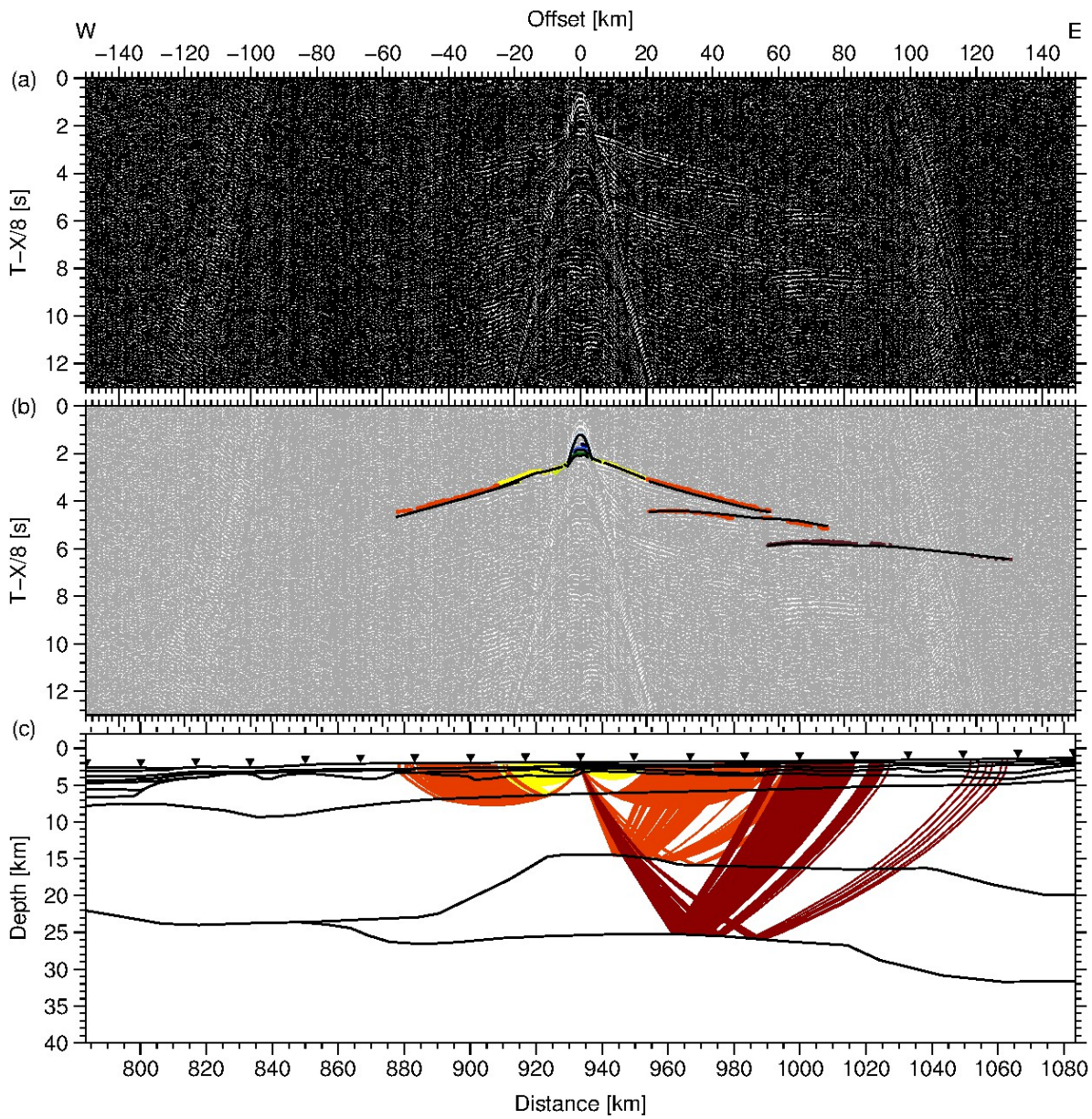


Figure A45.: Data example for OBS 66. (a) Seismic section filtered with a 4-15 Hz bandpass filter and displayed with a reduction velocity of 8 km/s. (b) Picked phases with error bars and corresponding phase names. The modelled first arrivals are plotted as black lines. (c) Ray path for picks shown in (b). Station positions are marked as triangles.

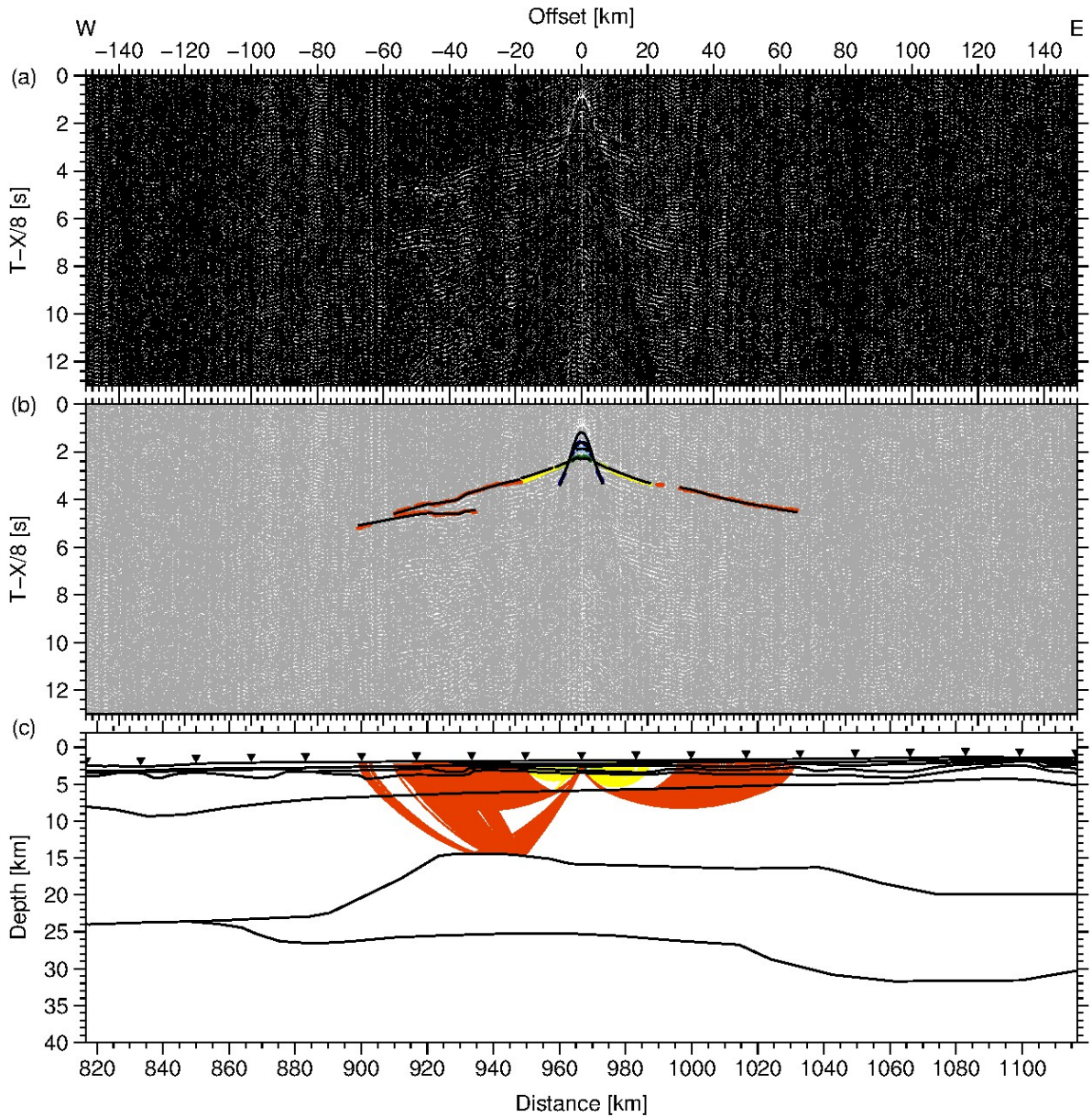


Figure A46.: Data example for OBS 68. (a) Seismic section filtered with a 4-15 Hz bandpass filter and displayed with a reduction velocity of 8 km/s. (b) Picked phases with error bars and corresponding phase names. The modelled first arrivals are plotted as black lines. (c) Ray path for picks shown in (b). Station positions are marked as triangles.

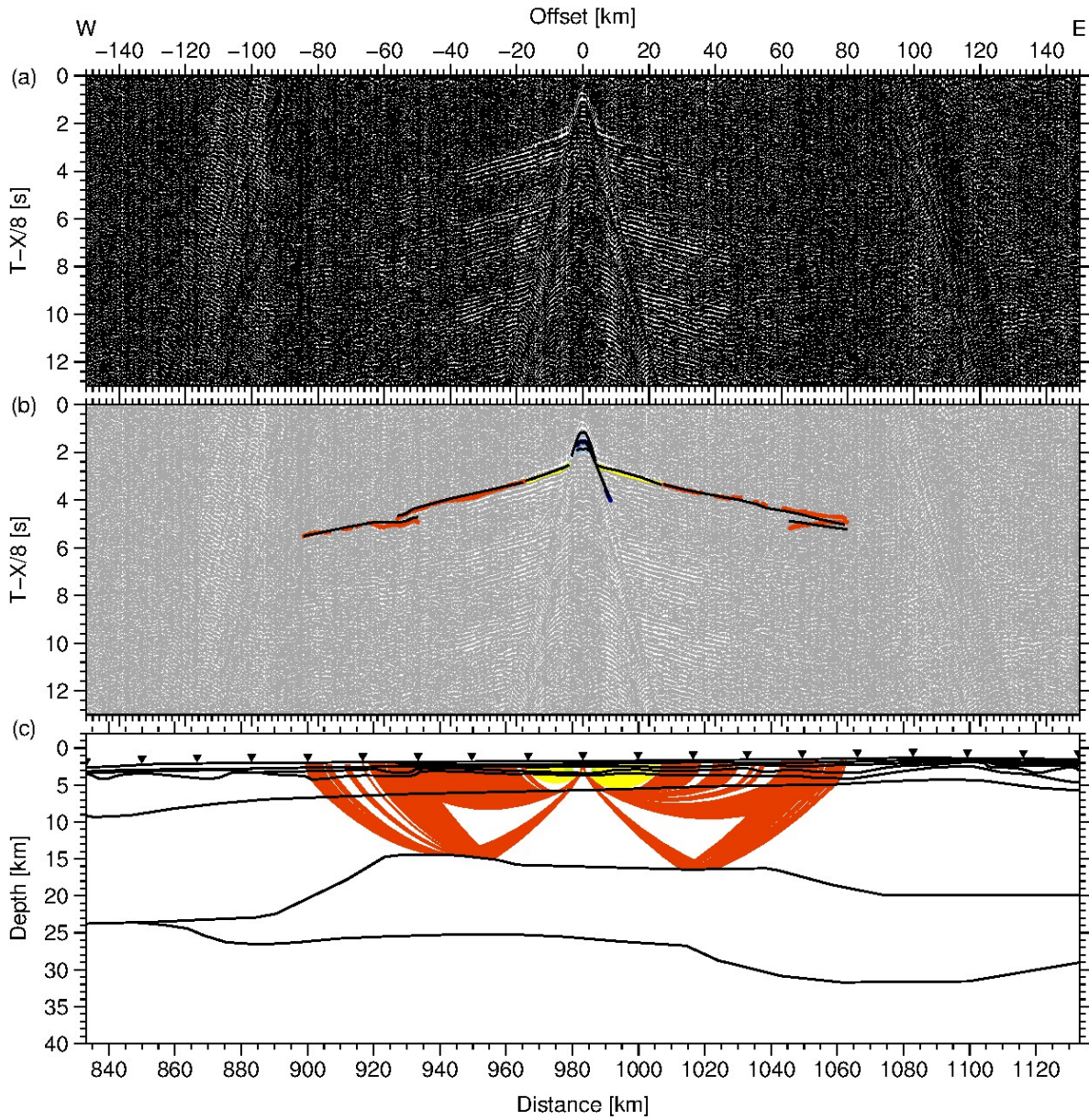


Figure A47.: Data example for OBH 69. (a) Seismic section filtered with a 4-15 Hz bandpass filter and displayed with a reduction velocity of 8 km/s. (b) Picked phases with error bars and corresponding phase names. The modelled first arrivals are plotted as black lines. (c) Ray path for picks shown in (b). Station positions are marked as triangles.

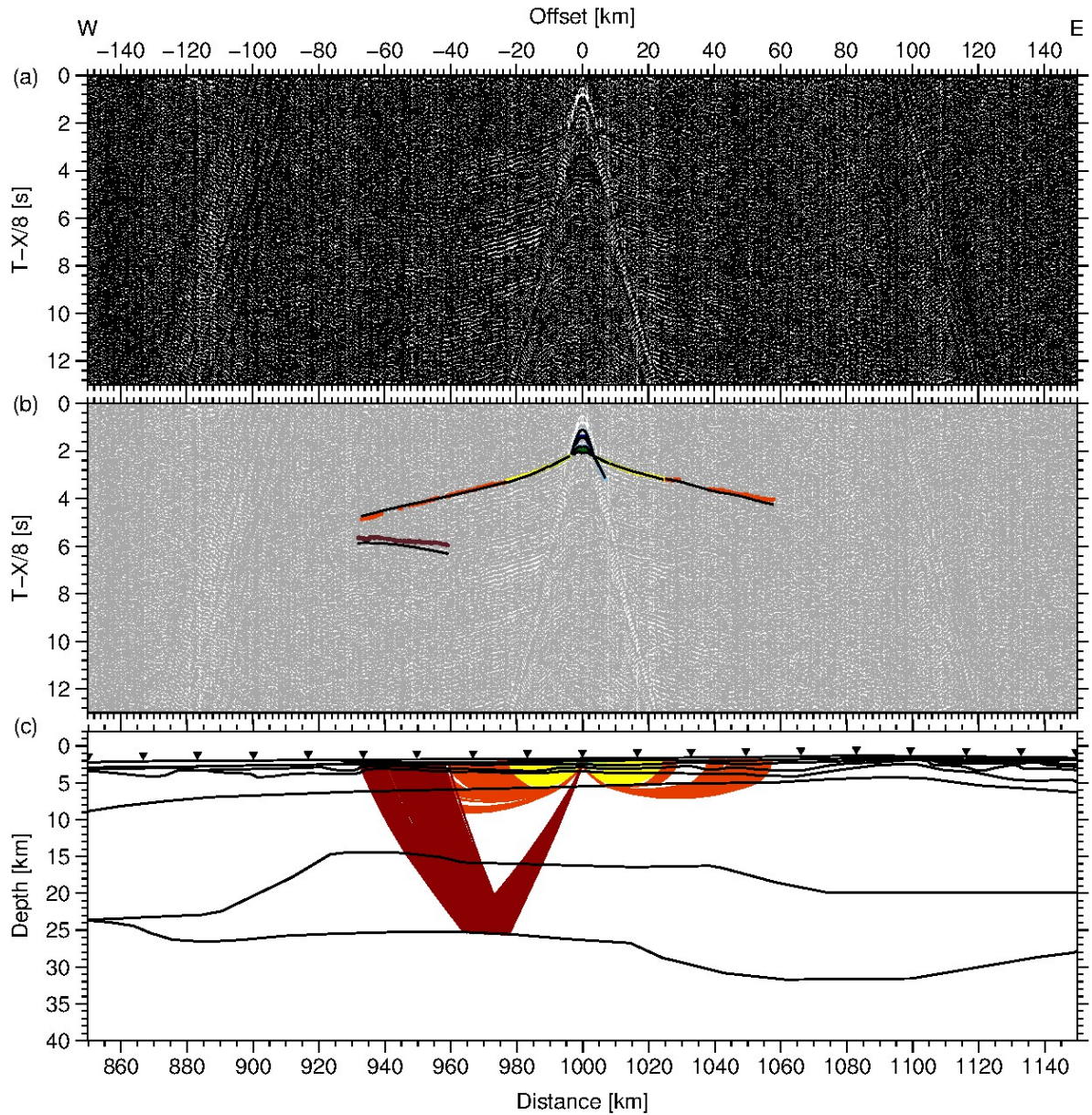


Figure A48.: Data example for OBS 70. (a) Seismic section filtered with a 4-15 Hz bandpass filter and displayed with a reduction velocity of 8 km/s. (b) Picked phases with error bars and corresponding phase names. The modelled first arrivals are plotted as black lines. (c) Ray path for picks shown in (b). Station positions are marked as triangles.

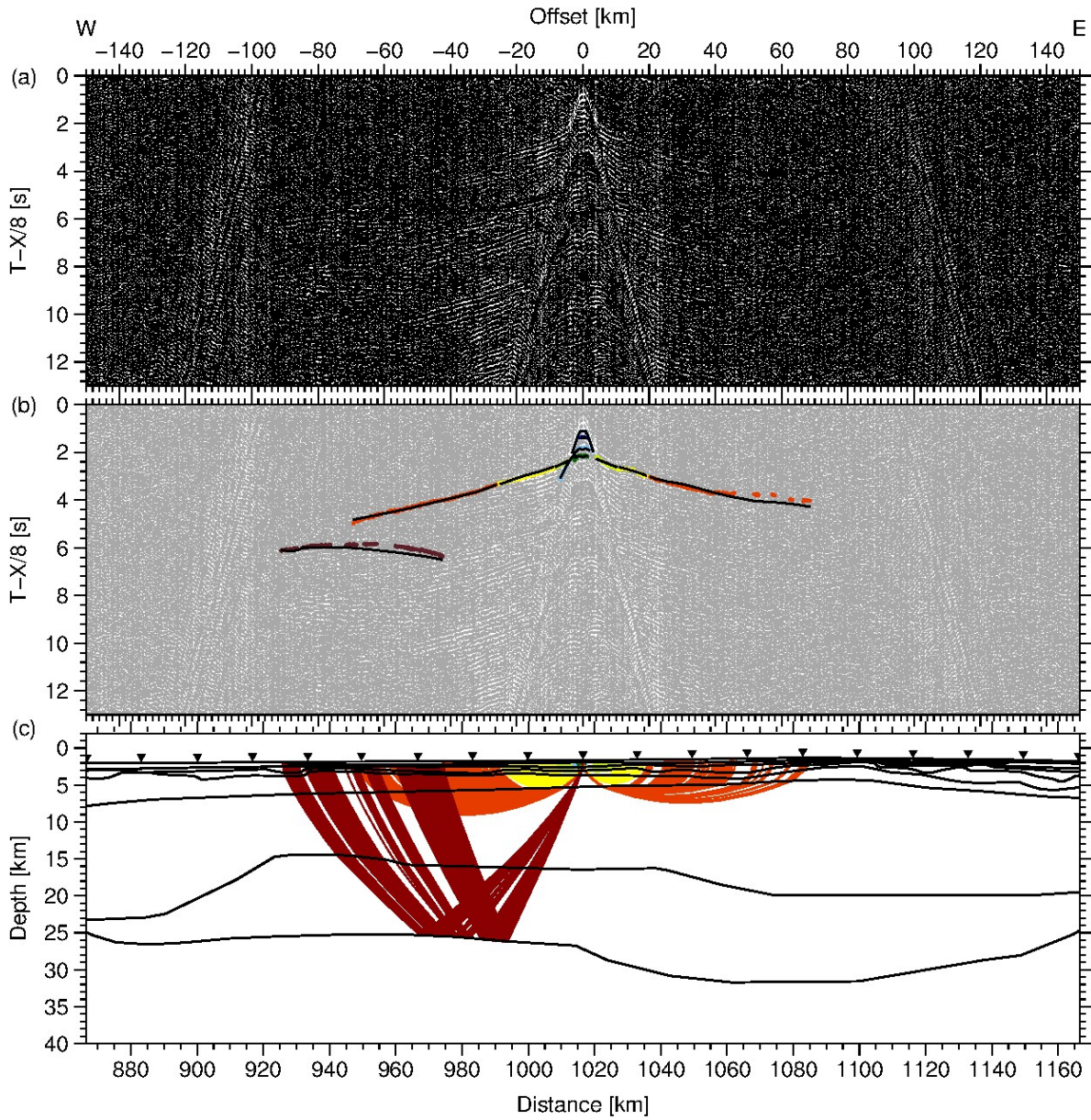


Figure A49.: Data example for OBH 71. (a) Seismic section filtered with a 4-15 Hz bandpass filter and displayed with a reduction velocity of 8 km/s. (b) Picked phases with error bars and corresponding phase names. The modelled first arrivals are plotted as black lines. (c) Ray path for picks shown in (b). Station positions are marked as triangles.

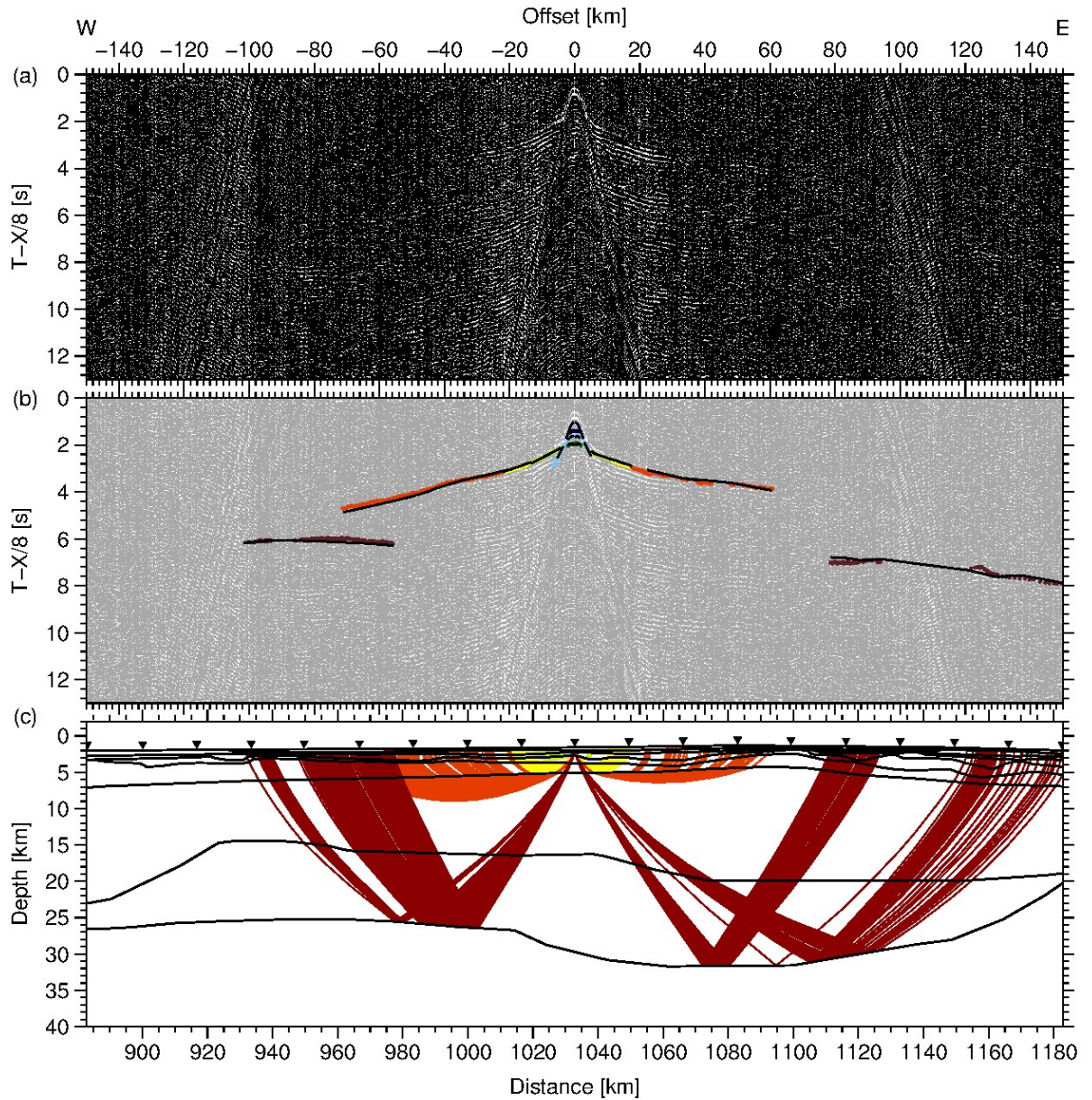


Figure A50.: Data example for OBS 72. (a) Seismic section filtered with a 4-15 Hz bandpass filter and displayed with a reduction velocity of 8 km/s. (b) Picked phases with error bars and corresponding phase names. The modelled first arrivals are plotted as black lines. (c) Ray path for picks shown in (b). Station positions are marked as triangles.

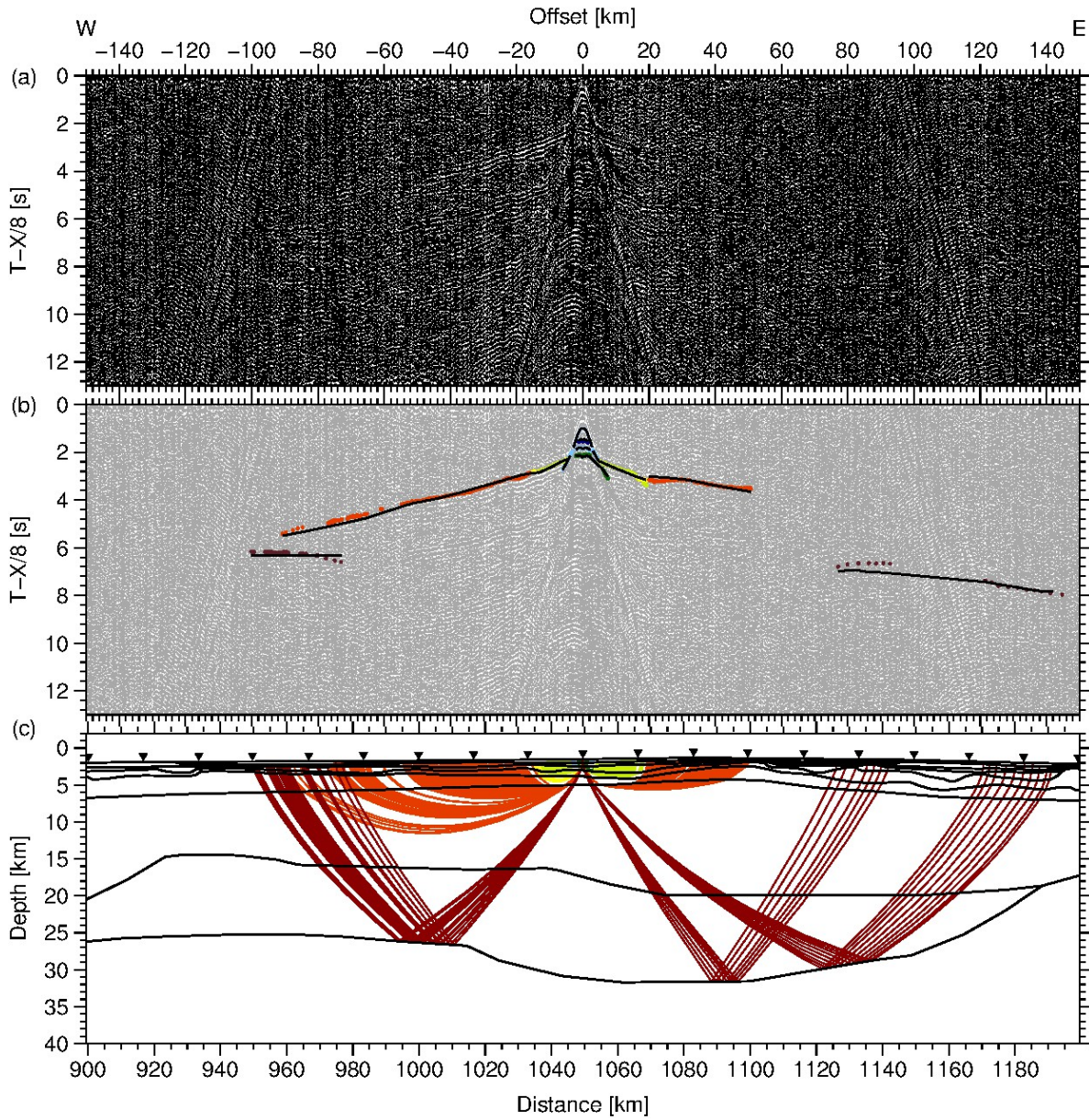


Figure A51.: Data example for OBH 73. (a) Seismic section filtered with a 4-15 Hz bandpass filter and displayed with a reduction velocity of 8 km/s. (b) Picked phases with error bars and corresponding phase names. The modelled first arrivals are plotted as black lines. (c) Ray path for picks shown in (b). Station positions are marked as triangles.

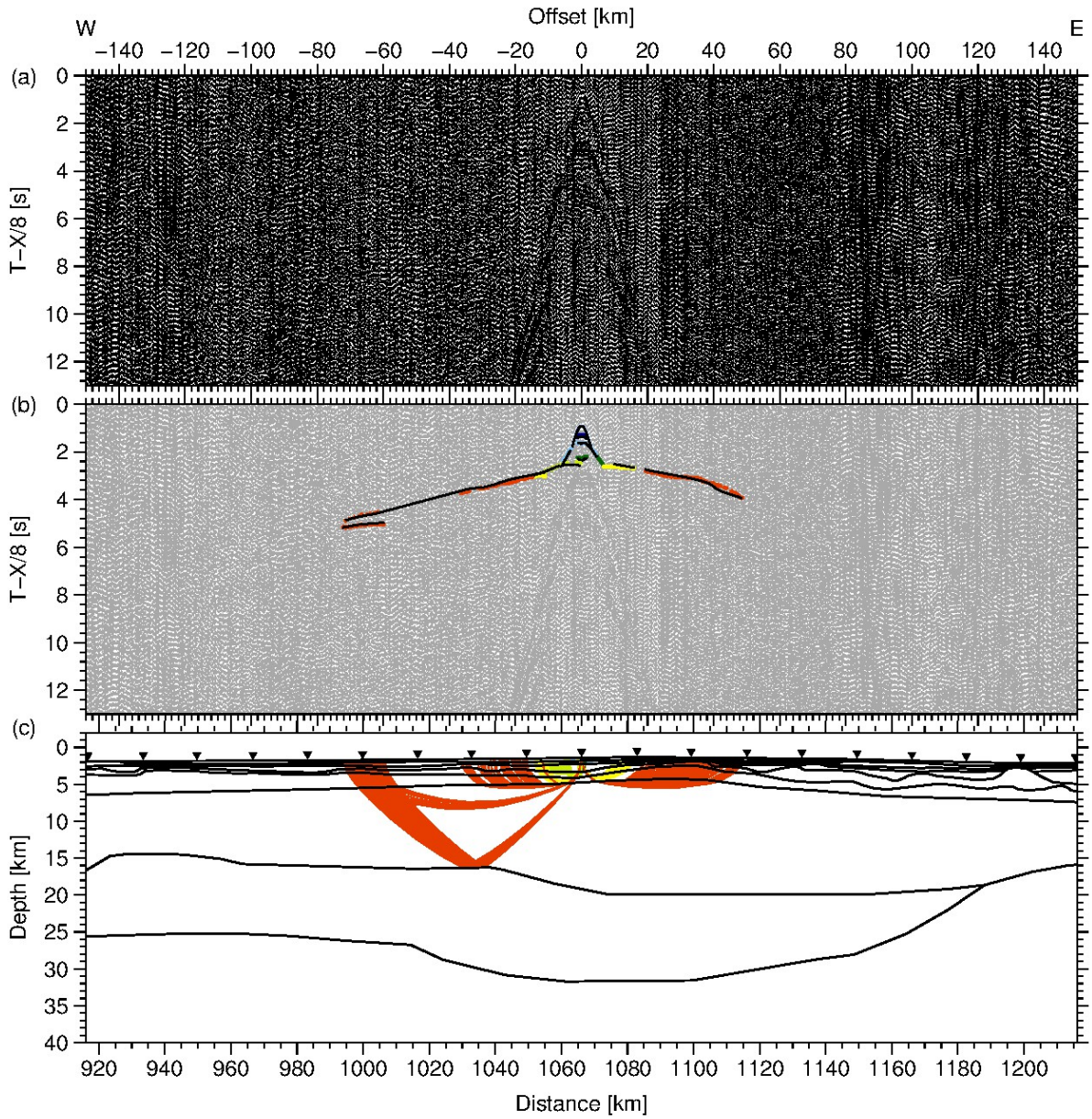


Figure A52.: Data example for OBS 74. (a) Seismic section filtered with a 4-15 Hz bandpass filter and displayed with a reduction velocity of 8 km/s. (b) Picked phases with error bars and corresponding phase names. The modelled first arrivals are plotted as black lines. (c) Ray path for picks shown in (b). Station positions are marked as triangles.

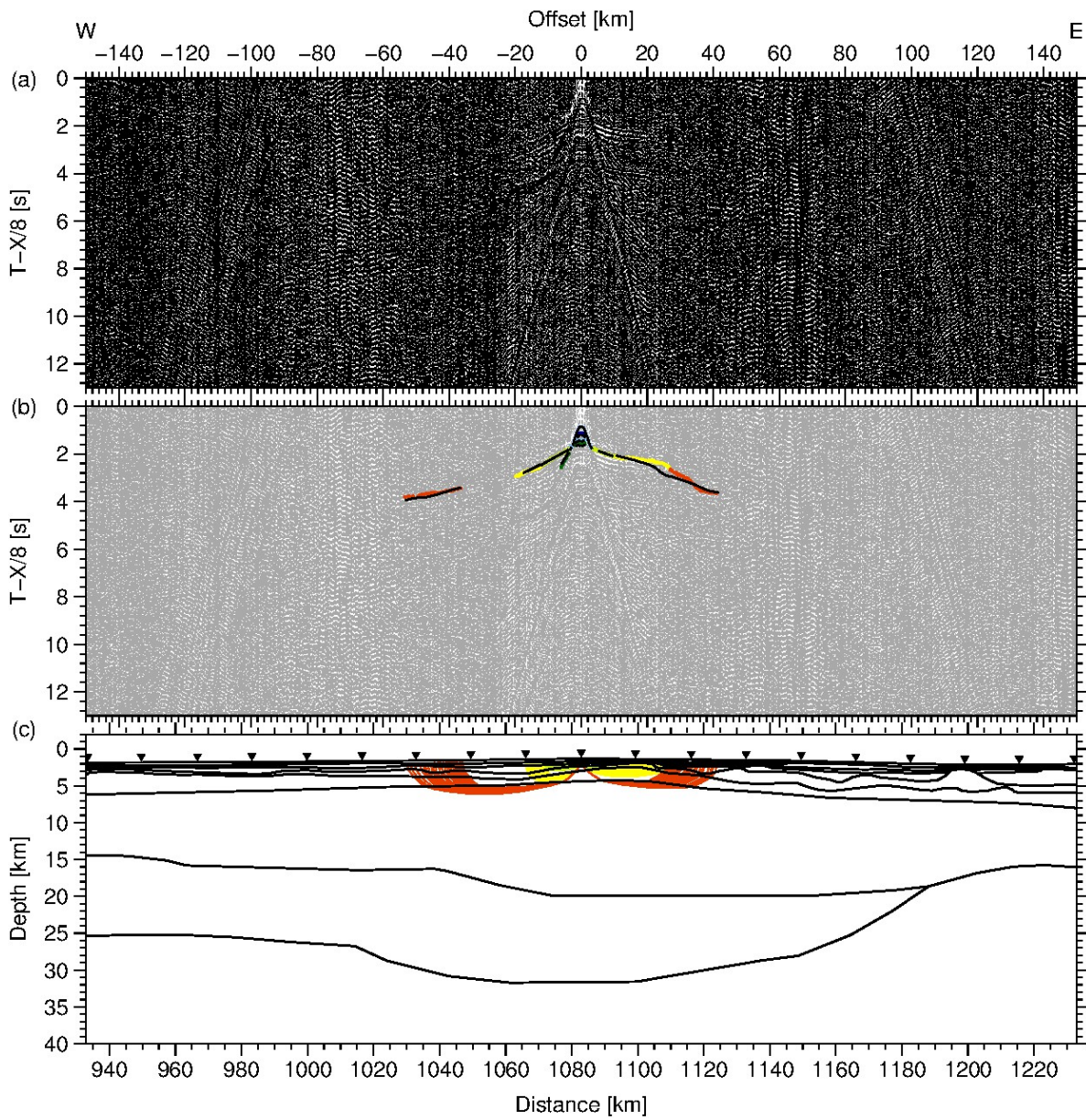


Figure A53.: Data example for OBS 75. (a) Seismic section filtered with a 4-15 Hz bandpass filter and displayed with a reduction velocity of 8 km/s. (b) Picked phases with error bars and corresponding phase names. The modelled first arrivals are plotted as black lines. (c) Ray path for picks shown in (b). Station positions are marked as triangles.

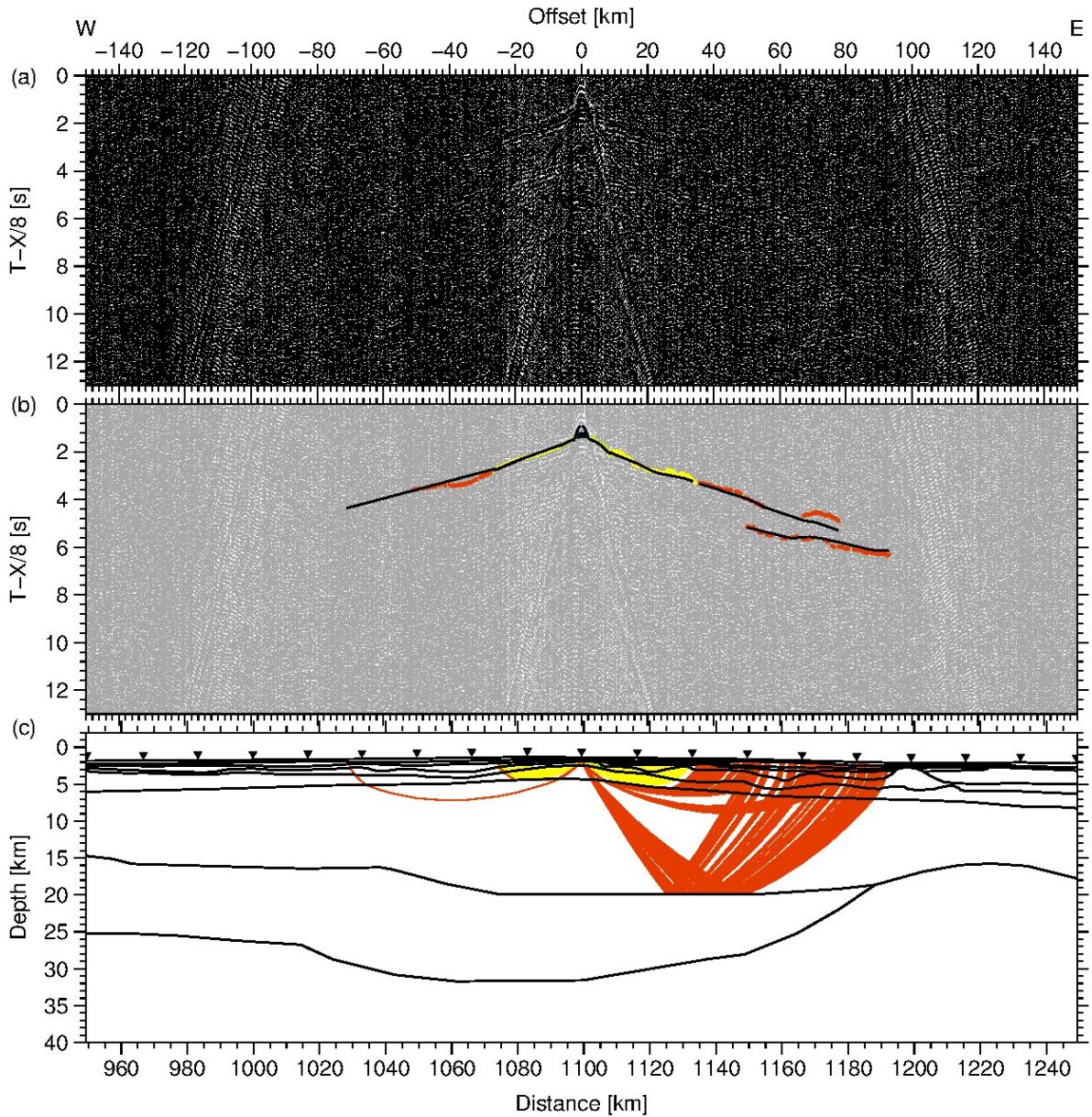


Figure A54.: Data example for OBS 76. (a) Seismic section filtered with a 4-15 Hz bandpass filter and displayed with a reduction velocity of 8 km/s. (b) Picked phases with error bars and corresponding phase names. The modelled first arrivals are plotted as black lines. (c) Ray path for picks shown in (b). Station positions are marked as triangles.

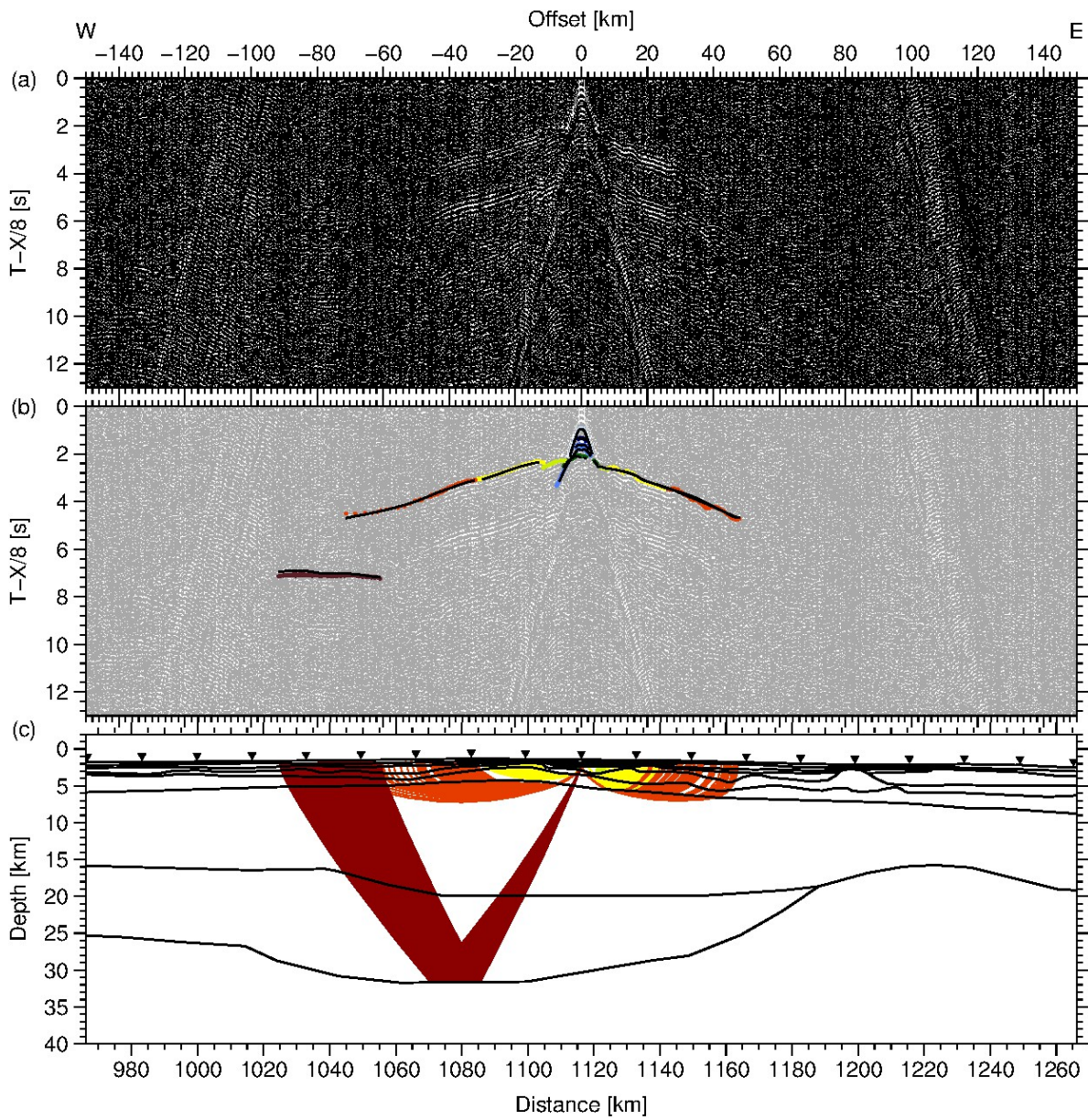


Figure A55.: Data example for OBS 77. (a) Seismic section filtered with a 4-15 Hz bandpass filter and displayed with a reduction velocity of 8 km/s. (b) Picked phases with error bars and corresponding phase names. The modelled first arrivals are plotted as black lines. (c) Ray path for picks shown in (b). Station positions are marked as triangles.

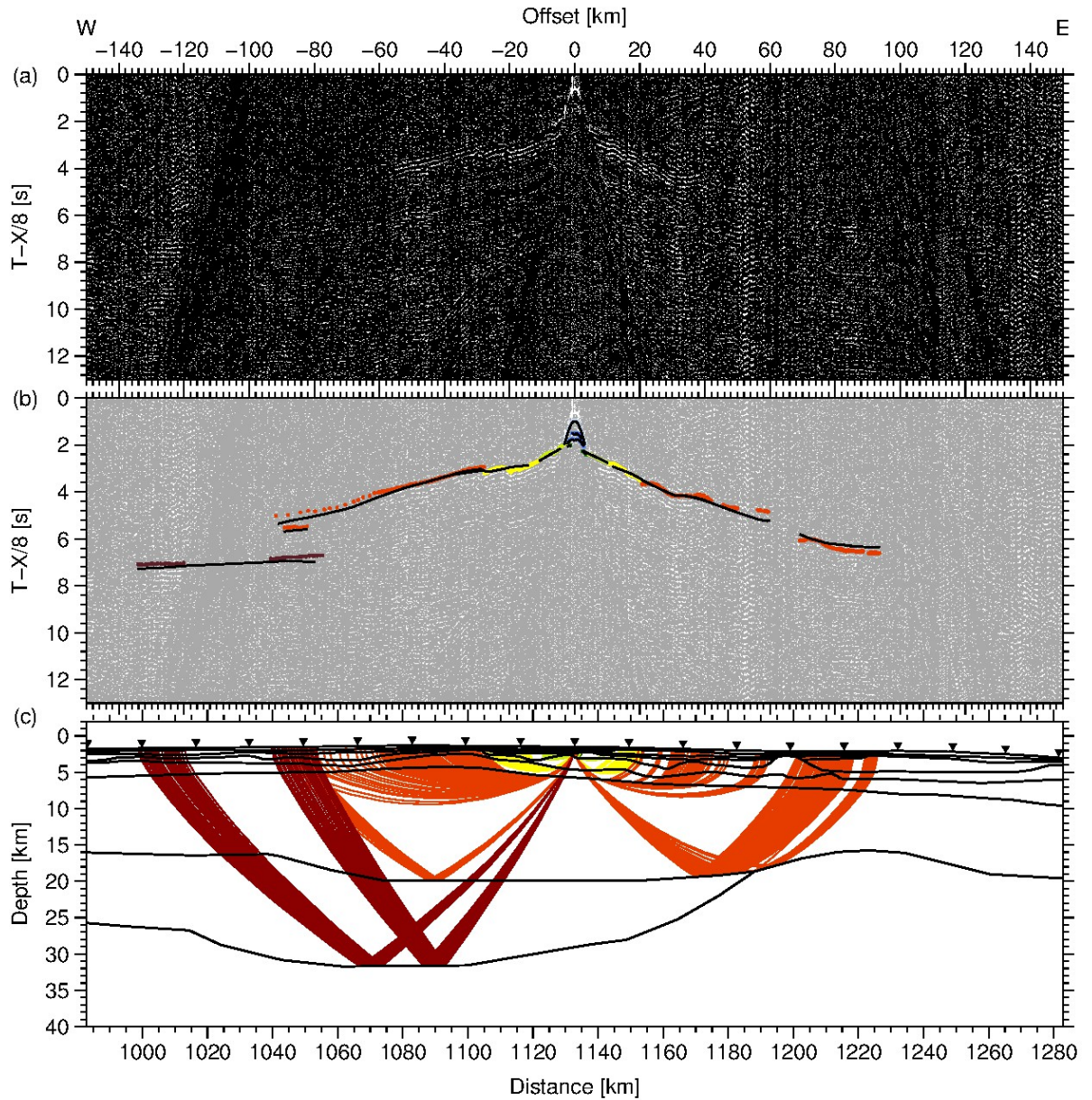


Figure A56.: Data example for OBS 78. (a) Seismic section filtered with a 4-15 Hz bandpass filter and displayed with a reduction velocity of 8 km/s. (b) Picked phases with error bars and corresponding phase names. The modelled first arrivals are plotted as black lines. (c) Ray path for picks shown in (b). Station positions are marked as triangles.

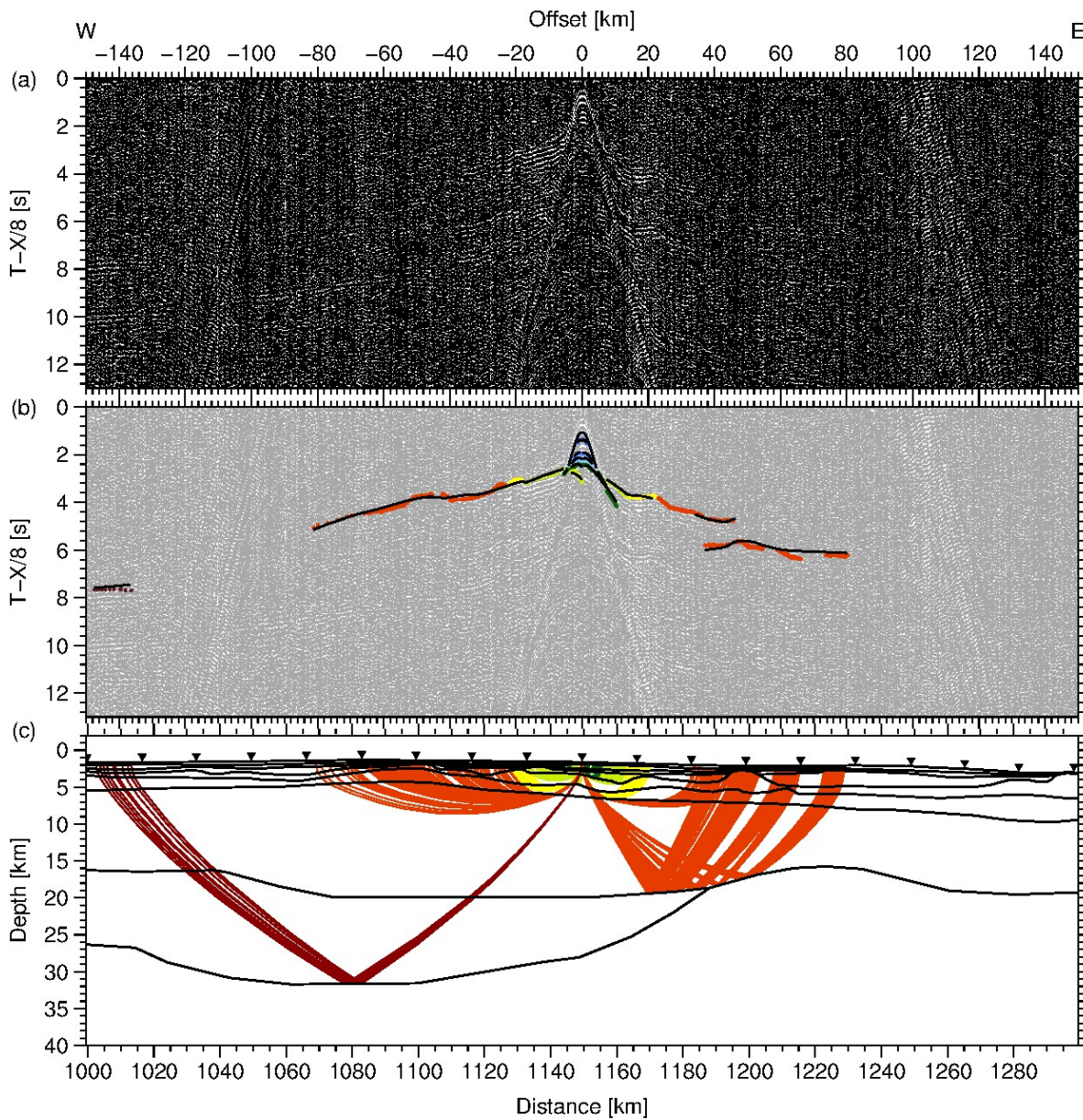


Figure A57.: Data example for OBS 79. (a) Seismic section filtered with a 4-15 Hz bandpass filter and displayed with a reduction velocity of 8 km/s. (b) Picked phases with error bars and corresponding phase names. The modelled first arrivals are plotted as black lines. (c) Ray path for picks shown in (b). Station positions are marked as triangles.

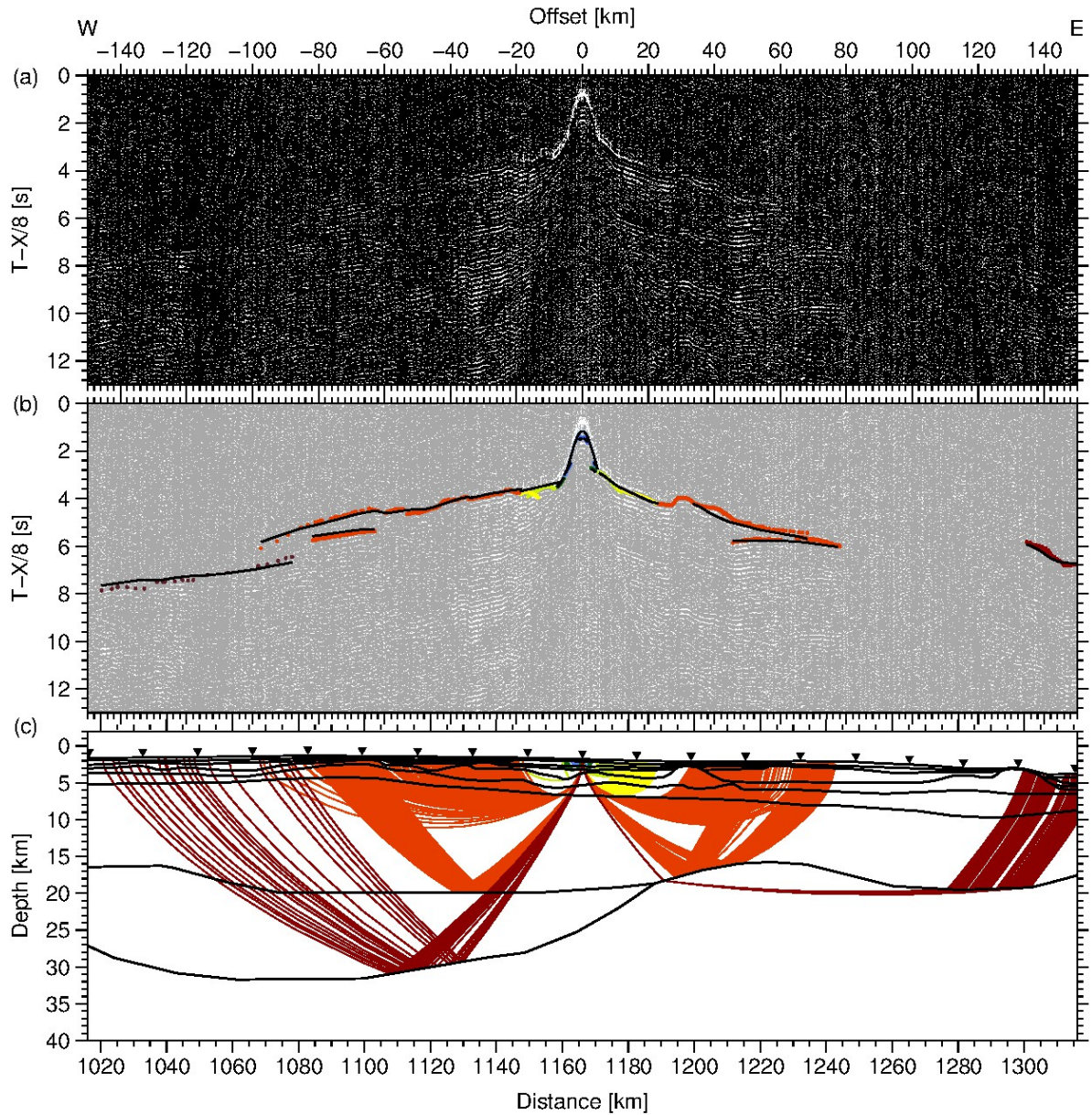


Figure A58.: Data example for OBS 80. (a) Seismic section filtered with a 4-15 Hz bandpass filter and displayed with a reduction velocity of 8 km/s. (b) Picked phases with error bars and corresponding phase names. The modelled first arrivals are plotted as black lines. (c) Ray path for picks shown in (b). Station positions are marked as triangles.

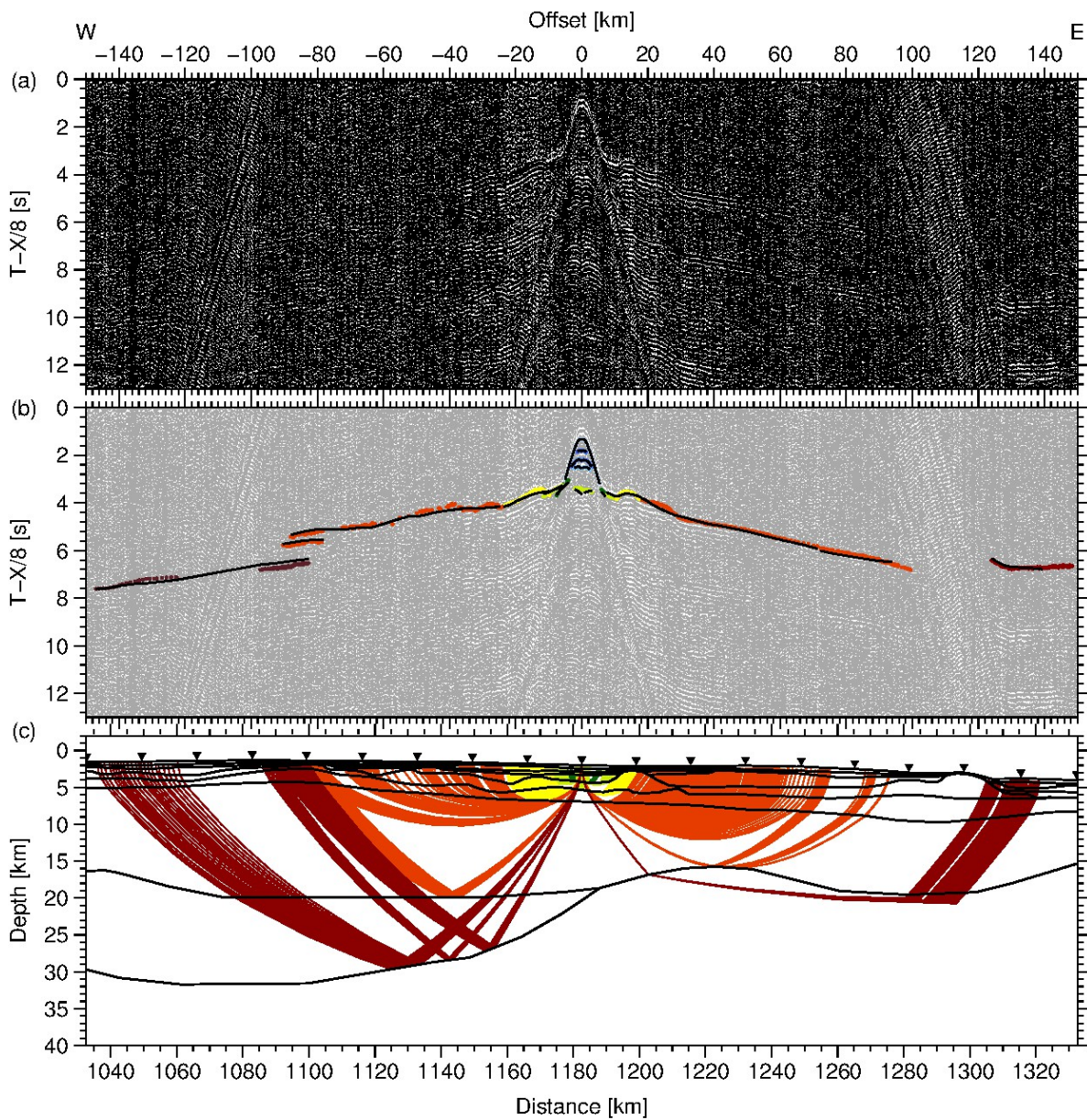


Figure A59.: Data example for OBS 81. (a) Seismic section filtered with a 4-15 Hz bandpass filter and displayed with a reduction velocity of 8 km/s. (b) Picked phases with error bars and corresponding phase names. The modelled first arrivals are plotted as black lines. (c) Ray path for picks shown in (b). Note that for the calculation of the P_n the Moho had to be shifted (visible in its ray path), otherwise no rays would be traced for the P_n . This results from the limitations of the ray tracing method and the shift does not necessary represent the Moho topography.

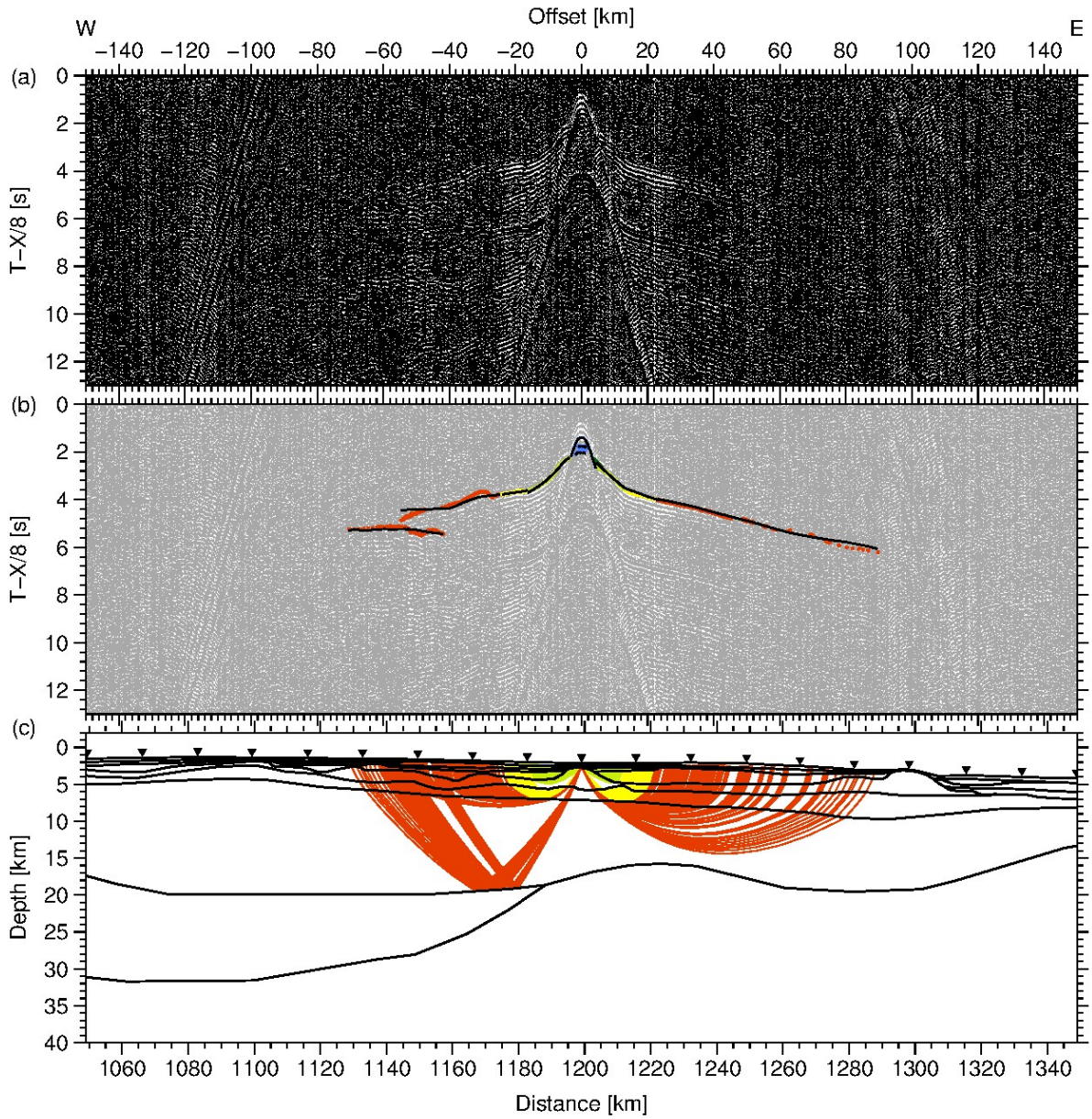


Figure A60.: Data example for OBS 82. (a) Seismic section filtered with a 4-15 Hz bandpass filter and displayed with a reduction velocity of 8 km/s. (b) Picked phases with error bars and corresponding phase names. The modelled first arrivals are plotted as black lines. (c) Ray path for picks shown in (b). Station positions are marked as triangles.

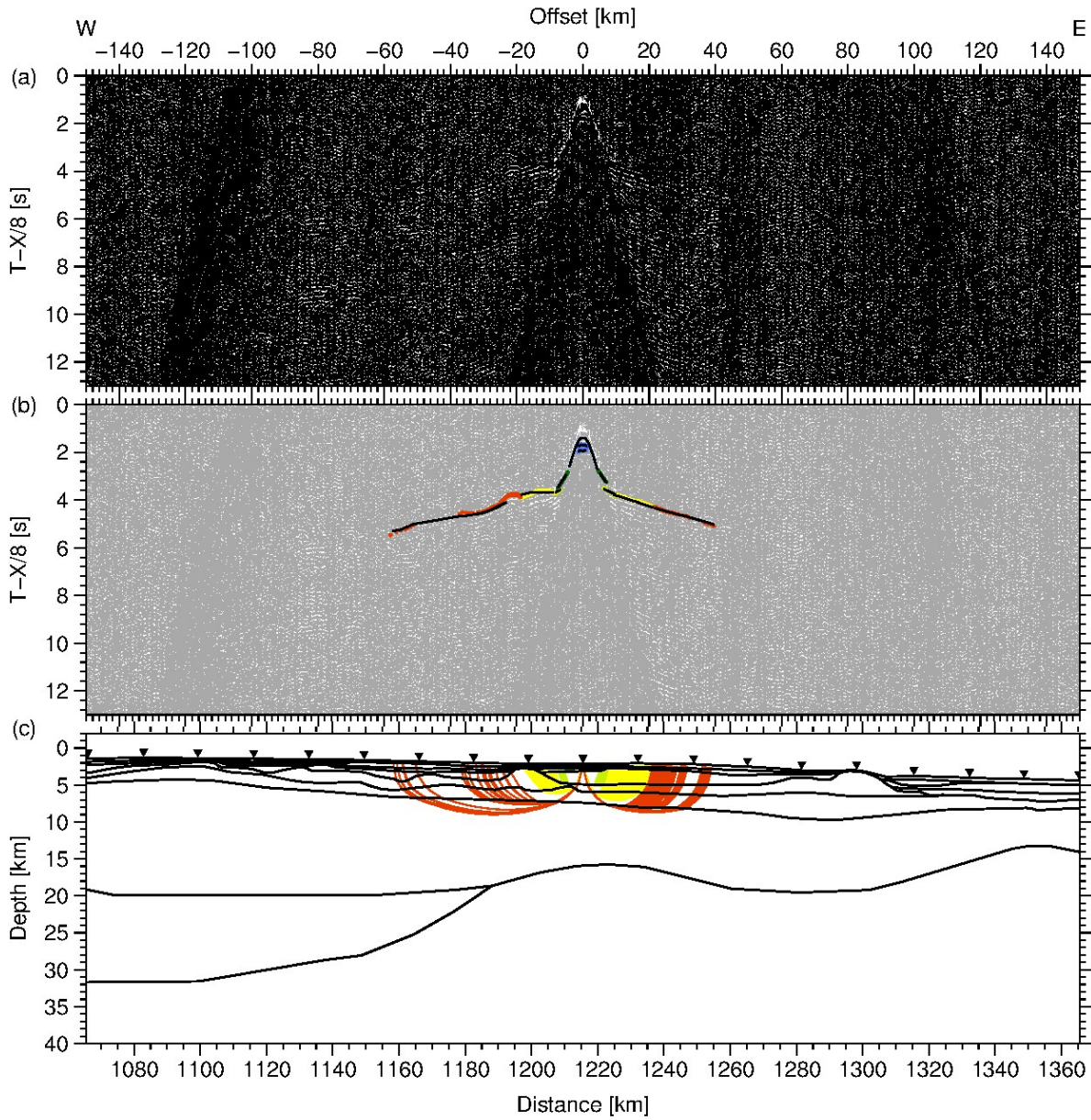


Figure A61.: Data example for OBS 83. (a) Seismic section filtered with a 4-15 Hz bandpass filter and displayed with a reduction velocity of 8 km/s. (b) Picked phases with error bars and corresponding phase names. The modelled first arrivals are plotted as black lines. (c) Ray path for picks shown in (b). Station positions are marked as triangles.

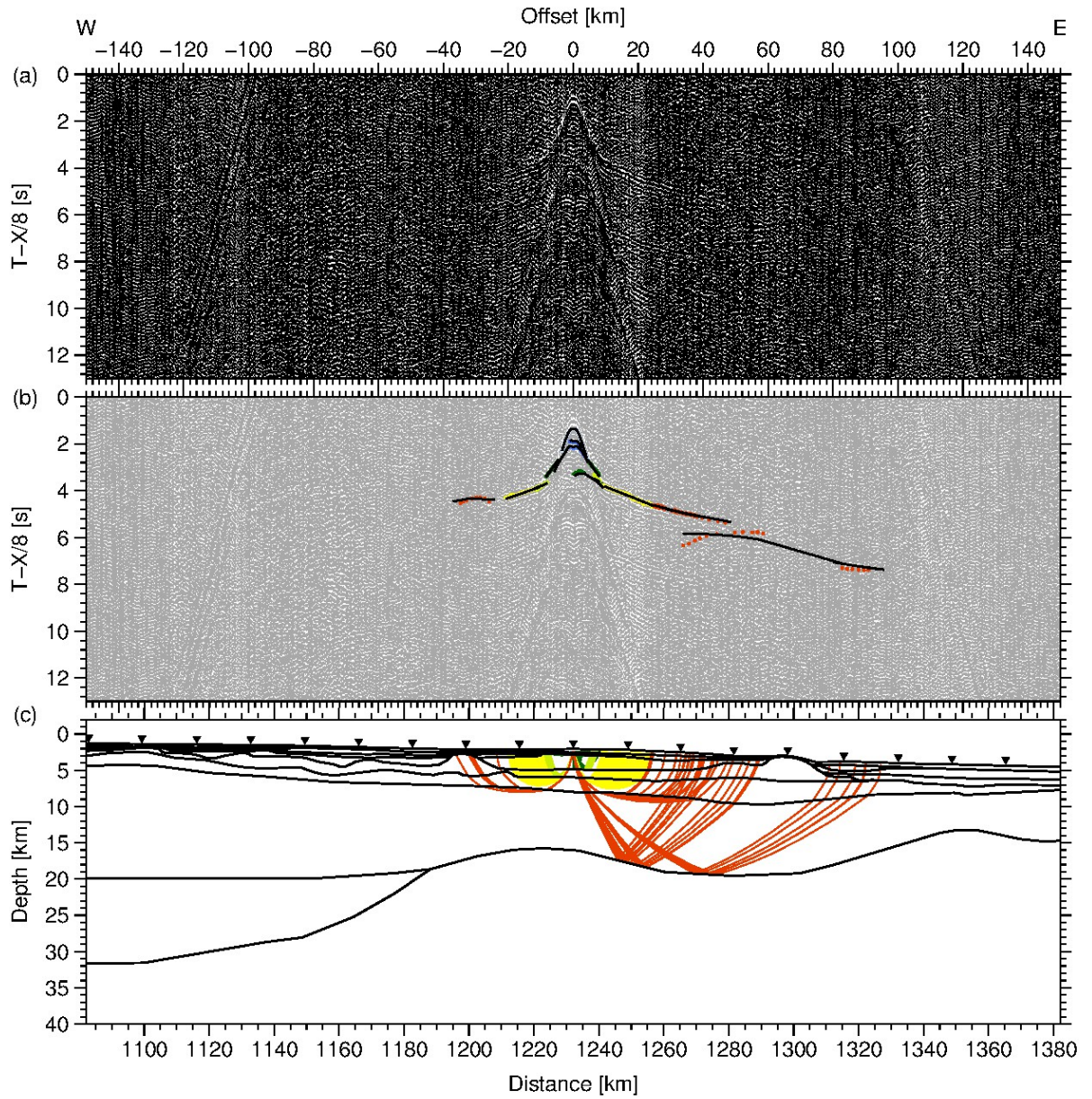


Figure A62.: Data example for OBS 84. (a) Seismic section filtered with a 4-15 Hz bandpass filter and displayed with a reduction velocity of 8 km/s. (b) Picked phases with error bars and corresponding phase names. The modelled first arrivals are plotted as black lines. (c) Ray path for picks shown in (b). Station positions are marked as triangles.

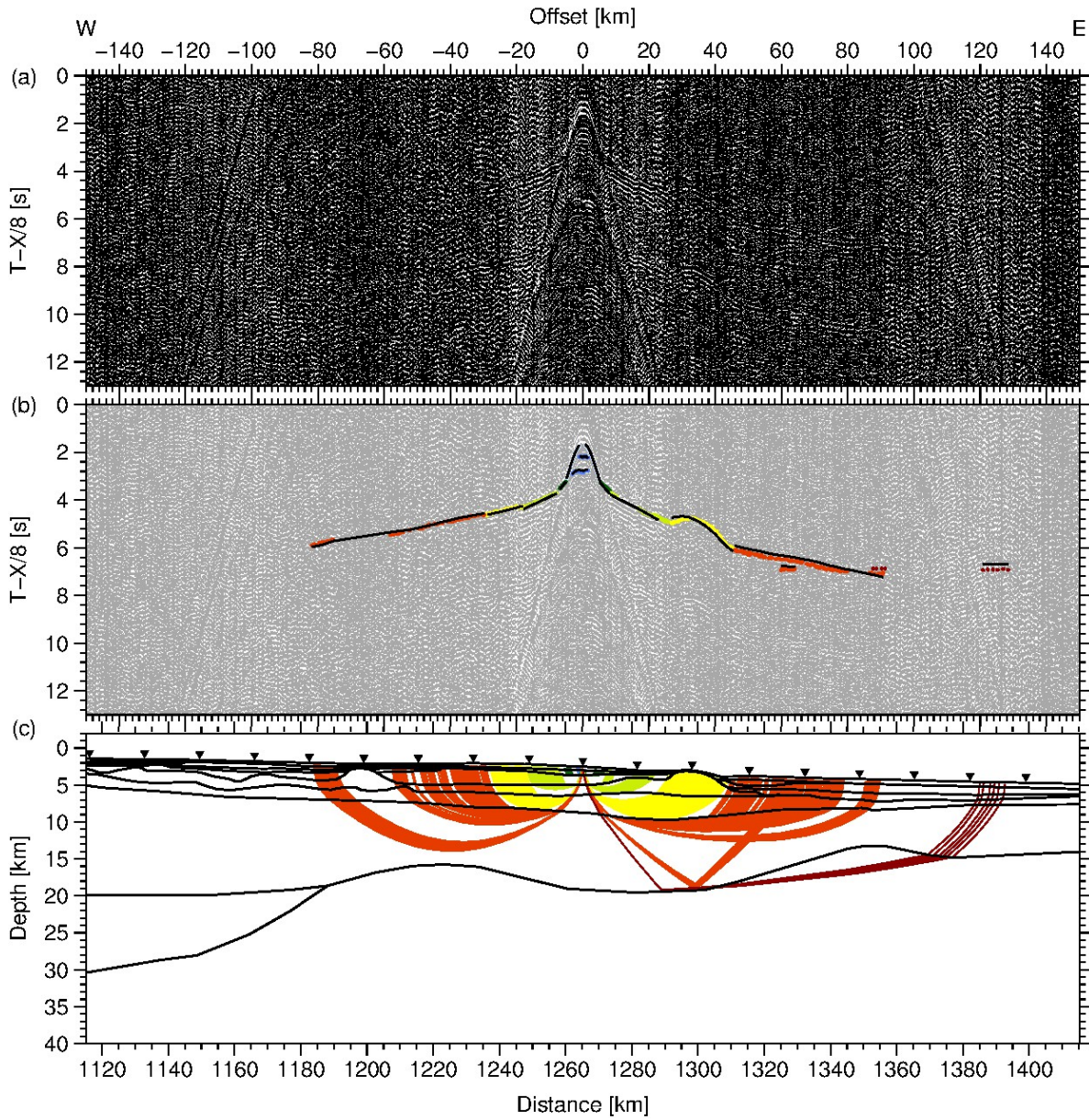


Figure A63.: Data example for OBS 86. (a) Seismic section filtered with a 4-15 Hz bandpass filter and displayed with a reduction velocity of 8 km/s. (b) Picked phases with error bars and corresponding phase names. The modelled first arrivals are plotted as black lines. (c) Ray path for picks shown in (b). Station positions are marked as triangles.

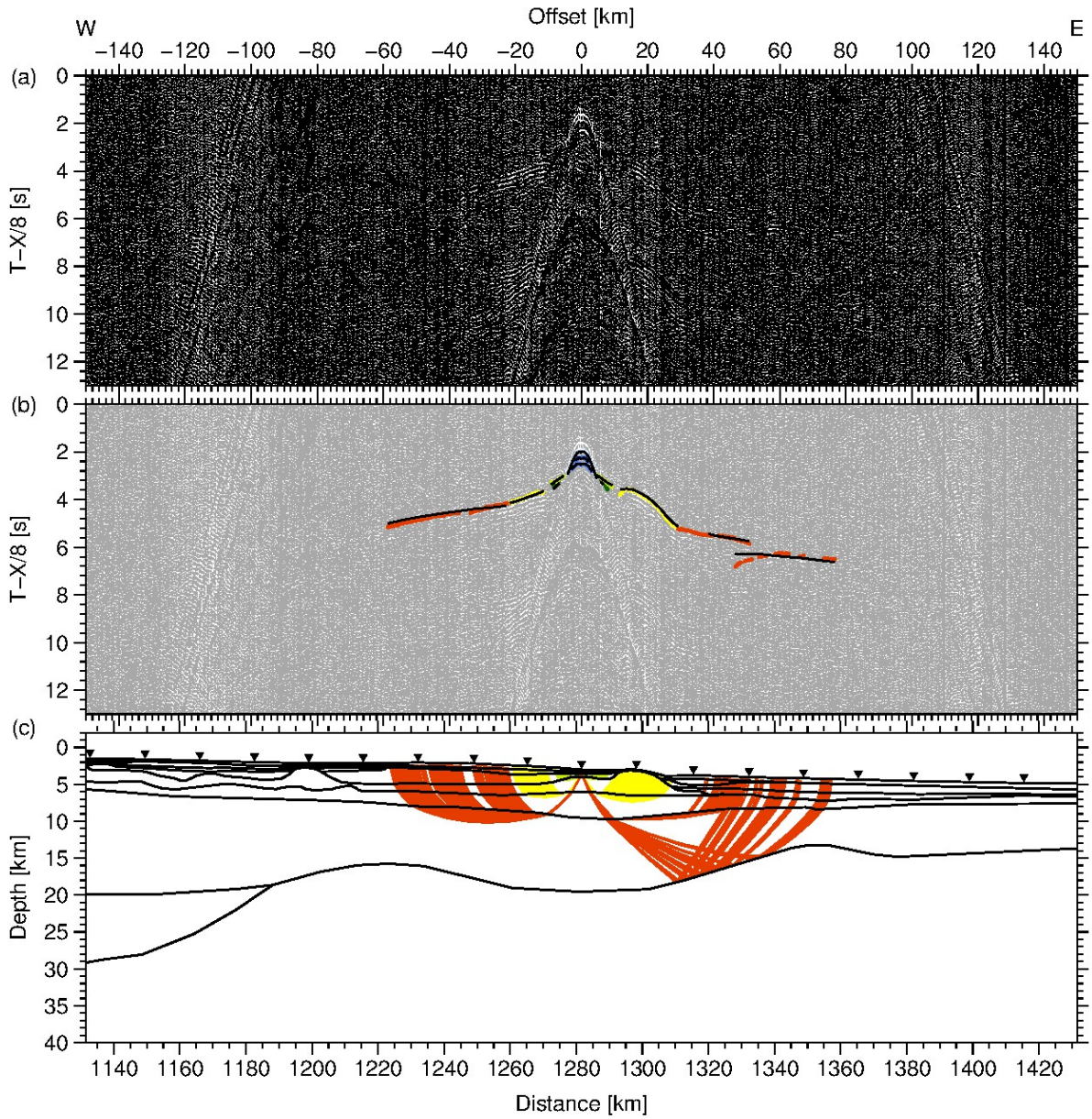


Figure A64.: Data example for OBS 87. (a) Seismic section filtered with a 4-15 Hz bandpass filter and displayed with a reduction velocity of 8 km/s. (b) Picked phases with error bars and corresponding phase names. The modelled first arrivals are plotted as black lines. (c) Ray path for picks shown in (b). Station positions are marked as triangles.

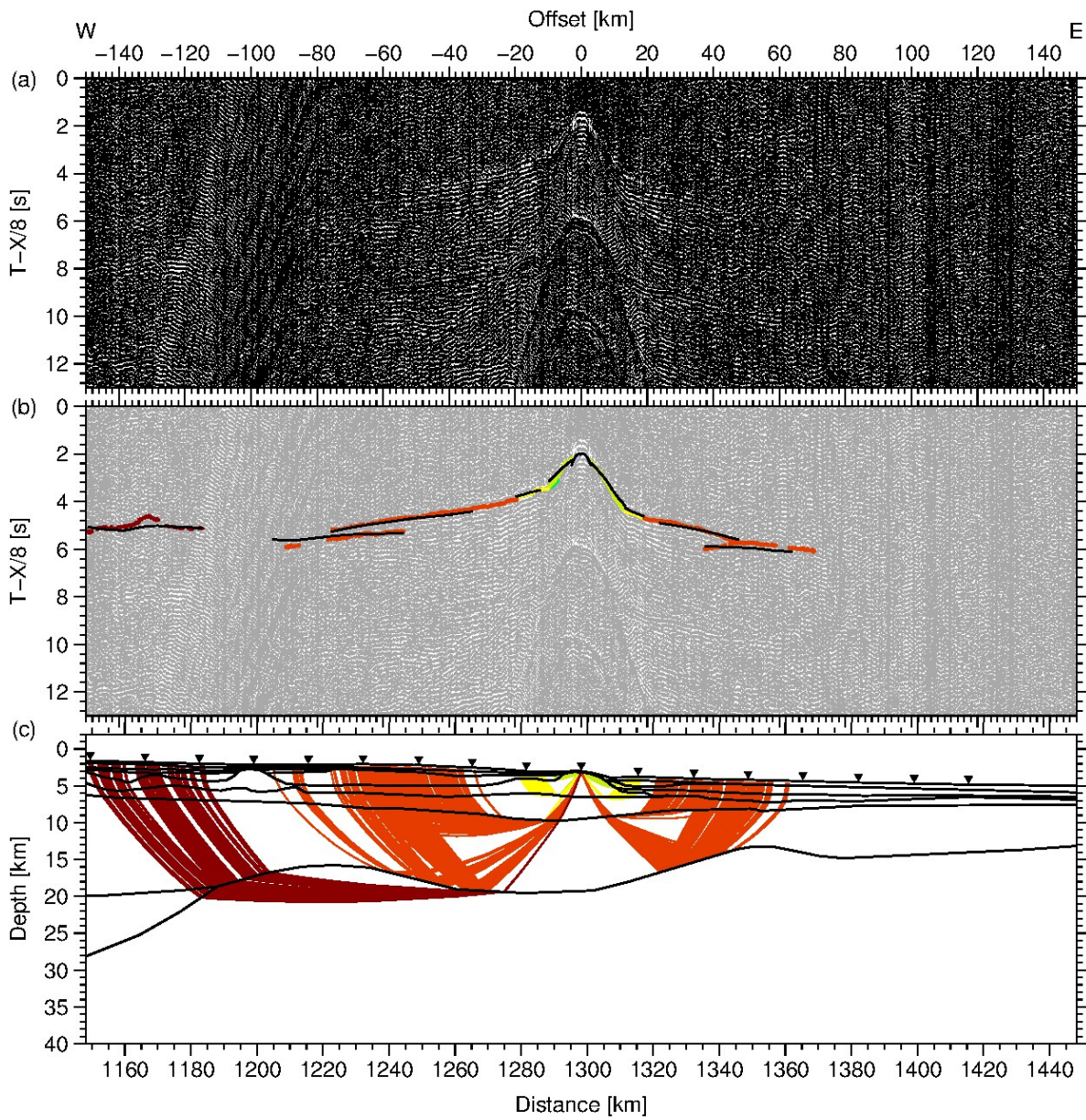


Figure A65.: Data example for OBS 88. (a) Seismic section filtered with a 4-15 Hz bandpass filter and displayed with a reduction velocity of 8 km/s. (b) Picked phases with error bars and corresponding phase names. The modelled first arrivals are plotted as black lines. (c) Ray path for picks shown in (b). Station positions are marked as triangles.

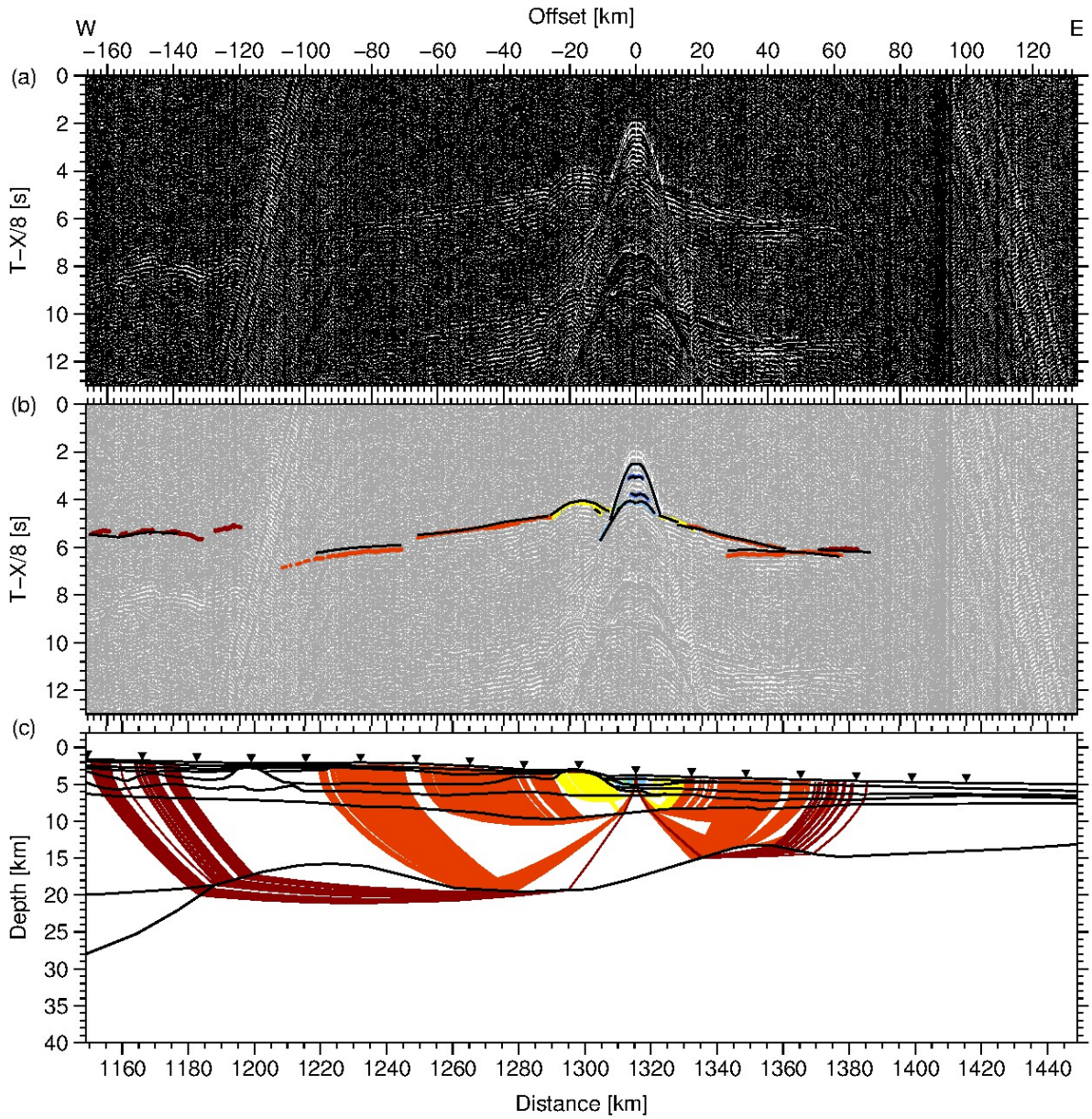


Figure A66.: Data example for OBS 89. (a) Seismic section filtered with a 4-15 Hz bandpass filter and displayed with a reduction velocity of 8 km/s. (b) Picked phases with error bars and corresponding phase names. The modelled first arrivals are plotted as black lines. (c) Ray path for picks shown in (b). Station positions are marked as triangles.

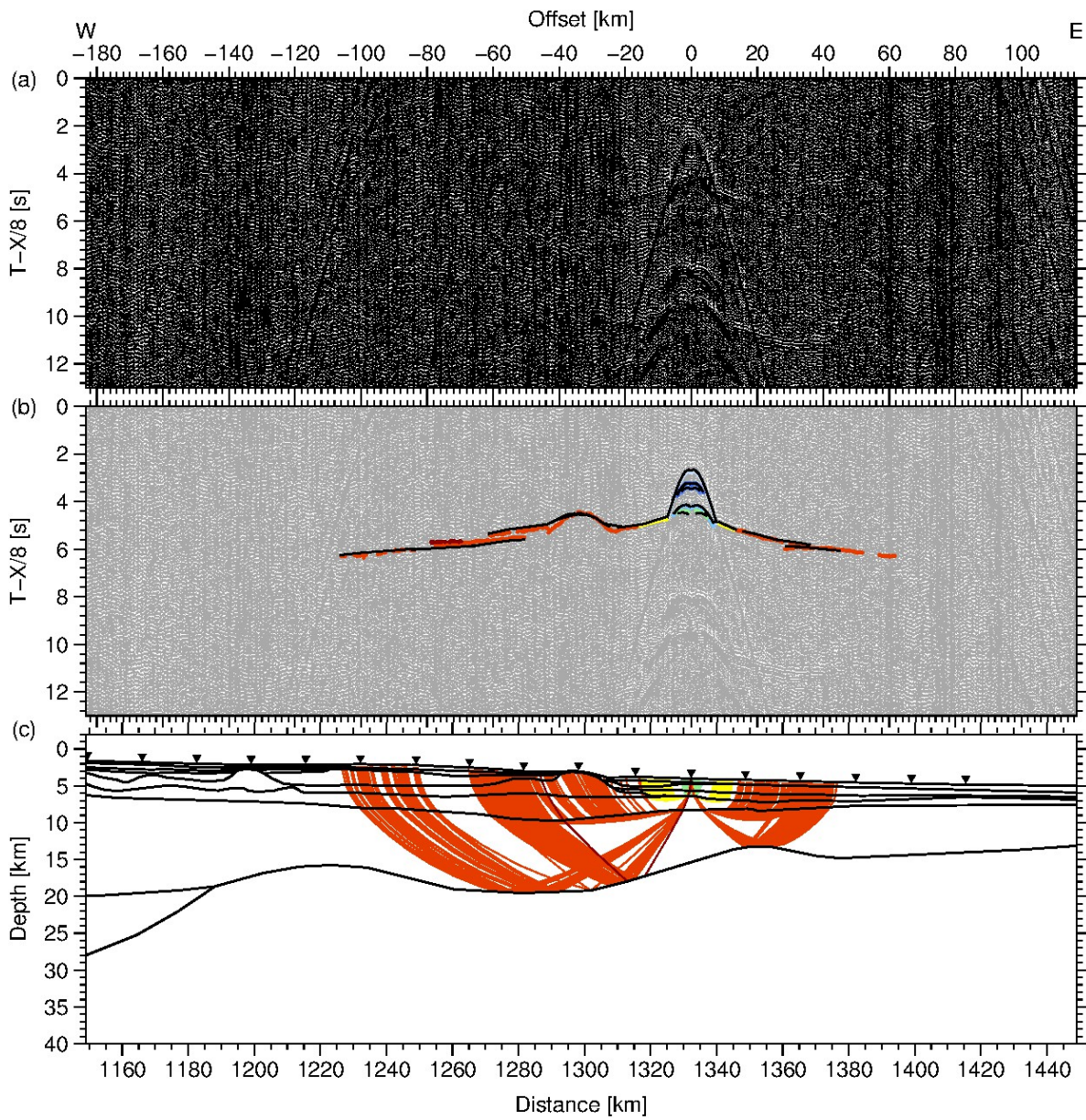


Figure A67.: Data example for OBS 90. (a) Seismic section filtered with a 6-12 Hz bandpass filter and displayed with a reduction velocity of 8 km/s. (b) Picked phases with error bars and corresponding phase names. The modelled first arrivals are plotted as black lines. (c) Ray path for picks shown in (b). Station positions are marked as triangles.

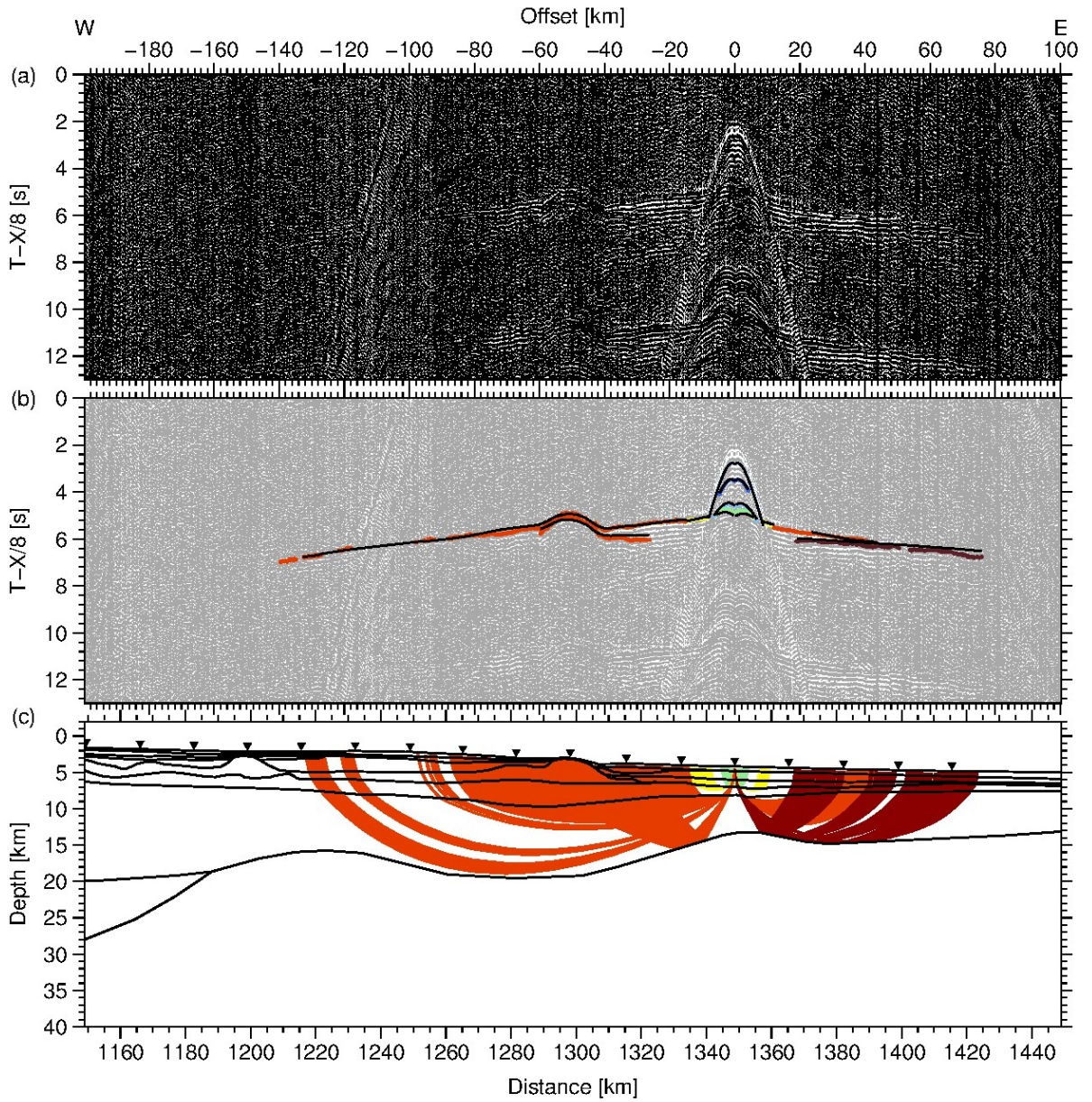


Figure A68.: Data example for OBS 91. (a) Seismic section filtered with a 4-15 Hz bandpass filter and displayed with a reduction velocity of 8 km/s. (b) Picked phases with error bars and corresponding phase names. The modelled first arrivals are plotted as black lines. (c) Ray path for picks shown in (b). Station positions are marked as triangles.

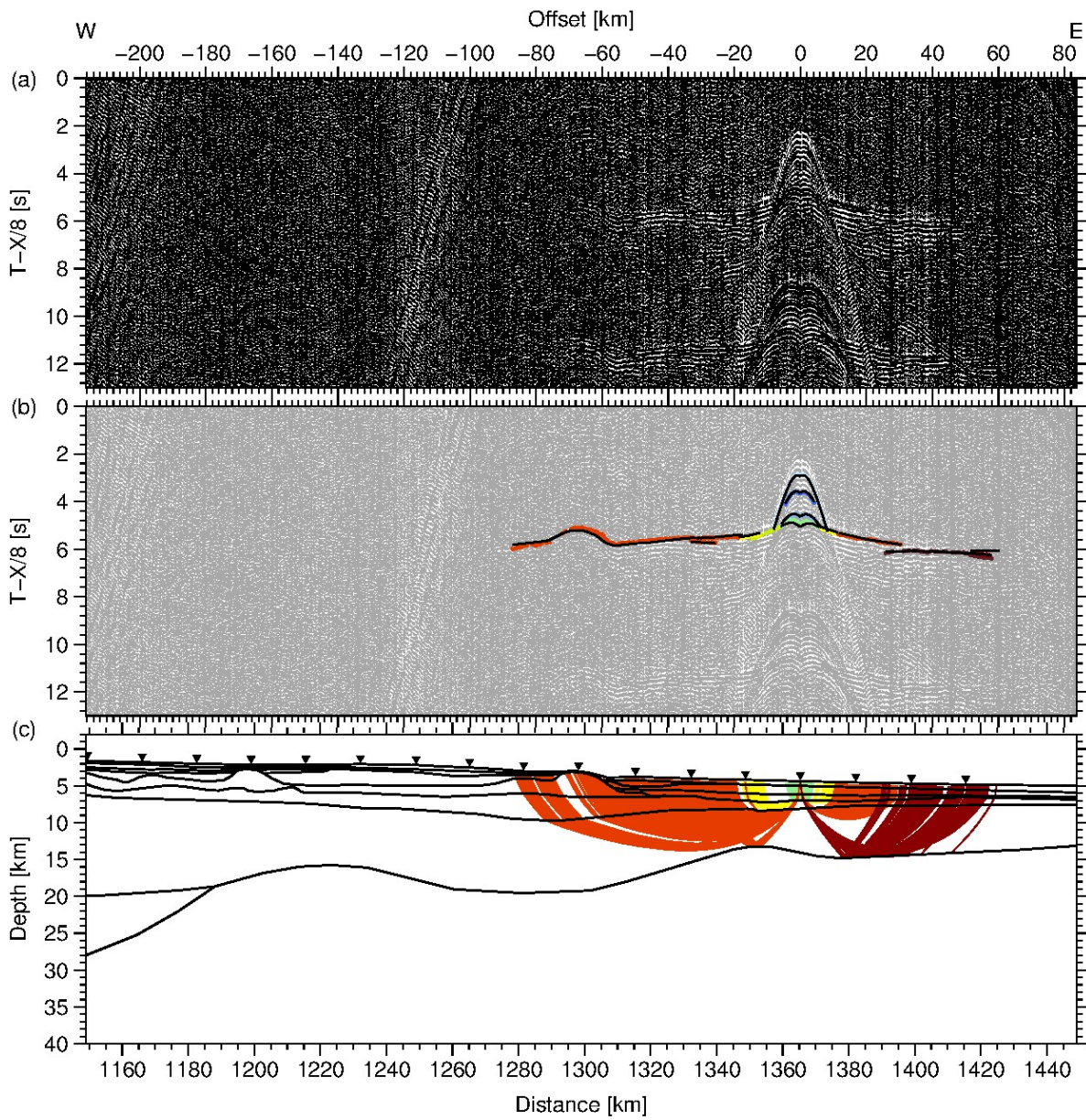


Figure A69.: Data example for OBS 92. (a) Seismic section filtered with a 4-15 Hz bandpass filter and displayed with a reduction velocity of 8 km/s. (b) Picked phases with error bars and corresponding phase names. The modelled first arrivals are plotted as black lines. (c) Ray path for picks shown in (b). Station positions are marked as triangles.

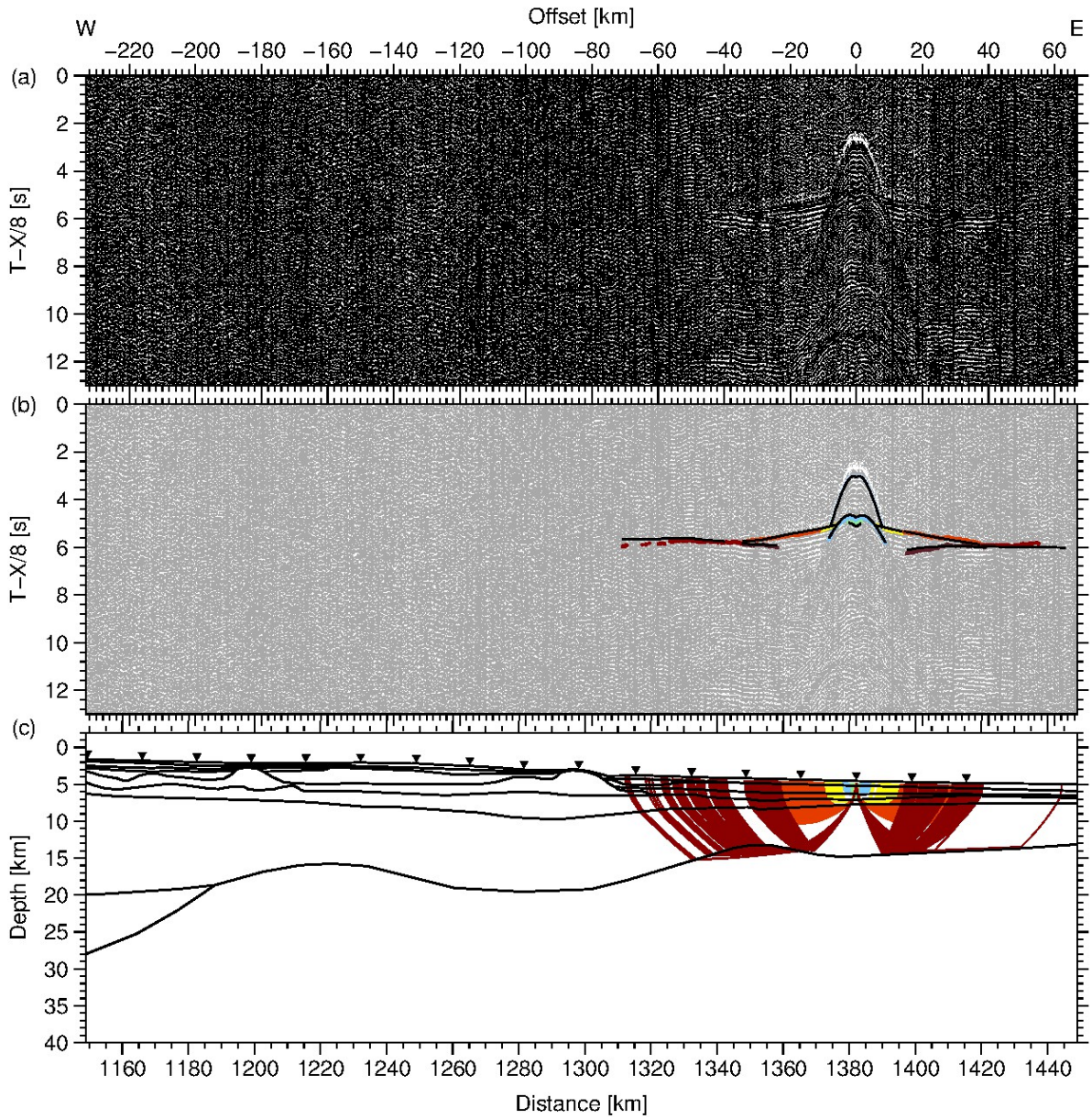


Figure A70.: Data example for OBS 93. (a) Seismic section filtered with a 4-15 Hz bandpass filter and displayed with a reduction velocity of 8 km/s. (b) Picked phases with error bars and corresponding phase names. The modelled first arrivals are plotted as black lines. (c) Ray path for picks shown in (b). Station positions are marked as triangles.

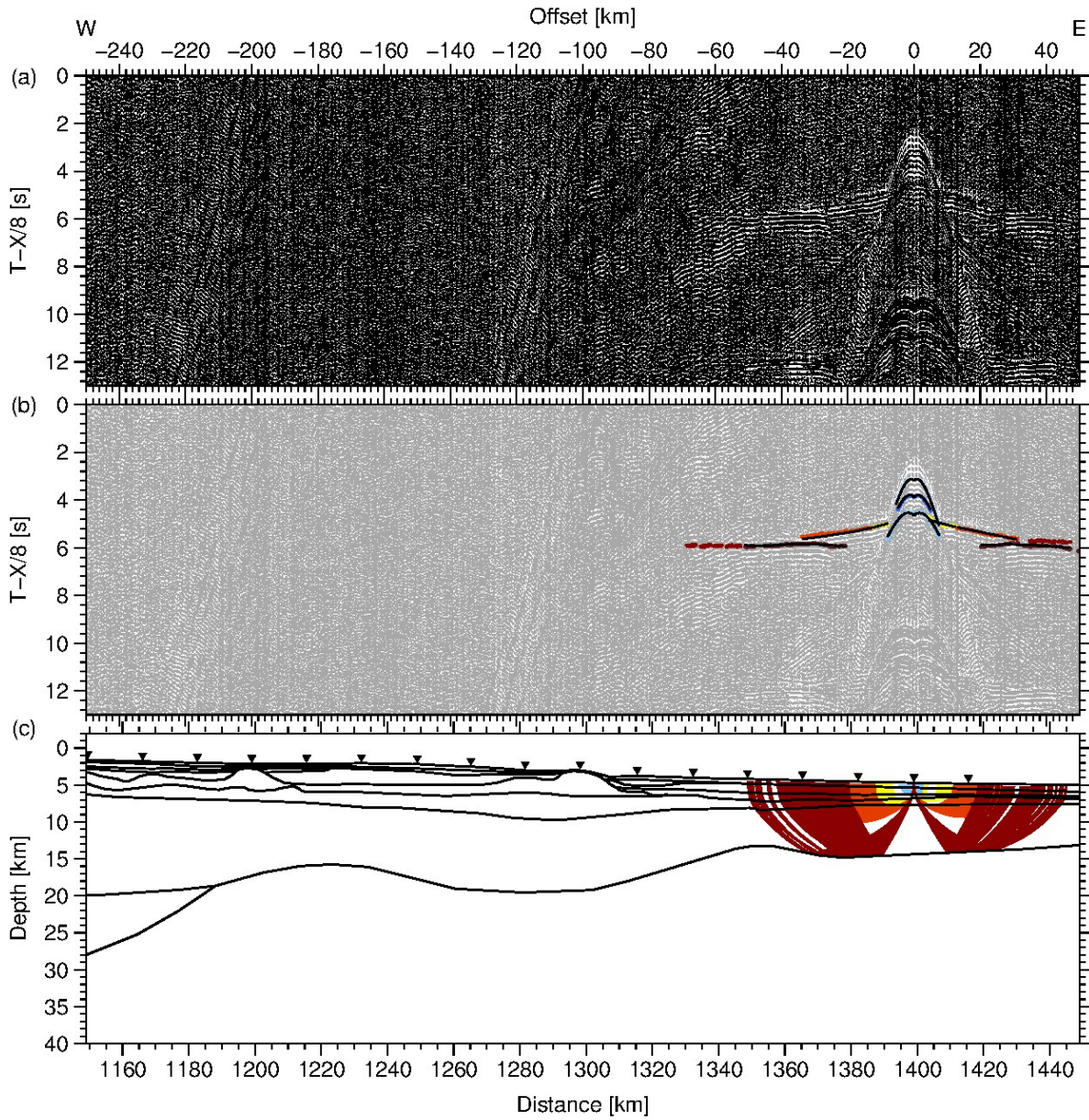


Figure A71.: Data example for OBS 94. (a) Seismic section filtered with a 4-15 Hz bandpass filter and displayed with a reduction velocity of 8 km/s. (b) Picked phases with error bars and corresponding phase names. The modelled first arrivals are plotted as black lines. (c) Ray path for picks shown in (b). Station positions are marked as triangles.

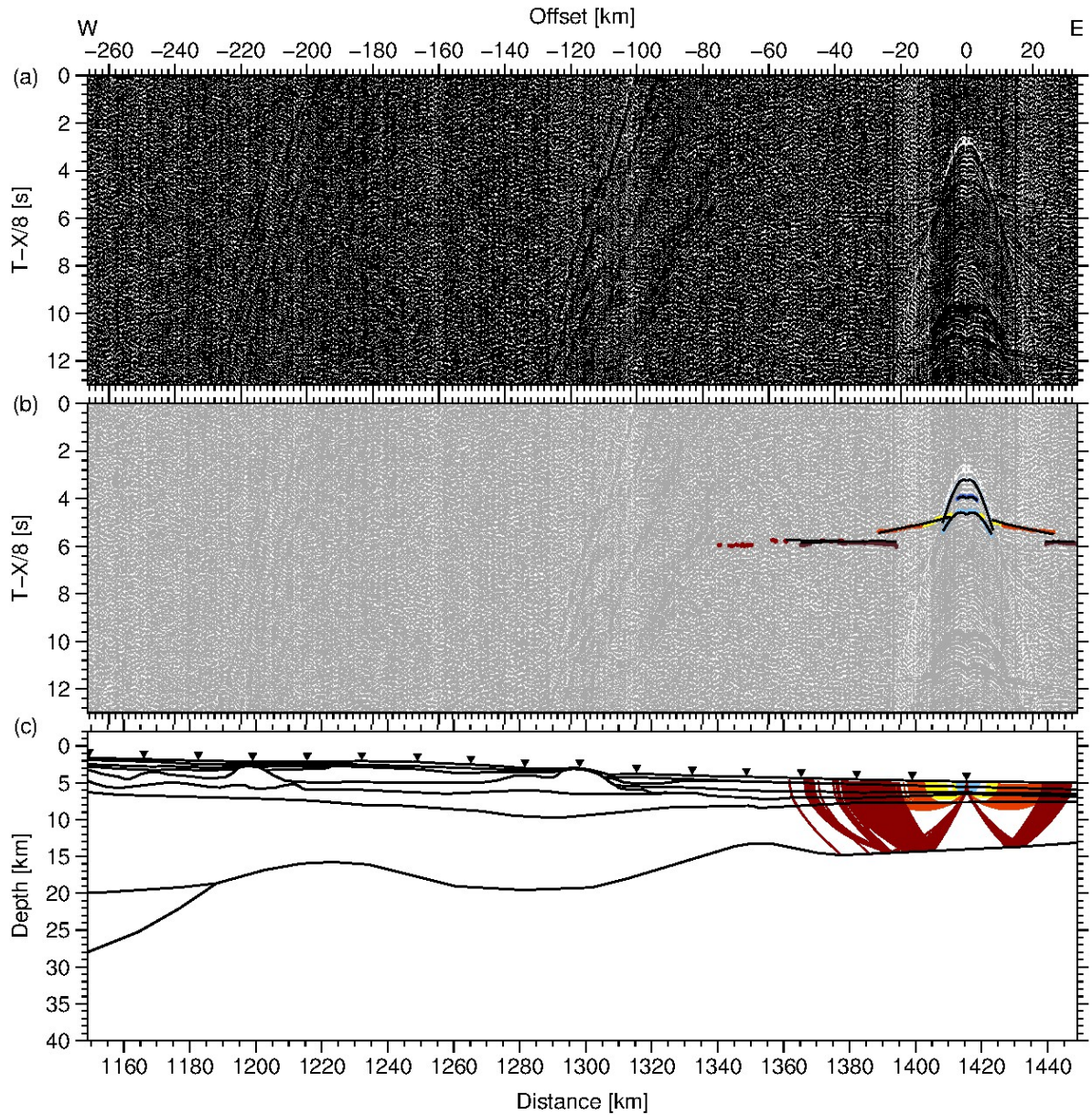


Figure A72.: Data example for OBS 95. (a) Seismic section filtered with a 4-15 Hz bandpass filter and displayed with a reduction velocity of 8 km/s. (b) Picked phases with error bars and corresponding phase names. The modelled first arrivals are plotted as black lines. (c) Ray path for picks shown in (b). Station positions are marked as triangles.

Danksagung

Ich hatte eine super Zeit in Bremerhaven (was ich nicht unbedingt erwartet habe) und ich möchte allen danken, die dazu beigetragen haben und mich während bei meiner Doktorarbeit unterstützt haben.

Besonderer Dank geht an

Wilfried Jokat für seine Erfahrung in der Wissenschaft und seine Gelassenheit und Geduld.

Cornelia Spiegel für die Begutachtung dieser Arbeit.

Graeme Eagles für das Kontrollieren der Manuskripte und die Unterstützung mit den Magnetik-Daten.

Christian Olaf Mueller für die Hilfe bei der Datenbearbeitung und die insgesamt witzige Zeit. Wenigstens einer, der Ahnung von Winter-Sport hat.

Maren Vormann für die nette gemeinsame Zeit im Büro und die vielen Schwangerschaftsgespräche.

die "Mensa-Jungs" für die Gesellschaft beim Essen von Ofen-Kartoffeln.

die ganze Geophysik Sektion, besonders Antje, Katharina, Tanja, Tabea, Ricarda, Gabi und Flo für die schöne Zeit mit euch und die Unterstützung bei allen Fragen rund um die Diss.

Marko Rothe für die konstante Unterstützung vor allem beim Bearbeiten der Refteks und allen Matlab (oder wie du jetzt anmerken würdest 'MATLAB') Problemen.

meinen Bruder, du bist der coolste Bruder den man haben kann.

meine Eltern, ihr habt mir Wurzeln und Flügel geschenkt.

Schimi und mein Happy Baby Lia, ihr seid das Beste was mir je passiert ist. Ich liebe euch.